Optical Read-out Techniques for the Control of Test-masses in Gravitational Wave Observatories

Stuart Mark Aston
M.Sci.

A Thesis submitted to
The University of Birmingham
for the degree of
Doctor of Philosophy

Astrophysics and Space Research Group
School of Physics and Astronomy
University of Birmingham
Birmingham, UK
B15 2TT

January 2011

Abstract

This thesis discusses the development of optical read-out techniques, including a simple shadow sensor and a more elaborate compact homodyne interferometer, known as EUCLID. Both of these sensors could be utilised as part of a seismic isolation and suspension system of a ground-based gravitational wave observatory, such as Advanced LIGO.

As part of the University of Birmingham's commitment to the upgrade of the Advanced LIGO, it was responsible for providing a large quantity of sensor and actuator units. This required the development and qualification of the shadow sensor, through to production and testing. While characterising production units, an excess noise issue was uncovered and eventually mitigated; demonstrating that even for a 'simple' shadow sensor, ensuring a large quantity of units meet the target sensitivity requirement of 3×10^{-10} m Hz$^{-1/2}$ at 1 Hz, is not a trivial exercise.

Over the duration of this research, I played a key role in the design and fabrication of a novel compact interferometer. The objective of this work was to demonstrate that the interferometric technique offers a significant improvement over the existing shadow sensors and could easily be deployed in current, or future, generations of gravitational wave observatories. Encouraging sensitivities of $\approx$ 50 pm Hz$^{-1/2}$ at 1 Hz, over operating ranges of $\approx$ 6 mm have been achieved, whilst maintaining $\pm$ 1 degree of mirror tilt immunity. In addition, this design overcomes many of the drawbacks traditionally associated with interferometers.

Declaration

This thesis is a presentation of my original research work. Wherever contributions of others are involved, every effort is made to indicate this clearly, with due reference to the literature, and acknowledgement of collaborative research and discussions. The work was done under the guidance of Professor Clive Speake, at the University of Birmingham, UK.

The Advanced LIGO project work discussed in Chapter 3, can be broken down as follows. The development of the imaging sensor, including opto-mechanics and support electronics was carried out by myself, at the University of Birmingham under the guidance of Clive Speake. A parallel, but completely independent development of imaging sensors was also being conducted by a project collaborator, Dr Nick Lockerbie, at the University of Strathclyde. Following the culmination of the imaging sensor work, the focus switched to the shadow sensor, where Nick Lockerbie conducted the sensor study to optimise the shadow sensor performance and specify the design. I was responsible for the mechanical design of the BOSEM, incorporating the shadow sensor design. The low-noise support electronics, including the Satellite Box, was produced by colleagues at Birmingham. I was responsible for characterising the production batch of BOSEMs and at this time I identified the excess noise issue. I then embarked on a investigation to locate the source of the excess noise, which I later attributed to the IRLED. I identified an alternative IRLED and outlined a screening procedure that would offer a substantially higher yield and I oversaw the retro-fitting of these devices into production BOSEMs. Finally, I characterised a large quantity of the final deliverables, to demonstrate their compliance with the requirements and that the excess noise issue had been mitigated.

Acknowledgements

If I were able to list here all those that have assisted or inspired me in writing this thesis, this section would be longer than would be deemed acceptable. So I will try to limit my acknowledgements to those who have aided me directly during my postgraduate studies at the University of Birmingham.

First and foremost, I wish to thank my PhD supervisor, Professor Clive Speake, for all his continuous encouragement and guidance over the past 8 years. I thank him for his patience and for the regular discussions we have had, ensuring I never lost sight of the overall goal. I also wish to thank both present and past members of the group, Fabián Peña Arellano, Andreas Freise and my Graduate Technologist colleagues, George Dixon, Matthew Holder and Deepali Lodhia for their assistance and support.

Whilst conducting my post-graduate research, I have also been extensively involved in project work. Fortunately, the vast majority of my project tasks have either been closely related to my research area, or have provided me with essential skills and experience which has stood me in good stead with my experimental work. Specifically, I wish to thank both Birmingham Project Managers, Mike Cruise (LISA Pathfinder) and Alberto Vecchio (Advanced LIGO) for not overwhelming me, too much, with project work. Moreover, whilst undertaking project work both in the UK and further afield, I have had opportunities to meet many esteemed and renowned colleagues and travel to other institutes. So I wish to thank the funding agencies, such as the STFC for supporting the UK's role in large international collaborations, through grants and project funding.

Throughout my project work and research I have also been fortunate to work with skilled and dedicated technical staff; many of whom have been able to handle my endless list of requests and have provided a fountain of knowledge. To name but a few, Dave Hoyland, Ron Cutler, Dave Smith, John Bryant, Bill Parry, Anthony Page and Steve Brookes.

Last, but certainly not least, I wish to acknowledge the support of all my friends and family. I am exceptionally grateful to Scott Porter and Stephen Fletcher for their friendship throughout my undergraduate and postgraduate studies at Birmingham.

Contents

List of Figures

List of Tables

Chapter 1

The Search for Gravitational Waves

"Nothing has such power to broaden the mind as the ability to investigate systematically and truly all that comes under thy observation in life". Marcus Aurelius.

1.1 Introduction

Throughout history, humans have been aware of the force of gravity. From the projectile weapons thrown by prehistoric man, to the manned moon landings in the twentieth century, gravity has played a pivotal part in human achievements. But for centuries the role of gravity has been silent and it is only now that we are at the threshold of uncovering its mystery.

Early efforts made at understanding the force of gravity, were mainly qualitative in nature. It was not until late in the seventeenth century that a viable theory on gravity was proposed.

In 1687, Sir Isaac Newton published in his *Philosophiæ Naturalis Principia Mathematica* [1], the universal law of gravitational attraction

$$F = G\frac{m_1 m_2}{r^2},$$

(1.1)

where F is the magnitude of the gravitational force in newtons, m_1 and m_2 are the masses in kilograms of two spherical or point masses, r is the distance between the masses in metres and G is the Newtonian gravitational constant. This inverse square law provided a breakthrough for those wanting a more quantitative understanding of gravity. However, it was over a century later, in 1798, when measurements of the density of the Earth conducted by Henry Cavendish [2], allowed a value to be determined for the gravitational constant (G $\approx 6.74 \times 10^{-11}$ m^3 kg^{-1} s^{-2}).

Although Newton's universal law of gravitational attraction appears valid for many Earth-based observations, it has an undeniable failing. Unfortunately this law gives

no insight into the speed of propagation for any change in the parameters of the system, since it was time-independent. As this law is written, any change of mass or separation between the masses, will result in an instantaneous effect anywhere in the universe. Hence, information about the state of the system would be required to propagate faster than the speed of light, which would later explicitly be forbidden, by Einstein's theory of special relativity [3].

1.2 Gravitational Wave Theory

Einstein's general theory of relativity [4] published in 1916, revolutionised our view of the universe and predicted the existence of gravitational radiation. Such radiation is generated by the acceleration of mass-energy distributions and is expected to behave like a wave like distortion in space-time propagating at the speed of light. Propagating gravitational waves change the curvature of four dimensional space-time and can change the measured separation between free masses. Gravitational waves are of very low intensity and interact weakly with matter. They can be better understood by analogy to electro-magnetic (E-M) waves. The motion of a particle carrying an electric charge can generate E-M radiation, just like the motion of a mass can produce a gravitational wave, since both waves are transverse and propagate at the speed of light. However, the fundamental difference is that both positive and negative charges exist for E-M interactions, whereas the mass of a particle can only have one sign. This leads to gravitational radiation being quadrupole in nature, with monopole and dipole radiation being forbidden [5].

Einstein proposed the field equation showing the interaction between the curvature of space-time and the mass distribution

$$\mathbf{G} = \kappa\,\mathbf{T},\qquad\qquad\qquad(1.2)$$

where $\mathbf{G}$ is defined as the Einstein curvature tensor. $\mathbf{T}$ is the stress-energy tensor, representing the mass-energy distribution and κ describes the Einstein constant of gravitation which is defined as

$$\kappa = \frac{8\pi\,\mathrm{G}}{c^4},\qquad\qquad\qquad(1.3)$$

where c is the speed of light in a vacuum. It is necessary for the value of constant, κ, to enable the Einstein approach to be consistent with the Newtonian approach, in the weak and slowly varying gravitational field regime. The large coupling constant implies space-time must be a very stiff and elastic medium.
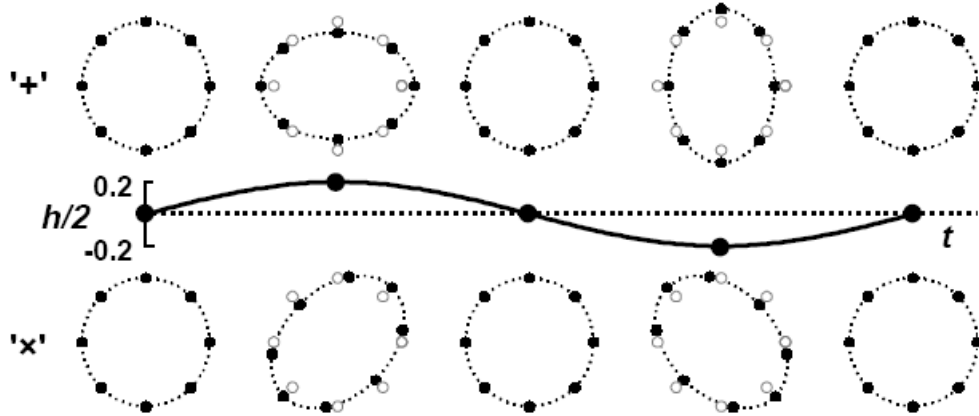
Figure 1.1: *Locations of free test masses for both polarisations (+ and ×) of a propagating gravitational wave. Source [6].*

The effects of a gravitational wave cannot be observed for isolated bodies, but only by observing the change in proper distance measured by a laser between pairs of masses. Therefore, to help visualise the effect of a propagating gravitational wave, consider a ring of free test masses, as shown in Figure 1.1. As the gravitational wave propagates normal to the page it will perturb the distance between these test masses. Assuming that this gravitational wave is of the + polarisation, then during the first half of its period test masses will be stretched apart along the horizontal axis and squeezed together along the vertical axis. During the second half of the gravitational wave's period the stretching and squeezing axes will be reversed. In Figure 1.1, the effect upon the test masses for the × polarisation of gravitational wave is shown. In this case the axes of the perturbations are rotated through 45°.

The magnitude of a gravitational wave is conveyed by the dimensionless strain amplitude

$$h(t) = 2\frac{\Delta L}{L}, \qquad\qquad (1.4)$$

17

or by its spectral component $\tilde{h}(v)$ (with units of $Hz^{-1/2}$), where L is the unperturbed length and ΔL is the measured change in length. For the purpose of Figure 1.1, the strain amplitude is exaggerated to demonstrate more clearly the influence of the propagating gravitational wave on the free test masses. However, in reality, gravitational waves generated by typical sources, are most likely only have strain amplitudes of $\approx 10^{-21}$ and are only expected to occur with rates of up to a couple of events per year [7].

1.3 Sources of Gravitational Waves

Sources of gravitational waves, at least the ones that are most likely to be detected are astrophysical in nature. These astrophysical sources may radiate away a significant proportion of their energy in the form of gravitational waves. It is also expected that such emissions will occur over a wide band of frequencies (10^{-4} Hz to 10^{10} Hz). What should we expect to observe? The following sections provide some insight into the various mechanisms by which astrophysical sources are predicted to emit gravitational waves.

It should be noted that sources already modelled may be just a fraction of what will be discovered when new observatories come online and detection becomes commonplace.

1.3.1 Chirp Signals

Chirp signals are associated with the coalescence in binary systems which could contain a combination of neutron stars and/or black holes. In such systems angular momentum is lost due to the emission of gravitational radiation. This will eventually lead to the two objects in-spiralling towards each other. As this occurs the frequency and amplitude of the gravitational wave emissions will increase until finally the bodies merge and coalesce.

If the binary system were to contain two black holes ≈ 10 $M_\odot$, where $M_\odot$ is the solar mass ($M_\odot \approx 1.99 \times 10^{30}$ kg), then due to the greater mass of the system, the coalescence of these bodies would lead to the emission of stronger gravitational radiation,

thus increasing the possibility of them being detected, and the range at which the event could be observed.

For even larger supermassive black holes, of mass 10^6 M$_\odot$ to 10^9 M$_\odot$, the in-spiral and coalescence of such objects will provide even stronger emissions of gravitational radiation. However, such emissions are also predicted to occur at very low frequencies and are most likely to be outside of the detection band of any ground-based instruments. During the various in-spiralling phases for different masses, the gravitational radiation emitted has been modelled so as to produce expected waveforms. Such waveforms would sound like a 'chirp' if listened to in the audio band. Therefore, the gravitational radiation emissions of coalescing binary systems can sweep through a wide frequency band, making them excellent candidates for detection. The event rate, for the first generation of detectors, is estimated to be approximately one per year [8].

1.3.2 Periodic Signals

Periodic signals are associated with the gravitational radiation emitted due to the rotation of neutron stars whose centre of mass does not lie on their rotation axis, possibly due to some deformation or surface irregularities. As gravitational radiation is emitted from the system, angular momentum would be lost and as a consequence the neutron star may slowly spin-down. However, such a signal is likely to remain in the detection band for some time [8].

1.3.3 Burst Signals

Burst signals are associated with the gravitational core collapse of stars, which can lead to the emission of gravitational radiation. A supernova is expected to be a typical process through which this could occur. However, there are two distinct classifications of supernovae. Type I contain dwarf stars, which are unlikely to yield substantial emissions of gravitational radiation. Type II events can involve core collapse, which if non-spherically symmetric, can lead to the emission of more substantial gravitational waves. However, the amplitude of gravitational radiation emitted is difficult to predict, given the challenge of ascertaining the likely amount of asymmetry in the core collapse. Supernova events within our galaxy are expected to occur approximately once every thirty years [8].

1.3.4 Stochastic Signals

Stochastic signals are associated with the gravitational waves emitted in the first moments of the early universe. At least two detectors are required so that their observations of the background can be correlated [8].

1.4 Methods of Detection

In essence, to enable the detection of a gravitational wave an experiment is required that will provide a measurable signal whenever a gravitational wave is incident upon a detector. However, the anticipated magnitude of the strain makes the design and construction of such scientific instrumentation very challenging. This section discusses some of the history in this field and provides motivation for the current ground-based interferometric gravitation wave observatories.

1.4.1 Resonant Bars

The first instruments developed to directly detect gravitational waves were pioneered by Weber [9] during the early 1960's. These consisted of large aluminium bars that would resonate at frequencies of up to about 1660 Hz. Should a gravitational wave of similar frequency to the longitudinal resonant frequency of the bar pass through the instrument, the bar would become excited. Sensors covering the bar should be capable of detecting motion at the fundamental longitudinal resonance frequency. More recent experiments of this nature have increased the mass, reduced the thermal noise by cooling the experiment down, employed more sensitive superconducting quantum interference device (SQUID) read-outs and are investigating alternative geometries to the bar. MiniGRAIL for example exploits a spherical mass cooled to 20 mK and aims to observe a strain sensitivity of 4×10^{-21} [10]. However, the main drawback of resonant bar detectors remains; they are only sensitive over a very narrow frequency band, usually a few tens of Hertz, dictated by their physical dimensions.

1.4.2 Hulse-Taylor Pulsar

During 1975, whilst conducting searches for pulsars at the 300 m Arecibo antenna, Hulse and Taylor detected pulsed radio emissions from a pulsar dubbed PSR1913+16. The pulses were received from this object at 59 ms intervals, indicating that it rotates about its axis seventeen times per second. However, what was unusual about the pulsar was that, from deviations in the expected arrival times of pulses, it was deduced that it was accompanied by a companion, thus making it the first discovery of a binary pulsar [11]. The pulsar and its compact companion are each believed to have a mass of approximately 1.4 $M_\odot$ and a radius of only 10 km. This binary pulsar was measured to have an orbital period of 7 hours 45 minutes and an orbital radius of only several Earth-Moon distances. For such a relativistic system, Einstein's theory of general relativity [4] predicts that energy should be emitted in the form of gravitational waves.

In subsequent follow-up observations [12], [13] and [14], it was found that the orbital period is declining i.e. the two bodies are rotating faster and faster about each other in an increasingly tighter orbit. The observed shift in the perihelion passing time of the binary pulsar system could be explained by the loss of energy and angular momentum due to the emission of gravitational wave radiation and agreed with theory to better than 1 %. This agreement provide the first indirect evidence of the emission of gravitational wave radiation and following this work Hulse and Taylor were awarded the 1993 Nobel Prize in Physics.

1.4.3 Interferometers

The Michelson interferometer is capable of measuring path changes in orthogonal directions and was used in the Michelson–Morley experiment of 1887, investigating the relative motion of the Earth and luminiferous ether [15]. The basic Michelson interferometer configuration is usually comprised of a monochromatic source, beam-splitter, two mirrors and a photodiode detector. The optical layout of these components can be seen in Figure 1.2.

Key to Optical Components:

B1 – Non-Polarising beam splitter
M1, 2 – Mirror
PD1 – Photodiode
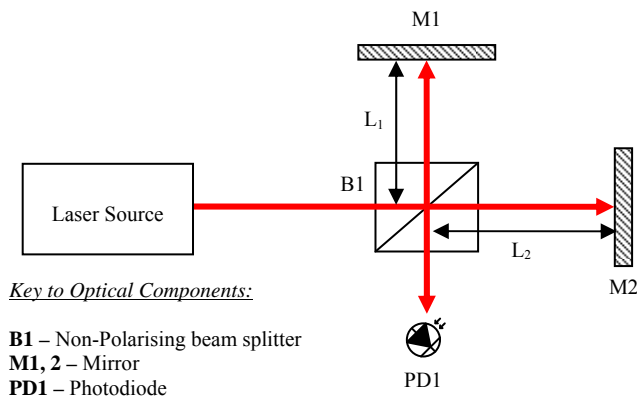
Figure 1.2: *Michelson interferometer optical layout.*

The two mirrors, M1 and M2, are perpendicular to each other and are distances, L_1 and L_2, respectively, away from the 50:50 beam-splitter, B1. The beam-splitter is orientated at 45° relative to both mirrors. The incident beam is split by the beam-splitter into equal intensity beams, one beam is reflected towards M1 and the other is transmitted towards M2. Each beam is reflected by their respective mirror and returns to the beam-splitter. After traversing these different paths, the two parts of the light are brought together to interfere with each other. The photodiode detector, PD1, measures the intensity of the interference pattern, thus enabling any changes in the relative path difference between L_1 and L_2 to be determined.

The Michelson interferometer can be considered ideally suited to the direct detection of gravitational waves. If free test-masses were attached to the end mirrors, then a gravitational wave of the correct polarisation passing through the instrument, would create an optical path difference between orthogonal arms of the interferometer. If we again consider a gravitational wave, with a + polarisation, propagating normal to the page, then this would have an effect on the interferometer arm-length as demonstrated in Figure 1.3, where starting at the top left at $\tau = 0$, time increments by $\tau/4$ going clockwise around each diagram.
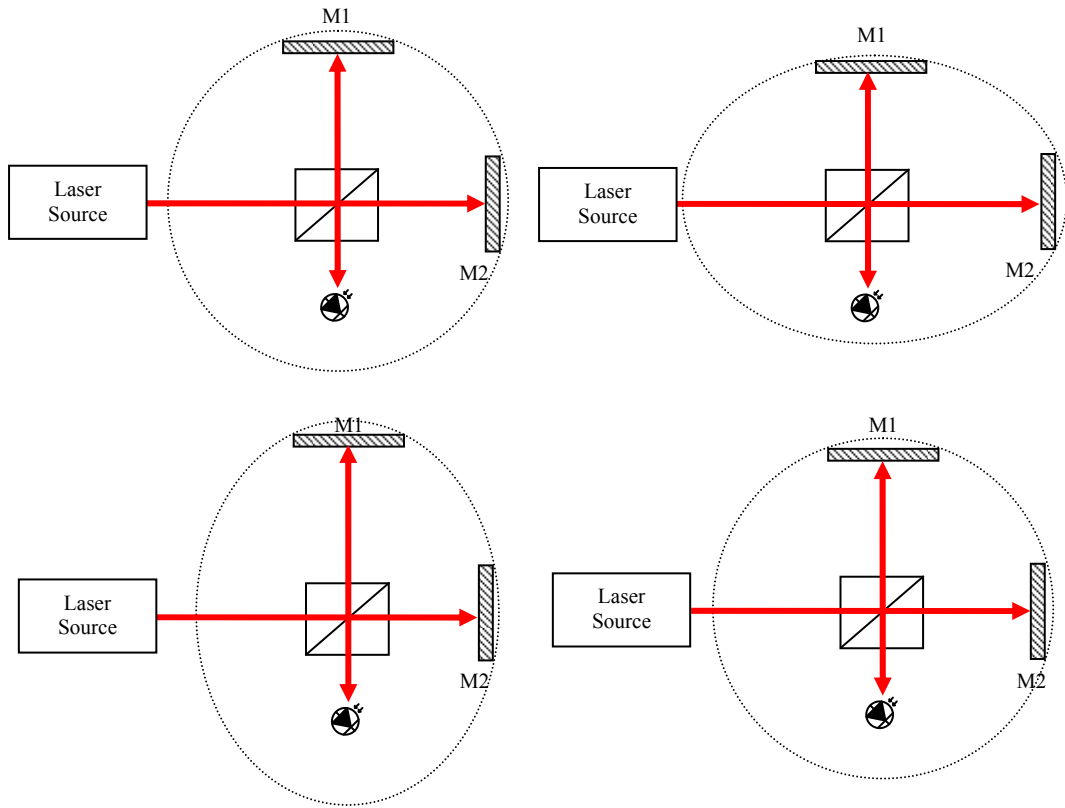
Figure 1.3: *Optical path length changes due to + polarisation propagating gravitational wave.*
(Top Left) τ = 0. (Top Right) τ/4.
(Bottom Left) 3/4 τ. (Bottom Right) τ/2.

In 1956, Pirani [16] was the first to point out the suitability of the Michelson interferometer to observe these effects. By 1971, a small prototype interferometer was built in Malibu [17], with the first search results published by Forward, in 1978 [18].

To optimise the configuration of the basic Michelson to improve its sensitivity to gravitational waves, then there are a number of modifications that can be made. Firstly, it should be ensured that, in the absence of a gravitational wave, the interferometer is configured so that the two return beams interfere destructively, i.e. the photodiode detector is operating at a dark fringe. Therefore, if a gravitational wave were to pass through the instrument and change the arm-lengths, a signal would be measured at the detector. Secondly, as demonstrated in Equation 1.4, the propagating gravitational wave causes a fractional length change. The phase change is proportional to the total optical path length change, i.e. the phase change observed at the beam-splitter for a given gravitational wave, can be increased by making the arms significantly longer. Finally, the optical power in the arms of the interferometer can be increased. Since an incident

gravitational wave will couple light into the photodiode, having more light in the arms, would thus couple more light into the photodiode, for the same gravitational wave signal.

However, increasing the optical power within the interferometer can have negative consequences, such as increasing the contribution of sources of noise. These and other noise sources and their impact upon performance are discussed in Chapter 2.

It has been seen that, to improve the sensitivity of the interferometer to gravitational waves, it should have long arms. This criterion has been adopted in the design of ground-based interferometric observatories. To reduce the acoustic coupling and effects of changes in local air density the entire interferometer itself is located within a vacuum environment. Within this vacuum, the test-masses are suspended from a seismic isolation system, in an attempt to isolate them from their local environment. Given the significant costs of constructing the interferometer and support facilities, financial constraints can often place a limit on the maximum arm-length for a ground-based observatory.

The Laser Interferometric Ground Observatory (LIGO) presently has two gravitational wave observatories and three interferometers. Interferometers with arm-lengths 2 km and 4 km are both located at the LIGO Hanford Observatory in Washington, USA. The third interferometer has an arm-length of 4 km and is located at the LIGO Livingston Observatory in Louisiana, USA. Aerial images of these two sites can be seen in Figure 1.4. These first generation interferometric detectors (Initial LIGO) have reached their design sensitivities and completed a number of science runs, searching for gravitational waves, over the past few years [19]. In October 2010 they were shut down and decommissioned in their current form. However, they are now in the process of being upgraded to second generation detectors (Advanced LIGO). These modifications are set to increase the sensitivity of these detectors by a factor of ten, within the next decade [20].

There are a number of other first generation ground-based gravitational wave observatories that have been operating. Some of these have also begun the process of being upgraded to second generation facilities.

- GEO600, a British-German collaboration, with 600 m long arms that is located in Hanover, Germany [21].

- VIRGO, a French-Italian collaboration, with 3 km long arms that is located in Cascina near Pisa, Italy [22].

- TAMA300, a Japanese instrument, with 300 m long arms that is located in Mitaka near Tokyo, Japan [23].

Figure 1.4: *Aerial images of USA ground-based gravitational wave observatories. Source [24]. (Left) LIGO Livingston Observatory. (Right) LIGO Hanford Observatory.*

All the observatories previously mentioned form the foundations of a worldwide network of detectors. They all operate in a complementary fashion, since each detector capable of detecting the gravitational radiation offers more information about the gravitational wave and its source. For example, with multiple detectors it becomes possible to determine the polarisation of the gravitation wave and reveal its likely point of origin on the sky. Once the point of origin is known, other more conventional astronomical telescopes can be targeted upon the source location to search for E-M counterparts to the gravitational emissions. Presently under consideration is the possibility of relocating one of the LIGO Hanford interferometers to the Australian International Gravitational Observatory (AIGO) [25]. An observatory in the southern hemisphere will greatly enhance the worldwide detector network, as it will enable significantly better localisation of the source on the sky [26].

Future observatories, to add to the existing worldwide network of detectors, are also planned. These observatories will most likely employ third generation facilities.

- Large Cryogenic Gravitational Telescope (LCGT), baseline design has 3 km arm-length, cryogenic mirrors and will be sited underground in the Kamioka mine, Japan [27].

- Einstein Telescope (ET), currently at the conceptual design study phase, which is due to be completed in July 2011. Novel underground interferometer geometries and topologies are being investigated [28].

Interferometers are not only limited to terrestrial applications. Space offers an ideal environment, given it overcomes the two main limitations of ground-based detectors, such as the arm-length restrictions and the seismic noise associated with ground motion and gravity gradients. Two space missions have been proposed that will take full advantage of the freedom afforded by this environment. Both missions employ multiple Michelson interferometers with slightly modified geometries.

- Laser Interferometer Space Antenna (LISA) comprises a constellation of three drag-free spacecraft in a heliocentric orbit, with three interferometers forming an equilateral triangle of five million kilometre arm-lengths. Aimed at observing very low frequency gravitational wave sources in the region 10^{-4} Hz to 10^{-1} Hz. LISA is a joint ESA/NASA mission, which should be returning science data by around 2022 [6]. Figure 1.5 provides two views of the LISA mission in orbit.

- Deci-hertz Interferometer Gravitational Wave Observatory (DECIGO), the pre-conceptual design has constellation of three drag-free spacecraft, with three interferometers of arm-length 1000 km. Aimed at bridging the gap between LISA and terrestrial detectors by observing in the 10^{-2} Hz to 10^{2} Hz frequency band [29]. DECIGO is a JAXA/ISAS mission with a proposed launch scheduled for 2027.
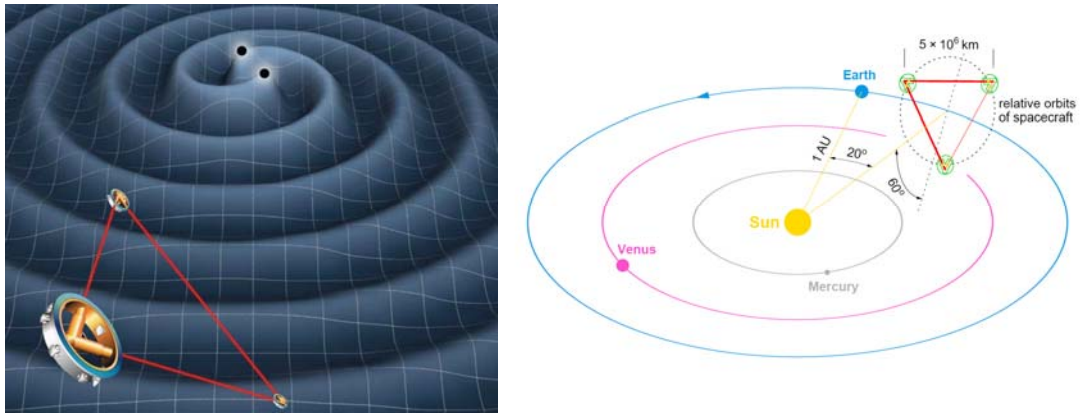
Figure 1.5: *LISA mission images.*

(Left) LISA constellation. Source [30]. (Right) The LISA proposed orbit. Source [6].

Both of these space missions are extremely technically challenging. For this reason it was decided that key technologies first need to be flight proven by flying technology demonstrator missions.

- LISA Pathfinder (LPF), will essentially comprise one interferometer arm of LISA reduced from five million kilometres, down to tens of centimetres. The aim is to test the inertial sensors, interferometry, micro-newton propulsion, drag-free and attitude control. Launch is currently scheduled for 2012 [31].

- DECIGO Pathfinder (DPF), will comprise of a single small satellite allowing a test of a Fabry-Pérot interferometer [32], with 30 cm arm-length. Launch is currently scheduled for 2015 [33].

The number of observatories where interferometers are being used in the search for gravitational waves is increasing, as is the knowledge and expertise of those who design and operate them. Many of the technical and data analysis challenges that are faced are common to all instruments. Therefore, there is a growing international collaboration which cooperates in the construction, operation and use of these facilities world-wide.

The current status of the existing observatories is that the search for the first detection is ongoing, thus far no direct detection has been announced. It is anticipated that

the first direct detection of a gravitational wave will be made once the second generation facilities are up and running at (or near) their design sensitivity.

Figure 1.6 provides a comparison of the design sensitivities of both LISA and Initial LIGO. It can be seen that the two instruments complement each other, LISA being optimised for low frequency regime and LIGO covering higher frequency gravitational wave emissions. A subsequent mission has since been proposed (DECIGO) to cover the intermediate regime. The sensitivity curves of these instruments are determined by various noise sources, which are discussed in Chapter 2.

The primary motivation behind the development of these instruments is the aim to carry out astronomy with gravitational waves. It is believed that once the first detection is made, subsequent observations will eventually become commonplace. The world-wide network of interferometric detectors, complemented by those in space, will help construct a broader picture of the nature of gravitational waves and gain a significantly better understanding of their astrophysical sources, thus opening a new window through which the universe can be observed.
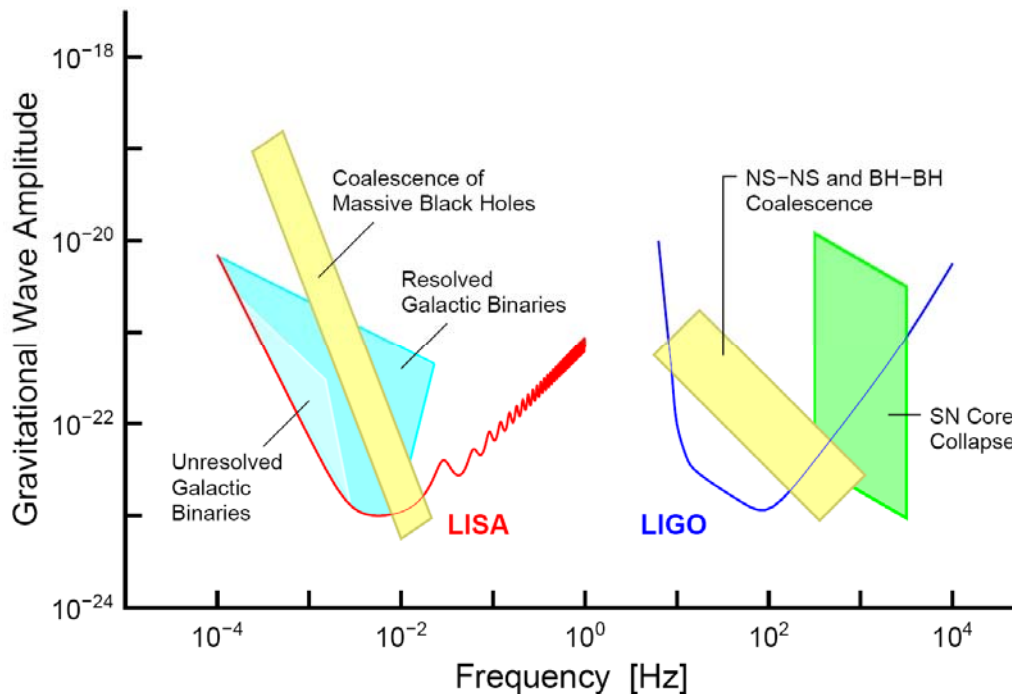
Figure 1.6: *LISA and LIGO design sensitivities to gravitational waves and potential sources. Source [6].*

Chapter 2

Gravitational Wave Detector Limitations

"The worst wheel of the cart makes the most noise". Benjamin Franklin.

2.1 Introduction

This chapter first discusses fundamental sources of noise and how this noise impacts upon gravitational wave detectors.

2.2 Fundamental Sources of Noise

The term noise can be considered to represent any unwanted signal that is obscuring the signal to be observed. It can be thought of as a random perturbation occupying the same spectral region in which the signal resides. Noise sources can be classified under two categories, extrinsic and intrinsic. Extrinsic noise can be attributed to coupling from external sources, interference or power supply fluctuations etc, and intrinsic noise is fundamental in nature. The significant difference between these two classifications is that, through thoughtful design, extrinsic noise can be made negligible, whereas intrinsic sources are due to fundamental properties and can only be minimised. Examples of intrinsic noise sources include, shot-noise, 1/f noise, Johnson noise, and laser frequency noise.

This section goes on to discuss and derive these intrinsic sources of noise. But first it is necessary to define how to describe noise mathematically, as discussed by Yariv [34]. The power spectral density of a time series is a function in the frequency domain which can be used to describe the spectral power of a signal in a unit bandwidth. The power spectral density is defined as the mean-square of signal within a selected frequency band divided by the measurement bandwidth. For example, if the Fourier transform of $v(t)$ is given as

$$V(\omega) = \frac{1}{2\pi} \int_{-\infty}^{+\infty} v(t)e^{-i\omega t} dt \,,$$

$$(2.1)$$

where the inverse Fourier transform is

$$v(t) = \int_{-\infty}^{+\infty} V(\omega)e^{i\omega t}d\omega .$$
(2.2)

However, for a signal $v(t)$, it is not possible for measurements to be taken over an infinite time period. Therefore, define a finite period, T, where the function $v(t)$ is determined to be equal to zero for $(t \leq -T/2)$ and $(t \geq +T/2)$. Hence, Equation 2.1 can be rewritten as

$$V_T(\omega) = \frac{1}{2\pi} \int_{-T/2}^{+T/2} v(t)e^{-i\omega t}dt .$$
(2.3)

The average power associated with $v(t)$ can be evaluated. For example, consider the real signal $v(t)$ to be the voltage across a 1 Ω resistor, then it follows from $P = V^2/R$, that the instantaneous power is $v^2(t)$. Therefore,

$$P = \frac{1}{T} \int_{-T/2}^{+T/2} v^2(t)dt ,$$
(2.4)

or

$$P = \frac{1}{T} \int_{-T/2}^{+T/2} v(t) \left[\int_{-\infty}^{+\infty} V_T(\omega)e^{i\omega t}d\omega \right] dt .$$
(2.5)

It follows that the complex conjugate is related to the real signal via the relation

$$V_T(\omega) = V_T^*(-\omega) .$$
(2.6)

Noting the limit as $T \rightarrow \infty$,

$$\lim_{T \rightarrow \infty} \frac{1}{2\pi} \int_{-T/2}^{+T/2} dt \, e^{i(\omega - \omega')t} = \delta(\omega - \omega') .$$
(2.7)

Integration of Equation 2.5, using the identities given in Equations 2.3 and 2.6, leads to,

$$P = \frac{4\pi}{T} \int_0^{+\infty} |V_T(\omega)|^2 \, d\omega. \tag{2.8}$$

Hence, the spectral density function can be defined as $S_T(\omega)$ of the signal $v(t)$ using,

$$S_T(\omega) = \frac{4\pi |V_T(\omega)|^2}{T}. \tag{2.9}$$

Therefore, $S_T(\omega)d\omega$ is the portion of the average power of $v(t)$ that has frequency components within the range ω to $\omega + d\omega$. It can be seen from Equation 2.9 that the power spectral density has units of $(\text{signal})^2 / \text{Hertz}$.

A time-dependent random variable $i(t)$, that consists of a large number of individual events $f(t-t_i)$, which occur at random intervals during a period T, is governed by the Poisson statistic and can be written as

$$i_T(t) = \sum_{i=1}^{N_T} f(t - t_i), \tag{2.10}$$

where $0 \leq t \leq T$ and N_T is the total number of events occurring in interval T. The Fourier transform of Equation 2.10 can be written as

$$I_T(\omega) = \sum_{i=1}^{N_T} F_i(\omega), \tag{2.11}$$

where $F_i(\omega)$ is the Fourier transform of $f(t-t_i)$,

$$F_i(\omega) = \frac{1}{2\pi} \int_{-\infty}^{+\infty} f(t - t_i) e^{-i\omega t} \, dt, \tag{2.12}$$

and

$$F_i(\omega) = \frac{e^{-i\omega t_i}}{2\pi} \int_{-\infty}^{+\infty} f(t)e^{-i\omega t} dt .$$

(2.13)

Using the Fourier transform, as given in Equation 2.3,

$$F_i(\omega) = e^{-i\omega t_i} F(\omega) .$$

(2.14)

Substituting Equations 2.11 and 2.14 gives

$$|I_T(\omega)|^2 = \frac{|F(\omega)|^2}{4\pi^2} \sum_{i=1}^{N_T} \sum_{j=1}^{N_T} e^{-i\omega(t_i - t_j)} ,$$

(2.15)

and

$$|I_T(\omega)|^2 = \frac{|F(\omega)|^2}{4\pi^2} \left(N_T + \sum_{i \neq j}^{N_T} \sum_{j=1}^{N_T} e^{i\omega(t_j - t_i)} \right).$$

(2.16)

The average of Equation 2.16 can be taken over a large ensemble. This also implies that the sum term can be neglected when compared to the N_T term, since the event times, t_i and t_j are random. This gives

$$\overline{|I_T(\omega)|^2} = \frac{|F(\omega)|^2}{4\pi^2} \overline{N_T} ,$$

(2.17)

where $\overline{N}$ is the average rate for the events to occur. Therefore, $\overline{N_T} = \overline{N}T$ meaning that Equation 2.17 can be rewritten as

$$\overline{|I_T(\omega)|^2} = \frac{|F(\omega)|^2}{4\pi^2} \overline{N}T .$$

(2.18)

Using the function previously generated for the spectral density in Equation 2.9, it is now possible to find the spectral density, $S_T(\omega)$ of $i_T(t)$,

$$S(\omega) = 4\pi \overline{N} |F(\omega)|^2 . \tag{2.19}$$

It should also be noted that $\omega = 2\pi\nu$ and that $S(\nu)d\nu = S(\omega)d\omega$. Therefore, Equation 2.19 becomes

$$S(\nu) = 8\pi^2 \overline{N} |F(2\pi\nu)|^2 . \tag{2.20}$$

This result is known as Carson's theorem and will be used in the following derivations of the fundamental noise sources.

2.2.1 Shot-Noise

An electrical current source in which the passage of each charge carrier is a statistically independent event (rather than a steady flow of many charge carriers) delivers an inherently noisy current, i.e. a current that fluctuates about an average value. If we consider two parallel plate electrodes in a vacuum, separated by a distance d, and assume that one of the electrodes is of a slightly higher potential than the other, then electrons will move between the electrodes at random time intervals. The average rate of electron emission being

$$\overline{N} = \overline{I} / e , \tag{2.21}$$

where $\overline{I}$ is the average current, and e the charge of an electron. A 'pulse' of current through the circuit can, therefore, be considered as

$$i_e(t) = \frac{ev(t)}{d} . \tag{2.22}$$

Taking the Fourier transform, Equation 2.1, of this single current pulse gives,

$$F(\omega) = \frac{e}{2\pi d} \int_0^{t_1} v(t) e^{-i\omega t} dt . \tag{2.23}$$

Note that, t_1 denotes the arrival time of an electron emitted at $t = 0$. If for example the transit time is sufficiently small, at the frequency of interest, $\omega t_1 << 1$, then the exponential term can be replaced by unity, leading to

$$F(\omega) = \frac{e}{2\pi d} \int_0^{t_1} \frac{dx}{dt} dt .$$

(2.24)

Noting that, $x(t_1) = d$, therefore,

$$F(\omega) = \frac{e}{2\pi} .$$

(2.25)

Recalling Carson's theorem, given in Equation 2.20, leads to,

$$S(v) = 8\pi^2 \overline{N} \left(\frac{e}{2\pi} \right)^2 .$$

(2.26)

Again, using the average rate of electron emission given in Equation 2.21, gives

$$S(v) = 2e\overline{I} .$$

(2.27)

This equation gives the shot-noise. The nature of the shot-noise is also demonstrated by this result. The noise has no frequency dependence and so it is flat across the spectrum. Hence, it is also commonly known as 'white' noise.

Exactly the same reasoning can also be applied to a stream of independent photons. For example, in the case of a photo-detector (of high quantum efficiency), electron statistics in the photocurrent will directly mirror the photon statistics. Therefore, if the light source is at the shot-noise level, then so will be the photocurrent.

2.2.2 Thermal Noise

Johnson noise [35] describes the fluctuations present in the voltages across a passive component, such as a resistor. These fluctuations are inherently due to the thermal motion of charge carriers. Charge neutrality is conserved for the whole volume of the device, however, local random motions of charge carriers set up charge gradients and ac voltages. For example, consider two matched resistors in parallel, which are maintained at the same temperature, T. A lossless transmission line of length L, exists between the two resistors as shown in Figure 2.1.
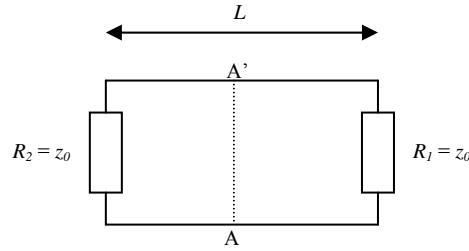
Figure 2.1: *Matched resistors in parallel.*

The resistances, $R_{1,2}$ are defined to be equal to the characteristic impedance of the circuit, z_0, to ensure there are no reflections. Such a transmission line supports a voltage waveform of the form

$$v(t) = A\cos(\omega t \pm kz),$$ (2.28)

where the wave number, $k = 2\pi / \lambda$ and the phase velocity, $c = \omega / k$. To assist the derivation, the solution is required to be periodic in the distance L. Hence the solution can be extended outside the limits $0 \leq z \leq L$ to obtain

$$v(t) = A\cos[\omega t \pm k(z + L)] = A\cos(\omega t \pm kz).$$ (2.29)

This condition is fulfilled for $kL = 2m\pi$, where, $m = 1,2,3....$ This implies that two adjacent modes have a difference in k of

$$\Delta k = \frac{2\pi}{L}.$$ (2.30)

So the number of modes that have k values in the range 0 to $+k$ are

$$N_{k+} = \frac{kL}{2\pi}.$$ (2.31)

Therefore, substituting in the wave number, $k = 2\pi\upsilon / c$, where c is the speed of light in a vacuum, gives the number of travelling modes (+) with frequencies lying between zero and υ,

$$N(\nu) = \frac{\nu L}{c}.$$ (2.32)

Thus, the number of modes per unit frequency is

$$p(\nu) = \frac{dN(\nu)}{d\nu},$$ (2.33)

or

$$p(\nu) = \frac{L}{c}.$$ (2.34)

Referring to Figure 2.1, consider the power flowing across a plane (A-A') in the positive direction. It is clear that this power must have been generated by R_2 (assuming no reflections). The power is transferred by the electromagnetic modes of the system,

$$\text{Power} = \frac{\text{energy}}{\text{distance}} (\text{velocity of energy}).$$ (2.35)

Therefore, the power P, due to frequencies between υ and $\upsilon + \Delta\upsilon$, can be given as

$$P = \left(\frac{1}{L}\right)\left(\begin{array}{c}\text{modes between}\\ \nu \text{ and } \nu + \Delta\nu\end{array}\right)(\text{energy per mode})(c).$$ (2.36)

Assuming thermal equilibrium, the energy per mode is given as

$$E = \frac{h\nu}{e^{h\nu/kt} - 1},$$ (2.37)

which can be substituted into Equation 2.36 to give

$$P = \left(\frac{1}{L}\right)\left(\frac{L}{c}\Delta\nu\right)\left(\frac{h\nu}{e^{h\nu/kt} - 1}\right)(c),$$ (2.38)

or

$$P = \frac{h\nu\Delta\nu}{e^{h\nu/kt} - 1}.$$ (2.39)

Replacing the resistance R in Figure 2.1 with a noise generator in series with R, that produces a mean-square voltage amplitude

$$v_N^2 = \frac{4h\nu R\Delta\nu}{e^{h\nu/kt} - 1},$$ (2.40)

which for the case that $kT \gg h\upsilon$,

$$v_N^2 = 4kTR\Delta\nu.$$ (2.41)

This equation gives the Johnson noise. The nature of Johnson noise is also demonstrated by this result. Johnson noise appears flat across a bandwidth and is also known as 'white' noise.

2.2.3 1/f Noise

1/f noise, also known as flicker or 'pink' noise, can be present in many physical systems and virtually all electronics devices. It can be associated with a dc current, and its average mean-square value is of the form [36]

$$\overline{i^2} = \int \frac{k_i^2}{v} dv,$$ (2.21)

where k_i is a constant appropriate to the specific device. In electronic devices, 1/f noise is most notably a low frequency phenomenon, since at higher frequencies white noise from other sources can dominate. 1/f noise is also present in metal oxide semiconductor field effect transistors, bipolar-transistors and carbon composition resistors, where it is often referred to as excess noise, because it appears in addition to the thermal noise. Other types of resistors also exhibit flicker noise to varying degrees, with wire-wound showing the least. Since flicker noise is proportional to the dc current in the device, if the current is kept low enough, thermal noise will dominate.

2.2.4 Radiation Pressure Noise

Radiation pressure refers to the force exerted on an object when photons strike the surface. The photon posses a momentum h/λ, where h is Plank's constant, which is imparted to the object (or mirror) when the photon strikes or is reflected. Under normal incidence conditions the mirror is given a momentum kick of $2h/\lambda$. Given the relatively high power laser beam, the total radiation pressure imparted to a mirror can become significant. For a single mirror, in the absence of technical noise, fundamental quantum noise will be present. If we were to consider two mirrors, at the ends of the arms of an interferometer, then radiation pressure noise will be present at each. However, common mode rejection will be able to mitigate some of these sources of noise. But the effectiveness of the common mode rejection will be compromised, if for example, the mirrors are not of identical mass, or if the beam-splitters are not exactly 50:50 balanced. Quantum mechanics also places a fundamental limit due to the partitioning of photons into each arm of the interferometer by the beam-splitter, leading to further power fluctuations in each arm. The common mode rejection is not capable of rejecting the quantum noise. The motion of the end mirrors results in phase fluctuations limiting the

sensitivity of the Michelson interferometer. This noise becomes even more problematic if even higher optical powers are employed, and is discussed further elsewhere [37].

Eventually, the absolute force fluctuations increase with the optical power until a limit is reached whereby the interferometer will be equally sensitive to, the number of photons, and the fluctuation in phase of the beam. This is known as the standard quantum limit, and is derived elsewhere [38].

2.2.5 Laser Frequency Noise

Phase instabilities in the laser can be converted into displacement noise for un-equal arm-length interferometers. This phase fluctuation manifests itself as an oscillating frequency width of the laser. The spectrum of the intrinsic frequency fluctuations of a single-mode laser is given by

$$f^2(v) = \frac{D}{\pi},$$
(2.22)

where D is the intrinsic laser line width. This is discussed further elsewhere [39].

2.2.6 Seismic Noise

In general, the seismic spectra for the Earth show increasing power towards lower frequencies. But there are two characteristic features that are responsible for generating large motions over small frequency bands. At around 10^{-5} Hz is a peak associated with Earth's tides and near 0.15 Hz is a feature known as the microseismic peak. The Earth's tides can be appropriately modelled, since they are driven by the motion of the Sun and the Moon. However, the frequency and shape of the microseismic peak is non-stationary and can, therefore, be considered an un-modelled source of noise. The source of this noise is complex, but it is most likely related to seismic surface waves generated by ocean waves and storms [40].

Substantial amounts of data have been collected from seismometer stations worldwide, allowing for refined modelling of the seismic background noise. The high and low noise traces from the Peterson model [41] are shown as dashed lines in Figure 2.2.
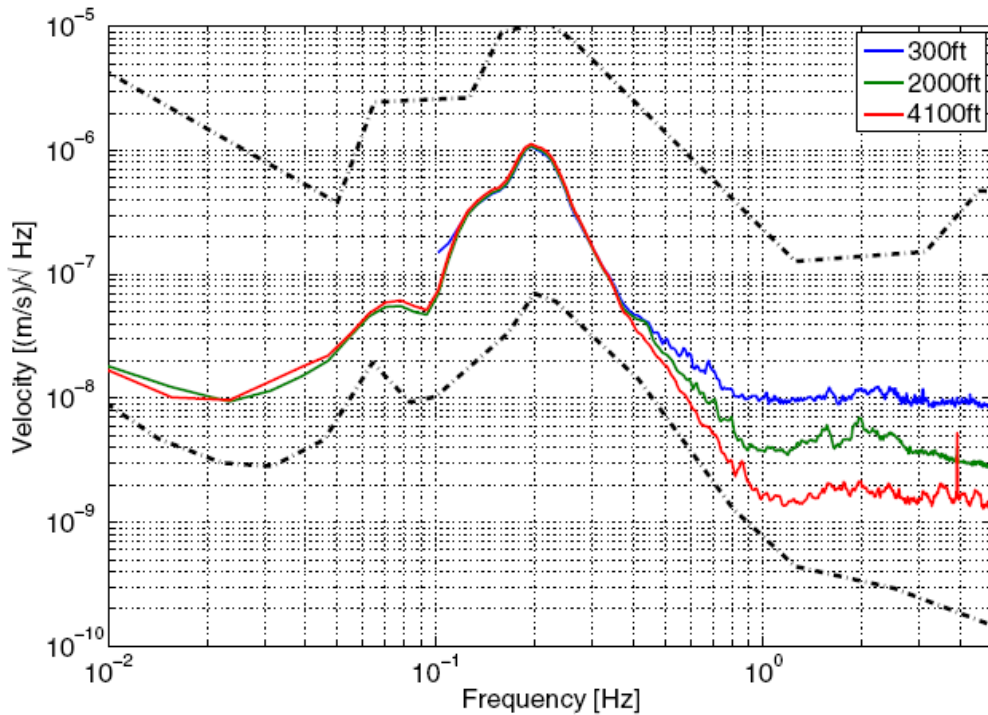
Figure 2.2: *Modelling of seismic noise background spectra. Source [42].*

Ground motion impacts upon all Earth-based detectors and is indistinguishable from the signals they are seeking to detect. For this reason, seismic noise can be considered fundamental in nature. Isolation systems can be constructed that aim to decouple the detectors from ground motion. For example, early gravitational wave detectors, such as the resonant bar detectors developed by Weber [9], employed a simple passive isolation technique to reduce the effect of seismic noise below that of other noise sources. In this system, the resonant bar detector was suspended by a wire, while isolating the point of suspension from the ground motion by using stacks of alternating layers of lead and rubber to act as passive vibration filters.

The active isolation of vertical disturbances upon a test mass supported by a spring, were developed by Melton and Johnson [43]. Such a system sensed changes in the extension of the spring and then moved the suspension point, so as to maintain the constant length of the spring. Robertson *et al* [44] describe a system whereby the relative horizontal displacement point of suspension of a test mass is monitored with respect to the mass itself and feeding back a suitably amplified and filtered form of the signal to a

transducer which controls the suspension point. Thus the active feedback reduces the response of the pendulum suspension to ground motion. Such a system can also be configured to include electronic damping and a suitable number of suspension stages to reach the isolation from ground motion required.

However, all such isolation schemes are most effective at higher frequencies and so the seismic noise still dominates at frequencies below 10 Hz. The red, green and blue lines in Figure 2.2 show measurements of the seismic background at various depths of the Sanford underground laboratory, formally the Homestake mine, South Dakota, USA. Some geographic locations (and depths) are less susceptible to seismic background noises. Therefore, it is essential to first conduct seismic noise surveys to help indentify the optimal locations for future gravitational wave observatories [42]. Due to the reduction in seismic noise, it is most desirable to build future facilities underground, but inevitably incurring higher costs.

2.2.7 Gravity Gradient Noise

Gravity gradient noise, also known as Newtonian noise, is associated with fluctuations in the local gravitational field of the detector and can be generated by density variations in the surrounding environment. Sources can be attributed to earthquakes, atmospheric or oceanic disturbances or human activity. For example, motions of mass could be associated with the experiment, or external factors such as motions of cars, trains, aeroplanes, etc. Gravity gradient noise can dominate below 10 Hz and is not possible to shield, since it couples directly into any suspended (i.e. seismically isolated) test-mass.

Gravity gradient noise can be minimised by giving careful consideration for the best location of the detector. For example, by conducting surveys to identify the best geographic location, and/or locating the detector underground. Such a scheme has been proposed for the third generation Einstein Telescope [45]. However, ground-based detectors will never be sensitive below around 1 Hz due to the terrestrial gravity gradient noise. A space-borne detector is free from such noise and would provide a window to observe gravitational wave sources from very low frequency sources, in the 10^{-4} Hz to 10^{1} Hz range, for example.

2.3 Detector Design Sensitivities

The final noise floor of a gravitational wave detector will originate from several different sources, each dominating the noise over different frequency ranges.

2.3.1 Space-borne Noise Budget

Figure 2.3 provides a plot of the LISA sensitivity for one year integration time and a signal to noise ratio of five. This is for the baseline LISA configuration, as outlined in Section 1.4.3. Below 2 mHz the sensitivity performance is limited by the acceleration noise of the drag-free sensor, leading to a decrease in sensitivity towards lower frequencies roughly proportional to f^{-2}. Above 2 mHz the noise is fundamentally limited by the shot-noise. Above 10 mHz the decline of the antenna transfer function causes a decrease in sensitivity, proportional to the frequency, given that the wavelength of the incident gravitational waves becomes shorter than the five million kilometre arm-lengths of the LISA instrument. Techniques for the cancelation of laser phase noise lead to the oscillations in sensitivity observed at high frequencies [46].
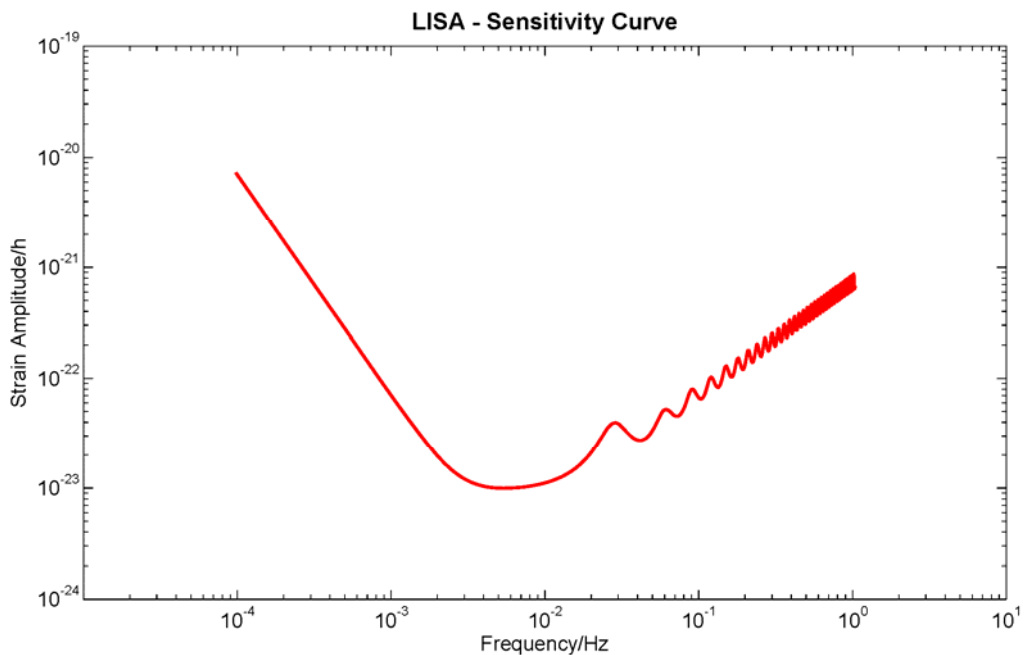
Figure 2.3: *LISA noise limited sensitivity performance. Plot data obtained from LISA Sensitivity Curve Generator [47].*

2.3.2 Ground-based Noise Budget

Figure 2.4 provides an equivalent noise budget for a ground-based interferometer, i.e. Advanced LIGO. Low frequencies are ultimately dominated by seismic noise, whereas higher frequencies are fundamentally shot-noise limited. Additional noise sources applicable to the Advanced LIGO interferometer configuration are also indentified in this noise budget. Thermal noise can arise as a consequence of the suspended mass being in radiative thermal equilibrium with its surroundings, i.e. the vacuum chamber, which is maintained at room temperature. Thermal motions of individual particles can cause fluctuations in the measured arm-length.

Thermal noise affecting gravitational wave interferometers has two different origins. The first one is due to dissipation in the wires used to suspend the test masses, known as suspension thermal noise. The second one is due to dissipation processes inside the test masses themselves, and is known as mirror thermal noise. In addition, fluctuations can occur within the mirror coating, via a similar process to that which they occur in the substrate. However, even though the coating substantially less thick than the substrate, the noise generated can be significantly higher. This is usually known as coating Brownian noise. An overview of the different thermal noises affecting the substrate and the coating of the interferometer mirrors is given by Gorodetsky [48].
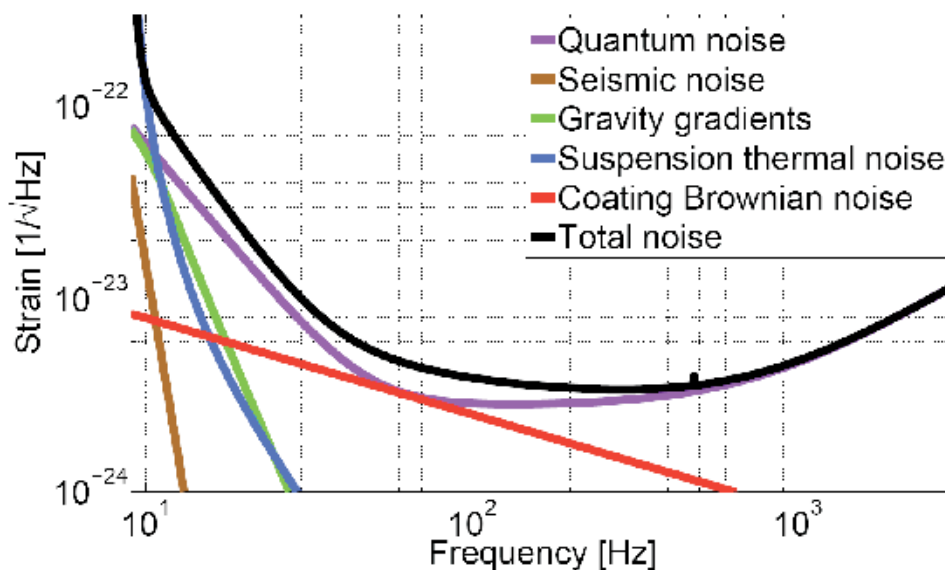
Figure 2.4: *Advanced LIGO noise limited sensitivity performance. Source [20].*

Chapter 3

Development of a Geometric Sensor

"Look and you will find it - what is unsought will go undetected". Sophocles.

3.1 Introduction to the BOSEM

As discussed in Section 1.4.3, the first generation of ground-based gravitational wave observatories have reached their design sensitivities and are now in the process of upgrading to second generation facilities, such as from Initial LIGO to Advanced LIGO. These modifications will ultimately increase the detection range and widen the sensitivity band for these observatories. Improvements in sensitivity towards lower frequencies are most desirable for these instruments.

The UK has played a significant role in providing new and improved technologies for these second generation facilities. The University of Birmingham as a member of the Advanced LIGO UK collaboration, funded by the Science and Technology Facilities Council (STFC), has provided sensors, actuators, low noise electronics and in-vacuum harnesses for the Advanced LIGO observatories. The exact scope of these deliverables is outlined in the UK scope document [49]. A significant proportion of this work has been in the development, and large scale production, of sensor and actuator units. These units are required to work in an ultra high vacuum (UHV) environment, where a failure can clearly not be tolerated. Similar sensor and actuator units had already been in operation in the Initial LIGO observatories, but there were a number of performance, reliability and production issues that needed to be addressed for the Advanced LIGO versions.

Working with a project collaborator, N. Lockerbie (University of Strathclyde), a study was undertaken to optimise the sensor performance. The work presented later within this chapter details results of experiments undertaken at Birmingham. Once the development of the prototype unit was complete and it had passed through the various review stages, the path was clear to proceed with large scale production. The production article was dubbed the Birmingham Optical Sensor and Electro-Magnetic actuator

(BOSEM) by our US colleagues to differentiate it from the Initial LIGO OSEM and the US version, Advanced LIGO OSEM (AOSEM). Over the duration of the project, Birmingham has delivered approximately 700 production BOSEMs to the Advanced LIGO observatories.

3.2 Requirements

The Advanced LIGO interferometers comprise of several different types of optical components, some of which are required to operate within a low noise environment. The most sensitive optics, i.e. the 40 kg fussed silica test masses, must be held in place to within 10^{-14} m by a combined seismic isolation and suspension system [20]. It can be observed from the seismic noise background, as presented in Figure 2.2, that there is approximately a 1 μm rms ground motion in the region 1 Hz to 10 Hz. It is therefore necessary to isolate the test masses from this source of noise. The active seismic isolation subsystem can provide a factor of ten isolation around the microseismic peak (approximately 0.15 Hz), increasing to a factor of 1000 isolation in the region 1 Hz to 10 Hz, with the remainder of the isolation being afforded by the suspensions subsystem [20].

To obtain the high isolation factors required, a quadruple suspension has been developed, with the aim to reach a target noise contribution at the test mass from residual seismic noise of approximately 10^{-19} m Hz$^{-1/2}$ at 10 Hz [50]. Figure 3.1 (left) shows a 3D CAD representation of the seismic isolation and quadruple suspension design. Note that, in this figure, the seismic isolation stage can be seen supported from the ceiling, whilst the test mass is suspended at the final stage of a multi-stage pendulum system. Alongside the main suspension chain, there is also a reaction chain, containing reaction masses which are independently suspended in parallel to the main chain. The reaction chain is included to provide a platform for mounting sensors and actuators, which is similarly isolated from sources of noise, such as ground motion etc. The locations and quantities of active dampers upon the main and reaction chains are highlighted in Figure 3.1 (right). The active damping is provided at the various stages via sensors and actuators. The sensors and actuators, known as BOSEMs and AOSEMs, can provide low frequency damping of resonances and also allow a means to maintain the arm-lengths of the Advanced LIGO interferometer.

Existing Initial LIGO sensors have a sensitivity of approximately 10^{-10} m Hz$^{-1/2}$ at 10 Hz. The isolation factor for residual sensor noise at 10 Hz is of order 10^7 [51]. Therefore, these figures indicate that for Advanced LIGO there needs to be approximately two orders of magnitude improvement over sensors used in the first generation of observatories, thus leading to a challenging sensitivity of around 10^{-12} m Hz$^{-1/2}$ at 10 Hz.
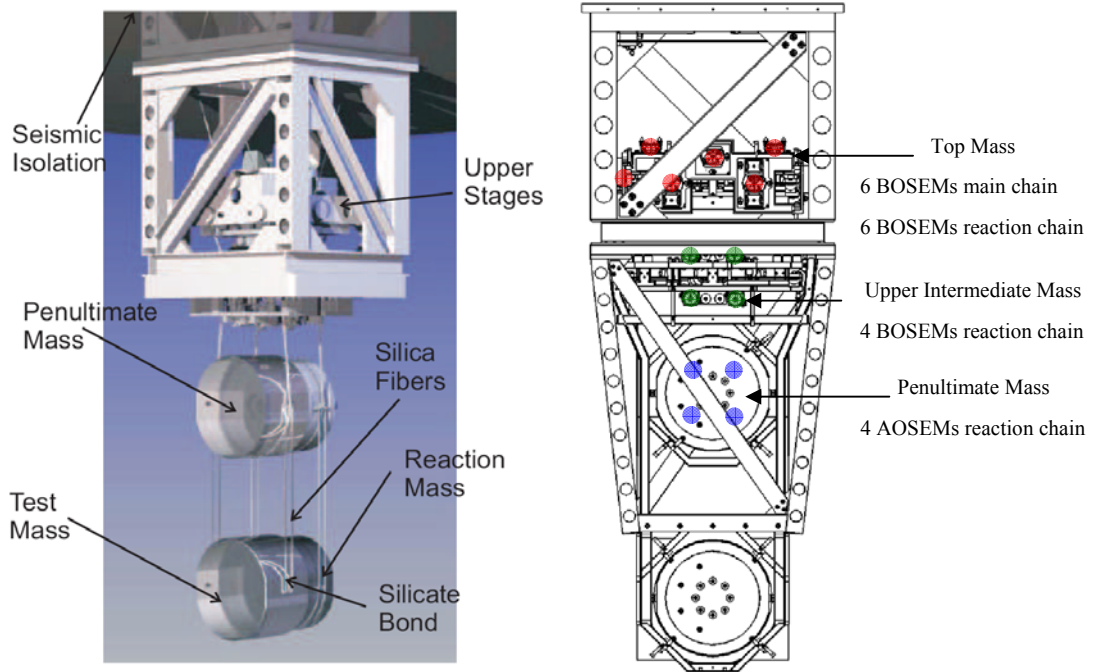
Figure 3.1: *Seismic isolation and suspension systems.*

(Left) 3D CAD representation of Advanced LIGO quadruple suspension. Source [20].

(Right) Location of BOSEMs and AOSEMs within the Advanced LIGO quadruple suspension.

In addition to the active damping of the quadruple suspension provided by the sensors and actuators, passive eddy current damping can also be used to provide low noise background damping of the suspensions [52]. Eddy current dampers comprise of a strong magnet moving through a copper sheath (without physical contact), and can be targeted towards the most sensitive suspension locations and degrees of freedom. The combination of both active and passive damping of the suspensions can serve to relax the most stringent sensitivity requirements. However, the copper parts of the eddy current damper add significant mass to the suspension and there are also limits placed on the amount of magnetic materials that can be present, which restricts the amount of eddy current damping that can be used. An investigation conducted by Strain [53] to determine

the initial sensor specification, assumed a minimal amount of eddy current damping and proposed the requirements presented in Table 3.1.

Specification	Frequency Band	
Worst Case Noise	1 Hz to 10 Hz $\approx 2\times10^{-11}$ m Hz$^{-1/2}$	10 Hz to 20 Hz $\approx 2\times10^{-11}$ m Hz$^{-1/2}$
Specification	Displacement (peak-peak)	
Operating Range	Minimum 3.00 mm	Target 3.00 mm

Table 3.1: *Initial sensor requirements.*

During the following twelve month period, refinements were made to the quadruple suspension design and concerns over using additional passive eddy current damping were mitigated. A subsequent investigation was conducted by Strain [54] to determine the optimal approach to sensing and actuation, assuming a modest amount of eddy current damping. This approach was successfully reviewed [55] and eventually resulted in the sensor requirements being relaxed, with the final sensitivity and operating range requirements placed on the sensor as presented in Table 3.2.

Specification	Frequency Band	
Worst Case Noise	1 Hz to 10 Hz 3×10^{-10} m/√Hz	10 Hz to 20 Hz 1×10^{-10} m/√Hz
Specification	Displacement (peak-peak)	
Operating Range	Minimum 0.35 mm	Target 0.70 mm

Table 3.2: *Final sensor requirements.*

In addition to the performance criteria, the sensor and actuator is required to fit within a specified envelope of 40 mm diameter by 70 mm long cylinder, as well as meet the UHV requirements of Advanced LIGO [56]. To help guide our selection of UHV compatible materials, an approved materials list was provided [57].

3.3 Geometric Sensor Overview

Geometric sensors provide a simple method of measuring the position of an object. The most common methods involve the use of position sensitive devices (PSDs) or split/quadrant photodiodes. The aim of research undertaken at Birmingham was to attempt to reach the performance and working range presented in the initial sensor requirements in Table 3.1.

3.3.1 Imaging Sensor

Optoelectronic sensors have previously been developed at the BIPM Paris by Speake [58]. Such devices have been employed as the sensors for servo systems used on mass comparators and active magnetic suspensions. These systems utilise a split photodiode detector and some form of focusing of the light source. Figure 3.2 shows the typical layout of the optical components of the imaging sensor. A cylindrical lens is used to focus a beam from a collimated light source down onto a split photodiode. This cylindrical lens would be attached to the object to be tracked, thus enabling the image that is formed on the photodiode to move transversely, in y.

The main advantages of the imaging approach are that, all the light is collected by the photodiode, and it is insensitive to displacement in the x and z planes. However, the imaging system can be sensitive to rotation of the object about the z axis. Sensitivity to rotation of the object may be alleviated by reducing the focal length of the cylindrical lens, but at the cost of reducing the magnification and dynamic range of the detector.
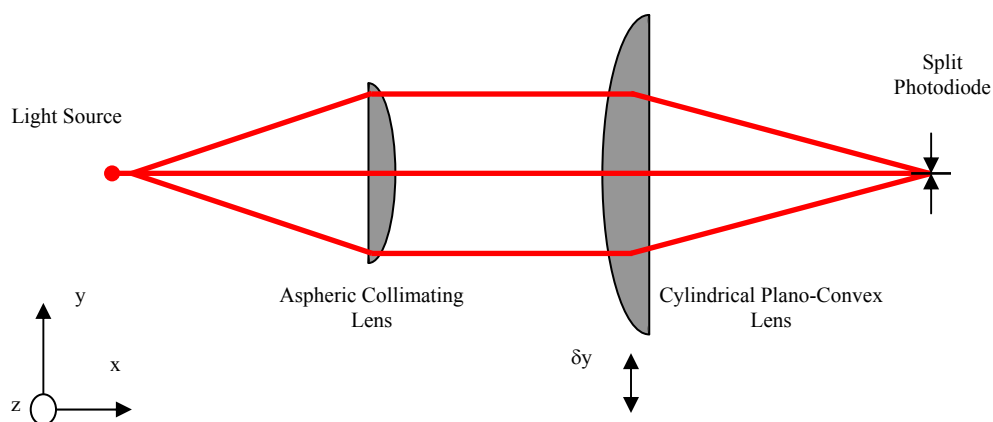
Figure 3.2: *Imaging sensor optical layout.*

The fundamental physical constraint of using the imaging sensor optical configuration is the limited incident intensity that can be focused onto the photodiode. For typical commercial devices, a linear response (to within 1 %) is specified up to 10 mW cm^{-2}. Incident power densities in excess of this rating will first cause non-linearity in the response and eventually lead to saturation of the device. A maximum sensitivity estimate of the device can, therefore, be derived incorporating this photodiode limitation. The conventions shown in Figure 3.3 are used throughout the following derivation, where l is the length of image formed and w is the image width.
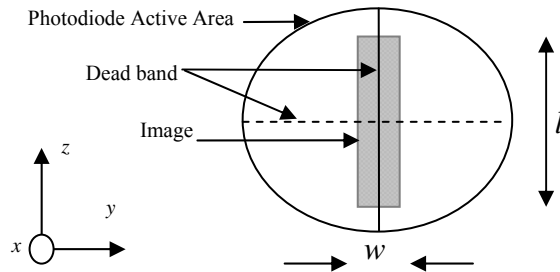
Figure 3.3: *Photodiode active element nomenclature.*

Consider that the total incident power upon a photodiode is P_T. Then the power density equates to

$$p = \frac{P_T}{wl} \; .$$
(3.1)

The responsivity for the silicon photodiode is given as $\alpha = 0.65$ (A W^{-1}) at 880 nm (i.e. the IRLED peak emission wavelength). Therefore, the currents induced for each side of the device are

$$i_1 = \alpha p s_1 \, ,$$
(3.2a)

and

$$i_2 = \alpha p s_2 \, .$$
(3.2b)

Thus, the areas illuminated for each side are

$$s_1 = \left(\frac{w}{2} + y\right)l,$$
(3.3a)

and

$$s_2 = \left(\frac{w}{2} - y\right)l.$$
(3.3b)

Hence, the change in induced current can be shown to be

$$\Delta i = i_1 - i_2 = \alpha pl\frac{w}{2} + \alpha ply - \alpha pl\frac{w}{2} + \alpha ply,$$
(3.4)

or

$$\Delta i = 2\alpha ply = \frac{2\alpha P_T y}{w}.$$
(3.5)

This, therefore, leads to

$$\frac{d(\Delta i)}{dy} = \frac{2\alpha P_T}{w}.$$
(3.6)

Assuming that any electrical noise sources and Johnson noise will be negligible compared to the shot-noise of the system (i.e. shot-noise limited system). As derived in Section 2.2.1, the shot-noise limit follows

$$\sigma_{i_1,i_2} = \sqrt{2ei_{1,2}},$$
(3.7)

where e is the charge of an electron (1.602×10^{-19} C). Substituting in the Equations (3.2a) and (3.2b) for i_1, i_2, leads to

$$\sigma_{i_1,i_2} = \sqrt{2e\alpha\left(\frac{P_T}{wl}\right)\left(\frac{wl}{2}\right)},$$

(3.8)

$$\sigma_{i_1,i_2} = \sqrt{e\alpha P_T} .$$

(3.9)

Adding the shot-noise terms for each element in quadrature gives

$$\sigma_{i_1,i_2} = \sqrt{\sigma_{i_1}^2 + \sigma_{i_2}^2} ,$$

(3.10)

$$\sigma_{i_1,i_2} = \sqrt{2e\alpha P_T} .$$

(3.11)

Hence, the sensitivity can be determined from the previous result in Equation 3.11 and 3.6 as follows

$$\sigma_y = \frac{\sigma_{i_1,i_2}}{\left(\dfrac{d(\Delta i)}{dy}\right)},$$

(3.12)

$$\sigma_y = w\sqrt{\frac{e}{2\alpha P_T}} .$$

(3.13)

The limiting photodiode power density value, p_{max}, and responsivity, α, can be substituted into this function. But first p_{max} shall be defined, such that the maximum power density

$$p_{max} = \frac{P_T}{wl} = 100 \text{ W m}^{-2}.$$

(3.14)

By substituting the new variable p_{max}, Equation (3.13) now becomes

$$\sigma_y = w\sqrt{\frac{e}{2\alpha p_{max} wl}},$$

(3.15)

$$\sigma_y = \sqrt{\left(\frac{e}{2\alpha p_{\max}}\right)}\sqrt{\left(\frac{w}{l}\right)}. \tag{3.16}$$

Substituting in the values, gives the formulae for the sensitivity as a function of the image size parameters

$$\sigma_y = \sqrt{\left(\frac{1.602 \times 10^{-19}}{2 \times 0.65 \times 100}\right)}\sqrt{\left(\frac{w}{l}\right)}. \tag{3.17}$$

If the width of image formed is, $w \approx 1.4$ mm, and length of image formed is, $l \approx 10$ mm, the sensitivity that should be achievable can be estimated to be

$$\sigma_y \approx 1 \times 10^{-11} \, \text{m Hz}^{-1/2}. \tag{3.18}$$

This ideal result is encouraging, as it indicates a performance should be comparable to the initial sensor requirements given in Table 3.1. But to reiterate, this calculated noise performance assumes that the operation of the sensor is shot-noise limited. It was necessary to construct the sensor in the laboratory to determine if the sensitivity result, obtained analytically, could be realised. However, it was imperative to ensure that other noise sources, notably the front-end electronics components, did not exceed the equivalent voltage noise.

The technical noise admissible to reach the shot-noise limited sensitivity can be found. Given the target responsivity of the sensor can be defined as 10 V over a 3 mm working range, i.e. 3.3 kV m^{-1}, results in a voltage noise of, $V_n \approx 3.3 \times 10^{-8}$ V Hz$^{-1/2}$. Using the maximum power density given in Equation 3.14, the dimensions of the active area provided above and α, a nominal photodiode current of approximately 1 mA can be calculated. Therefore, a current-to-voltage gain of 10 kΩ would be necessary for the required amplification. Using this gain factor, the equivalent current noise can be found to be, $I_n \approx 3.3 \times 10^{-12}$ A Hz$^{-1/2}$. Attaining such a low-level of technical noise, of the order of a few picoamps, is certainly challenging, but not insurmountable. Careful component selection and noise calculations enabled this to be achieved. For example, low noise OP07 operational amplifiers were used throughout, and feedback resistors values were

chosen to ensure that Johnson noise did not dominate over the shot-noise limited performance.

An image of the experimental set-up is provided in Figure 3.4. Highlighted are the mechanical translation stages and key optical components. An IRLED (Opto Diode Corp, OD-50L) was selected. This device has a typical power output of 50 mW at 500 mA forward current, is well collimated, with a beam emission half-angle of 7° and is available mounted in a hermetically sealed package. A quadrant photodiode (UDT, SPOT-9D) is employed as the split detector. The dead band between elements is 0.102 mm and active area per element of 19.6 mm^2. This device has a spectral response in the range 350 nm to 1100 nm and a maximum recommended incident power density of 100 W m^{-2}.
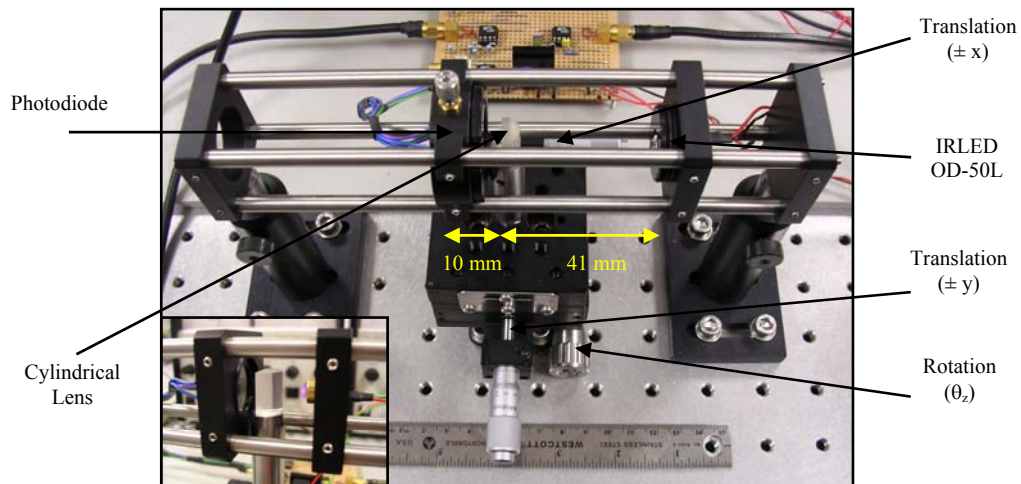
Figure 3.4: *Imaging sensor experimental set-up.*

Figure 3.5 gives the measured response function of the sensor, which was generated by taking incremental measurements as the cylindrical lens is translated orthogonally to the optical path. The near linear region corresponds to a maximum responsivity of approximately 4.5 kV m^{-1} over a 3 mm (peak-peak) range, equivalent to a full range voltage output of the differential amplifier equal to $\pm$ 7 V. Application of a reverse bias to the photodiode (photoconductive operation) allows for an increase in the linearity of the device response and potentially lower noise.
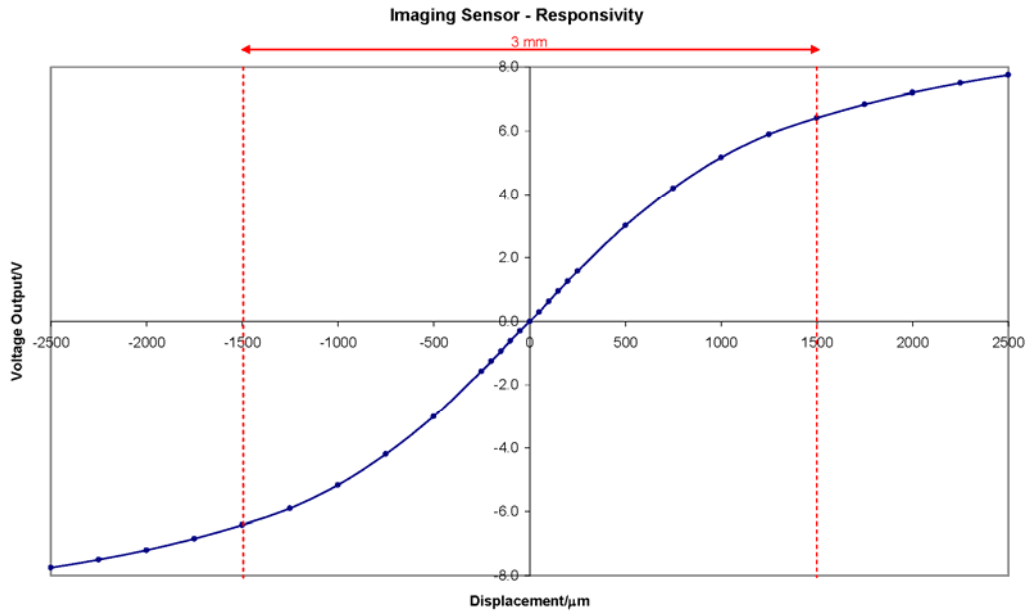
Figure 3.5: *Imaging sensor response function.*

Once the noise floor and response function of the sensor had been measured, the sensitivity of the device was determined. Using both un-modulated and ac modulated, lock-in schemes, the sensitivity of the prototype geometric sensor is presented in Figure 3.6. Note that, the dashed red line denotes the shot-noise limited sensitivity. It can be seen that the sensitivity performance of the un-modulated and lock-in methods are very similar for higher frequencies, resulting in obtaining a sensitivity of approximately 2×10^{-11} m Hz$^{-1/2}$ above 25 Hz. It is the low frequency performance, below 25 Hz, of the ac modulated lock-in scheme that shows a significant improvement when compared to the dc un-modulated method. Unfortunately, however, it is not permissible to employ a lock-in scheme for the Advanced LIGO sensors, due to concerns that the modulation frequency (or harmonics thereof) are likely to be observable within the detection band of the instrument.

To summarise, the sensor's ac performance has demonstrated reaching a sensitivity of approximately 1.5×10^{-11} m Hz$^{-1/2}$ for frequencies above 1 Hz. These sensitivities were achieved whilst coupling approximately 12 mW of incident light intensity onto the photodiode. The IRLED emitter has a steady-state total power dissipation of 620 mW.
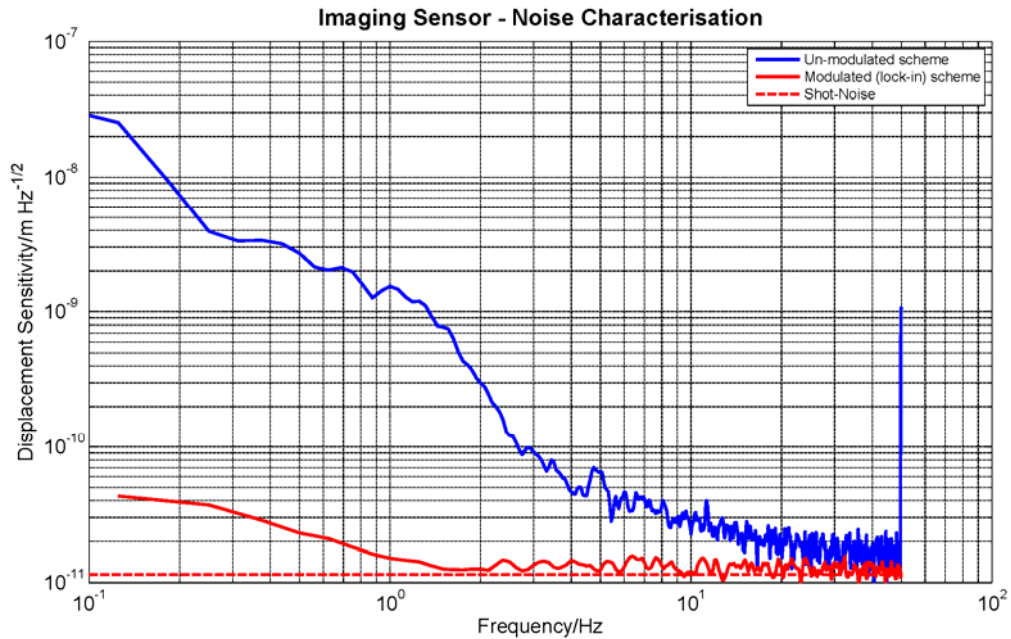
Figure 3.6: *Imaging sensor modulated and un-modulated sensitivity.*

The performance of this sensor was encouraging for such a simple design. However, during further characterisation a feature was uncovered that constitutes a fundamental deficiency with this approach. Results presented so far have all been taken at the detectors 'null' position, i.e. the image is formed at the centre of the photodiode (image falling across the dead-band). It has been observed that moving the detector away from the 'null' position proportionally raises the noise floor by a considerable margin. This increased off-null noise is demonstrated for the modulated scheme in Figure 3.7, with similar behaviour also exhibited in the un-modulated scheme. Hence the sensitivity performance detailed above could not be realised over the whole 3 mm (peak-peak) range.
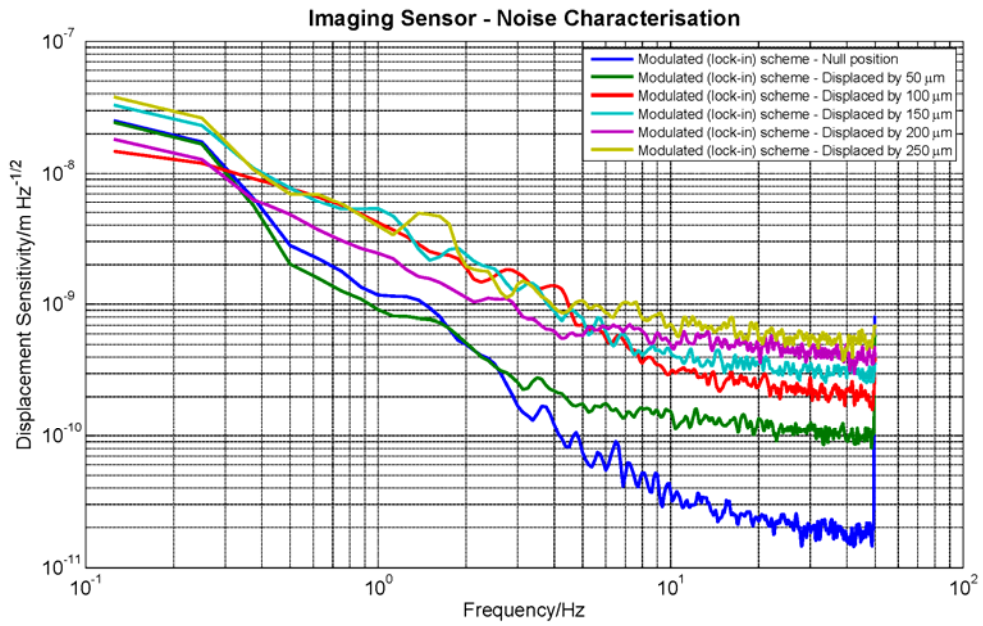
Figure 3.7: *Imaging sensor off-null sensitivity for modulated scheme.*

An off-null increase in noise was also observed with a similar prototype geometric sensor developed by Lockerbie [59]. Both designs of geometric sensor independently selected and share a key component, the IRLED. It has been proposed that the IRLED could be the source of the increased noise. However, given the requirements had been relaxed to those presented in Table 3.2, there was no need to pursue the noise issue further.

3.3.2 Shadow Sensor

The shadow sensor method utilises a similar optical configuration to that shown in Figure 3.2, but with an opaque cylindrical (or spherical) object placed between the collimated light source and detector. The optical configuration of the existing sensor already employed in Initial LIGO, takes the form of a shadow sensor, and is shown in Figure 3.8. With this scheme it is likely that some of the optical power will be scattered by the opaque object, so the object surface should be highly non-reflecting. In the Initial LIGO sensor configuration, the opaque object is a 2 mm diameter cylindrical flag. The flag is attached to a magnet (for actuation purposes) and then the test-mass, whose position is to be monitored.
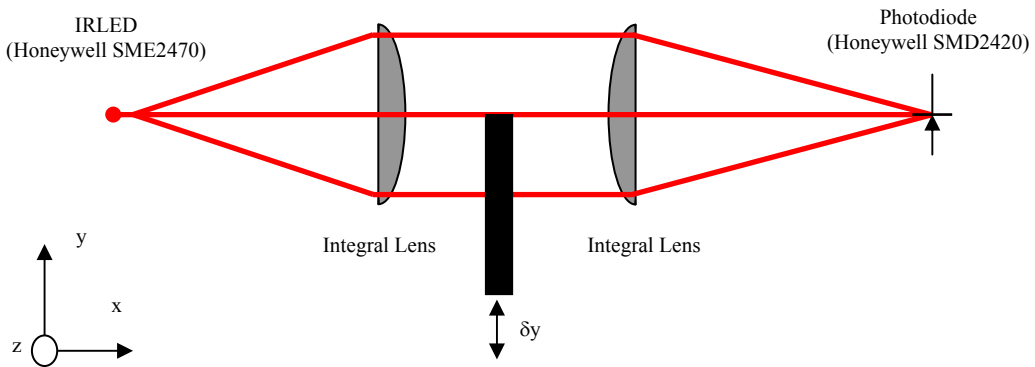
Figure 3.8: *Initial LIGO shadow sensor optical layout.*

The shadow sensor, as shown in Figure 3.8, comprises of a flag, a surface mount single element photodiode and a surface mount infrared light emitting diode (IRLED). Both of these device packages incorporate an integral lens that weakly collimates the emission, or focuses the optical beam. Displacement of the flag along the y axis changes the proportion of the collimated beam that is incident upon the photodiode. The flag can conceivably be located in either of two extreme conditions. For example, the flag all the way in the sensor, restricting the light from being incident on the photodiode constitutes the closed-light condition. Conversely, with the flag completely withdrawn from the sensor, results in the full illumination of the photodiode and constitutes the open-light condition. Within these two extremes, a linear operating range can be determined. Under normal operating conditions, the flag would usually reside in the centre of this operating range at the half-light position.

Development of this sensing technique, for the Initial LIGO sensors, was carried out by Fritschel and Adhikari [60]. Their scheme employed a separation of 6.35 mm between the IRLED and photodiode. The IRLED was driven with a constant current of 42 mA and resulted in a mean photocurrent (i.e. flag in half-light position), i_{pd}, of 12.5 µA. As derived in Section 2.2.1, the shot-noise limit can be calculated for this sensor configuration using,

$$\sigma_{i_{pd}} = \sqrt{2ei_{pd}} \ . \tag{3.19}$$

The photodiode was reverse biased at 5 V and operated in a transimpedance amplifier configuration, with a transimpedance, R_f, of 100 kΩ. The voltage noise can be found using

$$\sigma_{v_{pd}} = \sqrt{2ei_{pd}} \times R_f \ . \tag{3.20}$$

The responsivity, R_{es}, of the sensor over an operating range of 0.7 mm (peak-peak) was found to be approximately 3 kV m^{-1}, thus leading to a shot-noise limited performance of

$$\sigma_y = \frac{\sqrt{2ei_{pd}} \times R_f}{R_{es}} \ . \tag{3.21}$$

Substituting in the values provided gives

$$\sigma_y = \frac{\sqrt{2 \times 1.602 \times 10^{-19} \times 12.5 \times 10^{-6}} \times 100 \times 10^3}{3 \times 10^3} \ . \tag{3.22}$$

Leading to a shot-noise limited sensitivity of

$$\sigma_y \approx 7 \times 10^{-11} \, \text{m Hz}^{-1/2}. \tag{3.23}$$

Noise measurements originally made by Fritschel and Adhikari [60] and more recently repeated by Lockerbie [61], both found the sensitivity to be equal to

59

approximately 3×10^{-10} m Hz$^{-1/2}$ at 1 Hz and around 1×10^{-10} m Hz$^{-1/2}$ at 10 Hz, over a linear working range of 0.7 mm (peak-peak). The sensitivity performance was observed to be 1/f noise limited at low frequencies around 1 Hz, and shot-noise limited at higher frequencies of 1 kHz and above [60].

Following the refinement of the sensor requirements, as given in Table 3.2, it was determined that the sensitivity already obtained by the Initial LIGO shadow sensor would be sufficient to meet the relaxed sensor requirements for the Advanced LIGO sensor. However, an optimisation process (also known as the sensor study) was conducted to indentify alternative (leaded) photodiodes and IRLEDs that may offer improved low frequency performance. It had long been suspected that the original surface mount devices were the source of the increased 1/f noise observed above the shot-noise at 1 Hz, and this was confirmed by further measurements made by Lockerbie [62]. A subsequent investigation by Lockerbie [62] also investigated alternative flag geometries, optical configurations, light pipes and lenses. The final scheme proposed incorporated a mask with a slit, collimating lens, and lens integral to the emitter assembly, as shown in Figure 3.9. The additional lens improves the collimation of the emission from the IRLED, the mask ensures only paraxial rays contribute to the noise floor. The IRLED and photodiode devices shown in Figure 3.10 were put forward as replacements for the surface mount components [63]. Key parameters of these devices, extracted from the data-sheets, are listed in Table 3.3.
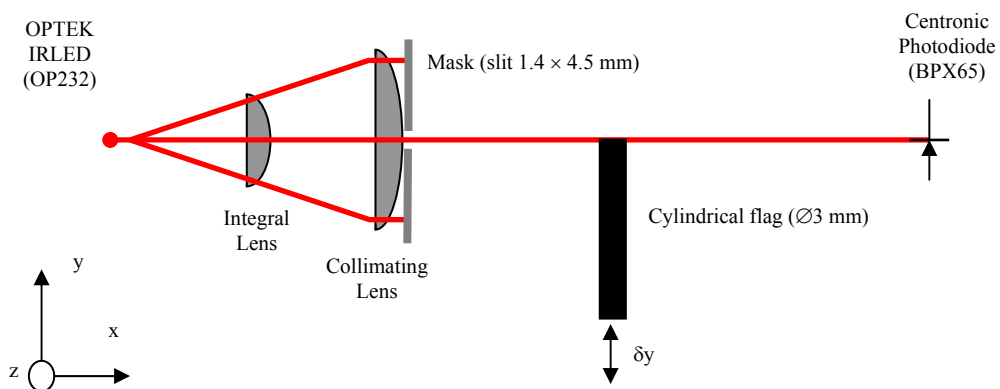
Figure 3.9: *Advanced LIGO shadow sensor optical layout.*

Figure 3.10: *Images of leaded sensor components.*
(Left) OPTEK OP232 IRLED. (Right) Centronic BPX65 photodiode.

IRLED (OP232)	Photodiode (BPX65)
TO-46 ($\varnothing$ 4.7 mm) Kovar Package	TO-18 ($\varnothing$ 4.8 mm) Steel Package
Anode to case	Cathode to case
Hermetically Sealed	Hermetically Sealed
Peak emission = 890 nm	Peak sensitivity = 850 nm
Maximum forward current = 100 mA	Responsivity = 0.55 A W^{-1} (at 900 nm)
Operating forward current = 35 mA	Capacitance = 15 pF
Maximum radiant power = 8 mW (at 100 mA)	Dark Current = 5 nA

Table 3.3: *Key specification of leaded sensor components.*

Characterisation of a small quantity of prototype sensors of the Advanced LIGO configuration, using the IRLED driven at constant 35 mA, resulted in a mean photocurrent, i_{pd}, of 62.5 μA, with a transimpedance, R_f, of 320 kΩ and a measured responsivity, R_{es}, of 20 kV m^{-1} over a linear operating range of 0.7 mm (peak-peak). Substituting these figures into Equation 3.21, provides a shot-noise limited performance equivalent with the result previously obtained in Equation 3.23, of approximately 7×10^{-11} m Hz$^{-1/2}$. Following the completion of the sensor study, the optical configuration design was frozen, and incorporated into the Advanced LIGO BOSEM.

3.4 BOSEM Design

The work undertaken in developing the BOSEM, builds upon previous design work carried out by Romie *et al* on the Hybrid OSEM [64]. The Hybrid OSEM is the first incremental step away from the Initial LIGO OSEM towards an Advanced LIGO BOSEM. Figure 3.11 shows 3D CAD realisations of these two designs, with key features highlighted. The most noticeable refinement of the Hybrid OSEM design is the modification to the actuator coil geometry, due to stronger actuation coils being necessary to actuate upon the much heavier Advanced LIGO test-masses. Significant refinements have also been made to the clamping and adjustment scheme, to provide easier and repeatable alignment of the unit.
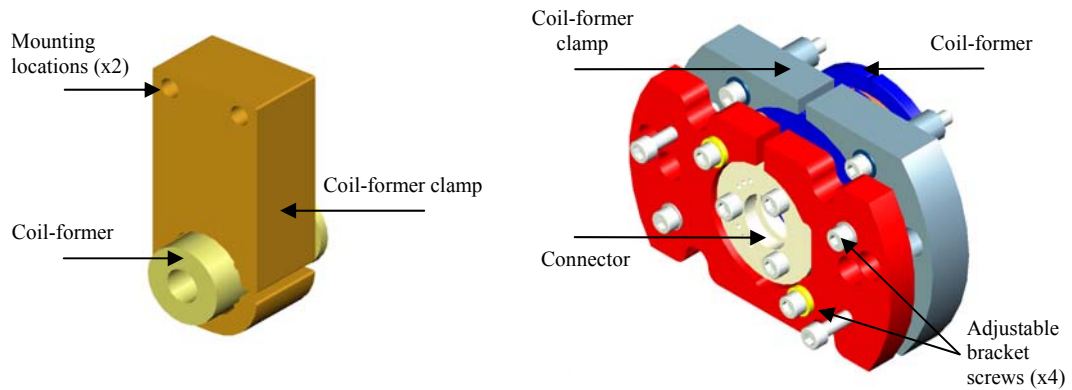
Figure 3.11: *3D CAD models of previous OSEM designs.*
(Left) Initial LIGO OSEM assembly. (Right) Hybrid OSEM assembly. Source [64].

The sensors are not visible in the two models shown in Figure 3.11, but they can be located within the central aperture of the coil former. Note that, Initial LIGO sensors are fitted in each case. The surface mount sensor components are aligned and bonded down to a substrate with a ceramic adhesive. Concerns have been raised with this approach, regarding the misalignment that can result of the adhesive curing process. The curing can also be considered a time consuming and complex production task. The aim was to mitigate the risk associated with this approach by instead considering using a standard metal-can package, thus enabling alternative mounting schemes to be realised. Moreover, parts can be machined to defined tolerances, so as to ensure ease of assembly and reproducibility of the alignment of the sensor. To facilitate large scale production of the BOSEM a number of other issues also had to be addressed, such as finding a robust

and reliable method of making interconnections within the device, and indentifying a suitable external connector. The BOSEM comprises the following sub-assemblies:

- Optical sensor (incorporating IRLED and photodiode detector).
- Electromagnetic actuator (coil wound onto coil-former).
- Clamping/mounting and adjustment.
- Electrical interconnect (sensor, coil winding and external connector).
- Magnet and flag.

Most of these sub-assemblies can be seen highlighted in the final mechanical design, shown in Figure 3.12.
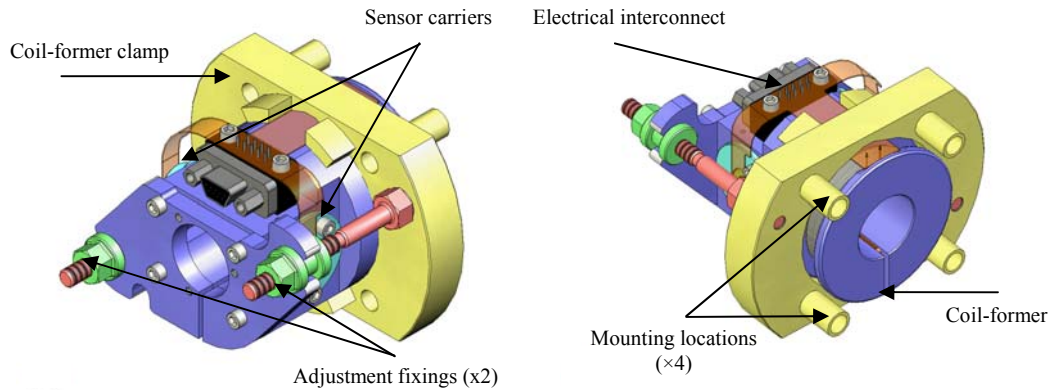
Figure 3.12: *3D CAD model of BOSEM assembly.*
(Left) Rear isometric view. (Right) Front isometric view.

Electrical isolation requirements state that the device package should be insulated from its aluminium carrier and hence the rest of the Advanced LIGO suspensions structure. To ensure this requirement is met, each device is insulated from the carrier by a ceramic sleeve, into which the device is push-fit. Figure 3.13 shows the assembled IRLED carrier and a component part explosion. Figure 3.14 shows the equivalent scheme for the photodiode carrier assembly. A recess machined in the ceramic sleeve accommodates the flange and tag located on the sensor package. A flat machined onto the ceramic sleeve outer diameter (as indicated in the diagram), corresponds to an aperture (pin-hole) on the carrier and enables the orientation of the device to be fixed during the assembly process. The orientation is constrained to maintain the correct polarity of the leads when mating with the flexible circuit. The same technique is used in both IRLED and photodiode carrier assemblies.
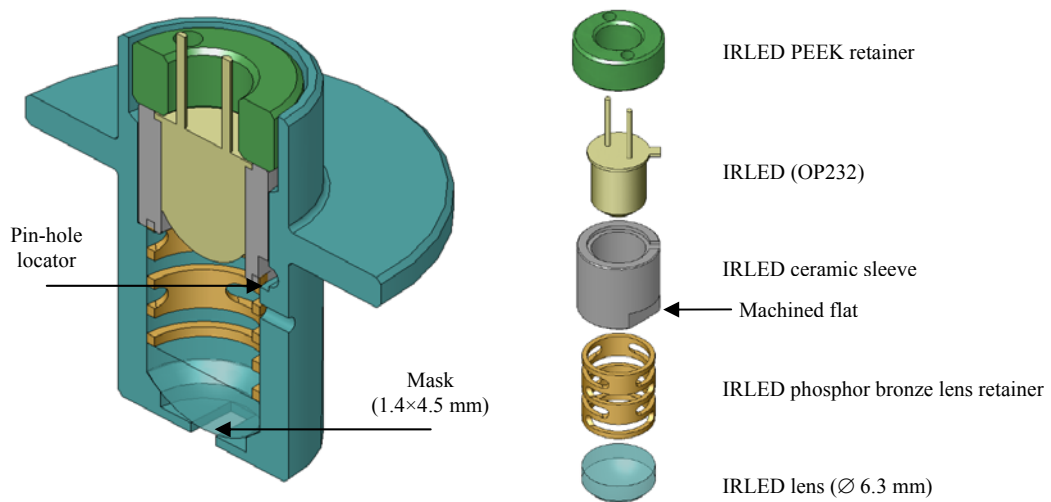
Figure 3.13: *IRLED carrier assembly.*

(Left) Section through IRLED carrier. (Right) IRLED carrier part explosion.
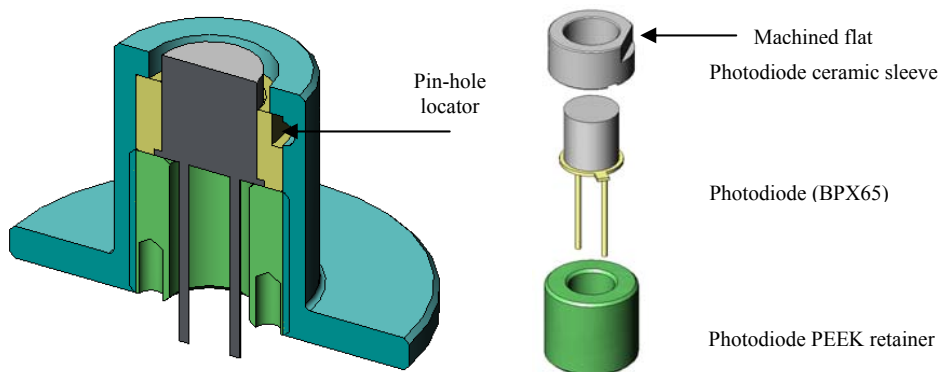
Figure 3.14: *Photodiode carrier assembly.*

(Left) Section through photodiode carrier. (Right) Photodiode carrier part explosion.

The complete sensor assembly, and relative separation of the emitter and receiver sub-assemblies is shown through a section view in Figure 3.15.
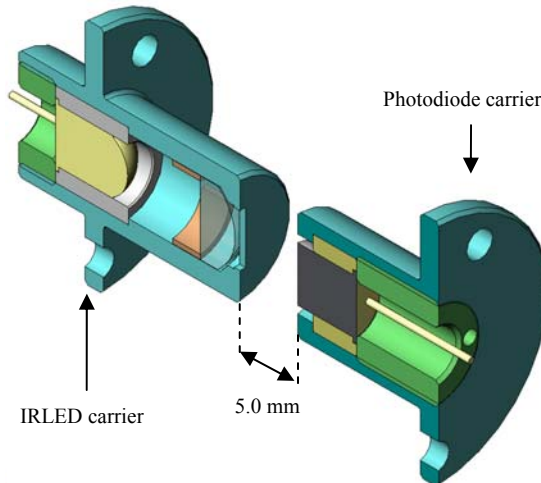
Figure 3.15: *Section through sensor carrier assemblies.*

The properties for the actuation coil have evolved since the Initial LIGO OSEM design. This was done so as to cater for the change in the suspended mass, i.e. it was necessary to revise the coil geometry to provide stronger actuator forces. The recommendations regarding coil dimension, number of turns etc. put forward by Strain, were adopted into the design [65].

Parameter	Specification
Wire Type	32QML, 32 gauge copper wire, quad coating of polyimide-ML
Coil-former material	Aluminium (6082)
Coil inner diameter	17.78 mm
Coil length	8.00 mm
Coil number of turns	800

Table 3.4: *BOSEM electromagnetic actuator properties.*

Table 3.4 gives the properties of the electromagnetic actuator. Further characteristics, such as electrical properties, of the actuator coil are detailed elsewhere [66]. Figure 3.16 shows the key dimensions for the coil-former.
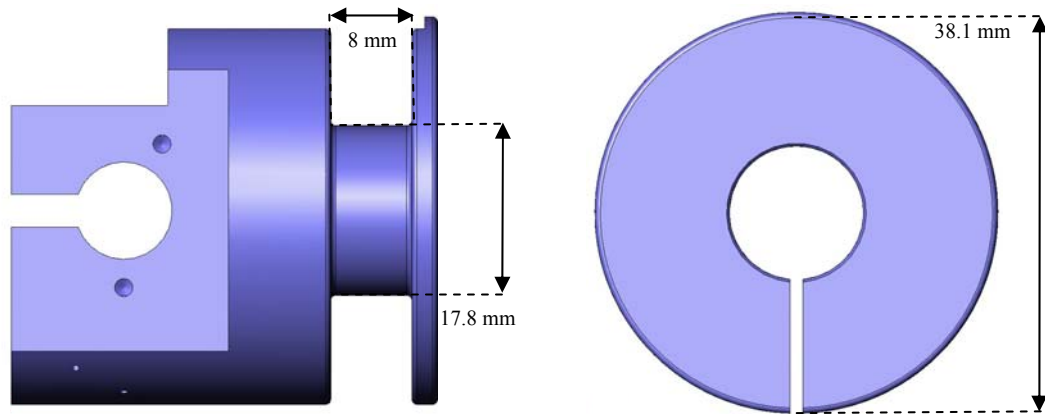
Figure 3.16: *Actuator coil-former geometry.*
(Left) Profile of coil-former. (Right) Front face of coil-former.

The operating point or 'sweet-spot' of the magnet and actuator coil has had to be redefined as a consequence of the revised coil geometry. The location has been calculated using a Mathematica model generated by Barton [67]. For the Advanced LIGO Quadruple suspensions, $\varnothing$10 mm × 10 mm long Nd-B-Fe nickel plated magnets have been selected. Since the separation between the sensor and actuator has now changed when compared to the Initial LIGO OSEM, new flag dimensions are also required. A proposed magnet and flag assembly is shown in Figure 3.17.
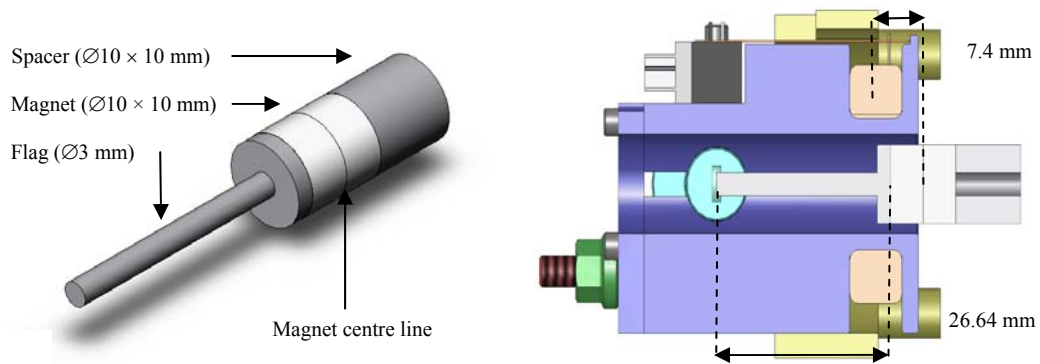
Figure 3.17: *Flag, magnet and coil-former assemblies.*
(Left) Isometric view of flag and magnet. (Right) Section through coil-former and flag.

Use of magnetic materials in the construction of the BOSEM is restricted to ensure that any residual actuation force (with actuator coil unbiased and actuator magnet positioned on the BOSEM z axis in line with the front face of the coil-former) is less than 5 mN (i.e. 10 % of the original peak actuation force). For example the magnetic coupling

between the magnet and sensor packages is responsible for determining the length of the flag.

The interconnect encompasses all of the circuit routing and connections required to link together the various electrical components of the BOSEM, as well as provide an interface for an external connection. The connector specification and pin-out details can be found in Appendix B.

Figure 3.18 shows the interconnection assembly, including all the individual parts to be connected. For completeness, the sensor devices have their anode and cathode denoted by A and K respectively. The start (S) and end (E) pins of the coil winding are also indicated.
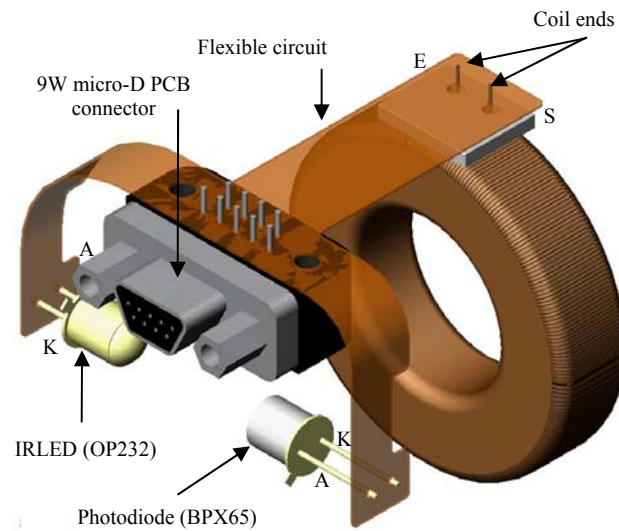
Figure 3.18: *Interconnection assembly.*

A full list of materials, and their Advanced LIGO UHV approval status, can be found in Appendix C.

3.5 Fabrication, Assembly and Testing

Following the successful outcome of the Final Design Review [68], the BOSEM 2D CAD drawings were signed-off and released to external contractors. These drawings are available in Appendix F.

A manufacturing study was carried out to identify vendors that could undertake the fabrication work on a timescale compatible with the project schedule. Once vendors were selected, parts they produced were received for inspection at Birmingham. Parts that were accepted (i.e. within the specified tolerances) could then go forward for cleaning and bake-out in accordance with LIGO UHV requirements. Figure 3.19 shows images of clean-room facilities at Birmingham and parts going through the bake-out process.

Figure 3.19: *Images of Birmingham BOSEM production clean-room facilities. (Left) Dedicated clean-room assembly suite. (Right) Cleaned parts in bake-out oven.*

Whilst building and evaluating prototypes, it was observed that there was a significant variation in the off the shelf optical output intensity of the IRLEDs. This device to device variation, as large as 50 %, was also confirmed by the manufacture's data-sheets. The manufacturer was approached, to establish if were possible to procure a batch of graded parts, but unfortunately it was not feasible for them to assist, given the relatively small batch size of approximately 2000 units. This implied that screening of the output intensity of these devices would have to be conducted in-house. Prior to intensity screening, devices were subjected to a burn-in procedure carried out at their maximum forward current, for a period of fifty hours. The burn-in helped to normalise the output intensities and identify any instances of infant mortality from within each batch. Mock BOSEM sensor jigs were constructed to allow the screening of IRLEDs and devices were

then binned depending upon their output intensity. IRLEDs could then be prepared, cleaned and baked prior to being assembled into the BOSEMs.

Assembly of the BOSEMs was conducted in Birmingham's clean-room facilities, by technicians trained in the necessary LIGO UHV clean handling procedures. A BOSEM assembly specification was generated to provide a step-by-step guide to assembly and helped ensure consistency across the whole batch of units [69].

Upon the completion of the assembly task, the assembled BOSEMs are tested using automated test equipment (ATE). The functionality of the BOSEM can be tested by the ATE during a 30 s operation. A 35 mA drive current is passed through the IRLED and the corresponding photodiode current measured. The actuator coil dc resistance and inductance is also measured and logged to a text data file. Figure 3.20 provides images from within the clean-room suite, showing the assembled BOSEMs at the testing station and undergoing tests using the ATE. Testing is conducted in accordance with the BOSEM test specification [70].

Figure 3.20: *Images of assembled production BOSEMs.*
(Left) Assembled BOSEMs at test station. (Right) BOSEMs undergoing testing using ATE.

Figure 3.21 provides a screen capture of the graphical user interface (GUI) which is used to collect BOSEM/operator identification information and interact with the ATE hardware. Once the various BOSEM parameters have been measured, they are checked by the ATE software to ensure they are within agreed tolerances. Should any parameters be out of range, the BOSEM is deemed to have failed the test and would, therefore, require remedial action.

Figure 3.21: *BOSEM ATE software GUI.*

3.6 BOSEM Characterisation

The testing previously conducted by the ATE enables fast functionality tests of each BOSEM to take place, within the clean-room environment. However, the ATE does not fully characterise BOSEM performance, given that measurements of the responsivity and noise floor for each unit are not made. Such measurements are usually quite involved and significantly more time-consuming.

Therefore, the aim of the full characterisation tests is to simulate the real-world operation of the BOSEM. To provide an extensive end to end test of the BOSEM, a spare Satellite Box has been used to drive the IRLED and provide front-end amplification for the photodiode currents. The BOSEM harness has also been fabricated as per the current design specification (twisted pairs, with a copper shield and an overall PEEK braid).

3.6.1 Free-Air Measurements

The BOSEM is mounted using custom fixtures to an optical bench. A 3 mm diameter flag is attached to a translation stage which allows it to be translated along the sensitive z axis of the BOSEM. Figure 3.22 (left) shows the BOSEM ready to be characterised, mounted on the test fixtures. Figure 3.22 (right) shows a Satellite Box.
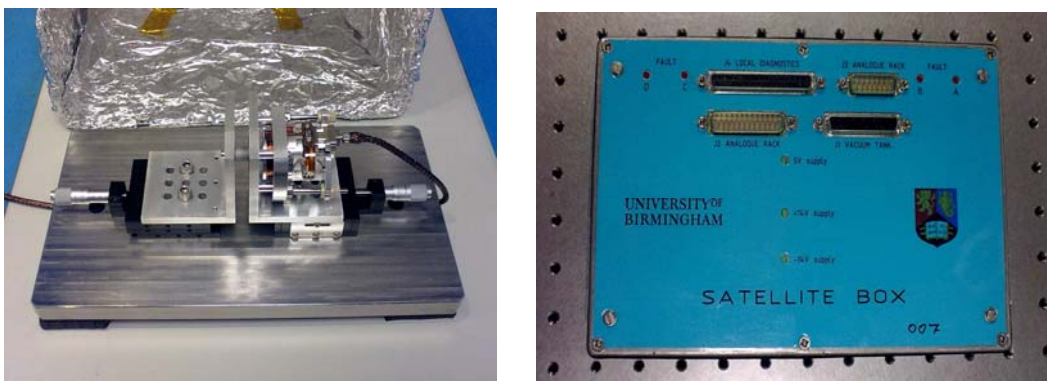
Figure 3.22: *BOSEM free-air test set-up.*
(Left) BOSEM and test fixtures. (Right) Satellite Box support electronics.

Measurements of BOSEM noise performance are made at the centre of the operating range of the sensor (half-light). The first task is, therefore, to establish the operating range. A voltmeter can be used to observe the differential output voltage from

the Satellite Box amplifier for various positions of the flag as it is translated along the sensitive axis of the BOSEM. Figure 3.23 shows a typical example of the measurement of the BOSEM responsivity. Ideally the differential output voltage should reside between 0 V and 20 V.

BOSEM Characterisation #539 - Responsivity
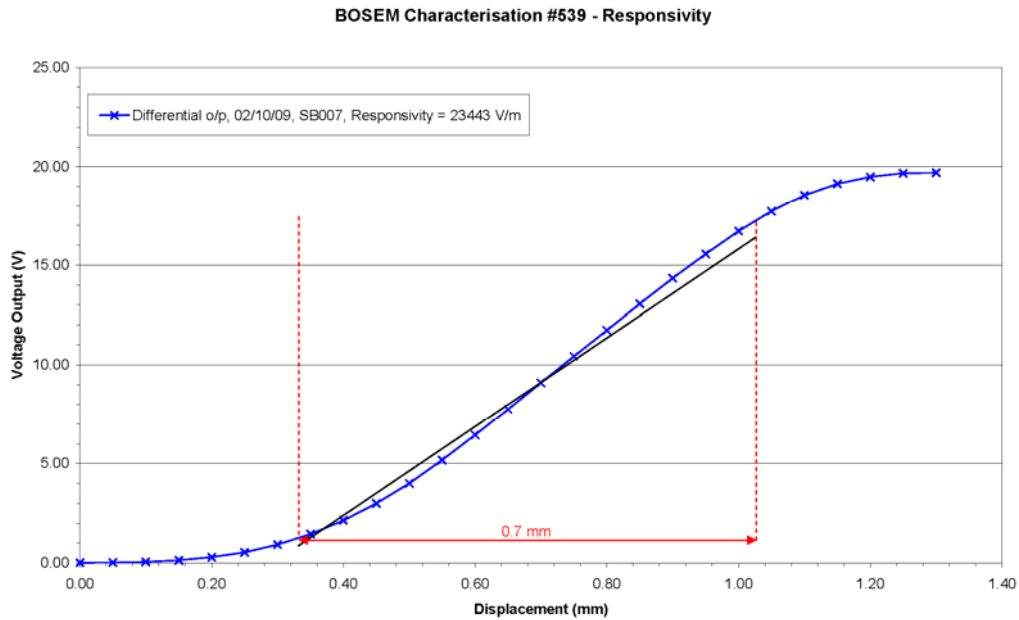
Figure 3.23: *BOSEM typical response function.*

Once the minimum (closed-light) and maximum (open-light) voltages have been indentified the centre of the operating range can be determined and a noise spectrum taken. A number of spectra were taken and averaged over the range 0 Hz to 12.5 Hz or 0 Hz to 50 Hz. Responsivity measurements are taken for each BOSEM under test.

3.6.2 In-Vacuum Measurements

Figure 3.24 shows the experimental set-up used for the duration of the tests. The BOSEM is situated within a vacuum chamber, which has been pumped down to a pressure of less than 3 Pa. An electrical feedthrough is incorporated to enable drive current to be provided to the IRLED and pass through the current generated by the photodiode. The BOSEM is mounted using four fixings screws through its own clamp assembly into a custom fixture, which has previously been used for the free-air measurements. However, only a single fixture is necessary, i.e. the flag is fixed and thus does not need a translation stage. Instead the in-built adjustment of the BOSEM is used to position the flag in the centre of the operating range. Once the adjustment is complete the

bell jar can be fitted and the air pumped out. This is representative of an operational test of a non-suspended BOSEM mounted onto the structure of an Advanced LIGO quadruple pendulum suspension.
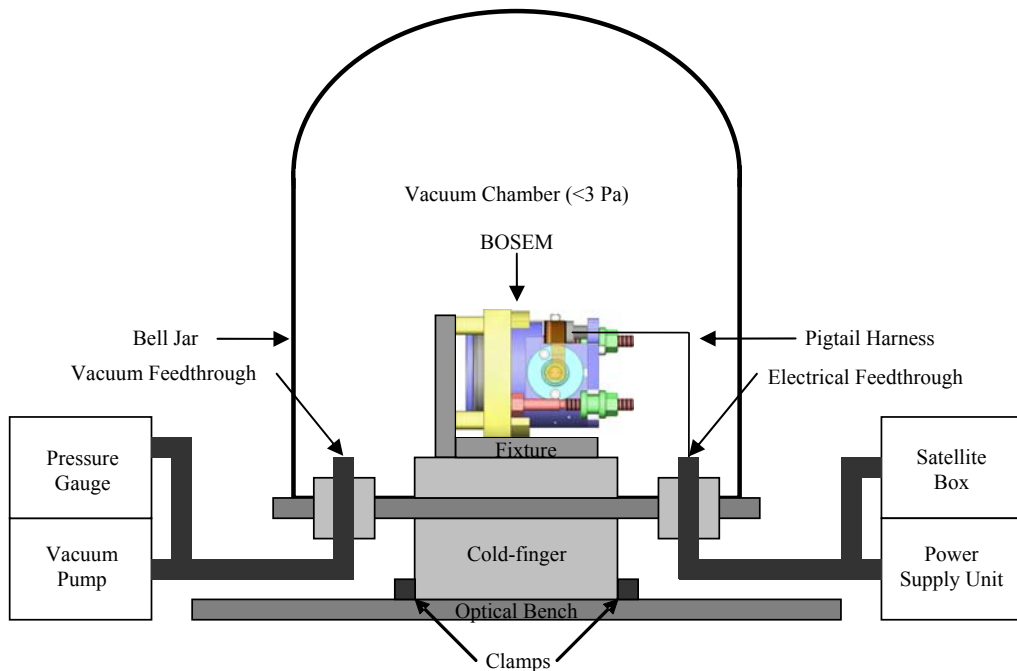
Figure 3.24: *BOSEM in-vacuum test set-up.*

Figure 3.25 shows an image taken during the measurement process, noting that the implosion shield has been removed to give an unobstructed view of the BOSEM under test.

Noise measurements in the laboratory from sensor mock-ups and bench-top prototype units were encouraging and appeared to meet the requirement with a small margin. Note that, both the free-air and in-vacuum measurements for the BOSEM were consistent. Individual units were characterised at Birmingham and by our collaborator, Lockerbie, at the University of Strathclyde. Following feedback from US/UK colleagues and at various review stages, minor refinements were made to the design. Production of the required number of BOSEMs was completed at the end of September 2009 and these units were ready to ship.
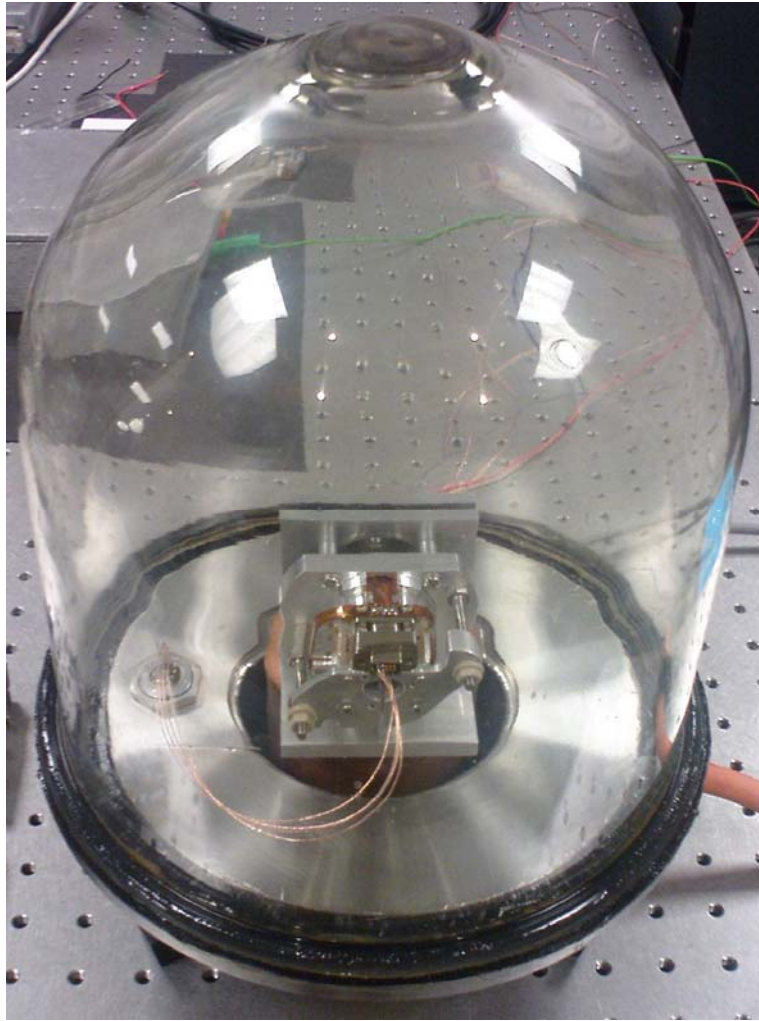
Figure 3.25: *BOSEM in-vacuum laboratory set-up (without implosion shield).*

3.7 BOSEM Production Issues

Prior to commencing with the shipment of BOSEMs to the Advanced LIGO observatories, a request was put forward from US collaborators to provide additional noise performance testing for each individual unit. This was not part of the original production plan, but it was agreed to perform noise measurements on a random sample of twelve units. The results obtained can be seen plotted in Figure 3.26. The black line approximates the requirement from 1 Hz to 10 Hz and each BOSEMs performance is shown as a different colour line. The photodiode currents as measured by the ATE and the measured responsivities are also included within the legend.
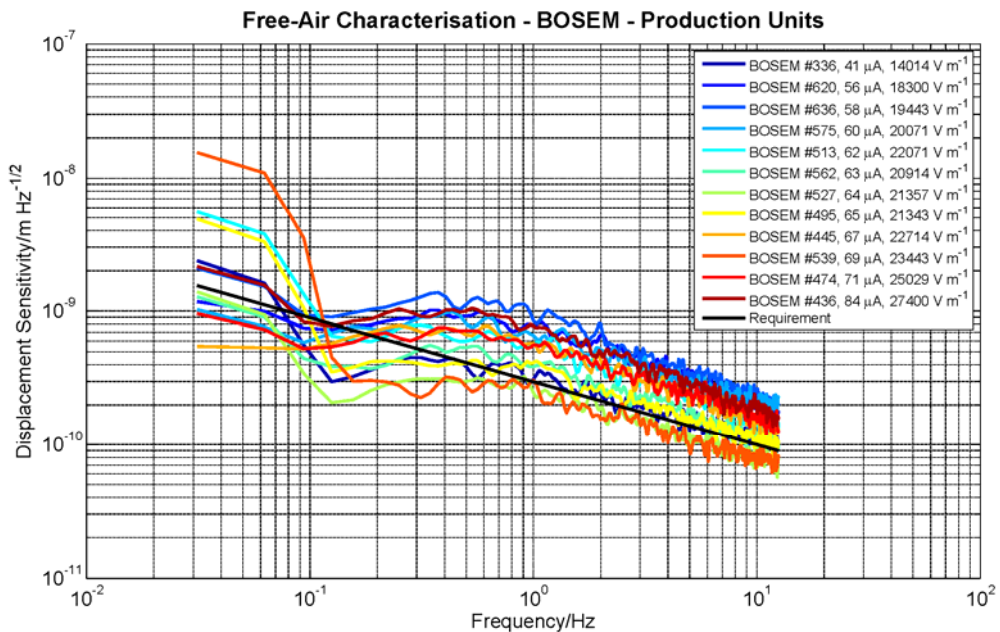
Figure 3.26: *BOSEM production unit free-air characterisation.*

The distribution of results obtained in Figure 3.26 was somewhat disappointing, especially since previous measurements of prototypes had raised no performance concerns. It can be seen that for the twelve BOSEMs characterised, only two meet the requirement, while the remaining ten units fail. There appears to be no obvious correlation between measured photodiode current and responsivity versus BOSEM noise performance.

3.7.1 Cleaning and Baking of Parts

It should be noted that, there are a large number of additional processes that the production units have undergone, when compared with bench-top prototype units tested in the past. It was, therefore, vital to establish if any part of the subsequent cleaning or bake-out process could have contributed to the observed degradation in noise performance. The use of cleaning solvents, ultra-sonic baths and high temperature bake-outs may have provided ample mechanisms for damage or degradation to occur. To establish if the cleaning and baking could have been the cause of the excess noise, it was necessary to measure the noise performance of BOSEMs that had not gone through the additional cleaning and baking processes. For this purpose, five prototypes that had previously been employed as IRLED screening jigs were reconstituted and characterised.
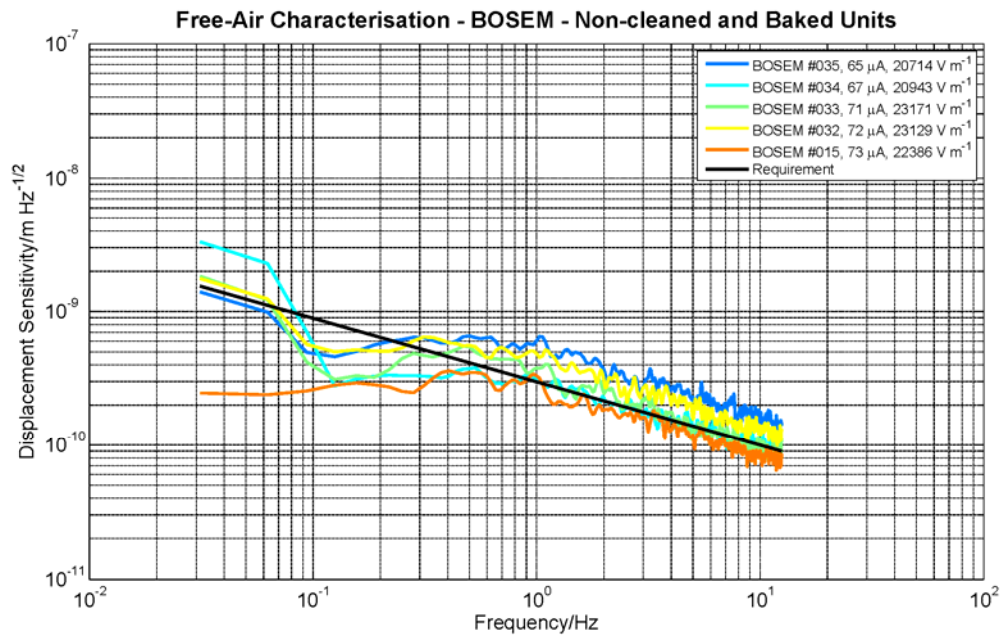
Figure 3.27: *BOSEM prototypes free-air characterisation.*

Results obtained can be seen plotted in Figure 3.27. The black line approximates the requirement from 1 Hz to 10 Hz and each BOSEM is shown as a different colour line. It can be seen that only two of the five units characterised appear to meet the requirement. This indicates that the distribution of noise performances for the prototype BOSEMs is similar to that which was obtained for the production BOSEMs shown in Figure 3.26. This establishes that the noise is inherent within the BOSEM and is not likely due to any

of the additional cleaning and baking processes subjected by the production units. Again there is no obvious correlation between measured photodiode current and responsivity versus noise performance.

3.7.2 Reproducibility of Measurements

Before embarking on an investigation to identify the source of the excess noise, it was first necessary to demonstrate the reproducibility of these noise performance measurements. It was essential to ensure that if the measurement were repeated, after the unit had been disassembled and reassembled, that it exhibited reproducible noise performance on each occasion. Otherwise mechanical tolerances, deviations in the assembly procedure or variations in the measurement procedure could conspire to give inconsistent results and would make indentifying the source of excess noise a significantly greater challenge. Figure 3.28 shows a black line approximating the requirement from 1 Hz to 10 Hz and sensitivity plots for both the best and worse case BOSEMs shown in different colour lines. Each unit's sensor assembly was completely disassembled, before being reassembled and retested. The results obtained demonstrate good reproducibility, both in the assembly of the sensor and the experimental technique. This consistency is encouraging for further tests that will need to be conducted in the search to identify the source of the excess noise.
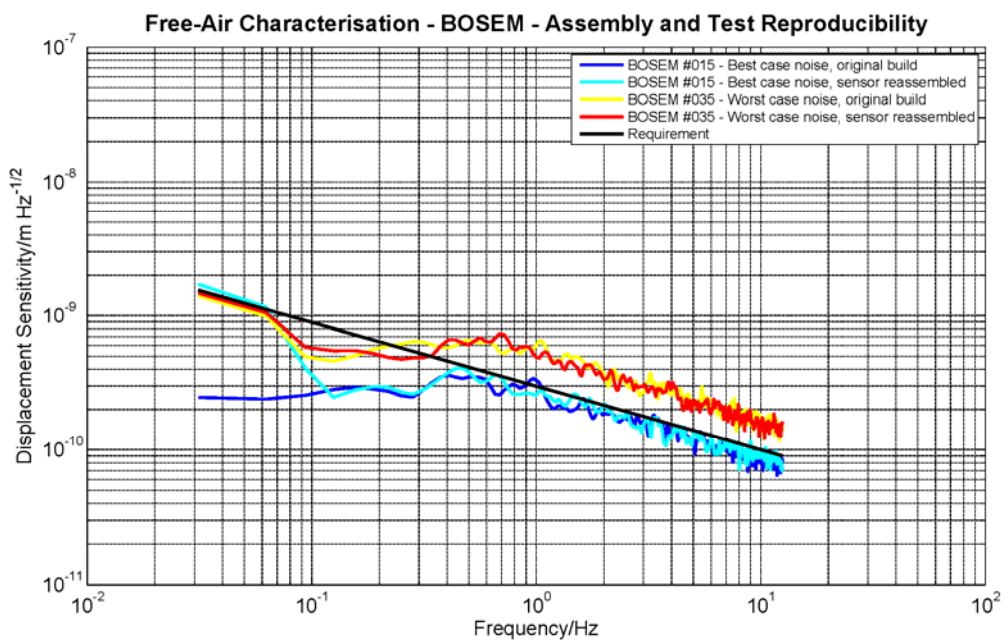
Figure 3.28: *BOSEM assembly and measurement reproducibility.*

3.7.3 IRLED and Photodiode Sensor Assemblies

A number of potential sources and mechanisms for the excess noise were considered, and could be eliminated from the investigation, such as, the routing and bending of the flexible circuit. All the evidence pointed towards some component of the sensor assembly itself. The two key components of the sensor assembly are the photodiode and the IRLED. It was, therefore, necessary to be able to discount either the photodiode or the IRLED as the source of the excess noise. This was achieved by exchanging either photodiodes or IRLEDs between compliant and non-compliant BOSEMs. Figure 3.29 shows the consequences, of taking a compliant BOSEM #015, i.e. one that meets the sensitivity requirement, and exchanging its sensor carrier assemblies with those from a non-compliant BOSEM #035. It can be see that by exchanging the photodiode carrier assembly, there is no impact upon the sensitivity. However, by exchanging the IRLED carrier assembly the sensitivity noise performance is immediately degraded, to level consistent with the non-compliant BOSEM. To determine if the excess noise was due to the sensor components themselves, or with their associated mechanical carriers, the measurements above were repeated, but by exchanging just the photodiode and IRLED, and not the complete carrier assemblies. It can be observed from Figure 3.29 that the performance was consistent, no matter which carrier was used.
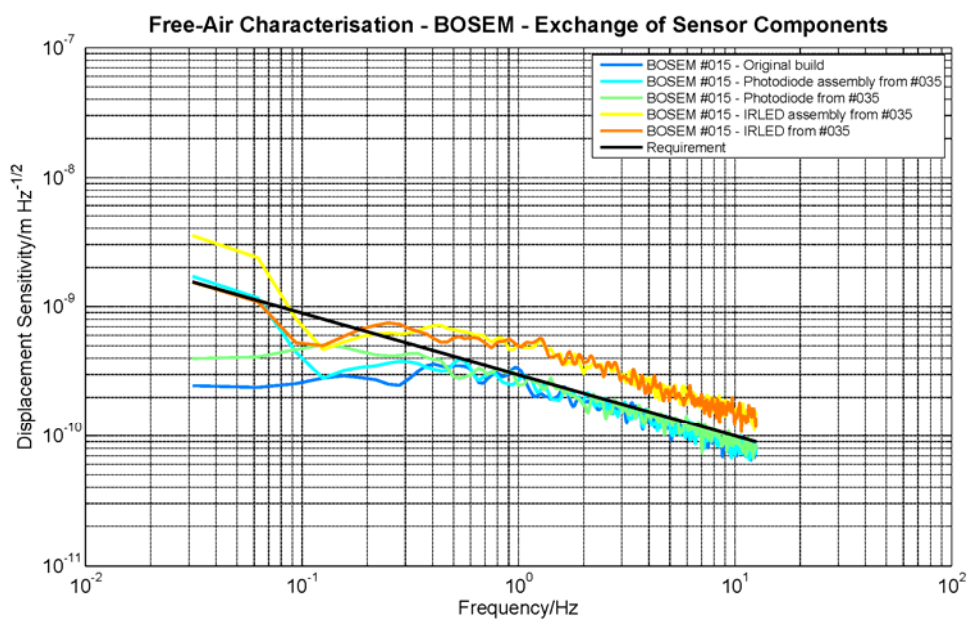
Figure 3.29: *Compliant BOSEM with non-compliant sensor components installed.*

These aforementioned measurements provided convincing evidence that the excess noise was associated with the individual IRLED. To add weight to this evidence, the measurements were repeated, but this time using the non-compliant BOSEM #035, and swapping into it sensor components from a compliant BOSEM #015. Figure 3.30 shows the results of this investigation. As anticipated, the non-compliant BOSEM #035 could be made compliant, by installing an IRLED from the compliant BOSEM #015. This confirmed beyond any doubt, that the IRLED was the source of the excess noise. Following these results, all of the future measurements were focused upon the IRLED itself.
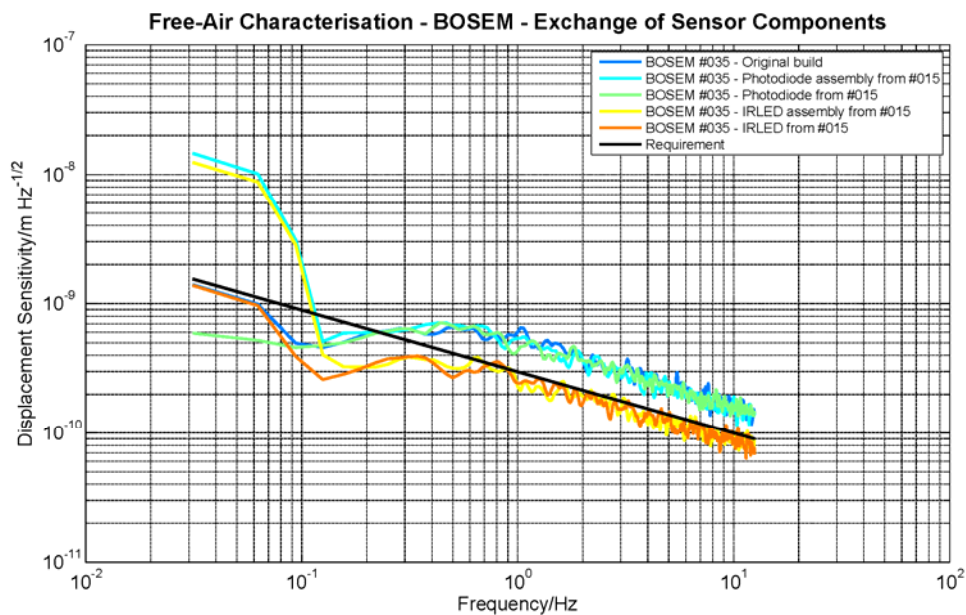
Figure 3.30: *Non-compliant BOSEM with compliant sensor components installed.*

3.7.4 IRLED Thermal Anchorage

When assembled into a BOSEM carrier assembly, the IRLED is located within a ceramic (Macor) sleeve, as depicted in Figure 3.13. This is to provide electrical isolation of the device whilst retaining some modest level of thermal conductivity with the rest of the environment. However, it was conceivable, that due to variations in mechanical tolerances of the IRLED package, that the resulting thermal link may be inconsistent from device to device. It had also been thought that the low frequency (1/f) noise performance of the device is driven by the thermal environment of the IRLED. In addition, all previous

79

prototyping work conducted at Birmingham and by our collaborator, Lockerbie [63], was conduced using metallic (aluminium) sleeves with a significantly higher thermal conductivity. Thus, there were concerns that the final BOSEM design may not have provided the optimal thermal environment for the IRLED. For this reason it was necessary to demonstrate BOSEM performance for a range of different IRLED thermal regimes. Figure 3.31 presents the BOSEM sensitivity obtained for the cases of, the standard ceramic sleeve, an alumina sleeve, and finally alumina with high thermal conductivity paste present between the sleeve and IRLED interface. No change in BOSEM sensitivity is observed, in the frequency band 1 Hz to 10 Hz, for these three conditions, thus the IRLED thermal anchorage was ruled out as a source of the excess noise.
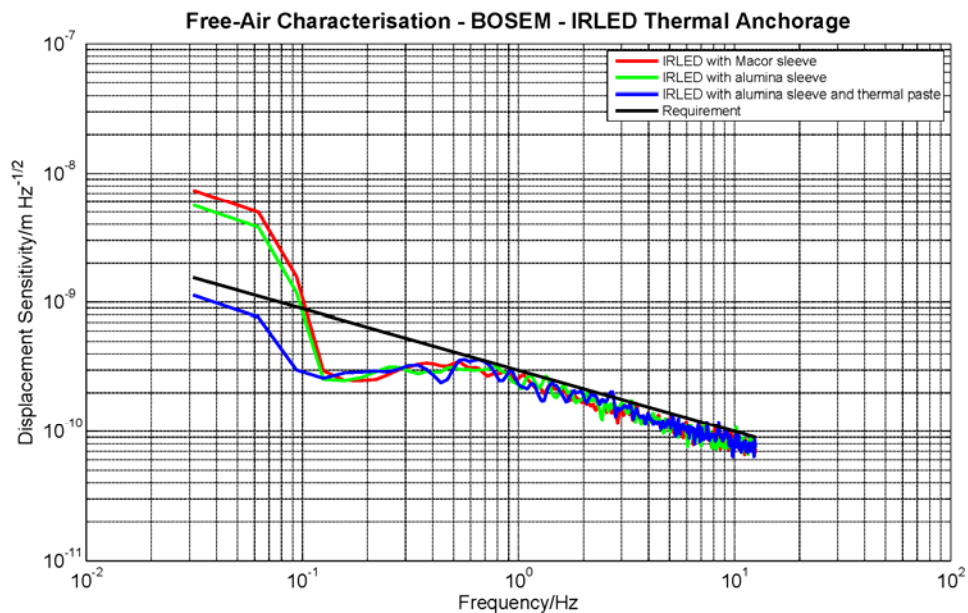
Figure 3.31: *IRLED thermal anchorage impact upon BOSEM performance.*

3.7.5 Sensor Open-Light Fixture

In light of all the previous results, it had become evident that the source of the excess noise was intrinsic to the IRLED. It was, therefore, necessary to comprehensively study the device to device characteristics of a sample batch of IRLEDs, aiming to find correlations between parameters measured and the final noise performance of the BOSEM sensor. To expedite the testing process a simple stand-alone open-light screening

fixture was constructed, which could be used to mount the IRLED and photodiode, as shown in Figure 3.32. The sensor components are held within PTFE inserts and can be translated along, and rotated about, the emission axis of the IRLED. Concentricity of the IRLED and photodiode is maintained throughout. Note that, the same photodiode is used throughout the duration of the open-light fixture tests and a nominal operating drive current of 35 mA is supplied to the IRLED.
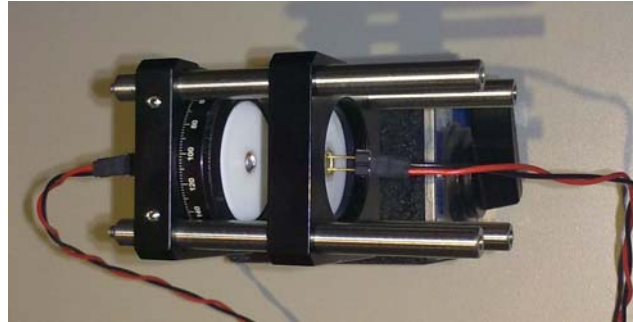
Figure 3.32: *Sensor open-light fixture.*

3.7.6 IRLED Axial Orientation

The axial orientation of the IRLED and photodiode are constrained when the devices are installed into the BOSEM. This is necessary to ensure the correct lead polarity, when connecting to the flexible circuit. The orientation is maintained by means of a pin-hole locater, which when a pin is inserted, locks them in place during the assembly process, as depicted for the IRLED in Figure 3.13 and for the photodiode in Figure 3.14. It was conceivable that there could be minor misalignments (<5°) in the final orientation of the device. It was worth ensuring that the excess noise is not sensitive to the rotation of the IRLED about its emission axis. Results taken using the open-light fixture, shown in Figure 3.33, demonstrate conclusively that photo-current noise emissions from the IRLED are axially symmetric i.e. there is no dependence on the final orientation of the device.
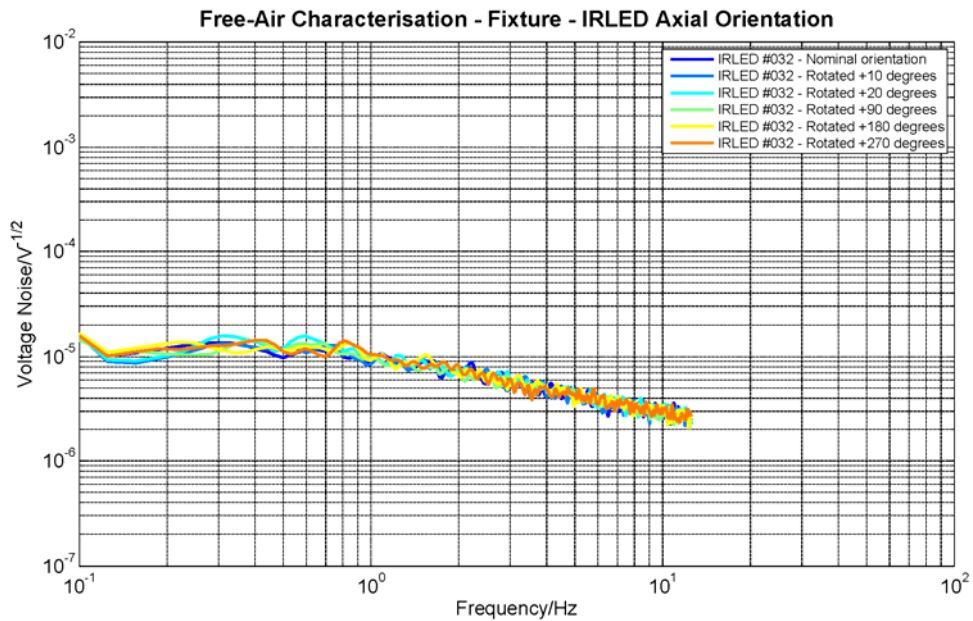
Figure 3.33: *IRLED axial orientation impact upon photo-current noise.*

3.7.7 IRLED Device to Device Screening

A large quantity of commercial off the shelf (COTS) IRLED devices was procured and the open-light fixture, shown in Figure 3.32, employed in screening their photo-current noise. Figure 3.34 shows the spread in noise performance for the COTS batch of IRLEDs. This provides conclusive proof of the variation in photo-current noise from device to device. It should be noted that these devices all originated from the same manufacturing batch. In addition, there were a couple of interesting candidates in the COTS batch worth highlighting. A couple of the very first devices tested, IRLEDs #011 and #013, were observed to exhibit significantly lower photo-current noise when compared with the rest of the batch. The black line has been taken for an IRLED that just meets the required sensitivity; it is, therefore, representative of the requirement.
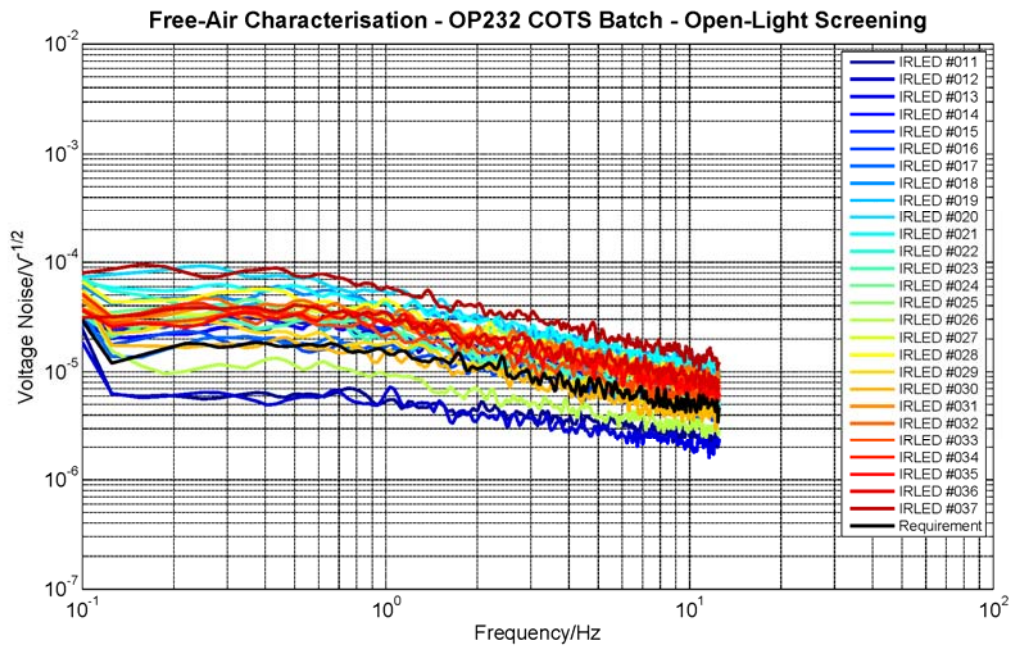
Figure 3.34: *IRLED COTS batch open-light screening of photo-current noise.*

3.7.8 Verification of IRLED Noise Performance

It was necessary to verify that the noise performance demonstrated by the IRLED mounted within the open-light fixture is consistent with the sensitivity obtained when it is installed into the BOSEM. Following the IRLED screening process, IRLEDs were identified from both extremes of the photo-current noise plots. IRLED #013, whose open-light photo-current noise appears to meet the requirement, with a significant margin, is installed into a BOSEM for characterisation. Also, a device which exhibited the highest photo-current noise, IRLED #037, was installed into another BOSEM and characterised. Figure 3.35 shows the sensitivity measurements obtained with the IRLED with the highest photo-current noise shown in blue and the lowest photo-current noise shown in red. Note that, the responsivity of this BOSEM increased by approximately 30 % for the lowest noise case, indicating that this IRLED is particularly efficient. Such devices would have most likely been filtered out of our production batch due to the IRLED intensity screening process rejecting extreme cases. This plot demonstrates dramatically the contrast in performance due to the intrinsic low frequency noise of the IRLED. A variation in the output intensity of the IRLEDs of up to 50 %, had been anticipated, and was observed. However, the output intensity variation is overwhelmed by the intrinsic

excess photo-current noise within the IRLED, which can account for up to almost an order of magnitude difference between best and worse devices at low frequencies. Also included within this plot are the measured electronics noise, in green and shot-noise in the dashed red line. The IRLED exhibiting the least photo-current noise can be seen to be shot-noise limited from around 5 Hz and above.
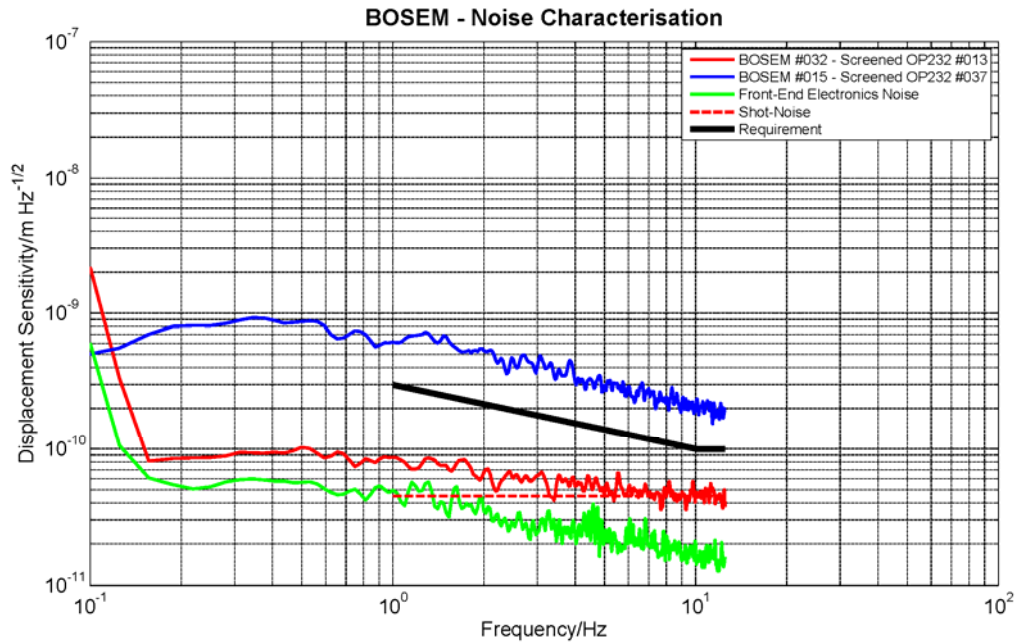
Figure 3.35: *BOSEM noise budget and verification of IRLED screening at both sensitivity extremes.*

Interestingly, the very best sensitivity measurements obtained appear to concur with a previous measurement taken by our collaborator, Lockerbie, at the University of Strathclyde [71]. However, it should be noted that, a surface mount photodiode and a slightly different optical configuration were employed in the Strathclyde set-up. Until now, it had not been possible to reproduce this level of performance at Birmingham. After characterising the whole batch of eighty IRLEDs it can be observed that about 10 % of them would just meet the sensitivity requirement and roughly 2.5 % very low noise devices would do so with ample margin to spare. These results suggest IRLED photo-current noise screening is a viable way forward.

3.7.9 IRLED Burn-In Performance

The only other remaining difference between the bench-top prototype BOSEMs and the production units is the additional burn-in procedure carried out upon all of the IRLEDs, as discussed in Section 3.5. Therefore, the aim of the burn-in performance tests was to establish if the burn-in process has contributed to the excess noise observed in the production BOSEMs.

For these burn-in tests, four COTS IRLEDs were selected; two that exhibited the lowest photo-current noise, #011 and #013, and two others that exhibited the highest photo-current noise, #020 and #037. Open-light measurements were made of the photo-current noise for a range of different burn-in conditions. Initially the units were measured at time zero (i.e. after no burn-in at all) and then following 25 hours and 94 hours duration. The burn-in was carried out at the maximum forward current rating of the IRLED of 100 mA, and forced air cooling was used throughout. A final measurement was made after leaving the devices burning-in for a further 24 hours, but with the forced air cooling turned off. With this final condition, the worst-case conceivable burn-in conditions and thermal stress environment for the devices can be simulated.
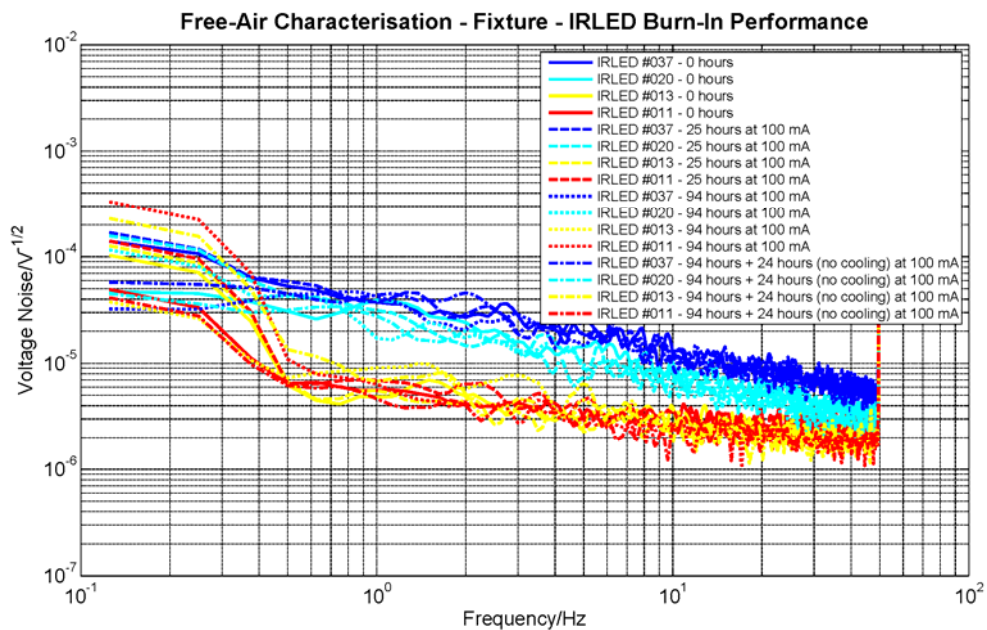
Figure 3.36: *IRLED burn-in performance.*

Figure 3.36 shows the photo-current noise measurements obtained at each stage of the burn-in testing. It can be seen that photo-current noise for each device is not adversely affected by the burn-in process. Each IRLED device maintains a consistent level of noise performance both before and after burn-in. Even under the worst-case scenario, the IRLED devices still maintain a similar photo-current noise performance as achieved prior to the start of the burn-in process.

3.7.10 IRLED Dissection

The measurements that have been taken demonstrate that the excess noise is intrinsic to the IRLED. However, the mechanism which is responsible has yet to be identified.

The IRLED packages contain an integral lens and a wide range of focal lengths were observed in the devices characterised. This suggests some margin in the manufacturer's placement of this internal lens or in the lens geometry itself. It is conceivable that this lens may not have an anti-reflection coating on internal surfaces and as a consequence there could be back-reflections de-stabilising the device. To establish if the integral lens contributed to the excess noise, an IRLED was selected that had exhibited a large amount of excess noise. A baseline open-light photo-current noise measurement was made. The device package was then carefully sliced in two, thus removing the integral lens, and the noise measurement was repeated. Figure 3.37 shows the results for these two configurations of the device, and it can be seen that there is no difference in the noise behaviour; hence there is no dependence on the location or even the existence of the integral lens. This shows conclusively that the source of the excess noise is fundamental in nature and resides within the silicon chip/active area of the IRLED.
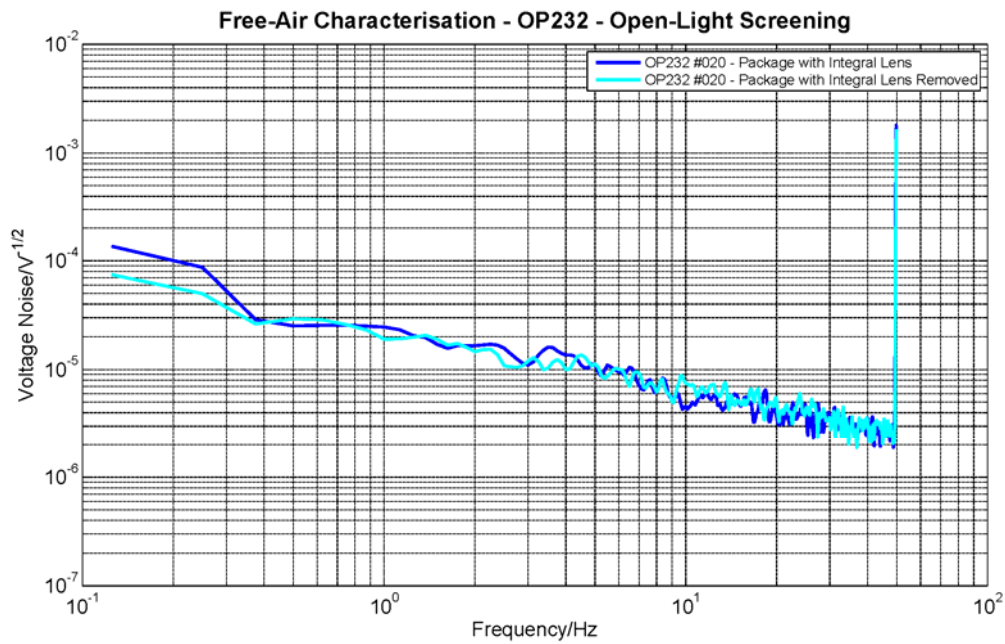
Figure 3.37: *IRLED photo-current noise; package with lens versus package with lens removed.*

A number of samples were scrapped perfecting a technique for slicing the device package in two. During these operations a visual inspection highlighted a significant difference in the appearance of the active area from device to device. A few of these units were observed in more detail under a digital microscope. Figure 3.38 (left) shows an image of a scrap IRLED (OP232) device with a generous amount of epoxy covering the chip and bridging the cathode to the case. Figure 3.38 (right) shows OP232 #020 which exhibited high photo-current noise.
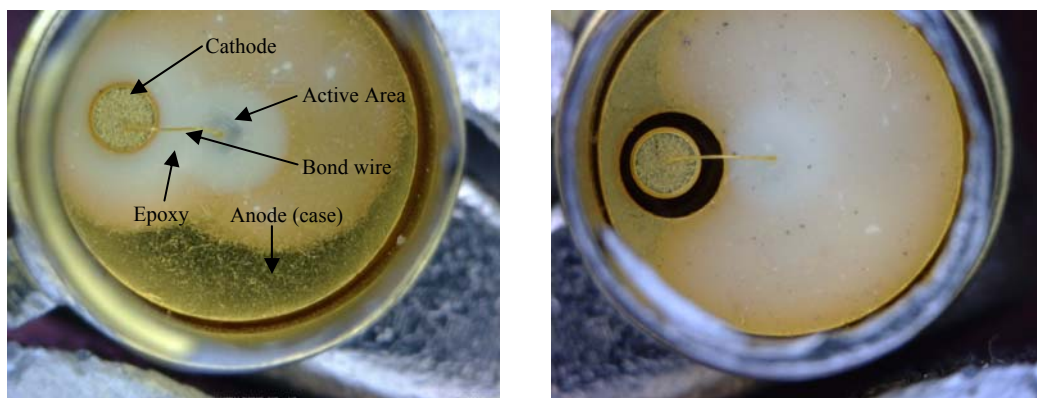
Figure 3.38: *Dissections through IRLED packages.*
(Left) Scrap OP232. (Right) OP232 #020 High photo-current noise.

For comparison, a very low noise IRLED was also dissected. Figure 3.39 (left) shows the distribution of epoxy for a device that exhibited low photo-current noise. The amount and distribution of epoxy visible is quite different to the high noise case. Also, there is an apparent difference in the thickness/transparency of the epoxy layer for each device. This provides some indication that there may be a relationship between the distribution of the epoxy and the photo-current noise of the device. It was assumed that the process of delivering the epoxy would have formed part of a controlled manufacturing operation, and so these variations in the distribution of epoxy were unexpected.
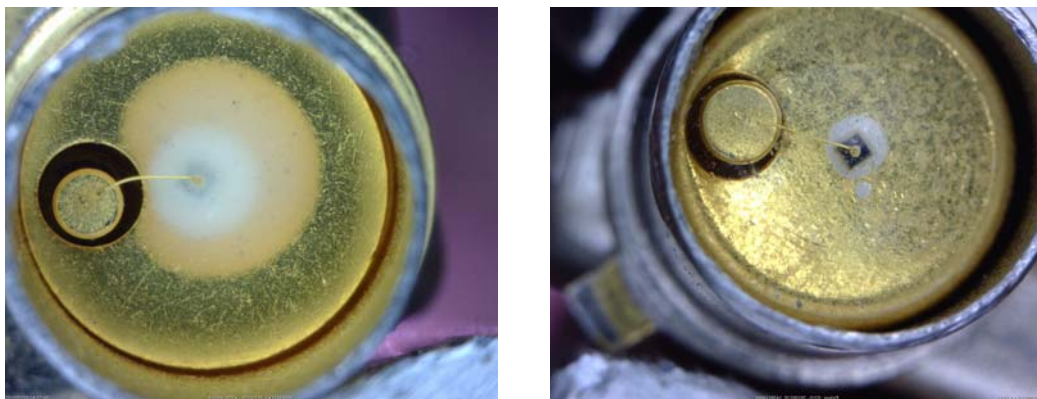
Figure 3.39: *Further dissections through IRLED packages.*
(Left) OP232 #013 Very low photo-current noise. (Right) Vishay TSTS7100.

3.7.11 Alternative IRLED

The OP232s were originally proposed as the culmination of the sensor study (see Section 3.3.2). At the time (2004) these were found to be the best devices available. However, more recent state-of-the-art devices are now available from alternative manufacturers.

The Vishay TSTS7100 was identified as a comparable device to the OP232. The opto-mechanical properties are essentially identical. However, the electrical properties differ slightly, for example the pin-outs are reversed and the TSTS7100 has a much larger forward current handling capability than the OP232 (250 mA and 100 mA respectively). Figure 3.39 (right) shows the dissection through the TSTS7100 device. Again the distribution of epoxy is quite different to what has been seen for its OP232 counterpart. This quick visual inspection indicated that the process of applying the epoxy is possibly a more controlled for this part. Unfortunately, these characteristics of the epoxy can only be

observed under destructive testing, which there would be little benefit in pursuing in terms of finding a viable solution for the BOSEM excess noise issue.

A quantity of approximately 2000 of the alternative IRLEDs were procured and it was noted that they came from different production batches. The open-light photo-current noise was measured for a random sample of devices from each of these batches. Figure 3.40 illustrates the distribution of open-light photo-current noise measurements for the batch denoted 909 (i.e. production date, week 9 of 2009).
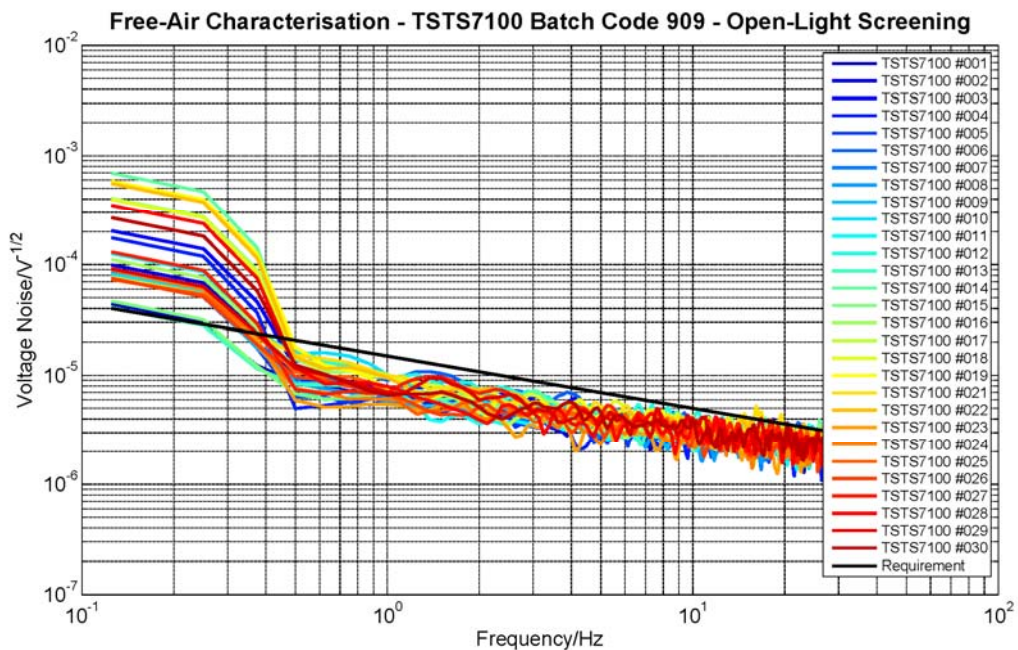
Figure 3.40: *Alternative IRLED batch 909 open-light photo-current noise.*

Figure 3.41 illustrates the distribution of open-light photo-current noise measurements for the batch denoted 940 (i.e. production date, week 40 of 2009).
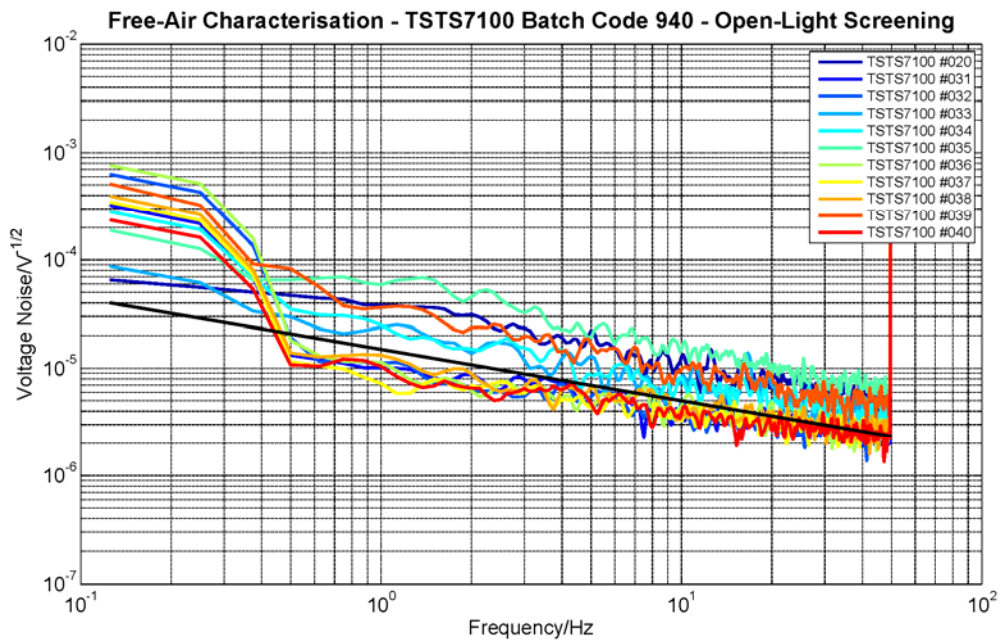
Figure 3.41: *Alternative IRLED batch 940 open-light photo-current noise.*

Finally, Figure 3.42 illustrates the distribution of open-light photo-current noise measurements for the batch denoted 001 (i.e. production date, week 1 of 2010).
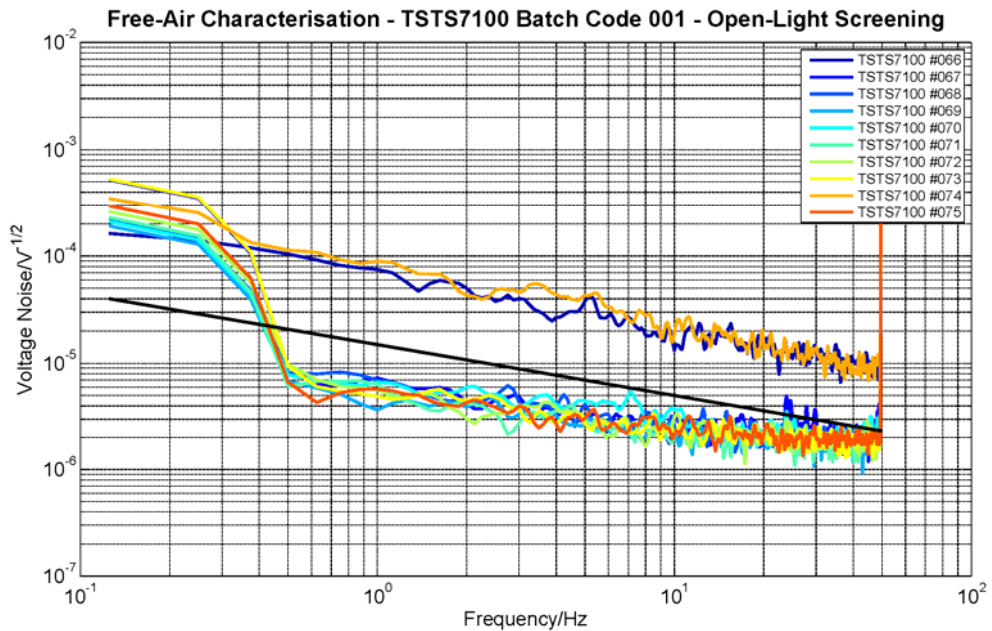
Figure 3.42: *Alternative IRLED batch 001 open-light photo-current noise.*

It can be seen from Figure 3.40, Figure 3.41 and Figure 3.42 that there was a variation in the IRLED noise performance from batch to batch. Batch 909 exhibited 100 % pass rate, batch 940 exhibited 50 % pass rate and finally batch 001 exhibited 80 % pass rate. This suggested that any additional units procured, were most likely to come from a recently produced, i.e. lower-yield, batch. A 100 % pass rate could no longer be assumed; therefore, additional photo-current noise screening would be required. However, the alternative IRLED still offered a substantial improvement over the original IRLED, by having a significantly higher yield.

Due to device to device variations in photo-current noise for the original IRLEDs, only 10 % were found that met the noise requirement. Screening approximately 700 assembled BOSEMs to identify which units met the requirement and which do not, would not be viable on the timeframe of the Advanced LIGO UK project. Because of the low yield of the original IRLEDs, approximately 7000 would be needed to proceed with screening and retro-fitting into assembled BOSEMs. This scenario also assumes that the 10 % yield is sustainable for future batches of IRLEDs, for which there is insufficient evidence to support this.

Fortuitously during the course of these excess noise investigations a viable alternative candidate to the original IRLED was identified. Some batch to batch variation in pass rates still persists, ranging from 100 %, down to 50 % in the worst case. It was proposed to our US collaborators that the alternative IRLEDs were screened for photo-current noise (procedure available in Appendix D) and the successful candidates retro-fitted into BOSEMs. The proposal was found acceptable; however, there were still a number of barriers to overcome before implementing this proposal. For example, approval to use these new parts in the Advanced LIGO UHV environment was sought, and after a couple of months it was obtained. Also, mean time to failure (MTTF) data was provided by the manufacture to the Advanced LIGO project management, which raised no concerns.

Given that all the obstacles for switching to the alternative IRLED had been overcome, a trial-run was attempted, i.e. screening and installing the devices into approximately fifty BOSEMs. A sufficient quantity of IRLEDs were screened for photo-current noise, burned-in, cleaned and baked, using identical procedures outlined as for the

original IRLEDs [72]. The alternative IRLEDs would then be retro-fitted into the BOSEMs, before being tested by the ATE. This provides functional measurements such as the photodiode current and transfer ratio. However, for this first batch of BOSEMs it was requested that each unit be fully characterised, i.e. the responsivity and noise being measured for each of the fifty units.
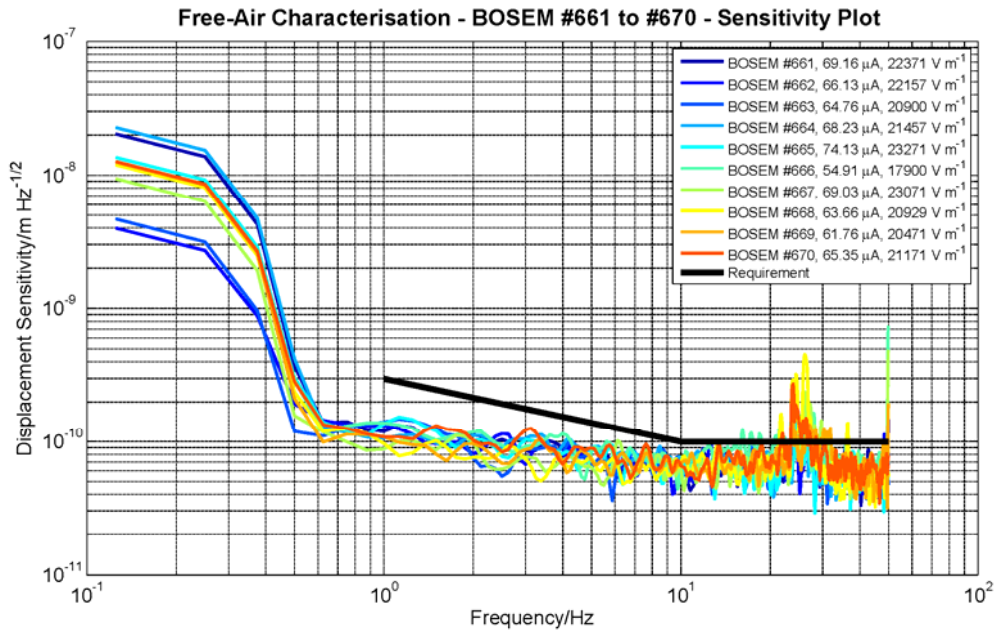
Figure 3.43: *BOSEM typical sensitivity results.*

Figure 3.43 shows typical sensitivity results for a sample quantity of units. The black line represents the exact performance requirement. All fifty of the BOSEMs have been observed to meet the sensitivity requirement. In some cases external environmental noise can be seen to be coupling-in within the band 10 Hz to 50 Hz. This is related to air-conditioning fans, mains peaks and harmonics thereof.

The trial-run was deemed a success, with a 100 % pass rate. It was therefore rolled out to the entire production batch of BOSEMs. A sufficient quantity of the alternative IRLEDs were screened, burned-in, cleaned and baked, before being retro-fitted into already assembled production BOSEMs. Of the approximately 700 units that were delivered to the Advanced LIGO observatories in March 2011, over 100 randomly sampled finished BOSEMs had been successfully characterised, with the 100 % pass rate being maintained.

Chapter 4

Development of the Interferometric Sensor

"Things which equal the same thing also equal one another". Euclid.

4.1 Introduction to EUCLID

One of the principle drivers, contributing to the development of an interferometric sensor, was the more stringent sensitivity and range requirements (see Table 3.1) placed upon the BOSEM sensor at the early stages of the Advanced LIGO UK project. It soon became evident, that the simple shadow sensing technique could not readily achieve the sensitivities or operating range required. This, therefore, encouraged the consideration of other optical sensor schemes. One possible alternative technique is to employ an optical lever. Such a scheme, for example, is currently under development for the optical read-out system for the LISA gravitational reference sensor [73]. However, even with this technique it would not be trivial to meet the stringent Advanced LIGO requirements. In addition, integrating an optical lever sensor into the volume available for the BOSEM could prove challenging.

The most obvious alternative would be to adopt an interferometric approach to sensing. It has been discussed in Section 1.4.3 how long arm-length Michelson interferometers are being employed in the search for gravitational waves. Interferometers are ideally suited for measuring small changes in arm-length difference. However, for this application a much smaller scale instrument would be desired, whereby everything (for example, laser source, collimation, optics, etc) are all integrated into a single compact enclosure. Conventionally, whilst offering good performance, interferometers have usually been considered too expensive, too cumbersome, unreliable as well as requiring significant skills and expertise to assemble, align and maintain. For the intended application it is clear that these obstacles must be overcome. This has led to the design of the Easy to Use Compact Laser Interferometric Device (EUCLID).

Throughout the duration of this research, there have been a number of iterations of the design of the interferometric sensor. These were made as part of a continuous effort to evolve the design as well as our understanding. This chapter details the development of

the prototype and the first production batch of EUCLID units. Finally, results are presented for the characterisation of each.

4.2 Requirements

The interferometric sensor is expected to at least achieve the same stringent sensitivity and operating range requirements originally outlined for the BOSEM in Table 3.1. In addition, all other requirements applicable to the BOSEM would also need to be met by EUCLID. For example, the interferometric sensor must also conform to similar envelope, material restrictions and have the potential to be qualified for use in the Advanced LIGO UHV environment.

It is also important to keep an open mind, given that there may be many other opportunities and applications for EUCLID. For example, as a geophone sensor, in length metrology, monitoring nano-position stages for the atomic force microscopy industry, or other industrial processes such as semiconductor lithography. Therefore, it is intended that the interferometric sensor aims to reach sensitivities beyond what is required by the existing applications and also aims to extend this performance down toward even lower frequencies, thus making EUCLID relevant and desirable, for both present and future generations of gravitational wave observatories.

4.3 Prototype Interferometric Sensor Design

Significant progress has been made in the field of metrology and in the development of accurate and robust interferometric sensors. Recent research has focused on the Michelson interferometer, as discussed in Section 1.4.3 and has employed either heterodyne or homodyne techniques as a means of determining displacements.

In an attempt to minimise sources of low frequency instability, the homodyne method has been adopted, due to its simple design and lack of moving or active (modulating) elements. Interferometer outputs in quadrature enable the displacements to be determined, with a resolution of much less than one fringe but over operating ranges of many millimetres.

4.3.1 Laser Source Selection

An investigation was undertaken to identify the optimal laser source for the compact interferometric sensor. Bench-top prototype interferometers had previously been set-up using conventional helium-neon (He-Ne) visible lasers, operating at 633 nm. He-Ne lasers are convenient to work with in a laboratory environment, stable and provide a well collimated output. But the typical dimensions of these lasers ($\approx$ 20 cm) already exceed the envelope requirements for the Advanced LIGO sensor, even for the relatively low power He-Ne lasers ($\approx$ 1 mW).

An alternative to the traditional He-Ne laser are semiconductor lasers, which due to their compact size (typically $\varnothing$5.6 mm packages), high efficiency and simple structure, have been used extensively in the optical telecommunications field. As a consequence, semiconductor lasers are a well established, mature technology and are available in a range of wavelengths covering the visible and IR end of the spectrum. Semiconductor lasers can simply be considered as a forward biased p-n junction in a resonant cavity which can be formed by cleaving the end face (or facet) of the structure, as demonstrated in Figure 4.1 (right). The presence of the p-n junction ensures that semiconductor lasers behave in a similar way to how a normal diode operates. However, the major difference between a normal diode and a laser-diode is that light is able to exit this junction region. Transitions occur between conduction and valance bands, and stimulated emission takes place within the immediate vicinity of the p-n junction. Thus, as current flows under forward bias condition, electrons from the n-type conduction band will recombine with the p-type holes, resulting in the emission of energy in the form of photons. This radiative process competes with other absorption processes within the diode, but dominates when the current flow becomes large enough and the recombination layer is small (the lasing threshold). To ensure that the diode begins to lase, the cleaved surfaces are polished to form a resonant cavity. Given that the emission occurs from the edge of the device, these are also commonly known as edge emitting lasers (EEL).
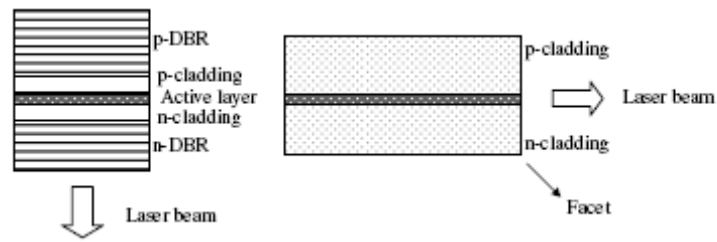
Figure 4.1: *Different semiconductor laser structures. Source [74].*
(Left) VCSEL diode. (Right) Laser-diode.

A further development of semiconductor lasers are the vertical cavity surface emitting laser (VCSEL) diodes, as shown in Figure 4.1 (left). VCSELs differ from EELs in their construction. Typically VCSELs are manufactured by stacking layers of alternative materials of varying refractive indices to form a distributed Bragg reflector (DBR), which can provide a highly reflective cavity. In contrast to EELs, VCSEL diodes have their laser emission perpendicular from the top surface. Due to the VCSEL output aperture being larger, they consequently suffer less divergence of the output beam, when compared to their EEL counter-parts. This can be of great benefit for telecommunications applications as it enables substantially higher coupling efficiency into optical fibres. For an interferometric based sensor application, the diverging, asymmetric, output beam of the EEL diode makes it more difficult and expensive to collimate. Conversely, the narrow, circular, beam of the VCSEL can be easily and cheaply collimated with, for example, an aspheric lens. However, the more desirable output beam properties are only a small fraction of the potential advantages offered by the VCSEL.

The most significant benefit of the VCSEL is that it operates in a single longitudinal mode. A laser can simply be considered as comprising of a gain medium located within an optical cavity as depicted in Figure 4.2 (left), with some method of pumping or injecting energy. Light of a specific wavelength that propagates through the gain medium is repeatedly amplified. Thus, a longitudinal mode of a resonant cavity is a particular standing wave pattern formed by waves confined in the cavity. These modes correspond to the wavelengths of the wave which are reinforced by constructive interference after many reflections within the cavity. Hence, other wavelengths are suppressed by destructive interference. Figure 4.2 (right) illustrates the gain curve, and the longitudinal modes versus frequency, for both VCSEL and EEL diodes. The gain curve serves to amplify only specific range of these longitudinal modes. It can be seen

that for the EEL diode there are many closely spaced modes, which can be amplified and emitted by the laser. For a VCSEL, the homogenous gain medium promotes mode competition in the widely space modes, which can result in only a single mode being amplified, making them desirable for interferometric applications. The competing multi-modes of the EEL laser render them unsuitable for interferometric applications. Note that, it is important to distinguish between the line-width of the laser, and the line-width of a specific longitudinal mode. Although mono-mode EEL lasers are available (with suppression of secondary modes) the single-mode can mode-hop between competing longitudinal modes over time. This phenomenon is characteristic of this type of laser and can be provoked by external factors, such as a temperature change in the environment. The temperature change can affect the gain maximum more than the cavity resonance, which can then result in the previously lasing mode, no longer being the mode with highest gain, and so the power of a competing mode with higher gain can quickly rise.
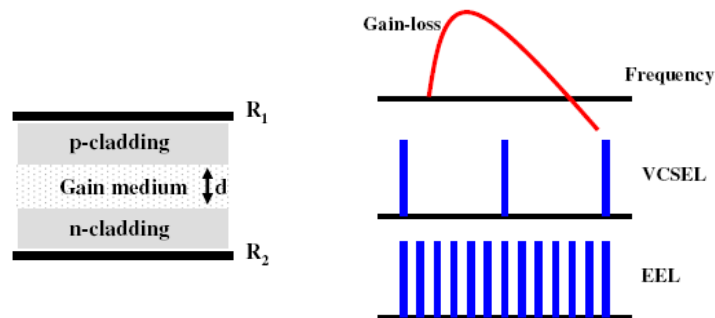
Figure 4.2: *Semiconductor gain structure. Source [74].*
(Left) Gain medium and cavity. (Right) Gain curve and mode separation.

For the prototype interferometric sensor a VCSEL diode, AVAP-850SM, was selected from Avalon Phototonics. This device is specified as being single-mode, with no polarisation flips, and having high reliability. These devices operate at $\approx$ 850 nm with a Gaussian beam profile and small divergence. An EXFO Wave-meter (model WA-1000-NIR-89) was used to characterise the device in-house, verifying the threshold current and emission wavelength.

4.3.2 Optical Configuration

The heterodyne method of measuring displacements [75] can involve mechanical actuation (modulation) of a target mirror, which produces a phase shift in the light in the measurement arm relative to that in the reference arm of the interferometer. Alternatively, acousto-optic modulators (AOMs) or electro-optic modulators (EOMs) can be used to implement the frequency offset between the two beams. However, the homodyne method adopted for the interferometric sensor employs no such modulation. Instead, two different polarisation states or intensity variations due to interference can be used to enable the displacement to be determined.

A polarisation-based interferometer was originally proposed by Raine and Downs, in 1978 [76]. This device employed three interferometric outputs, where output, I_n, varied sinusoidally with the target mirror displacement, but with phase offsets of zero, $\pi / 2$ and π,

$$I_n = I_{out}\left(1 + V\cos\left(\phi + (n-1)\frac{\pi}{2}\right)\right),\qquad(4.1)$$

where $n = 1,2,3\ldots$, V is the fringe visibility

$$V = \left(I_{max} - I_{min}\right)/\left(I_{max} + I_{min}\right),\qquad(4.2)$$

and

$$\phi = \frac{2\pi}{\lambda}\Delta l\,,\qquad(4.3)$$

Δl is the difference in optical path length and λ is the wavelength of the light employed. It can be shown that ϕ is determined using

$$\phi = \arctan\left(\frac{I_1 - I_2}{I_2 - I_3}\right) - \frac{\pi}{4}\,.\qquad(4.4)$$

Finally, the displacement can now be calculated using

$$\Delta z = \frac{\phi}{2\pi} \cdot \frac{\lambda}{2} .$$ (4.5)

Note that, this result is consistent for a standard Michelson, where the mirror motion is usually given as

$$\Delta z \approx \frac{\Delta l}{2} .$$ (4.6)

A further modification was made to the technique by Downs and Raine [77], by using only two outputs that were polarisation independent. The phase shift between the outputs is generated by a purpose built metallised beam-splitter which was optimised for operation at a specific wavelength (nominally 633 nm). This system had the obvious advantage that it required fewer optical components and also has an output that is independent of the polarisation state of the source.

Figure 4.3 shows the optical layout of the prototype interferometric sensor. A polarisation-based design has been adopted, which has been developed from Greco *et al* [78]. A VCSEL diode source emits radiation collimated by L1, which is horizontally polarised and attenuated by a combination of the polariser, P1, and polarising beam-splitter, A1. I_{in} can, therefore, be considered as the optical intensity entering the interferometer. Note that this combination of polariser and polarising beam-splitter is incorporated simply in an attempt to reduce optical feedback into the VCSEL and is not as effective as a Faraday isolator. Unfortunately, Faraday isolators are generally quite cumbersome and are not particularly well suited to this application. Optical feedback can cause undesired instability in the laser; therefore, further precautions also need to be taken to mitigate it, such as using suitable anti-reflection coatings on optical surfaces and slightly tilting the optical components to ensure optical surfaces are not parallel.
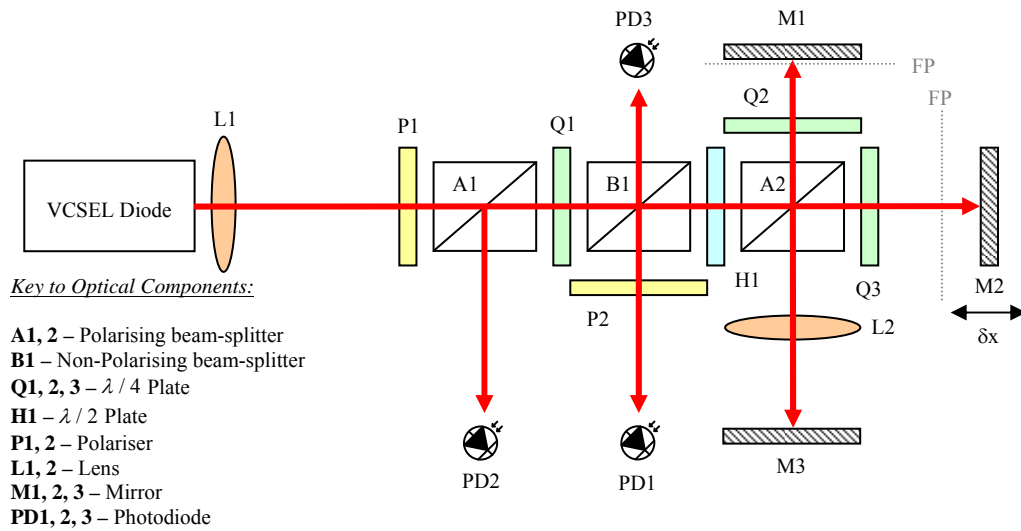
Figure 4.3: *Prototype interferometric sensor optical layout.*

Following A1, the beam passes through a quarter-wave plate, Q1, and a non-polarising beam-splitter, B1, where the input intensity, $I_{in}/2$, is sampled by photodiode PD3. The optical axis of the half-wave plate H1 is inclined at 22.5° and rotates the plane of polarisation by 45°. The input quarter-wave and half-wave plates have the primary function of conditioning the light that exits the beam-splitter, A2. Approximately equal intensities of two orthogonal polarisations (in-plane and perpendicular to the plane) pass through the polarising beam-splitter, A2, and on into the measurement and reference arms of the interferometer. The quarter-wave plates, Q2 and Q3, force the beams in each arm to be reflected from the cat's eye (M3 and L2 combination) before exiting through the same face of the polarising beam-splitter, A2, which they entered, after two reflections from their respective mirrors. On exiting the beam-splitter the two polarisation components are rotated back by 45° by the half-wave plate, H1, and again pass through a non-polarising beam-splitter, B1. A polariser, P2, selects the vertical polarisation component from the reflected beam and interference fringes, I_1, are measured on photodiode PD1. The un-reflected beam passes back through the quarter-wave plate, Q1, and the vertically polarised light forms a second interference pattern, I_2, on PD2 after being reflected by the beam-splitter at A1. The quarter-wave plate, Q1, introduces a phase shift of $\pi/2$ between the fringe patterns measured by PD1 and PD2 which can be interrogated to track the distance through which that the measurement mirror has moved.

The aforementioned cat's eye retro-reflector is one of the key novel features of the interferometer design. Inherently, the interferometer is insensitive to lateral movement

of the target mirror, M2. However, a tilt of this mirror will compromise the visibility of the interference fringes, which can result in making the alignment of target mirror challenging. In such cases, cube-corner retro-reflectors could be employed. Rather than bringing the incident beams to a focus, as takes place in the cat's eye, the cube-corner reflects the incident beam off their three mutually perpendicular intersecting flat surfaces. In cube-corners, therefore, the beam is reflected back directly towards the source, but with the disadvantage that it has also been translated. Another significant disadvantage of using cube-corners in polarisation based interferometers is that each reflection changes the polarisation state of the light. The cat's eye realised in the interferometer configuration, uses a combination of a plane mirror, M3, and lens, L2. The focal plane of L2 falls at the sweet-plane, or sweet-spot, which is where the largest immunity against tilt of the target mirror can be obtained. The design and optimisation of the cat's eye, to achieve the best tilt immunity, is discussed elsewhere [79]. This work also models the effects of aberrations which can conspire to limit the cat's eye performance.

4.3.3 Fringe Interpolation Method

In the ideal case two outputs, PD1 and PD2, when plotted against each other (on an oscilloscope in *x-y* mode) describe a circular Lissajous figure. In the case where only two outputs are available and when *V* is unity, the centre of the Lissajous figure lies at the radius of the pattern in both *x* and *y* directions. Displacement of λ/4 of the target mirror produces a complete revolution of the Lissajous figure. In order to track the displacement over completed revolutions software must perform Equation 4.4 with at least two measurements per revolution, and sum the number of integer rotations. For the standard Michelson configuration, a sampling frequency of f_s gives a maximum mirror speed of

$$\dot{z}_{max} = \frac{\lambda}{4} f_s \, .$$
(4.7)

The PD3 output can be used to subtract electronically a voltage proportional to the mean intensity and to centre the Lissajous figure. The displacement is calculated using the arctangent function in a way similar to that described in Equation 4.5, but with the modified optical layout, this has now become

$$\Delta z = \frac{\Delta \phi}{2\pi} \cdot \frac{\lambda}{4}. \tag{4.8}$$

Figure 4.4 provides a simulation of the voltages present at the photodiode quadrature outputs (PD1 and PD2). It should be noted that the dc offset has been removed from this Lissajous figure, i.e. it appears centred along each axis.
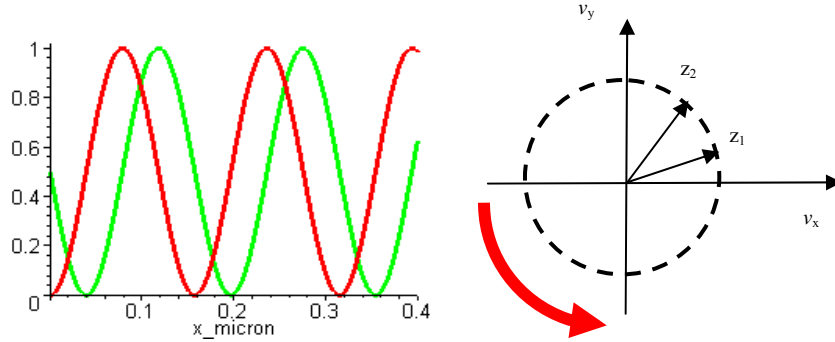
Figure 4.4: *Simulation of photodiode quadrature outputs and Lissajous figure.*

Based on Equation 4.4, $\Delta\phi$, can now be calculated using

$$\Delta\phi = \arctan\left(\frac{v_{y2}}{v_{x2}}\right) - \arctan\left(\frac{v_{y1}}{v_{x1}}\right). \tag{4.9}$$

A low noise electronics front-end provides amplification of the photodiode signals. The photocurrents from the three diodes are converted into voltages using AD743 trans-impedance amplifiers, while a three channel, 16-bit resolution analogue to digital converter acquires the samples at a rate of 33 kHz over a maximum input range of 10 V (peak-peak). The data is sent via USB to the PC, where it is decimated down to 50 Hz and stored in an ASCII data file for subsequent post-processing using a MATLAB analysis script. The decimation process first filters the 33 kHz data with a low-pass filter and then re-samples the resulting smoothed signal at the lower 50 Hz rate. The MATLAB script (available in Appendix I) reads in the data and outputs plots of the time history of the displacement measurement and the power spectral density. The time series data is de-trended and passed to the P. Welch [80] function (available in the MATLAB data processing toolbox). This algorithm is in use (with its default windowing options) as a

standardised convention for the LISA Pathfinder mission and is described in more detail elsewhere [81].

A significant disadvantage of homodyne and heterodyne interferometers in sensing applications is that the output at any instant is the sum of previous displacements and is, therefore, not absolute. If the system suffers a critical event and looses power for instance, the absolute position of the target being tracked would not be available upon re-initialisation. It is possible to overcome this problem by employing a back-up sensor, such as a shadow sensor or capacitive sensor for such eventualities. However, using both types of sensor would not be the optimal approach. The ideal method to overcome this drawback with the interferometric sensor is to use a frequency modulation scheme, which enables absolute interferometry (discussed later in Section 5.2.2).

Another concern with the fringe interpolation approach is that too rapid motion of the target being tracked could result in fringes being lost and, therefore, displacement measurement errors. The minimum sampling frequency required to track a test-mass speed of 1 mm s^{-1} is 12.6 kHz, from Equations 4.5 and 4.7, note that this results includes the double pass feature of the prototype interferometer design.

4.3.4 Prototype Realisation

Figure 4.5 illustrates a 3D CAD representation of the prototype interferometer design. Overall dimensions of the prototype interferometric sensor and VCSEL collimation assemblies are 87 mm × 40 mm × 25 mm.

The VCSEL is located in a detachable barrel, along with an aspheric collimating lens. The VCSEL can be translated with respect to this lens so that collimation of the beam can be achieved. The position of the lens is also translatable, to ensure the collimated beam emerges along the optical axis. 10 mm beam-splitters are bonded onto a titanium base-plate using UV activated adhesive, while wave-plates and polariser are bonded into titanium retaining rings. Once in position these wave-plates are free to rotate through 360° to provide in-situ adjustment. A top-plate assembly incorporates threads for ball-plunger screws to clamp the wave-plates and polarisers in place. The reference and retro-reflector arm mirrors are mounted against an o-ring, which allows for some tilt

adjustment (pitch and yaw) and a minimal amount of translation normal to the mirror surface.
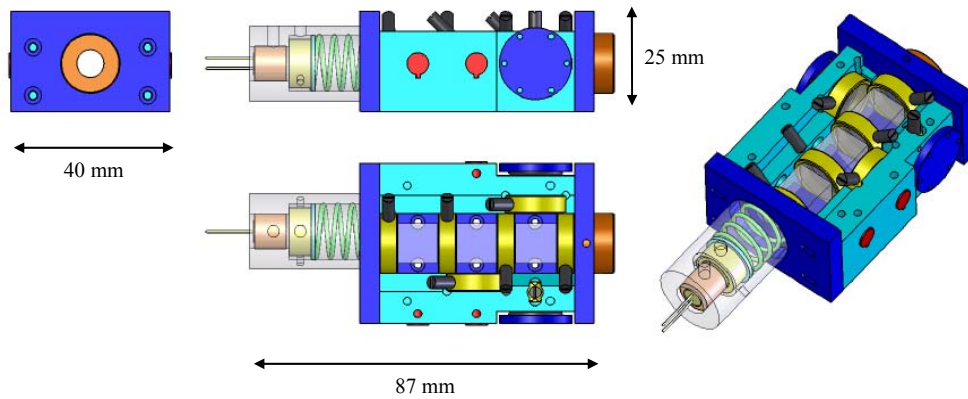
Figure 4.5: *3D CAD model of the prototype interferometric sensor.*

An image of the realised prototype interferometric sensor is shown Figure 4.6, scaled against a €1 coin. The unit has been fabricated from titanium and phosphor-bronze material. It incorporates adjustment for virtually all optical components, with exception of the beam-splitters. Initial alignment of the unit was carried out using a visible (633 nm) externally mounted He-Ne laser. This was then substituted for the collimated near infrared (850 nm) VCSEL assembly when the optical components were configured with interference fringes just visible at the outputs. Further minor adjustment of some optical components is then required to maximise the fringe amplitude for operation with the VCSEL. Once the alignment process is complete the top-plate assembly is fitted, which completely encloses all optical components and enables them to be locked in place, as can be seen on the fully assembled unit in Figure 4.7.
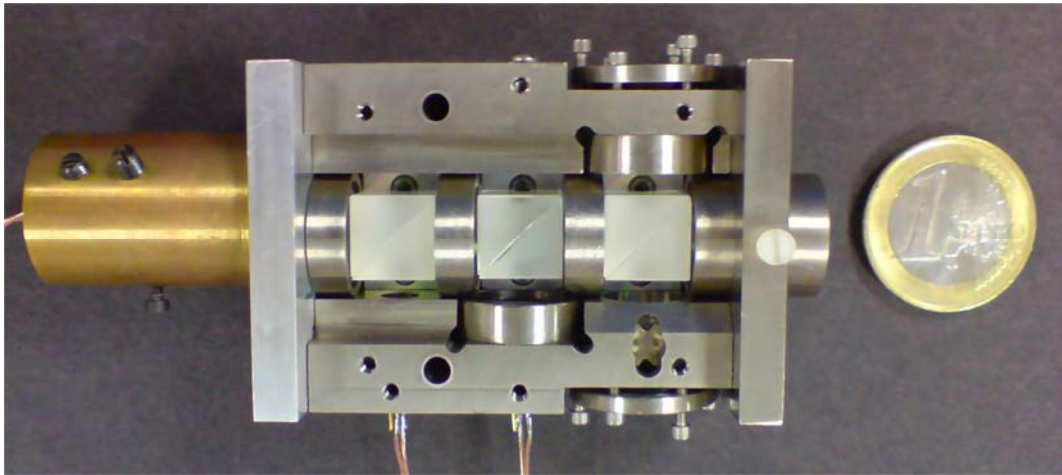
Figure 4.6: *Realisation of the prototype interferometric sensor.*
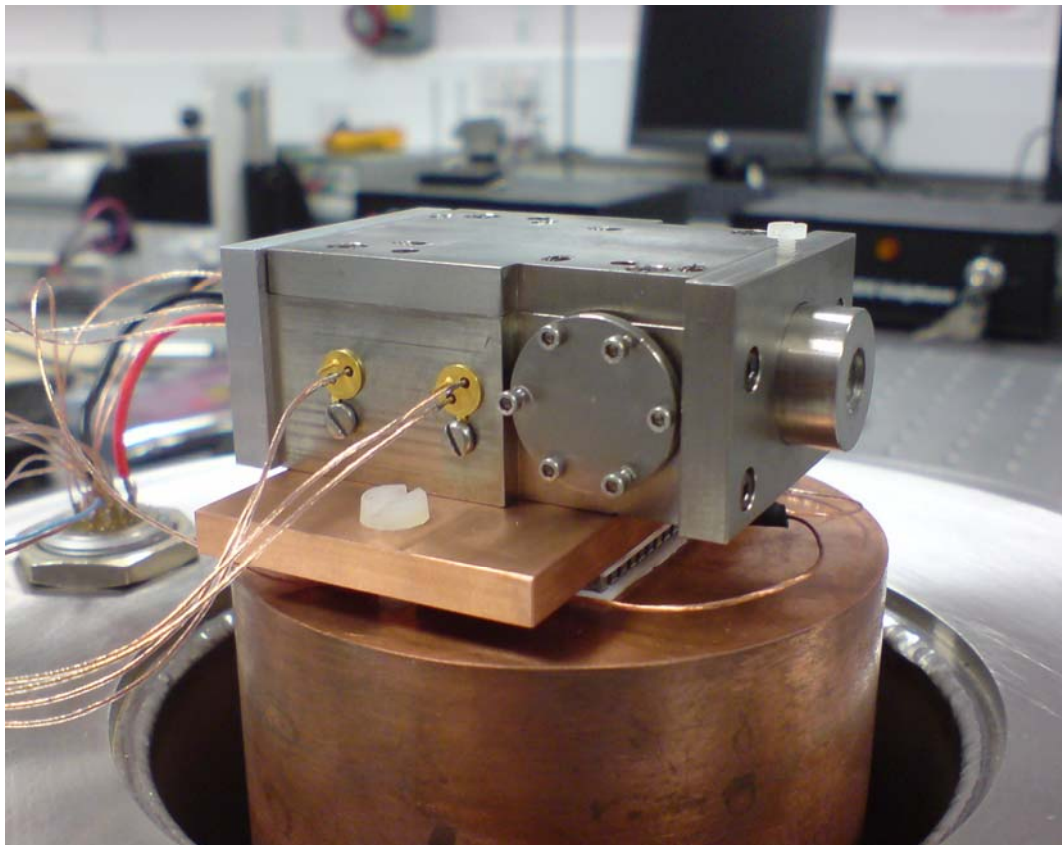
Figure 4.7: *Fully assembled prototype interferometric sensor mounted within vacuum vessel for characterisation measurements.*

4.3.5 Demonstrated Performance

Figure 4.8 shows a typical noise spectrum obtained from the prototype interferometric sensor. The resolution limit due to quantisation noise of the ADC can be estimated by assuming that variations at its input, due mainly to drift, produce a random Gaussian sampling. Given that is 16-bit resolution, 50 kHz sampling, with full scale voltages of $\pm$ 5 V, means that the minimum detectable voltage in a sampling time of 1 s is approximately 0.7 μV. This corresponds to a minimum displacement of about 2 x 10^{-13} m Hz$^{-1/2}$, which is observed at higher frequencies ($f > 10$ Hz). The shot-noise limit for 0.3 μW is about 5 x 10^{-14} m Hz$^{-1/2}$. In the mid-frequency range (10^{-2} Hz $< f < 10$ Hz) it is possible to observe what was initially thought to be the 1/f electronics noise in the operational amplifiers.
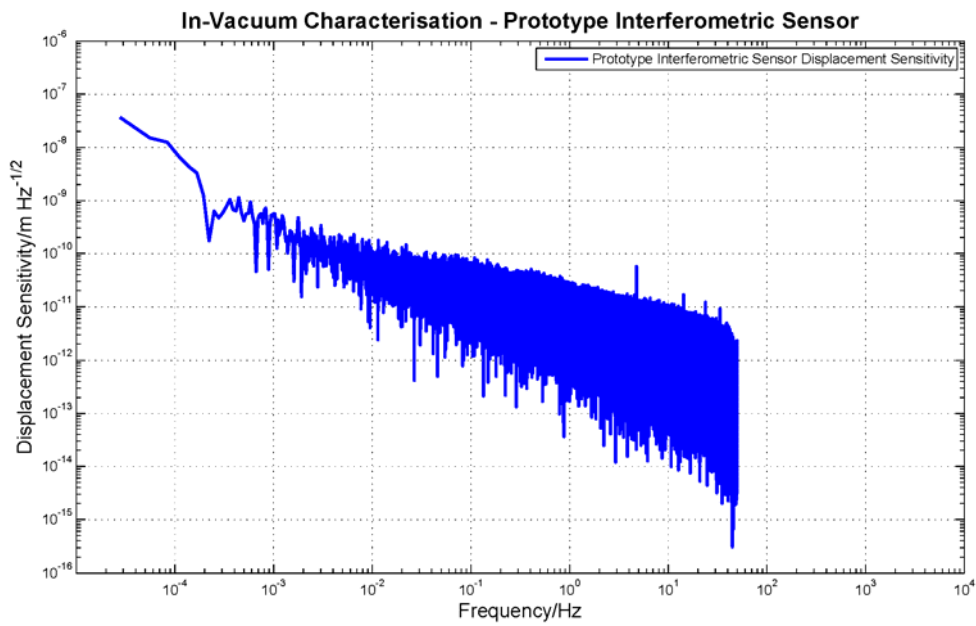
Figure 4.8: *Prototype interferometric sensor performance.*

4.4 EUCLID Interferometric Sensor Design

The prototype interferometric sensor successfully demonstrated that the concept of a compact, reliable, robust and cost effective sensor, with good sensitivity, was achievable. After presenting the prototype interferometric sensor results [95] and publicising this technology at trade shows and conferences, colleagues and international collaborators provided encouraging feedback. Following this initial interest, orders were received, to develop, produce, characterise and deliver a small quantity of production versions of EUCLID to other institutes.

There were many lessons to learn from the experience gained with the prototype and many refinements made to the design. However, it was also necessary to keep in mind the commercial significance of these developments. Patent protection was sought, and granted, for some novel aspects of the design [96] [97].

4.4.1 Laser Source Selection

During the time that had elapsed between developing the prototype interferometric sensor and EUCLID, difficulties were encountered obtaining the original VCSEL diode. The manufacturer of these devices, Avalon Photonics was in the process of being acquired by Bookham Inc. One of the implications of this acquisition process, was that it was unclear if existing product lines (i.e. including the part already characterised) would be available in the future. For this reason, alternative devices were sought.

However, during this period, new devices had also been released onto the market. As the technology and manufacturing processes matured, VCSELs with the features required by EUCLID were becoming available in visible wavelengths, such as 665 nm. Switching to a visible wavelength would be both preferable from an assembly perspective, but would also be advantageous to the end user, to aid alignment and for laser safety concerns.

Two candidate devices were indentified from an Irish manufacturer, Firecomms Ltd. The first device was a single-mode RVS665S, available in a surface mount PLCC4 package. The second device was a multi-mode RVM665T, available in a standard T0-46

package. Ideally the features of the single-mode device were required, but unfortunately the surface-mount package would be challenging to integrate into EUCLID. However, following discussions with the manufacturer, they were able to offer a hybrid device, RVS665T-101, which was mono-mode but mounted in the more conventional TO-46 package.

A total of fourteen VCSELs were procured so that they could be characterised prior to being installed within the EUCLID units. These devices were driven with a Thorlabs Laser Diode Controller (model LDC200C) and analysed on an Agilent Optical Spectrum Analyser (model 86140B). Parameters of these devices that were being investigated included; the threshold current (i.e. the forward current at which they begin lasing) and the properties of the emission spectra. The VCSELs were coupled into the OSA via an optical fibre and their emission spectra was monitored whilst the drive current was increased, beginning from 1 mA. In Table 4.1 the results from these measurements are presented. Devices that showed good suppression of secondary modes were selected to be used in EUCLID. However, it should be noted that some devices, such as those underlined, had not yet reached the lasing threshold by 1 mA. In such instances, the drive current at which point they actually began lasing is noted.

VCSEL #	Drive Current/mA	Centre Wavelength/nm	EUCLID #
01	1.00	667.59	
02	1.00	667.83	
03	1.00	667.79	1
04	1.30	665.94	
05	1.00	667.50	2
06	1.00	667.79	3
07	1.27	667.21	
08	1.00	666.99	
09	1.00	667.76	4
10	1.25	667.33	
11	1.30	667.19	
12	1.30	667.04	
13	1.00	667.77	
14	1.00	667.65	

Table 4.1: *VCSEL lasing threshold results.*

The EUCLID electronics module was configured to supply the drive current to the VCSELs. Ideally, it should have been possible to provide one common drive current, at which point all devices would be lasing and exhibiting mono-mode behaviour. After studying the VCSEL data sheet, the maximum threshold current was stated as 0.8 mA, so

the current sources were configured to supply this, plus a small margin, giving a nominal 1.1 mA. However, given these findings, it may be necessary to measure threshold characteristics of individual VCSEL in future. Figure 4.9 shows the results obtained for a typical VCSEL, which was installed within one of the EUCLID units. The plots show the emission spectra of the VCSEL over a range of drive currents. Starting in the top left at 1 mA, the drive current is increasing in 1 mA increments clockwise around each plot. For the specific device under test, there appears good suppression of secondary modes, until 3 mA is reached. Beyond this drive current, the VCSEL output becomes dual-mode and unsuitable for EUCLID. Note that, the amplitude of the wavelength peak is arbitrary and appears unrelated to drive current in these plots (most likely due to the poor coupling into the OSA optical fibre).
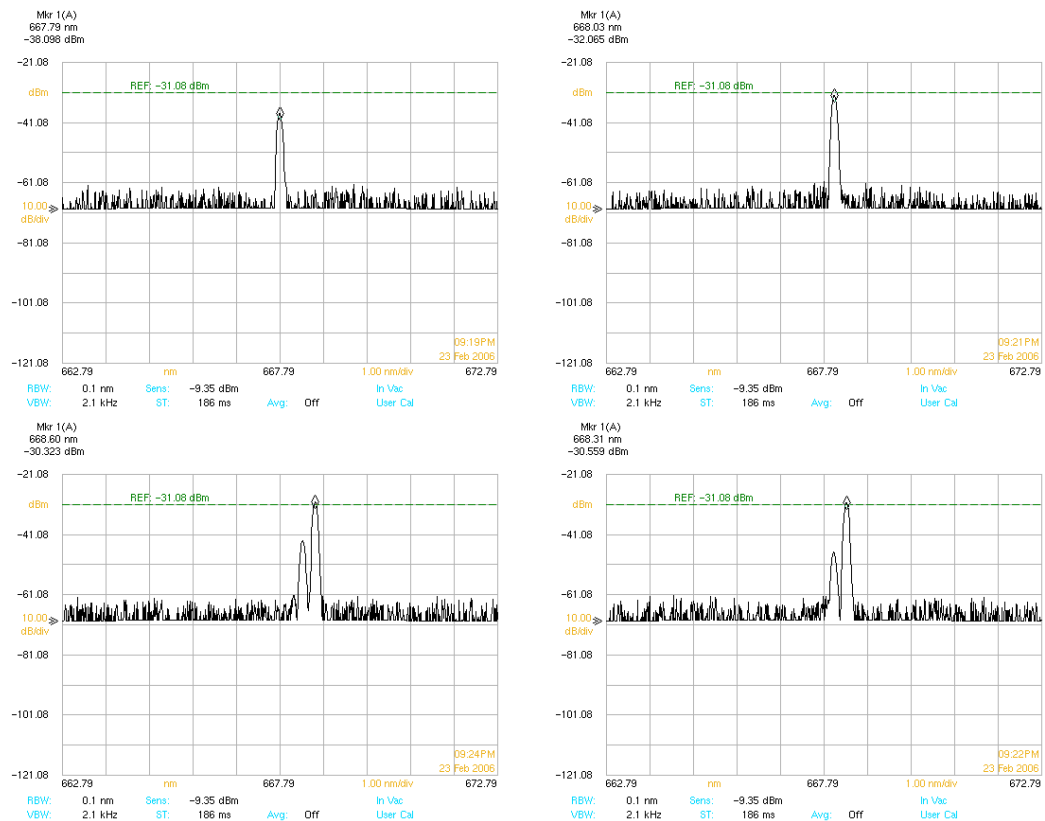
Figure 4.9: *Typical VCSEL emission spectra characterisation results.*

(Top left) VCSEL # 03 1 mA drive current. (Top right) VCSEL # 03 2 mA drive current.

(Bottom left) VCSEL # 03 4 mA drive current. (Bottom right) VCSEL # 03 3 mA drive current.

It would be ideal to be able to identify a drive current regime where all VCSELs have exceeded their threshold and yet would still also be exhibiting mono-mode behaviour. Unfortunately, however, some candidates were found to become multi-mode

at relatively low drive currents (see Figure 4.10), thus making it difficult to specify an optimum drive current. Subsequent batches of VCSELs would need to be characterised to help determine the optimal approach.
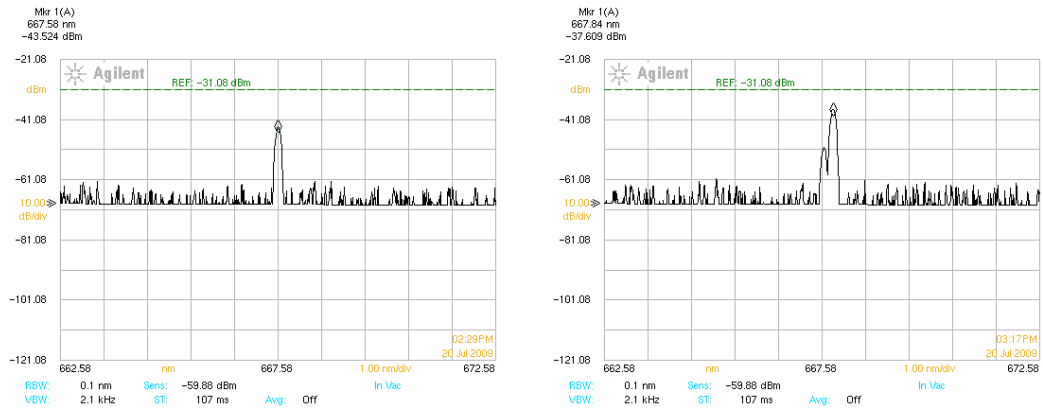
Figure 4.10: *Further VCSEL emission spectra characterisation results.*

(Left) VCSEL # 02 1 mA drive current. (Right) VCSEL # 02 2 mA drive current.

4.4.2 Optical Configuration

Following the prototype interferometric sensor, there have been a number of areas in which the optical configuration has been refined for EUCLID. One of the principle concerns raised by the prototype was the optical feedback into the VCSEL, since semiconductor lasers can be susceptible to even very minor amounts of optical feedback. Firstly, and most significantly, to address this issue, rather than using a co-axial optical scheme, an off-axis approach was adopted for EUCLID. This resulted in the optical axis being geometrically offset from the centre of the optics by 3 mm (i.e. 6 mm beam separation) and ensures that any return beam avoids entering the VCSEL. Secondly, as before, all optical surfaces include suitable AR coatings wherever possible. Thirdly, the provision to deliberately tilt the optical components with respect to the VCSEL was again available. Finally, precautions were taken with the machined finishes of some of the internal surfaces, for example, anodising or vapour blasting metallic parts to dull the finish.

Another area of the design that has been refined for EULCID is the approach to removing the dc offset. Adding the third output (PD3), as demonstrated previously in Figure 4.3, to monitor the intensity of the incoming beam, goes some way to eliminating the dc offset from the Lissajous figure, but is not the most robust technique. Given the

difference in the optical paths, each beam present at the photodiode will have travelled through varying amounts of attenuating optics. So this scheme requires careful setting of gains to compensate. However, this scheme would, for example, still remain susceptible to a change in the reflectance of the measurement mirror (M2), thus requiring gains to be re-evaluated. Instead, it is much more effective to replace this third output, with an output proportional to, say -cosϕ.

The final optical scheme for EUCLID can be seen in Figure 4.11. This incorporates all of the features previously discussed, such as an off-axis beam path, three outputs, and a more optimised cat's eye configuration. A VCSEL diode source emits radiation collimated by L1, which is horizontally polarised and passes through the polarising beam-splitter, A1. The beam continues to the beam-splitter B1, where the 50 % transmitted is lost, the reflected beam propagates on toward the half-wave plate, H1. The optical axis of the half-wave plate is inclined at 22.5^o and rotates the plane of polarisation by 45°, resulting in approximately equal intensities of two orthogonal polarisations (in-plane and perpendicular to the plane) passing through to the polarising beam-splitter, A2, and on into the measurement and reference arms of the interferometer. The quarter-wave plates, Q1 and Q2, force the beams in each arm to be reflected from the cat's eye (M3, L2 and L3 combination) before exiting through the same face of the polarising beam-splitter, A2, which they entered, after two reflections from their respective mirrors. On exiting the beam-splitter, A2, the two polarisation components are rotated back by 45° by the half-wave plate, H1, and again pass through a non-polarising beam-splitter, B1. The beam reflected by B1, propagates to the polarising beam-splitter A1, which reflects the +sinϕ component towards PD2. The beam transmitted by the beam-splitter, B1, passes through the quarter-wave plate, Q3, introducing a π/2 phase shift, and on towards the polarising beam-splitter, A3, which splits the −cosϕ and +cosϕ components, which can then be measured by PD1 and PD3. Thus, PD1, PD2 and PD3 can be interrogated to track the distance through which that the measurement mirror has moved. Note that, first the DC offset can be removed using, PD1-PD2 and PD3-PD2.
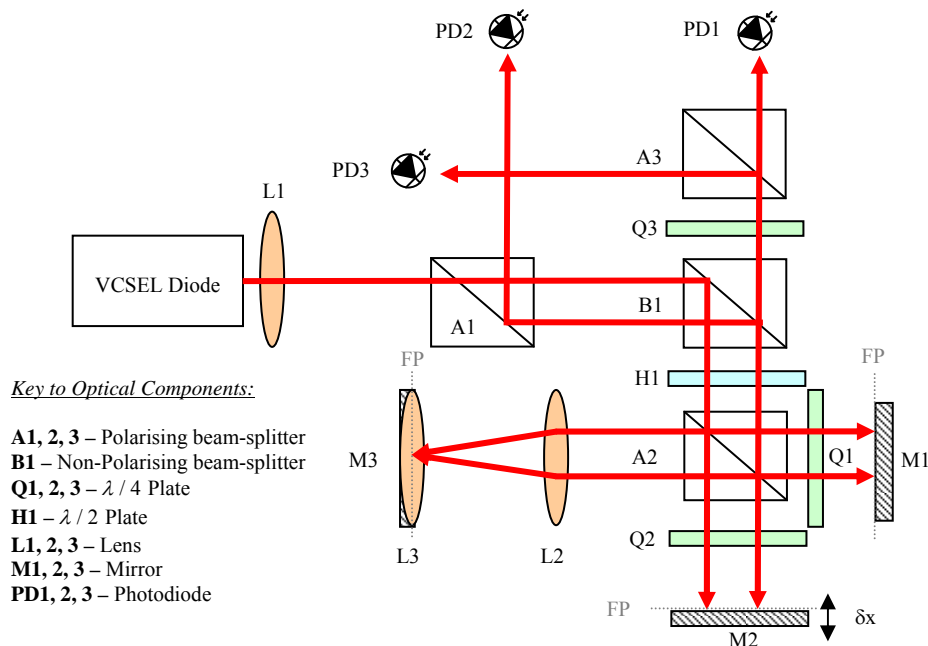
Figure 4.11: *EUCLID final design optical layout.*

4.4.3 Fringe Interpolation Method

For the production EUCLID, a significantly more sophisticated and professional electronics unit has been developed by our in-house electronics engineer. The goal was to produce a simple plug-and-play electronics module that comprises a laser driver current source (including slow start and transient suppression), low-noise front-end electronics for amplifying the photodiode currents and a high speed data acquisition system. The most significant change has been to incorporate a field programmable gate array (FPGA) within the electronics module. The FPGA comprises an array of logic units (or gates) that can be flexibly connected through a routing network, all of which is contained in a single chip. The FPGA allows for the phase calculation to be carried out 'locally' onboard the electronics module. A CORDIC engine [82] has been implemented within the FPGA code to output the difference in phase between the current and previous sample. The three ADC channels are each 16-bit and can acquire data at a maximum sample rate of 1 MHz. Figure 4.12 (left) provides an image of the EUCLID electronics module.
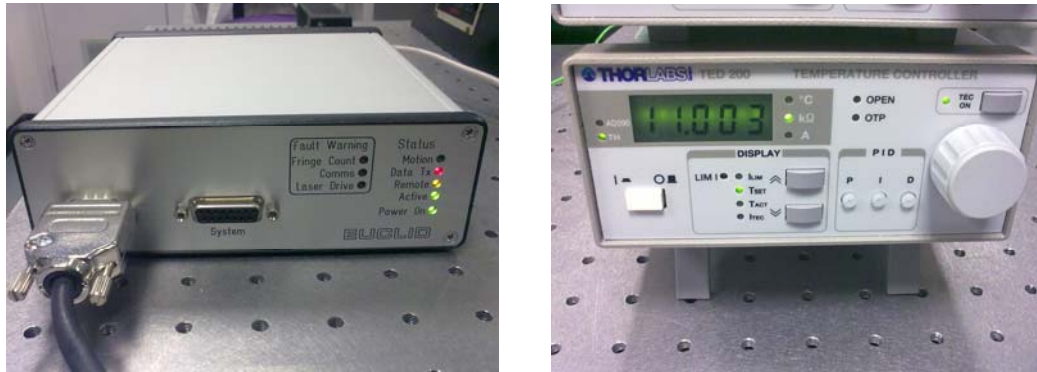
Figure 4.12: *EUCLID support equipment.*

(Left) EUCLID electronics module. (Right) Temperature controller.

There are two modes of operation for the EUCLID electronics module. The first mode is stand-alone, where an analogue distance output is provided along with digital pulse outputs corresponding to distance (one pulse every 2π, or equivalently every $\lambda/4$) and direction. In addition, three analogue outputs representing each photocurrent are also available for monitoring and diagnostics. The second mode of operation is via USB connection to a PC. In USB connection mode, the EUCLID electronics module has to be configured into the required state by the PC. Figure 4.13 shows a screen capture of the USB data acquisition software GUI for the EUCLID electronics module. The software configures the EUCLID electronics module by sending commands via the USB connection, which are then interpreted onboard the FPGA. Once the fringe tracking commences, the results of the calculations carried out onboard the FPGA are returned to the PC via the USB connection. Data validity is verified (using check-sums and packet counts) and the raw phase telemetry stored in a binary data file. Status and error flags are also present in the telemetry packets to report any errors. The status of these flags and errors can also be monitored in real-time by observing the indicator lamps on the front panel of the EUCLID electronics module. Raw phase data can be interrogated in pseudo real-time using MATLAB scripts to analyse and plot the data. The code listings for both the USB data acquisition software and the MATLAB analysis script can be found in Appendix I.
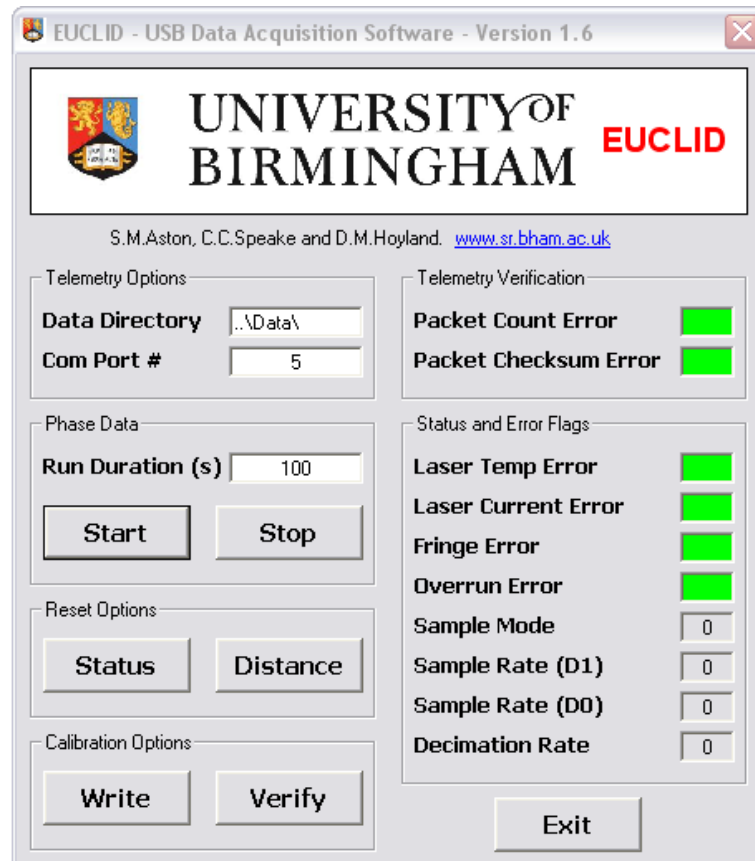
Figure 4.13: *EUCLID control software GUI.*

The FPGA can be considered as a configurable and highly customisable integrated digital circuit. Therefore, one of the major advantages to this approach is that the FPGA can be re-programmed (in-situ) at a later date, if required. This ensures that the EUCLID electronics module is sufficiently flexible to meet the needs of various applications, both now and in the future. For example, sample rates and decimation rates etc. can all be individually tailored for the needs of a particular application.

4.4.4 EUCLID Realisation

Figure 4.14 shows a 3D CAD representation of the EUCLID design. Overall dimensions of EUCLID are 60 mm × 56 mm × 22.5 mm. 2D CAD drawings for the prototype are available in Appendix G. Fully assembled, the EUCLID interferometer has a mass of approximately 131 grams.

The key difference between the prototype interferometric sensor and EUCLID mechanical design is that, essentially all of the adjustments for the optical components

have now been removed. Instead, components are aligned as part of a step-by-step, modular assembly process. This radically simplifies the enclosure, reducing the cost and fabrication time.
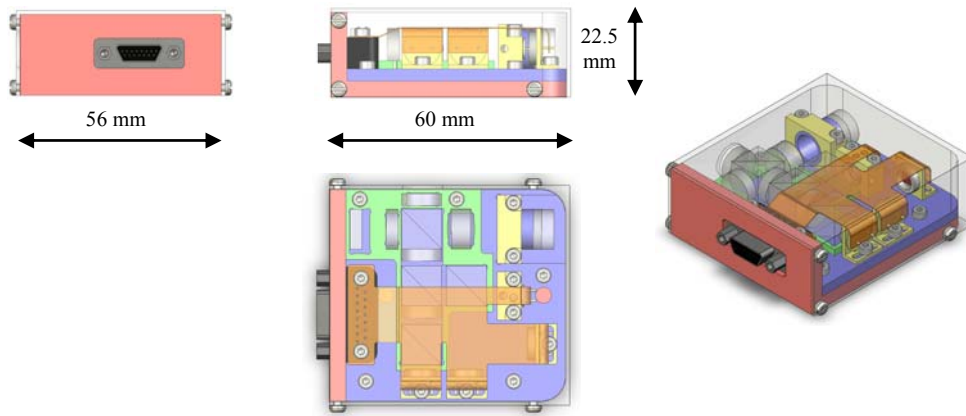
Figure 4.14: *3D CAD model of EUCLID.*

The VCSEL is integral to the unit and located within a custom laser mount. This mount enables rotation to ensure the correct polarisation of the VCSEL. Also, translation of the VCSEL can be performed with respect to an aspheric lens to provide optimal collimation. The position of the lens can then be translated to make sure that the collimated beam emerges along the off-set optical axis. Figure 4.15 (left) shows this first stage of the assembly process. Once all adjustments are complete, UV activated adhesive is used to fix all parts in place, i.e. no further adjustments are possible (or should be necessary).

10 mm beam-splitters are located within a template, see Figure 4.15 (right) and will eventually be bonded down to an aluminium base-plate using the UV activated adhesive. Some wave-plates are bonded directly to beam-splitters whilst others are constrained by the walls of the template. Prior to curing, these wave-plates are free to rotate through 360° to provide easy alignment. Slight adjustment of the template allows all the optical components held within to be tilted slightly with respect to the VCSEL mount. The reference mirror is located in place using the template. The cat's eye reflector, lens and barrel assembly are free to be adjusted. Once alignment is complete and fringes are visible by eye, the photodiodes can be installed as shown in Figure 4.16 (left). When the fringe amplitudes have been maximised, all the components can be

exposed to the UV light source for twenty minutes to fully cure the adhesive, as shown in Figure 4.16 (right).
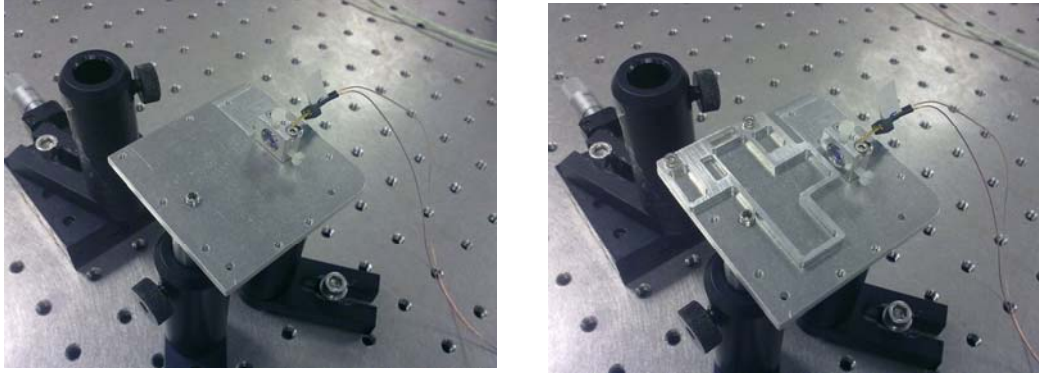
Figure 4.15: *EUCLID pre-assembly tasks.*
(Left) VCSEL beam collimation. (Right) VCSEL mount and template installed.

Figure 4.16: *EUCLID production processes.*
(Left) Populated template and photodiodes installed. (Right) UV curing of optical components.
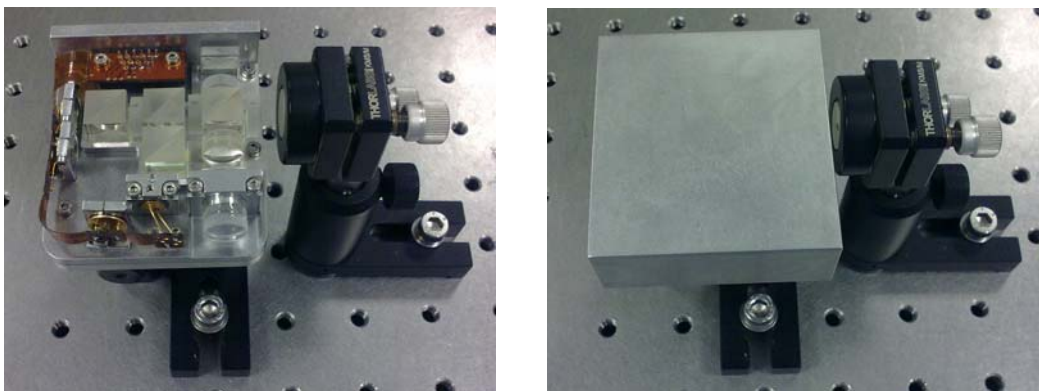
Figure 4.17: *EUCLID final assembly tasks.*
(Left) Flexible circuit and connector installed. (Right) Completed EUCLID unit.

Finally, the connector and flexible circuit are installed to interconnect all of the photodiodes and VCSEL. The connector specification and pin-out details can be found in Appendix B. Figure 4.17 (left) shows the connector and flexible circuit installed. Figure 4.17 (right) shows the completed EUCLID. For a more detailed step-by-step guide to EUCLID assembly and alignment, please refer to Appendix H.

A full list of materials, and their Advanced LIGO UHV approval status, can be found in Appendix C.

4.5 EUCLID Characterisation

The aim of the characterisation tests is to measure the noise floor of EUCLID. This was achieved by simulating the real world operation of EUCLID, using an end to end test setup, incorporating the new EUCLID electronics module. The performance of the EUCLID electronics module has also been modelled and measured.

4.5.1 Free-Air Measurements

EUCLID is mounted using standard fixtures to a passively damped optical bench. Figure 4.18 identifies the mechanical interfaces of the EUCLID enclosure. (Left) shows the positions of the connector and sensing aperture and (right) shows the location of the three blind tapped mounting holes (M4). Provision has been made to mount EUCLID in two orientations. Each orientation, horizontal or vertical, corresponds to a geometric axis of the internal optical components. The different mounting orientations are demonstrated in Figure 4.19 (left) and (right).
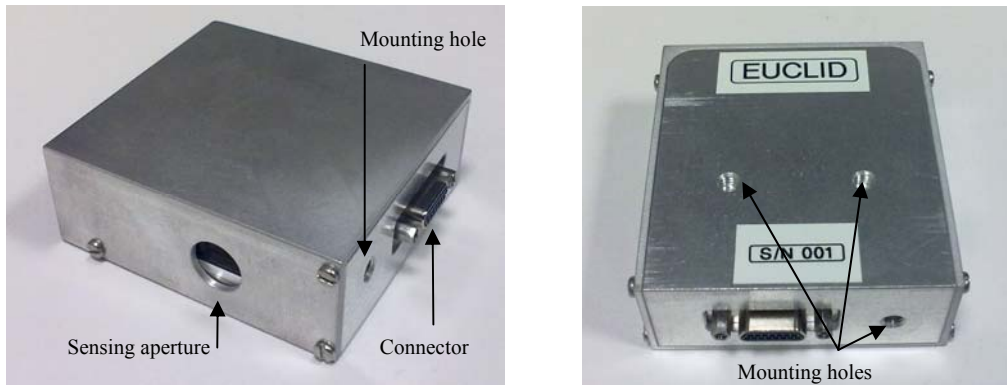
Figure 4.18: *EUCLID enclosure mechanical interfaces.*
(Left) Connector and sensing aperture positions. (Right) Mounting locations.

Once EUCLID has been mounted, it is then necessary to position the external measurement mirror. Figure 4.20 (left) demonstrates a typical external mirror setup for testing and characterising EUCLID. However, each EUCLID has a unique sweet-spot, where its tolerance to misalignment of the mirror is maximised. The following conventions are used when describing the location of the sweet-spot: the working distance, W_D, is the distance measured from the EUCLID enclosure along the sensing axis to the sweet-spot. The working range, W_R, is the distance about the sweet-spot where the fringe amplitude of the Lissajous pattern remains greater than or equal to 50 % of the maximum value. These conventions are shown explicitly in Figure 4.20 (right).
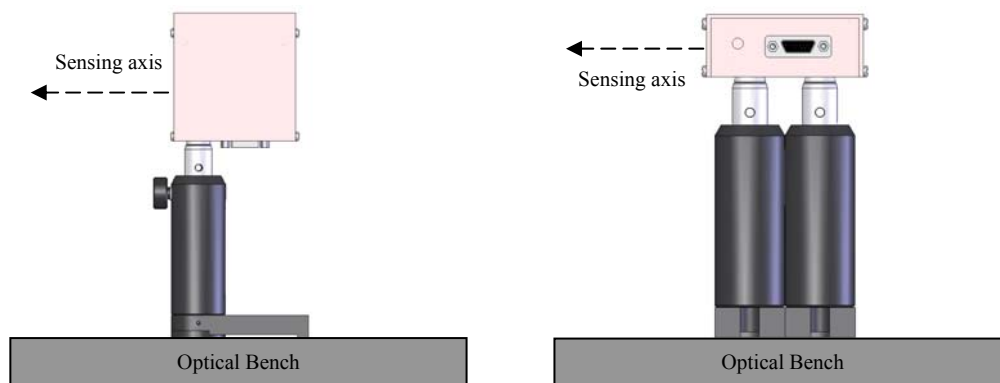
Figure 4.19: *EUCLID mounting orientations.*
(Left) Vertical mounting scheme. (Right) Horizontal mounting scheme.
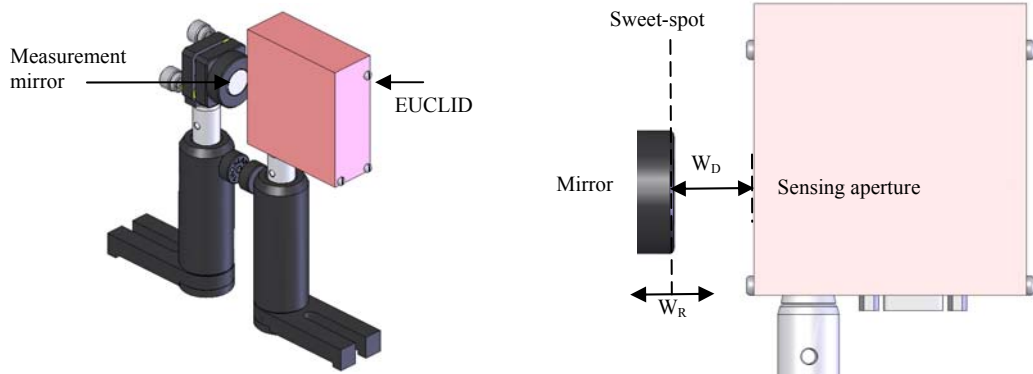
Figure 4.20: *EUCLID and measurement mirror positioning.*
(Left) EUCLID tracking a measurement mirror. (Right) Distance conventions.

Once the measurement mirror is aligned and EUCLID is operating with good fringe amplitude, it is possible to observe the Lissajous figure (with the dc offset removed by the third output) as seen in Figure 4.21. The new EUCLID electronics module enables sampling rates up to 1 MHz. Such a high sample rate ensures that the motion of a mirror attached to a hand driven micrometer translation stage to be tracked, without the loss of any fringes, therefore, a crude check of the EUCLID sensor functionality could be carried out. A calibration measurement was made by translating the mirror through a known distance and comparing this with the result reported by EUCLID; the error was found to be less than 1 %.
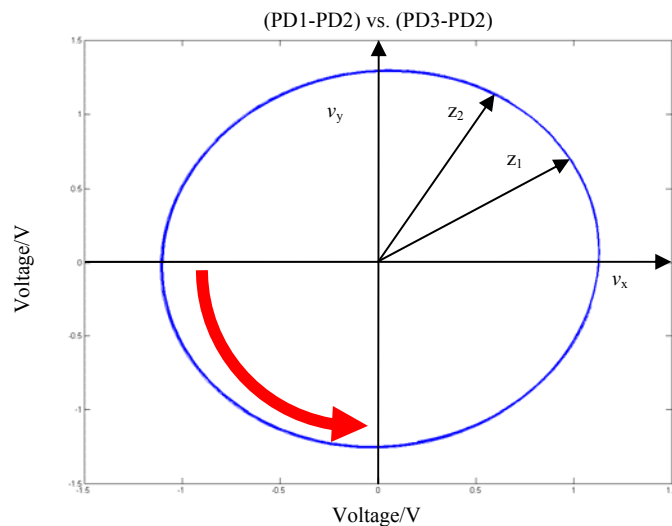
Figure 4.21: *EUCLID measured Lissajous figure.*

Using a configuration very similar to that shown in Figure 4.20 (left) the mirror tilt immunity of EUCLID can be determined for each unit. By mounting the mirror first on to a rotation stage and then on a linear translation stage, measurements of the fringe amplitude are made over a range of working distances, W_D. The aim of these measurements is to determine the working range, W_R, and hence sweet-spot for each unit. The acceptable working range is defined as: where the fringe amplitude drops to 50 % of peak value. Note that, the EUCLID electronics module is still capable of measuring displacement even in the regime where the fringe amplitude falls well below 50 %.

The results of the mirror tilt immunity measurements are shown for EUCLID #1 in Figure 4.22, EUCLID #2 in Figure 4.23, EUCLID #3 in Figure 4.24 and EUCLID #4 in Figure 4.25. Note that, the curves shown in these plots are only used to provide visual aid in representing the data. A summary of these mirror tilt immunity measurements is presented in Table 4.2.

EUCLID #	Fringe Amplitude/V	Tilt Immunity/θ	Working Range/mm	Working Distance/mm
1	≈ 10	± 1	≈ 6	6
2	≈ 7	± 1	≈ 4	6
3	≈ 9	± 0.5	≈ 10	6
4	≈ 9	± 1	≈ 6	6

Table 4.2: *EUCLID mirror tilt immunity summary.*
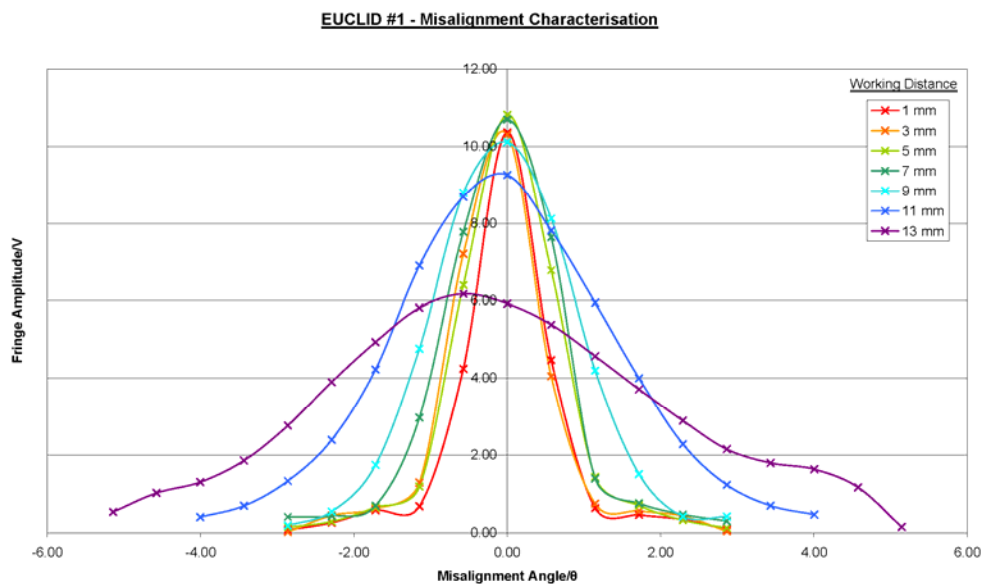
Figure 4.22: *EUCLID #1 mirror tilt immunity.*
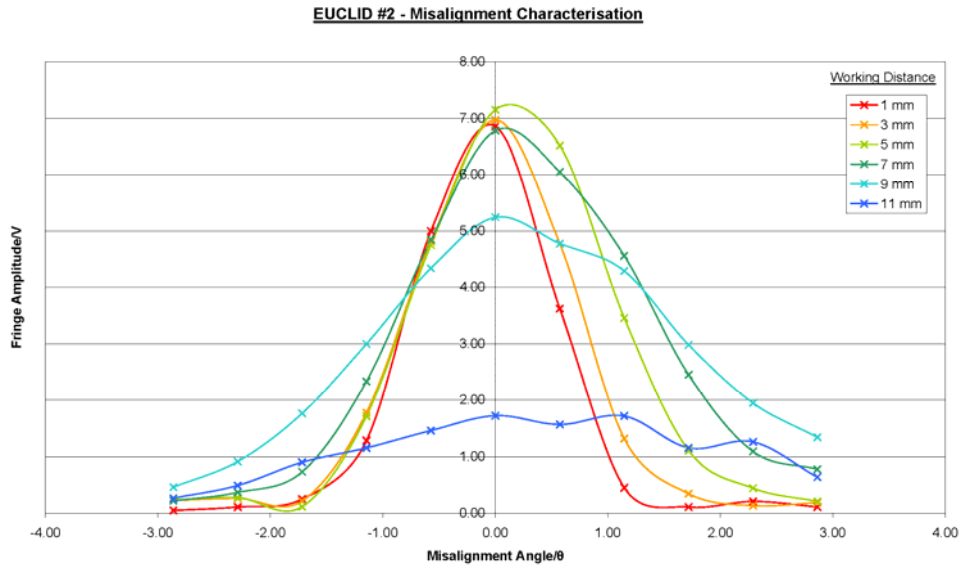
Figure 4.23: *EUCLID #2 mirror tilt immunity.*
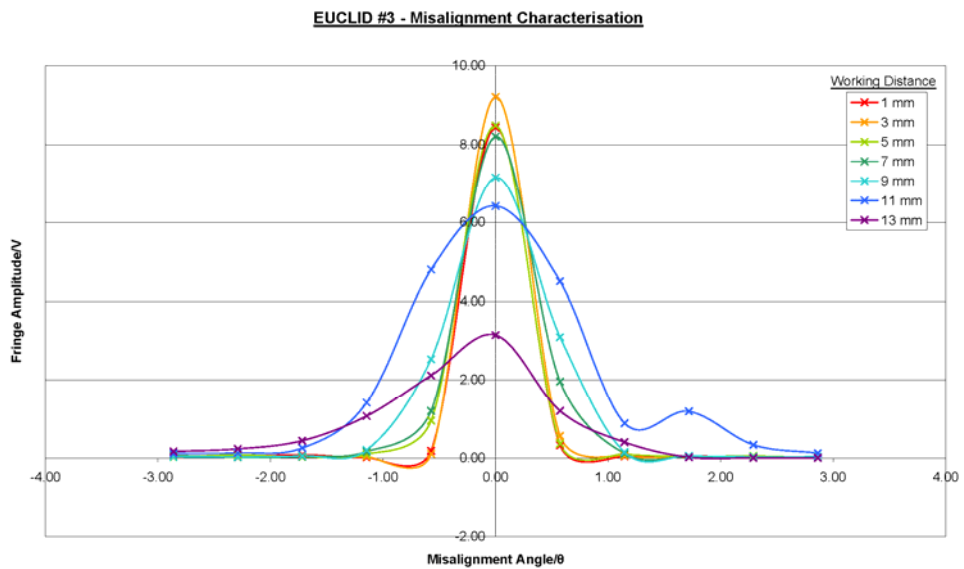
Figure 4.24: *EUCLID #3 mirror tilt immunity.*
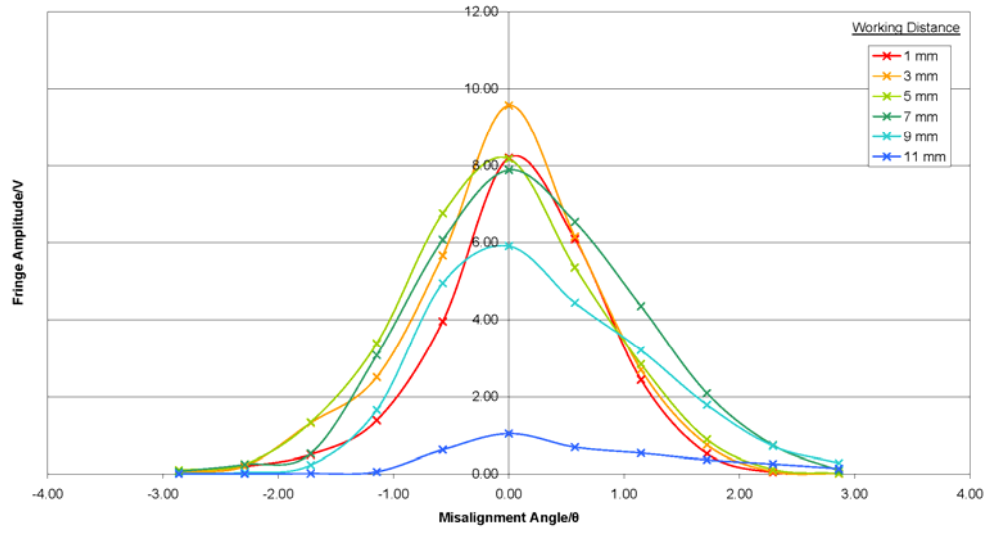
Figure 4.25: *EUCLID #4 mirror tilt Immunity.*

4.5.2 In-Vacuum Measurements

Figure 4.26 shows the experimental set-up used for the duration of the measurements. EUCLID is situated within a vacuum chamber, which has been pumped down to a pressure of less than 3 Pa. The vacuum vessel is situated upon a passively damped optical bench. An electrical feedthrough is incorporated to enable drive current to be provided to the VCSEL diode and pass through the currents generated by the three photodiodes. Provision is also made for a number of environmental monitors. EUCLID is mounted directly onto a copper plate via a Peltier element. The opposite side of the Peltier element is attached to a copper cold-finger, which is in contact with the optical bench. A thermocouple monitors the temperature of the copper plate and forms parts of a temperature controller servo loop. A Thorlabs Thermoelectric cooler (model TED 200), as is shown in Figure 4.12 (right), is used to maintain the desired temperature of 20 ^{0}C. The copper plate also serves as a substrate on which to mount the measurement mirror. The mirror is placed, aligned (by maximising the fringe amplitude) and secured using a UV activated adhesive.
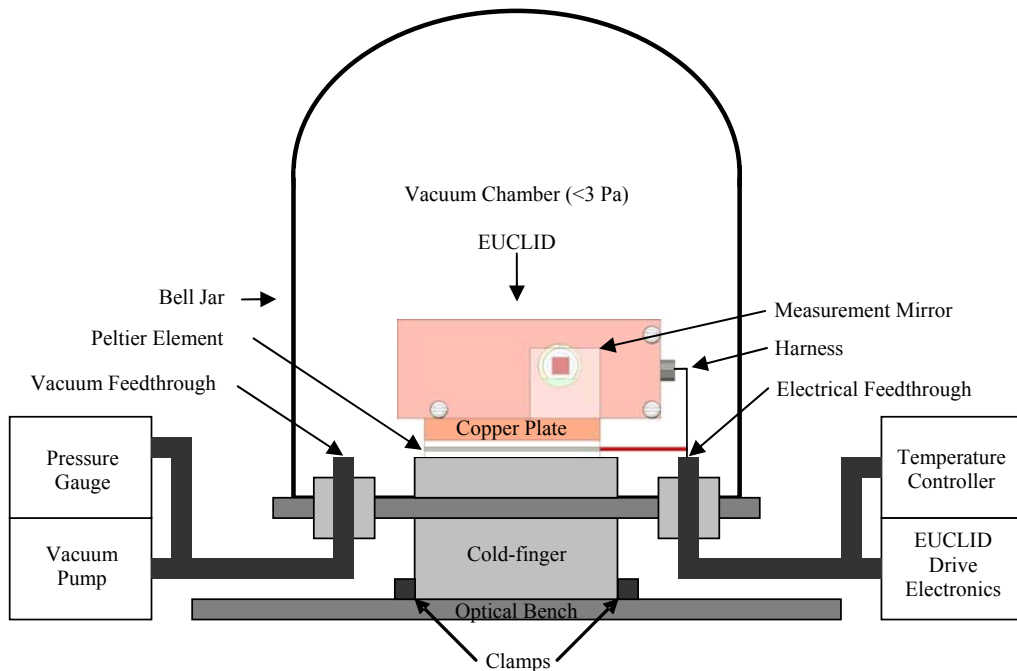
Figure 4.26: *EUCLID in-vacuum test set-up.*

Once the measurement mirror has been cured into position, the bell jar can be fitted and evacuation of the air with rotary pump can begin. During this process, EUCLID

can be operational, tracking the position of the mirror, as can be seen in Figure 4.27. The ambient temperature of the vacuum vessel and the temperature of the interferometer enclosure were also logged during this period.
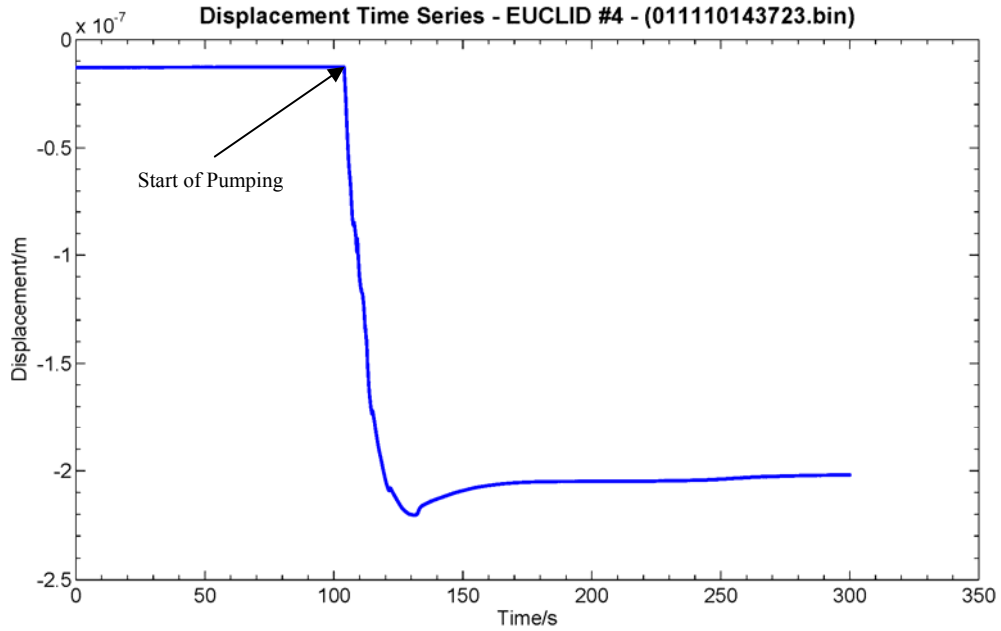
Figure 4.27: *EUCLID tracking mirror during vacuum pump down.*

This measurement can be used to determine the asymmetry between the reference arm and the measurement arm of the EUCLID interferometer. As the air is pumped out of the vacuum vessel there will be a change in the refractive index of the optical path. This leads to a change in the optical path length of each arm. If the arms were of equal length, then the optical path length would remain the same for each arm and no apparent displacement of the mirror would be measured by EUCLID. If there is asymmetry, Δl, in the arms then it can be determined from

$$\Delta l = \frac{2.\Delta z}{(n_a - n_v)},$$
(4.10)

where, Δz is the observed displacement of the mirror, n_a is the refractive index of air (1.000277 at standard temperature and pressure) and n_v is the refractive index of the vacuum. An apparent motion of the mirror, Δz, was observed to be 189 nm, over the duration of the pump down cycle, corresponding to an arm asymmetry of, $\Delta l = 1.36$ mm.

This measurement is repeated again for the venting cycle of the vacuum vessel. Figure 4.28 shows the mirror being tracked during the venting process. During the venting cycle, the mirror was observed to have been displaced through 221 nm. Again, using Equation 4.10, this corresponds to a calculated arm asymmetry of, $\Delta l = 1.60$ mm. Therefore, the calculated mean measurement of the arm asymmetry is, $\Delta l \approx 1.48$ mm. Taking a manual measurement (using a digital calliper) of the physical arm asymmetry, yields a result consistent with the calculated mean measurement of the arm asymmetry. Note that, EUCLID has been designed to incorporate an asymmetry in the arm-length of ≈ 1 mm. The slight disagreement between the two arm asymmetry measurements could be due to thermal transient effects during pump down and venting cycles of the vacuum. Interrogating the temperature logs taken during these periods reveals drops in temperature of up $1\ ^0C$ in the turbulent air flow.
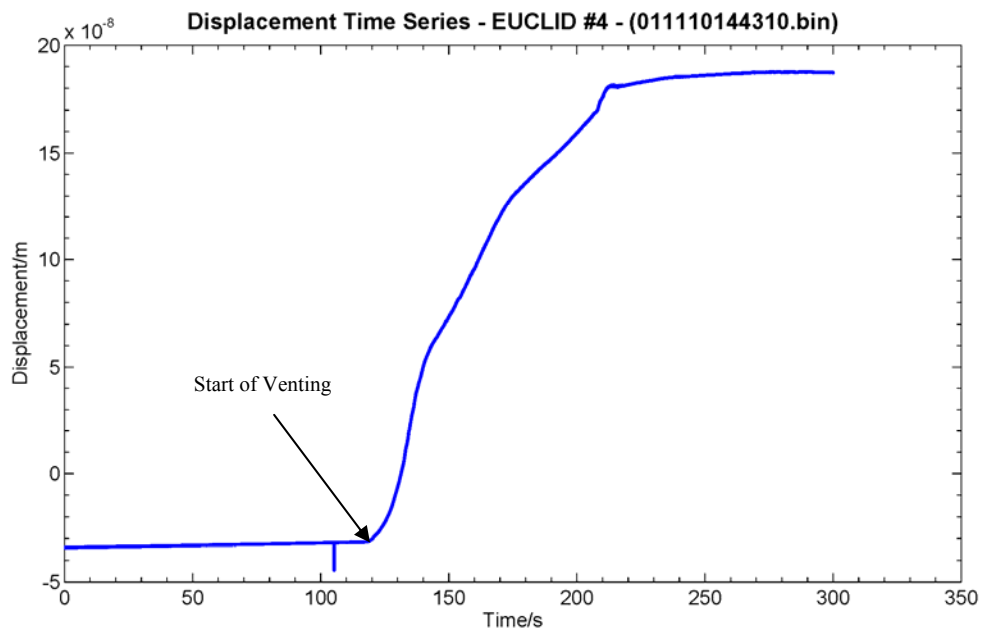
Figure 4.28: *EUCLID tracking mirror during vacuum venting.*

During quiet periods (for example overnight or at weekends) sensitivity measurements were made for EUCLID #4. Given the nominally high sample rate and the relatively long periods required to observe low frequency performance, the sample rate was reduced from 1 MHz down to 250 kHz for the long runs to ensure data files were manageable. In each case, further decimation decreases the signal bandwidth to 10 kHz and 250 Hz respectively.

In addition to the characterisation of EUCLID, the noise performance of the front-end electronics has also been characterised. A 'dummy' EUCLID was connected to the interface port, comprising of resistors configured to simulate half-scale illumination of the photodiodes. Again, measurements were taken and decimated in exactly the same way as those for EUCLID. The fundamental noise limits (as detailed in Section 2.2) that are applicable, are also indicated. This enables a noise budget for EUCLID to be produced, as shown in Figure 4.29. The shot-noise limited performance can be calculated, given that the Lissajous fringes generate full scale voltages of 0 V to 4 V, including a voltage gain, G, of 8 and a transimpedance amplifier gain, R_f, of 68 kΩ, results with a photodiode current, i_{pd}, of approximately 7 μA. Hence, as derived in Section 2.2.1, the shot-noise limit can be calculated using Equation 3.19, with the voltage noise given by

$$\sigma_{v_{pd}} = \sqrt{2ei_{pd}} \times R_f \times G .$$

(4.11)

This can then be converted into a displacement noise using the relation derived from Equation 4.8,

$$\sigma_y = \sqrt{2ei_{pd}} \times R_f \times G \times \frac{\lambda}{8\pi} .$$

(4.12)

Substituting in the figure given above, noting that the VCSEL wavelength, λ, equals 665 nm, leads to a shot-noise limited sensitivity of

$$\sigma_y \approx 2.2 \times 10^{-14} \text{ m Hz}^{-1/2}.$$

(4.13)

Also the Johnson noise (as derived in Section 2.2.2) limited performance can be determined using

$$\sigma_{v_{pd}} = \sqrt{\frac{4KT}{R_f}} \times R_f \times G ,$$

(4.14)

where, K is the Boltzmann constant, and T is the temperature in Kelvin. Again, this can be converted into an equivalent displacement noise using the relation derived from Equation 4.8,

$$\sigma_{v_{pd}} = \sqrt{\frac{4KT}{R_f}} \times R_f \times G \times \frac{\lambda}{8\pi} . \tag{4.15}$$

Substituting in the figures given above, and assuming a room temperature of 300 K, leads to a Johnson noise limited performance of

$$\sigma_y \approx 7.1 \times 10^{-15} \text{ m Hz}^{-1/2}. \tag{4.16}$$

MATLAB noise models for the fundamental limits presented (including ADC noise) are also available in Appendix I.
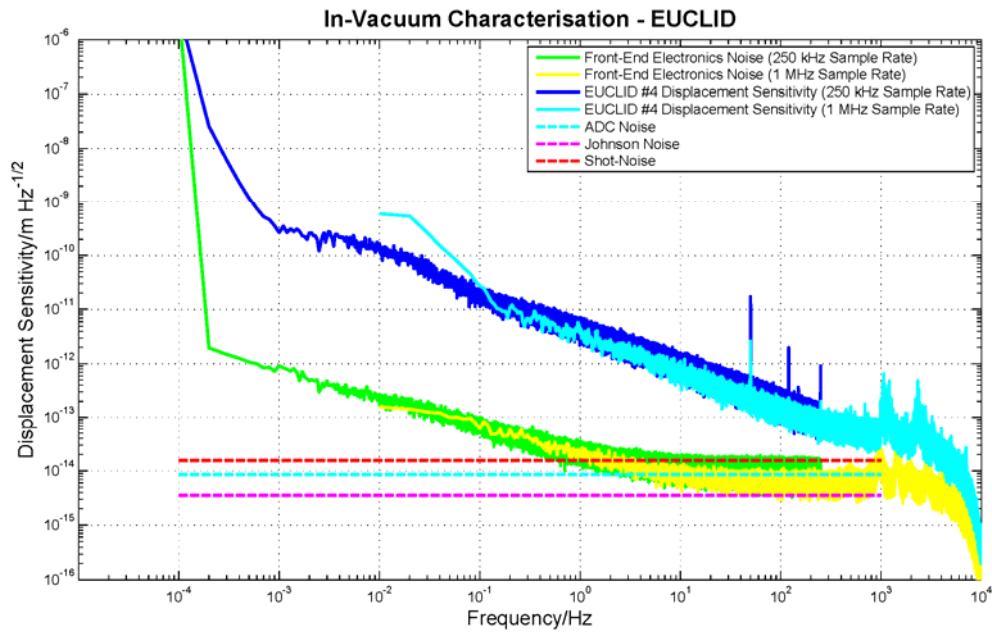
Figure 4.29: *EUCLID noise budget and measured sensitivity performance.*

It can be seen from Figure 4.29 that EUCLID achieves a sensitivity of $\approx$ 50 pm Hz$^{-1/2}$ at 1 Hz, improving to $\approx$ 1 pm Hz$^{-1/2}$ at 10 Hz. The measured electronics noise behaves consistently with the modelled ADC and Johnson noise. At low frequencies, 1/f noise from the operational amplifies (AD8630) dominates. At high

frequencies, above ≈ 1 kHz, a roll-off feature is present, due to the decimation filter. Note that, some spike features are observable at around 50 Hz (and harmonics thereof) in the spectra obtained. These spike features are most likely due to mains and air-conditioning fans coupling into the measurements.

At high frequencies, above ≈ 1 kHz, it can be seen that EUCLID starts to become fundamentally shot-noise limited. However, at lower frequencies there is significant, un-modelled excess noise exhibiting 1/f behaviour. A strong candidate for the source of this noise is laser frequency noise from the VCSEL. Therefore, it would be useful to compare the noise performance of EUCLID (with the integral VCSEL) to EUCLID with using an external He-Ne laser source.

Unfortunately, it is not feasible to install the He-Ne within the vacuum vessel, so other options had to be considered. Two of the options available were: using an optical fibre feedthrough to route the collimated beam into EUCLID, or using the vacuum vessel (bell jar) as an optical window. The first option would require some long-term re-engineering of the vacuum vessel to incorporate an optical fibre feedthrough. However, the suitability of the second option could be determined relatively quickly.
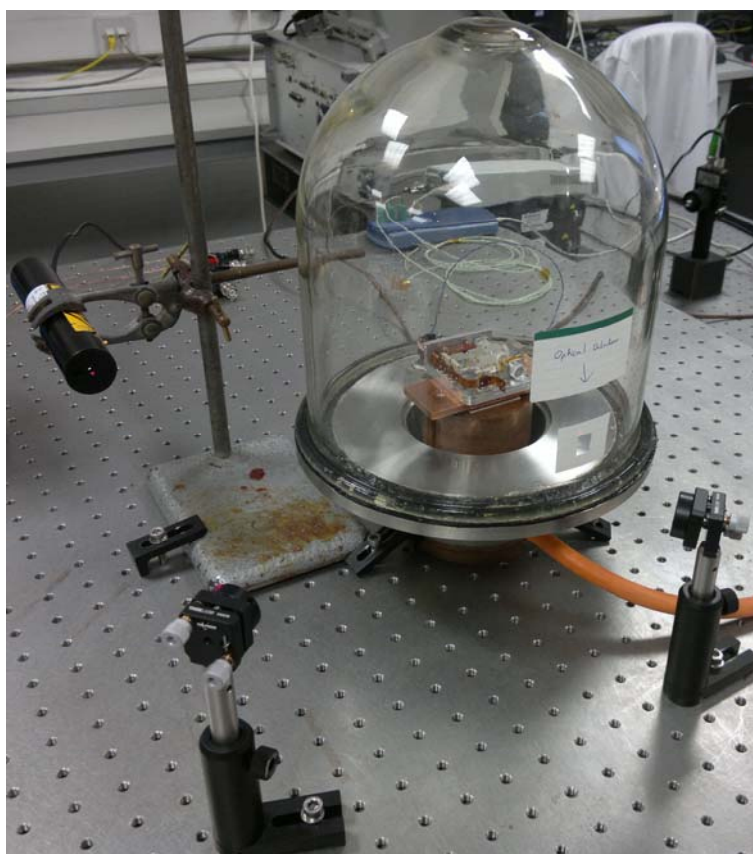
Figure 4.30: *EUCLID in-vacuum laboratory set-up with external He-Ne laser.*

Figure 4.30 shows the set-up for an external He-Ne laser, with the collimated beam being aligned and guided into EUCLID via folding mirrors and through the bell jar optical window. Initial alignment (and optimisation of the fringe amplitude) was first conducted without the bell jar being present. Next it was necessary to demonstrate that this alignment was maintained when the bell jar was in place and after the air had been removed. This was achieved by monitoring EUCLID's response to a step change in the temperature of the copper substrate (set using the temperature controller). Three measurements were taken: no bell jar, bell jar present but no vacuum, and finally for the bell jar and vacuum. EUCLID's response was found to be consistent in each case.

In-vacuum sensitivity measurements were repeated for EUCLID, but this time using the external He-Ne laser. The results are shown by the red line in Figure 4.31.
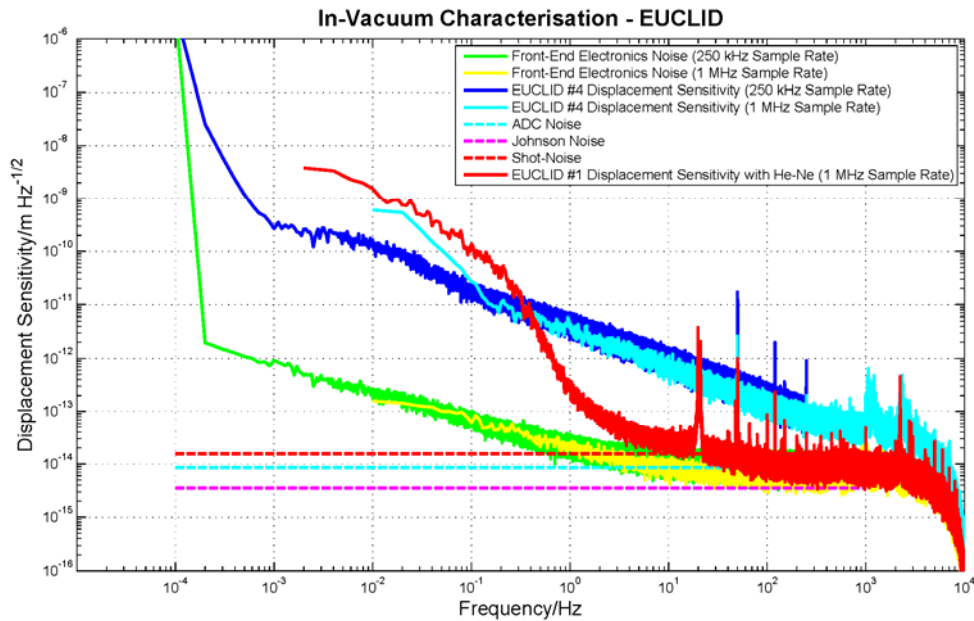
Figure 4.31: *EUCLID noise budget and measured sensitivity performance with external He-Ne laser.*

It can be seen that the EUCLID sensitivity was considerably different when using the He-Ne source, instead of the VCSEL. The device has now become shot-noise limited at a lower frequency than before, at around 50 Hz. Sensitivity performance was significantly improved by over an order of magnitude down to around 0.3 Hz. Interestingly, below this frequency, the sensitivity achieved was not as good as was obtained with the VCSEL.

The time series for a typical measurement can be seen in Figure 4.32. A significant low frequency drift can be observed, equating too approximately 28 nm over the duration of the measurement (500 s).
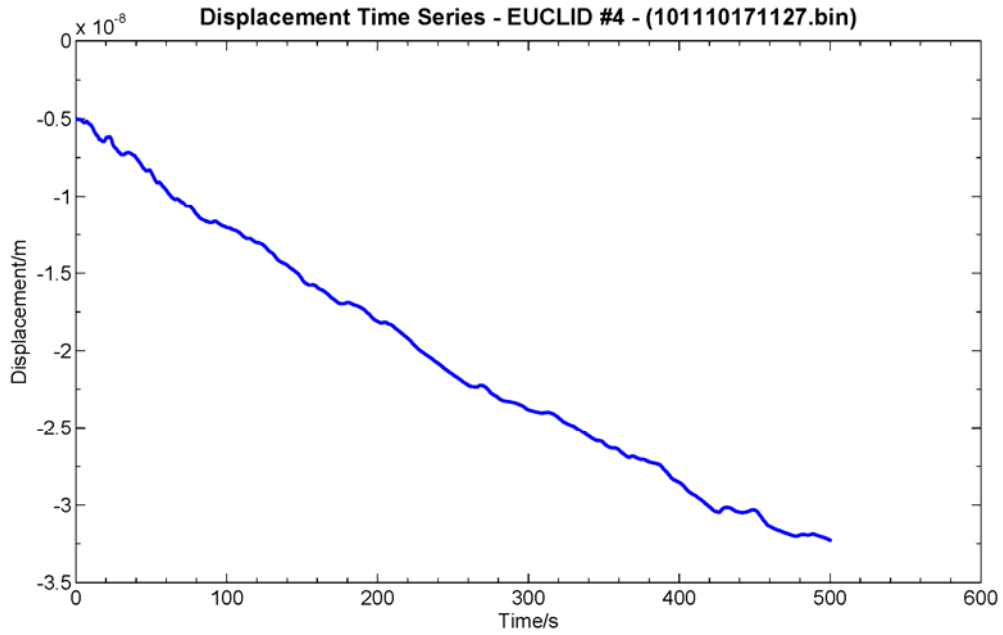
Figure 4.32: *EUCLID displacement measurement time series using external He-Ne laser.*

Ultimately, it is anticipated that EUCLID's low frequency performance will be limited by the stability of the reference arm of the interferometer, which is currently mounted on a copper base-plate. Given the asymmetry in the arms of the interferometer, Δl, as previously calculated, the coefficient of thermal expansion for copper (approximately 16.5×10^{-6} K^{-1}), it would require a 1 ^0C change in temperature of the interferometer arms to produce the 28 nm drift observed. However, temperatures logged over the duration of these measurements indicate variations of up to 0.08 ^0C, thus demonstrating that thermal expansion influences, at this time, can be discounted.

Frequency noise for a single-mode laser can now be calculated using

$$dz = \frac{\lambda \Delta l}{\sqrt{c\pi L}} \, , \tag{4.17}$$

where the arm asymmetry, Δl, is as previously calculated, c, is the speed of light, λ is the wavelength of the light employed (633 nm for the He-Ne) and L is the coherence length of the laser. For the He-Ne the coherence length can be assumed to be $\approx$ 20 cm. Therefore, leading to a frequency noise estimate of 6.8×10^{-14} m $Hz^{-1/2}$, which appears consistent with the measurement for the He-Ne laser in Figure 4.31, where frequency

131

noise begins to dominate below a few Hertz. Returning to the set-up with EUCLID and the integral VCSEL, it can be determined whether a thermally induced change in wavelength of the device can account for the apparent drift observed in displacement. The following relationship can be used to determine the induced change in VCSEL wavelength, $\Delta\lambda$,

$$\frac{\partial(\Delta\phi)}{\Delta\phi} = -\frac{\Delta\lambda}{\lambda}, \tag{4.18}$$

where, $\partial(\Delta\phi)$ is the apparent drift (in radians) and $\Delta\phi$ is the asymmetry in the arms (in radians). The value for the asymmetry in the arms, Δl, has previously been determined. Note that, λ, the VCSEL wavelength, is now 667 nm. In Figure 4.33 the time series of a measurement for EUCLID, with the internal VCSEL shows a drift of $\approx$ 33 nm over the 500 s measurement.
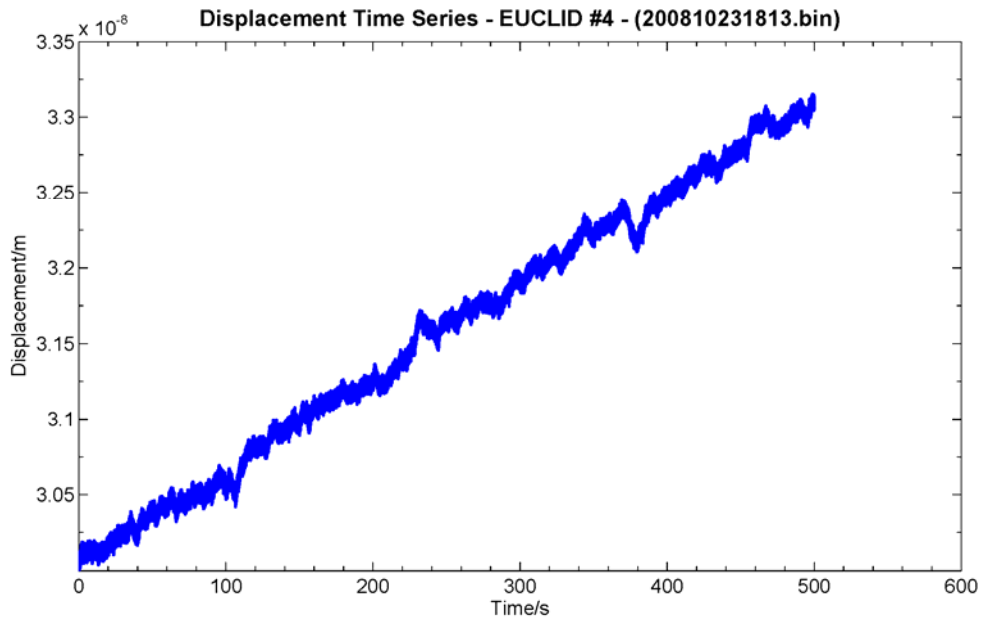
Figure 4.33: *EUCLID displacement measurement time series using internal VCSEL.*

Using the figures above, results in an induced change in the VCSEL wavelength of, $\Delta\lambda \approx 0.015$ nm. The manufacturer's data sheet gives a wavelength temperature tuning coefficient for this device of 0.04 nm K^{-1}. Therefore, the change in temperature required for the induced wavelength change is

$$\Delta T = \frac{\Delta\lambda}{0.04} \approx 0.38 \ {}^0\text{C}. \qquad\qquad (4.19)$$

The value calculated above is significantly larger than any temperature variations measured throughout the course of the experiment, indicating that sensitivity performance is not limited by the thermally induced wavelength changes in the VCSEL.

Should it have been necessary now, or in the future, to locally stabilise the VCSEL's temperature, then EUCLID can be adapted to do this. The EUCLID electronics module incorporates a thermoelectric driver and servo control circuit. EUCLID itself has the necessary flexible circuit routing to support the installation of a VCSEL with integrated Peltier element. Such parts are readily available at visible wavelengths, albeit at significantly higher cost.

The cause of the low frequency drift observed is still uncertain. Exchanging the VCSEL for the He-Ne laser clearly had an impact upon both the high and low frequency performance. It is therefore possible that the standard free running He-Ne output comprises of two or three competing longitudinal modes, which could explain why its low frequency performance is not as good as was observed for the single-mode VCSEL diode. However, in future it would be interesting to try a wavelength/frequency stabilised, mode-locked He-Ne laser. An improved low frequency performance for the EUCLID interferometer would be anticipated, but certainly not guaranteed.

Chapter 5

Conclusions of this Study

"Insanity: doing the same thing over and over again and expecting different results". Albert Einstein.

5.1 Sensor Development Discussion

Both of the sensors presented herein, after some endeavour, have met their respective performance requirements; EUCLID meeting the stringent requirements given in Table 3.1 and the BOSEM meeting the final requirements given in Table 3.2. Since the BOSEMs are Advanced LIGO project deliverables and were developed as part of a large scale production effort, signifies that they are at a more mature stage in their development than EUCLID. For example, they have had to be fully qualified for use in the Advanced LIGO UHV environment. EUCLID has been constructed using similar parts and materials to the BOSEM wherever possible, however, there are still some items outstanding (VCSEL, photodiodes etc) that would need to be explicitly qualified for use in the Advanced LIGO UHV environment. The most significant area of concern is the UV activated adhesive currently used to bond the optical components to each other and to the substrate. The existing adhesive, Norland NOA61, is not approved for Advanced LIGO use. However, we are now aware that in the interim, an alternative UV adhesive has since been approved, OPTOCAST 3553LV-UTF, manufactured by Electronic Materials Incorporated and is explicitly listed in an update to the vacuum compatible materials list [84]. There are slight deviations in the UV curing procedure compared to what has been carried out with the existing UV adhesive, but otherwise it looks suitable for use with EUCLID. Therefore, the route to achieving LIGO UHV compliance for EUCLID appears low risk and should need only minimal additional effort.

Figure 5.1 provides a comparison plot showing the displacement sensitivities achieved for both EUCLID and BOSEM sensors. It can be seen across the BOSEM band (1 Hz to 10 Hz) that EUCLID offers nearly two orders of magnitude improvement in sensitivity and essentially a one order of magnitude increase in working range (increasing from 0.7 mm to $\approx$ 6 mm).
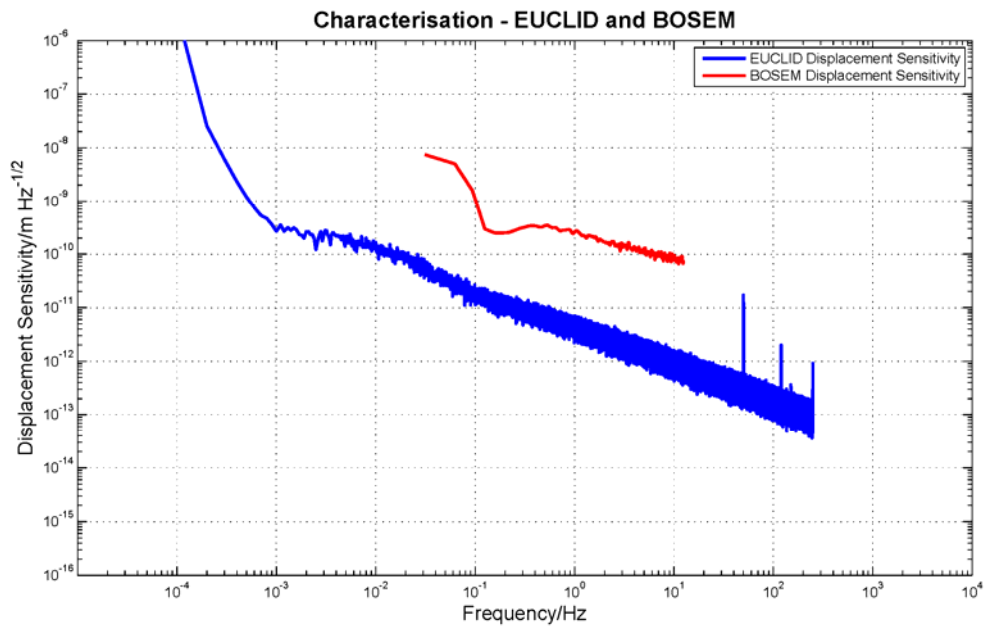
Figure 5.1: *EUCLID and BOSEM comparison of sensitivity performance.*
BOSEM sensitivity extracted from Figure 3.31. EUCLID sensitivity extracted from Figure 4.29.

The BOSEM sensitivity is representative of the limits of what can readily be achieved using this technique. The shadow sensor technique employed has been pushed to (and possibly beyond) its capability, in the end requiring significant screening effort to ensure that all units meet the desired specification. However, the IRLED screening process revealed some exceptionally low-noise devices, as shown in Figure 3.35. Such IRLEDs could potentially offer a factor three improvement over the required sensitivity within the 1 Hz to 10 Hz band. Therefore, there is scope for improving the sensitivity of similar types of unit in the future, but the amount of effort and resources required may prove prohibitive. Implementing modifications, such as IRLED power stabilisation schemes, may improve the sensitivity, but still may not overcome the need to screen devices. A key objective would, therefore, be in indentifying an IRLED that has the required level of performance and demonstrating consistency from batch to batch. It may be possible to collaborate with a manufacturer in the fabrication or procurement of such a device. However, experience so far suggests their interest would be purely academic, given the relatively low volume of devices required for our specific application. For the vast majority of their customers, excess noise at low frequencies is not a concern. Therefore, together with the fundamental limits discussed in Chapter 3, there remains an inherent risk in pushing this sensor technology further.

5.2 Future EUCLID Development

The EUCLID sensor still represents a work in progress and there are a number of low risk developments that would improve its effectiveness in the future. For example, revision of the flexible circuit geometry and routing (making it more robust and quicker to integrate), removing all optic to optic surface bonds (to reduce cost of optical components), implementing a real-time software control and data visualisation GUI (using LabVIEW), and incorporating vent-holes for enclosed volumes of gas (for UHV compliance). In addition to these minor refinements, there are also areas where more substantial research can be targeted in the future, as discussed later in this section.

5.2.1 Sensitivity

The sensitivity performance demonstrated by EUCLID went beyond what was required, even when considering the most stringent BOSEM sensor requirements in Table 3.1. For this reason, there has been no need to push the EUCLID performance any further. However, it was presented in Figure 4.31 how the performance would appear to be limited by the VCSEL and by switching to an alternative laser source, there is still scope to improve the sensitivity performance. It may be necessary to characterise more VCSELs of the same type, but from different batches to see if there is any variation in noise performance. Next it would be interesting to characterise VCSELs from different manufacturers, or operating at different wavelengths, to compare how they perform. It is interesting to note that the results obtained from the interferometer prototype, shown in Figure 4.8, exhibit very similar characteristics to EUCLID, but were obtained using an 850 nm VCSEL diode. This may indicate that such noise performance is inherent to all VCSELs, independent of wavelength. EUCLID's performance using a more stable and sophisticated distributed feedback (DFB) laser would be interesting to observe.

5.2.2 Absolute Interferometry

As mentioned previously in Section 4.3.3, a key problem with the incremental fringe counting technique is that power failure or too rapid displacement producing fringe shifts outside the sampling bandwidth of the electronics will result in loss of the absolute position of the target mirror. An absolute interferometry scheme allows the dc position of the target mirror to be tracked, albeit with lower resolution.

Ideally a laser source is required that exhibits mono-mode behaviour over a wide working range of current. It is known that the 850 nm VCSEL diode has wavelength tuning coefficients against current and temperature of 0.06 nm K^{-1} and 0.3 nm mA^{-1}, respectively, over a range of 4 mA to 7 mA. Therefore, this tunability would enable EUCLID to perform absolute interferometry. If the arm asymmetry in EUCLID arm-lengths is l, wavelength modulation between λ_1 and $\lambda_2 = \lambda_1 + \Delta\lambda$ will generate a phase shift $\delta\phi$,

$$\delta\phi = \frac{2\pi\, l}{\overline{\lambda}}\Delta\lambda\,, \tag{5.1}$$

where

$$\overline{\lambda} = \frac{\lambda_1\lambda_2}{(\lambda_2 - \lambda_1)}\,. \tag{5.2}$$

For the VCSEL specified above, the synthetic wavelength $\overline{\lambda} \approx 2.5$ mm. However, in this mode of operation, the shot-noise limit of the interferometer will be degraded by the ratio of $\lambda/\overline{\lambda}$, when compared to what has been characterised previously in Section 4.5.2.

The absolute interferometry scheme can be implemented in the homodyne device by modulating the wavelength, monitoring the change in optical phase using Equation 4.9 and then extracting the component that is coherent with the wavelength modulation. If the coherent change in phase is denoted as $\delta\phi$, then Equation 5.1 can be used to determine the absolute difference in arm-lengths, l.

This has already been seen to work in principle with the prototype interferometer, presented in Section 4.3. However, there were a few short-comings with this design that compromised its effectiveness. Firstly, a change in VCSEL forward current not only shifts the wavelength, but also can change the output intensity. Secondly, the arm asymmetry was very small, of the order 10 μm.

EUCLID has been designed to overcome these deficiencies. For example, using three optical outputs with an output proportional to, -cosϕ, enables much more effective elimination of the dc offset from the outputs of the photodiodes. Also, the EUCLID optical design incorporates $\approx$ 1 mm asymmetry in its arm-lengths. Finally, the EUCLID electronics module incorporates a connector on the rear panel that provides direct modulation of the laser drive current (and thus wavelength).

5.3 Spin-outs from this Study

EUCLID has primarily been designed for use in the field of gravitational wave astronomy. However, during the course of this research it has been noted that there are many other applications, both terrestrial and non-terrestrial where EUCLID could be employed. In addition to the scientific research conducted developing EUCLID, market research and business models have also been investigated, in an attempt to asses the commercialisation potential of EUCLID. This has led to the granting of an international patent [96] protecting some of the novel features of EUCLID, such as the mirror tilt immunity.

In parallel to the research on the linear sensor, EUCLID, work is also being conducted at Birmingham designing a rotation sensor, known as ILIAD. This will be used as the optical read-out scheme for a superconducting torsion balance [79] as well as being developed for a room temperature torsion-strip balance [83]. This work builds upon our experience with EUCLID and has progressed to the stage where another patent application has been granted [97].

5.3.1 Ground-based Applications

The most obvious applications for the optical sensors are those for which they were originally developed, i.e. being employed in the seismic isolation and suspension sub-systems of ground-based gravitational wave observatories. A large quantity of the crude shadow sensors (BOSEMs) have already been provided to the US LIGO observatories for their upgrade to Advanced LIGO. The BOSEM now represents a mature design and should any further units be requested, the development and fabrication costs can be kept relatively low.

LIGO is only one part of an ever expanding worldwide network of detectors. There are currently proposals to export one of the three LIGO interferometers to Australia, as well as upgrades of existing observatories in Italy, Germany and Japan. Also the list of nations showing a strong interest in joining the international gravitational wave community is growing. For example, new observatories are being considered in China (China Einstein Gravitational Wave Observatory, CEGO) and India (Indian Initiative in Gravitational-wave Observations, IndIGO).

New techniques, technologies, and interferometer topologies will need to be developed for future generations of observatories. These future detectors are certain to be pushing towards improving sensitivities at lower frequencies and this is likely to place ever more stringent requirements on all sensors employed in these future observatories. Fortunately, the research already carried out developing both the BOSEM and EUCLID has provided a head start in this field.

5.3.2 Space-borne Applications

The LISA mission has already been discussed in Section 1.4.3 and the sensitivity curve presented in Figure 1.6 and Figure 2.3. At low frequencies LISA's performance is limited by the capacitive read-out system employed in the drag-free system of the spacecraft.

A conventional drag-free satellite can be considered as two spacecraft in very close proximity, effectively a two-in-one satellite. A small test-mass is isolated within the internal cavity of the main spacecraft. The cavity incorporates sophisticated sensors that are able to determine the position of the test-mass relative to the main satellite structure. The satellite is then required to maintain the relative separation between itself and the test-mass by firing thrusters to cancel any external perturbations. The test-mass is shielded by the outer satellite structure from particulate collisions (drag) and solar radiation pressure. Ideally, this results in the test-mass being in free-fall and following a trajectory defined only by a gravitational field (geodesic). There can, however, be deviations arising due to small perturbation forces from the main satellite (for example, either from the sensing and control implementation or optimally the gravitational anomalies due to the spacecraft structure itself). This concept of the spacecraft drag-free system is shown in Figure 5.2. The figure shows how an external force, F_{EXT}, can act on

the outer structure of the spacecraft and change the separation, *x*, between the test-mass and cage. Sensors are then able to determine the change, *Δx*, and actuate field effect electron propulsion (FEEP) thrusters to help maintain a constant separation. Thus, ideally any external forces applied by the control system are equal (and opposite) to the force produced by the FEEP, i.e. $F_{EXT,} = -F_{FEEP}$.
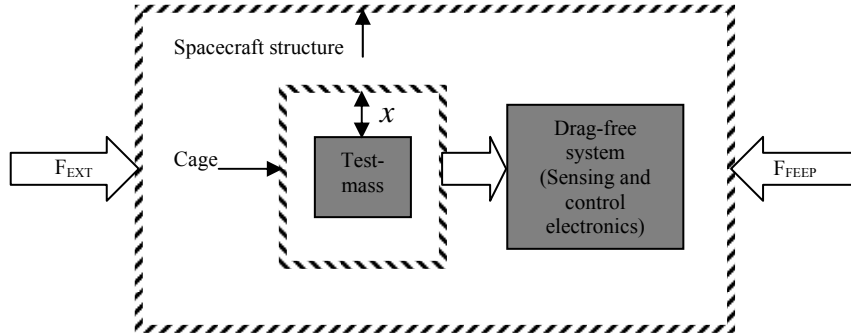
Figure 5.2: *Spacecraft drag-free concept.*

The development of drag-free technology is central to the exploitation of space as an environment for missions in fundamental physics. In addition to LISA, missions such as STEP [85], Gravity Probe B [86] and ASTROD [87] are key space missions that exploit drag-free technology to achieve their scientific goals. In these aforementioned missions, the key is to ensure that the test-mass (and not the surrounding spacecraft) remains in inertial space within the bandwidth required to achieve the science goal. This consideration leads naturally to a drag-free control system where the spacecraft is de-coupled as much as possible from the surrounding spacecraft. The acceleration, *a*, imposed on the test-mass by the spacecraft is given as

$$a \approx \frac{k_{eff}}{m} \Delta z \,, \tag{5.3}$$

where, k_{eff} is the effective stiffness or spring constant that couples the spacecraft to the test-mass of mass, *m*, and *Δz* is the motion of the test-mass relative to the spacecraft.

A perfect drag-free controller will position the spacecraft to minimise *Δz*, resulting in a residual displacement equal in magnitude to the sensor displacement noise,

δz. The spectrum of test-mass acceleration noise produced by spacecraft motion can then be written as

$$\delta a \approx \frac{k_{eff}}{m} \delta z \, . \tag{5.4}$$

However, it should be noted that there will be additional noise sources, such as thermal noise, which should be included in Equation 5.4 and that a more rigorous discussion can be found elsewhere [88]. Equation 5.4 is an important relationship when selecting a sensor design, as it demonstrates that a drag-free system can be realised by either decoupling the test-mass as much as possible from the spacecraft and using a low resolution sensor or by employing high sensitivity controller with a high stiffness. Clearly it is advantageous to reduce as much as possible both factors. In order to reduce k_{eff}, it is necessary to maximise the distance between the test-mass and spacecraft to eliminate electrostatic forces such as patch-fields [89] and forces due to charge accumulation from the space environment. Ultimately, k_{eff} will be limited by the gravity field of the spacecraft. Such a strategy may also minimise dissipative forces that lead to thermal noise.

Current techniques are largely focused on capacitive sensing, which is rather surprising given the above arguments. Capacitive sensors are intrinsically unstable (negative k_{eff}), apply substantial forces to the test-mass and require conducting surfaces in close proximity to it. Moreover, should an interferometric approach be taken, the bandwidth of the LISA instrument could potentially be extended to even lower frequencies. It is appreciated by the LISA scientific community that an extension of this bandwidth at low frequencies (to 10^{-5} Hz) would be extremely desirable to enable longer and more detailed observation of the inspiralling phase of coalescing black hole binaries of mass greater than 10^5 M$_\odot$ [90].

For EUCLID to be considered as a viable alternative to the capacitive sensor for LISA, there are a number of improvements that are now being incorporated into the design that are intended to further enhance the low frequency performance. For example, careful consideration of the laser source is required to avoid the laser frequency noise observed, also some VCSELs are now available with integrated Peltier elements, to

enable thermal stabilisation of the device. Ultimately, it is believed that the interferometer will be limited by the stability of the reference arm, due to the effects of thermal expansion of the substrate. It would therefore be necessary to construct the key components of the reference arm on an ultra low expansion (ULE) substrate, for example, by collaborating with the University of Glasgow, and using their hydroxide-catalysis bonding technique [91]. As a consequence of the aforementioned developments, two versions of EUCLID could result; the standard version optimised for high frequencies (EUCLID-HF) and a modified version optimised for low frequencies (EUCLID-LF). Figure 5.3 (left) provides an image of the EUCLID-LF 3D CAD design. Figure 5.3 (right) provides an image of a prototype device. The features of this design are beyond the scope of this document, but will be reported elsewhere in due course.
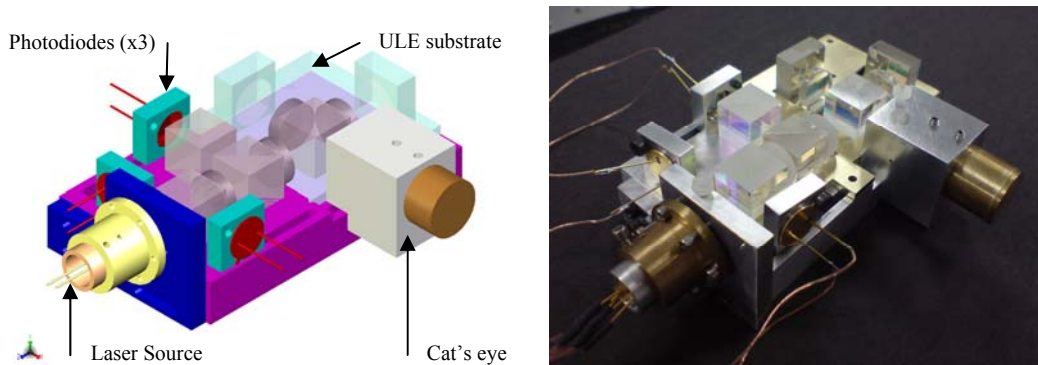
Figure 5.3: *EUCLID-LF concept and prototype images.*
(Left) EUCLID-LF 3D CAD concept. (Right) EUCLID-LF prototype realisation.

5.4 Summary

This thesis provides an account of the sources of gravitation waves and the instrumentation being employed in the search to make the first direct detection. The fundamental noise sources that constrain the performance of these instruments are also discussed. Detailed descriptions are then given of the development of two optical read-out schemes, including a crude shadow sensor employed in the Advanced LIGO BOSEM, and a more sophisticated compact interferometric sensor, known as EUCLID. Both of these aforementioned sensors are characterised and the performance of each is presented along with their respective noise budgets. The final section compares these two approaches to optical sensing and draws some conclusions from this work.

This work has been successful in mitigating the major concerns traditionally associated with using an interferometric approach to sensing. Historically, interferometers have been cumbersome, difficult to align, unreliable and potentially expensive to operate or maintain, due to the level of technical expertise required. However, by utilising emerging technologies, such as VCSELs and novel optical configurations, the alignment tolerances have been relaxed, thus making this technology accessible to non-experts.

EUCLIDs have recently been made available commercially and a number of units have been sold on to colleagues and collaborators at other institutes for further testing and characterisation. Initial feedback received has already been very positive, indicating that the EUCLID units are performing consistently with (or in excess of) the initial specification. However, a unit was recently returned and was diagnosed with a 'failed' VCSEL. Further investigation indicated that the threshold current characteristic of the device had deviated away from the datasheet value. It is unclear at present if this is a consequence of electrostatic discharge (ESD) damage caused by improper handing (or during shipping), or an effect of optical feedback, and enquiries are now being made to the distributor of these devices.

The next phase is to consider other potential spin-off ground-based and space-borne applications of EUCLID, including those outside the field of experimental gravitational research. In parallel, we are also seeking to improve the low frequency sensitivity and tilt immunity, whilst also attempting to drive down production costs.

Finally, it is timely to consider the original goals of this project, and if upon the completion of the project, they have been achieved. The first accomplishment was to provide Advanced LIGO with a sufficient quantity of compliant shadow sensors, on-time and on-budget. In this, we were successful, but it proved to be more technically demanding than originally expected and further illustrated just how close to the limit shadow-sensor technology is being pushed. The second goal was the development of a contingency sensor option for Advanced LIGO, i.e. the EUCLID interferometer. The design and characterisation of this device has been the greatest accomplishment of this project. Although there is still much to learn about its low frequency performance, it has resulted in spin-outs, leading to patents and commercialisation of this technology. Such accomplishments as these could never have been envisaged at the onset of the project.

References

[1]   I. Newton. *Philosophiae naturalis principia mathematica.* London. 1687.

[2]   H. Cavendish. *Experiments to determine the density of the Earth.* Philosophical Transactions of the Royal Society of London, Vol. 88, 469 – 526. 1798.

[3]   A. Einstein. *Zur elektrodynamik bewegter Körper.* Annalen der Physik, 17. Berlin. 1905.

[4]   A. Einstein. *Die grundlage der allgemeinen relativitätstheorie.* Annalen der Physik, 49. Berlin. 1916.

[5]   P. Saulson. *Fundamentals of interferometric gravitational wave detectors.* World Scientific. 1994.

[6]   LISA Study Team. *Pre-phase A report.* 2nd edition corrected version 2.09. 1998.

[7]   K. Belczynski *et al*. *A comprehensive study of binary compact objects as gravitational wave sources: evolutionary channels, rates, and physical properties.* Astrophysical Journal, 572 407. 2002.

[8]   C. Cutler and K. S. Thorne. *An overview of gravitational wave sources.* Proceedings of the 16th International Conference on General Relativity and Gravitation (pp. 72-112). World Scientific. 2002.

[9]   J. Weber. *Detection and generation of gravitational waves.* Physical Review, Vol. 1, 306 – 313. 1960.

[10]   A. de Waard, L. Gottardi, and G. Frossati. *MiniGRAIL progress report 2001: the first cooldown.* Classical and Quantum Gravity, 19, 1935–1941. 2002.

[11]   R. A. Hulse and J. H. Taylor. *Discovery of a pulsar in a binary system.* Astrophysical Journal, 195:L51–L53. 1975.

[12]   J. H. Taylor, R. A. Hulse, L. A. Fowler, G. E. Gullahorn, and J. M. Rankin. *Further observations of the binary pulsar PSR 1913+16.* Astrophysical Journal, 206:53–58. 1976.

[13]   J. H. Taylor and J. M. Weisberg. *A new test of general relativity: gravitational radiation and the binary pulsar PSR 1913+16.* Astrophysical Journal, 253:908–920. 1982.

[14]   J. M. Weisberg and J. H. Taylor. *The relativistic binary pulsar B1913+16: thirty years of observations and analysis.* ASP Conference Series, Vol. 328. 2005.

[15]   A. A. Michelson and E. W. Morley. *On the relative motion of the Earth and the luminiferous ether.* American Journal of Science, 34: 333–345. 1887.

[16]   F. A. E. Pirani. *On the physical significance of the Riemann tensor.* Acta. Phys. Polon., 15:389, 1956.

[17]   G. F. Moss, L. R. Miller, and R. L. Forward. *Photon-noise-limited laser transducer for gravitational antenna.* Applied Optics, 10:2495–2498. 1971.

[18]   R. L. Forward. *Wideband laser-interferometer gravitational-radiation experiment.* Physical Review D, 17, 379. 1978.

[19]   D. Sigg for the LIGO Scientific Collaboration. *Status of the LIGO detectors.* Classical and Quantum Gravity, 25, 114041. 2008.

[20]   G. Harry for the LIGO Scientific Collaboration. *Advanced LIGO: the next generation of gravitational wave detectors.* Twelfth Marcel Grossmann proceedings, P0900255-v5. 2009.

[21]   H. Grote and the LIGO Scientific Collaboration. *The GEO 600 status.* Classical and Quantum Gravity, 27, 084003. 2010.

[22]   F. Acernese *et al*. *Virgo status*. Classical and Quantum Gravity, 25, 184001 2008.

[23]   D. Tatsumi *et al*. *Current status of Japanese detectors*. Classical and Quantum Gravity, 24, S399. 2007.

[24]   LIGO Laboratory. http://www.ligo.caltech.edu/cit_local.html

[25]   P. Barriga *et al*. *AIGO: a southern hemisphere detector for the worldwide array of ground-based interferometric gravitational wave detectors*. Classical and Quantum Gravity, 27, 084005. 2010.

[26]   R. Weiss *et al*. *Report of the committee to compare the scientific cases for two gravitational-wave detector networks: (AHLV) Australia, Hanford, Livingston, VIRGO; and (HHLV) two detectors at Hanford, one at Livingston, and VIRGO*. LIGO-T1000251-v1. 2010.

[27]   K. Kuroda and the LCGT Collaboration. *Status of LCGT*. Classical and Quantum Gravity, 27, 084004. 2010.

[28]   M. Punturo *et al*. *The Einstein Telescope: a third-generation gravitational wave observatory*. Classical and Quantum Gravity, 27, 194002S. 2010.

[29]   S. Sato *et al*. *DECIGO : The Japanese space gravitational wave antenna*. Journal of Physics Conference Series, 154, 012040. 2009.

[30]   J. Baker *et al*. *LISA: Probing the universe with gravitational waves.* LISA-LIST-RP-436, 1.0 1-117. 2007.

[31]   M. Armano *et al*. *LISA Pathfinder: the experiment and the route to LISA*. Classical and Quantum Gravity, 26, 094001. 2009.

[32]   T. Torrey *et al*. *Shot noise in gravitational-wave detectors with Fabry–Pérot arms.* Applied Optics, Vol. 39, No. 36. 2000.

[33]   M. Ando *et al*. *DECIGO pathfinder*. Classical and Quantum Gravity, 26, 094019. 2009.

[34]   A. Yariv. *Optical electronics.* 3rd edition, Holt, Rinehart and Winston, Inc. 1985.

[35] J. B. Johnson. *Thermal agitation of electricity in conductors.* Physical Review, Vol. 32, p. 97. 1928.

[36] Texas Instruments. *Noise analysis in operational amplifier circuits.* Application Report. 2007.

[37] R. Weiss. *Electromagnetically coupled broadband gravitational antenna.* Quarterly Reports of the Research Laboratory of Electronics, MIT. 105, p. 54. 1973.

[38] C. M. Caves. *Quantum-mechanical radiation-pressure fluctuation in an interferometer.* Physical Review, Vol. 45, 75 – 79. 1980.

[39] D. K. Owens and R. Weiss. *Measurement of the phase fluctuations in a He-Ne Zeeman laser.* Review of Scientific Instruments, 45(9):1060-1062. 1974.

[40] J. M. Babcock *et al*. *Relationships between ocean bottom noise and the environment.* Bulletin of the Seismological Society of America, Vol. 84. 1994.

[41] J. Peterson. *Observations and modelling of seismic background noise.* Open-File Report, 93-322. 1993.

[42] J. Harms *et al*. *Characterization of seismic environment at the Sanford underground laboratory, South Dakota.* Classical and Quantum Gravity, 27, 225011. 2010.

[43] B. S. Melton and D. P. Johnson. *Inertial seismograph design – limitations in principle and practise*. Proc. IRE 50 2328. 1962.

[44] N. A. Robertson, R. W. P. Drever, I. Kerr and J. Hough. *Passive and active seismic isolation for gravitational radiation detectors and other instruments.* J. Phys. E: Sci. Instrum., Vol. 15. 1982.

[45] M. Beker *et al*. *Towards time domain finite element analysis of gravity gradient noise.* Journal of Physics, Conference Series, 228, 012034. 2010.

[46]   M. Tinto and J. W. Armstrong. *Cancellation of Laser Noise in an unequal-arm interferometer detector of gravitational radiation.* Phys. Rev. D, 59, 102003. 1999.

[47]   S. Larson. *Sensitivity curves for spaceborne gravitational wave observatories.* http://www.srl.caltech.edu/~shane/sensitivity/index.html.

[48]   M. L. Gorodetsky. *Thermal noises and noise compensation in high-reflection multilayer coating.* Physics Letters A, A , vol. 372, no. 46, pp. 6813-6822, 2008.

[49]   J. Greenhalgh. *UK scope document.* LIGO-M030162-D-K. 2008.

[50]   N. A. Robertson *et al*. *Quadruple suspension design for Advanced LIGO.* Classical and Quantum Gravity, 19, 4043–4058. 2002.

[51]   N. A. Robertson *et al*. *Seismic isolation and suspension systems for Advanced LIGO.* Proceedings of SPIE Vol. 5500. 2004.

[52]   M. V. Plissi *et al*. *An investigation of eddy-current damping of multi-stage pendulum suspensions for use in interferometric gravitational wave detectors.* Rev. Sci. Instrum, 75, 4516-4522, 2004.

[53]   K. Strain. *Advanced LIGO suspensions general interpretation of requirements for sensors - for use as an initial planning aid by the UK project team v1.01.* ALUKGLA0005aJUN03. 2003.

[54]   K. Strain. *Input to the OSEM selection review decision.* LIGO-T040110-01-K. 2004.

[55]   P. Fritschel. *Report on Advanced LIGO OSEM follow-up review.* LIGO-L040074-00-E. 2004.

[56]   A. Lazzarini *et al*. *LIGO vacuum compatibility, cleaning methods and qualification procedures.* LIGO-E960022- B- E. 2003.

[57]   D. Coyne *et al*. *LIGO vacuum compatible materials list.* LIGO-E960050-v4. 2009.

[58]   C. Speake. *Optoelectronic detectors; BIPM designs.* ALUKUOB0001aJUN03. 2003.

[59]   N. Lockerbie. *Technical note on the Strathclyde OSEM development.* LIGO-T040052-00-K. 2004.

[60]   P. Fritschel. *Characterization and comparison of a potential new local sensor.* LIGO-T990089-00. 1999.

[61]   N. Lockerbie. *Measurement of LIGO hybrid OSEM sensitivity.* LIGO-T040106-01-K. 2004.

[62]   N. Lockerbie. *Measurement of shadow-sensor displacement sensitivities.* LIGO-T040136-00-K. 2004.

[63]   N. Lockerbie. *Private Communication.*

[64]   J. Romie. *Hybrid OSEM assembly specification.* LIGO-E030084-02-D. 2003.

[65]   K. Strain. *Increased strength Advanced LIGO ITM/ETM suspension PM and UIM actuators.* LIGO-T060001-00-K. 2006.

[66]   D. Coyne, S. Aston and D. Hoyland. *(ICD) Suspension, UK scope – suspension, US scope.* LIGO-E050160-01. 2006.

[67]   M. Barton. *Private Communication.*

[68]   N. Robertson *et al. Resolution of BOSEM FDR and FRR design issues.* LIGO Laboratory. LIGO-L080076-00-R. 2008.

[69]   S. Aston and D. Lodhia. *BOSEM assembly specification.* LIGO-T060233-03-K. 2008.

[70]   D. Lodhia and S. Aston. *BOSEM test specification.* LIGO-T070107-08-K. 2009.

[71]   N. Lockerbie. *OP232 IR LED + SMD2420 photodiode: output vs flag displacement.* LIGO-T040178-00-K. 2004.

[72]   S. Aston. *BOSEM design document and test report.* T050111-04-K. 2009.

[73]   F. Acernese *et al. An optical readout system for the LISA gravitational reference sensors.* Classical and Quantum Gravity, 21 S621–S627. 2004.

[74]   R. Safaisini. *Impact of thermal management on vertical-cavity surface-emitting laser (VCSEL) power and speed.* Ph.D Dissertation, Electrical and computer Engineering Department. Colorado State University. 2011.

[75]   J. N. Dukes and Gary B. Gordon. *A two-hundred-foot yardstick with graduations every microinch.* Hewlett-Packard Journal, 21(12). 1970.

[76]   K. W. Raine and M. J. Downs. *Beam-splitter coatings for producing phase quadrature interferometer outputs.* Journal of Modern Optics, 25(7). 1978.

[77]   M. J. Downs and K. W. Raine. *An unmodulated bi-directional fringe counting interferometer system for measuring displacements.* Precision Engineering, 1(2):85-88. 1979.

[78]   V. Greco, G. Molesini and F. Quercioli. *Accurate polarization interferometer.* Review of Scientific Instruments, 66(7):3729-3734. 1995.

[79]   F. E. Peña-Arellano and C. C. Speake. *Mirror tilt immunity interferometry with a cat's eye retroreflector.* Applied Optics, Vol. 50, No. 7. 2011.

[80]   P. Welch. *The use of fast Fourier transform for the estimation of power spectra: a method based on time averaging over short, modified periodograms.* IEEE Trans. Audio Electroacoust. Vol. AU-15. 1967.

[81]   G. Heinzel, A. Rüdiger and R. Schilling. *Spectrum and spectral density estimation by the discrete Fourier transform (DFT), including a comprehensive list of window functions and some new flat-top windows.* ESA LISA Pathfinder document archive. 2002.

[82]   J. Volder. *The CORDIC trigonometric computing technique.* IRE Transactions on Electronic Computers, pp330-334. 1959.

[83]   H. Panjwani, L. Carbone and C. Speake. *Laboratory searches for preferred frame effects: ongoing work and results at Birmingham.* Proceedings of 5th Meeting on CPT and Lorentz Symmetry. 2010.

[84]   D. Coyne *et al*. *LIGO vacuum compatible materials list.* LIGO-E960050-v9. 2010.

[85]   J. W. Cornelisse. *STEP mission and system design.* Classical and Quantum Gravity, 13 A59. 1996.

[86]   J. W. Conklin and the Gravity Probe B Collaboration. *The Gravity Probe B experiment and early results.* Journal of Physics, Conference Series, 140 012001. 2008.

[87]   W. T. Ni. *ASTROD and ASTROD I - overview and progress.* International Journal of Modern Physics D, Vol. 17, No. 7, 921–940. 2008.

[88]   C. C. Speake and P. L. Andrews. *Capacitive sensing for drag-free satellites.* Classical and Quantum Gravity, 14 1557. 1997.

[89]   C. C. Speake. *Forces and force gradients due to patch fields and contact-potential differences.* Classical and Quantum Gravity, 13 A291. 1996.

[90]   S. A. Hughes and D. E. Holz. *Cosmology with coalescing massive black holes.* Classical and Quantum Gravity, 20, S65-S72. 2003.

[91]   E. J. Elliffe *et al*. *Hydroxide-catalysis bonding for stable optical systems for space.* Classical and Quantum Gravity, 22 S257. 2005.

Publications, Conference Proceedings and

Patents Granted

[92]   C. C. Speake and S. M. Aston. *Interferometric sensing for drag-free satellites.* Proceedings of SPIE Vol. 5500. 2004.

[93]   C. C. Speake and S. M. Aston. *An interferometric sensor for satellite drag-free control.* Classical and Quantum Gravity. 22, S269–S277. 2005.

[94]   A. M. Cruise, D. Hoyland and S. M. Aston. *Implementation of the phasemeter for LISA LTP.* Classical and Quantum Gravity. 22, S165–S169. 2005.

[95]   S. M. Aston and C. C. Speake. *An interferometric based optical read-out scheme for the LISA proof-mass.* 6th International LISA Symposium, CP873. 2006.

[96]   C. Speake, S. Aston, F. Pena Arellano and T. Copland. *Improved interferometer.* International Patent Publication Number, WO 2009/010750(A1). 2009.

[97]   C. Speake, S. Aston and F. Pena Arellano. *Innovative laser interferometric angular read-out device.* International Patent Publication Number, WO 2011/061514(A1). 2011.

Appendix A - Acronym List

Acronym	Description
ADC	Analogue to Digital Converter
AIGO	Australian International Gravitational Observatory
AOM	Acousto-Optic Modulators
ASTROD	Astrodynamical Space Test of Relativity using Optical Devices
ATE	Automated Test Equipment
BIPM	Bureau International des Poids et Mesures
BOSEM	Birmingham Optical Sensor and Electro-Magnet Actuator
CAD	Computer Aided Design
COTS	Commercial off the shelf
DECIGO	Deci-hertz Interferometer Gravitational Wave Observatory
DFB	Distributed Feedback Lasers
DPF	DECIGO Pathfinder
EOM	Electro-Optic Modulators
ESA	European Space Agency
ET	Einstein Telescope
EUCLID	Easy to Use Compact Laser Interferometric Device
FEEP	Field Effect Electron Propulsion
FPGA	Field Programmable Gate Array
GEO	German-British Gravitational Wave Observatory
GUI	Graphical User Interface
IRLED	Infra-Red LED
ISAS	Institute of Space and Astronautical Science
JAXA	Japan Aerospace Exploration Agency
LCGT	Large Cryogenic Gravitational Telescope
LHO	LIGO Hanford Observatory
LIGO	Laser Interferometric Ground Observatory
LISA	Laser Interferometer Space Antenna
LLO	LIGO Livingston Observatory
LPF	LISA Pathfinder
NASA	National Aeronautics and Space Administration
OSA	Optical Spectrum Analyser
PD	Photodiode
PEEK	Polyether ether ketone
PSD	Position Sensitive Devices
PTFE	Polytetrafluoroethylene
SNR	Signal to Noise Ratio
SQUID	Superconducting Quantum Interference Device
STEP	Satellite Test of the Equivalence Principle
STFC	Science and Technology Facilities Council
TAMA	Japanese Gravitational Wave Observatory
TEC	Thermoelectric Cooler
TO	Transistor Outline
UHV	Ultra High Vacuum
UK	United Kingdom
ULE	Ultra Low Expansion
USA	United States of America
UV	Ultraviolet
VCSEL	Vertical Cavity Surface Emitting Laser
VIRGO	French-Italian Gravitational Wave Observatory

Table A.1: *Acronym list.*

Appendix B - Connector Specifications and

Pin-outs

The connector located on the BOSEM head is a right angle, PCB mounting, 9 way, male micro D, part number MR7590-9P-1BSN-MC225 and is manufactured by GlenAir. Pin-outs for the BOSEM connector can be found in Table A.2.

Pin #	Signal Name	Description
1	PD-K	Photodiode Cathode
6	PD-A	Photodiode Anode
2	IRLED-A	IR Emitter Anode
7	IRLED-K	IR Emitter Cathode
3	-	Not Connected (on the BOSEM head side)
8	-	Not Connected (on the BOSEM head side)
4	FN	End of coil winding
9	ST	Start of coil winding
5	Shield	Not Connected (on the BOSEM head side)

Table A.2: *BOSEM connector pin-outs.*

The connector located on the EUCLID enclosure is a right angle, PCB mounting, 15 way, male Micro D, part number MR7590-15P-1BSN-MC225 (REV A) and is manufactured by GlenAir. Pin-outs for this connector can be found in Table A.3.

Pin #	Signal Name	Description
1	PD1-K	Photodiode 1 Cathode (-cosine)
9	PD1-A	Photodiode 1 Anode (-cosine)
2	PD2-K	Photodiode 2 Cathode (+sine)
10	PD2-A	Photodiode 2 Anode (+sine)
3	PD3-K	Photodiode 3 Cathode (+cosine)
11	PD3-A	Photodiode 3 Anode (+cosine)
4	-	Not Connected
12	-	Not Connected
5	LD-A	Laser diode Anode
13	LD-K	Laser diode Cathode
6	-	Not Connected
14	T1	Thermistor Terminal 1
7	T2	Thermistor Terminal 2
15	TEC-	Peltier Element Cathode
8	TEC+	Peltier Element Anode

Table A.3: *EUCLID connector pin-outs.*

Appendix C - List of Materials

The complete list of materials, and their Advanced LIGO ultra high vacuum compatibility status, used during the construction of the BOSEM, is provided in Table A.4.

Item #	Material	Where Used	Advanced LIGO UHV Approval Status
1	Beryllium Copper (ASTM-B194)	Male Connector	Approved
2	Phosphor Bronze (ASTM-139)	Female Connector and Emitter Lens Carrier	Approved
3	Gold (ASTM-B488)	Connector pin/socket Plating	Approved
4	Aluminium (Alloy 6082) see T050171-01	Connector Body, Coil-former, Mounting Plates	Approved
5	Electroless Nickel (ASTM B733-90,SC2,Type 1, Class J (MIL-C-26074)	Connector Body Finish	Approved
6	LCP (MIL-M-24519)	Connector Insulators and Inserts	Restricted
7	Hysol Epoxy #4215 (Black)	Connector Encapsulant	Approved
8	Stainless Steel (300 per SAE-AMS-QQ-S-763)	Connector Jackscrews and Posts	Approved
9	Copper Wire (32QML)	Coil Winding	Approved
10	Copper Wire (CZ1104)	Harness	Approved
11	Kapton (LF0110) Copper Clad (LF8515)	Flexible Circuit	Approved
12	Teflon PFA-440HP (DuPont)	Assembly Tooling	Restricted
13	PEEK 450G (Victrex)	Adjuster Mechanism	Restricted
14	Titanium	Adjustment Assembly and Sensor Carrier	Approved
15	Optek OP232	IRLED (Original)	Approved
16	Vishay TSTS7100	IRLED (Final Article)	Approved
17	Centronic BPX65	Photodiode	Approved

Table A.4: *BOSEM full materials list and vacuum compatibility status.*

The complete list of materials, and their Advanced LIGO ultra high vacuum compatibility status, used during the construction of EUCLID, is provided in Table A.5.

Item #	Material	Where Used	Advanced LIGO UHV Approval Status
1	Beryllium Copper (ASTM-B194)	Male Connector	Approved
2	Phosphor Bronze (ASTM-139)	Female Connector	Approved
3	Gold (ASTM-B488)	Connector pin/socket Plating	Approved
4	Aluminium (Alloy 6082)	Connector Body, EUCLID Structure	Approved
5	Electroless Nickel (ASTM B733-90,SC2,Type 1, Class J (MIL-C-26074)	Connector Body, Finish	Approved
6	LCP (MIL-M-24519)	Connector Insulators and Inserts	Restricted
7	PEEK 450G (Victrex)	Photodiode and VCSEL Mounts	Restricted
8	Hysol Epoxy #4215 (Black)	Connector Encapsulant	Approved
9	Stainless Steel (300 per SAE-AMS-QQ-S-763)	Connector Jackscrews and Posts	Approved
10	Kapton (LF0110) Copper Clad (LF8515)	Flexible Circuit	Approved
11	Firecomms RVS665T	VCSEL diode	Not tested
12	Centronic OSD15-5T	Photodiode	Not tested
13	Norland NOA61 UV Curing Optical Adhesive	Bonding Optical Components	Not Approved

Table A.5: *EUCLID full materials list and vacuum compatibility status.*

Appendix D - IRLED Screening Procedure

Overview of IRLED screening procedure (adapted from version 3).

The following steps were generated, so that they could be carried out by Birmingham technical support staff.

Preparation Tasks

(1) Turn OFF laboratory fluorescent lights, low-voltage halogen lights can be left ON.

(2) Other non-essential laboratory equipment should be turned OFF (soldering irons etc).

(3) Turn ON power supply unit (LT30-2).

      (a) Observe single red light (middle) illuminate on PSU.

      (b) Observe three green lights illuminate on Satellite Box.

(4) Turn ON low-noise preamplifier (SR560).

(5) Conduct visual check that SR560 front-panel settings are indicated as follows,

      (a) Filter Cutoffs (Hz) = DC, Coupling = AC, Source = A-B,

      (b) Gain Mode = Low-Noise, Gain = 1, Power = Line

(6) Turn ON dynamic signal analyzer (35670A).

      (a) Wait for unit to complete booting procedure.

      (b) Insert set-up disk into floppy drive.

      (c) Select "Recall/Recall State" ensure "Stat1.sta" selected and press "Enter".

(7) Turn ON DVM (T120B).

      (a) Ensure configured for 20 V DC range.

(8) Connect BNC co-ax cable between LNP (50 Ω output) and DSA (channel 1 input).

Screening Steps

(9) Select an alternative IRLED device (TSTS7100) at random from picking tray.

(10) Conduct visual inspection of device batch number (should be from batch #001).

(11) Insert IRLED into open-light fixture teflon mount, with leads protruding from rear.

(12) Connect IRLED to power lead ensuring polarity is correct as follows,

      (a) Device tab should be in 7-8 o'clock orientation.

      (b) Positive / anode (red cable) will be located on the left hand side.

      (c) Correct polarity confirmed if red LED (A) on Satellite Box is extinguished

(13) Slowly translate the photodiode along the open-light fixture towards the IRLED

(14) Monitor the voltage reading on the DVM and stop when voltage peak is reached (i.e. at the focus of IRLED beam). Ensure it is not saturated at 13.5 V, if it is, then back voltage off to approximately 12.9 V. If the peak voltage is below 10 V then reject IRLED (due to low intensity output).

(15) Use a fixing screw to lock the photodiode at this peak position.

(16) Cover the entire assembly with the aluminium foil box (to limit stray light).

(17) Ensure the low-noise preamplifier is not over-ranged (if so then wait).

(18) Ensure the dynamic signal analyzer is not over-ranged (if so then wait).

(19) Press "Start" button on dynamic signal analyzer.

(20) Wait while measurements are taken (nominally 10 averages take ~100 seconds).

(21) When "averaging complete" read marker value at 10 Hz.

      (a) if equal to -110dB V/$\sqrt{\text{Hz}}$ or lower then it's a PASS

      (b) otherwise it's a FAIL

(22) For IRLEDs that pass, save trace to disk, Select "Save/Save Data/Save Trace/Into File" ensure "Trac#.txt" selected and press "Enter". Remove IRLED from screening jig and place in burn-in jig.

(23) For devices that fail, remove IRLED from screening jig and put in "Failed" bin do not save trace.

(24) Repeat screening procedure for number of IRLEDs required.

(25) When complete, to shut-down equipment safely, reverse preparation steps 1-7.

Appendix E - Wiring Diagram
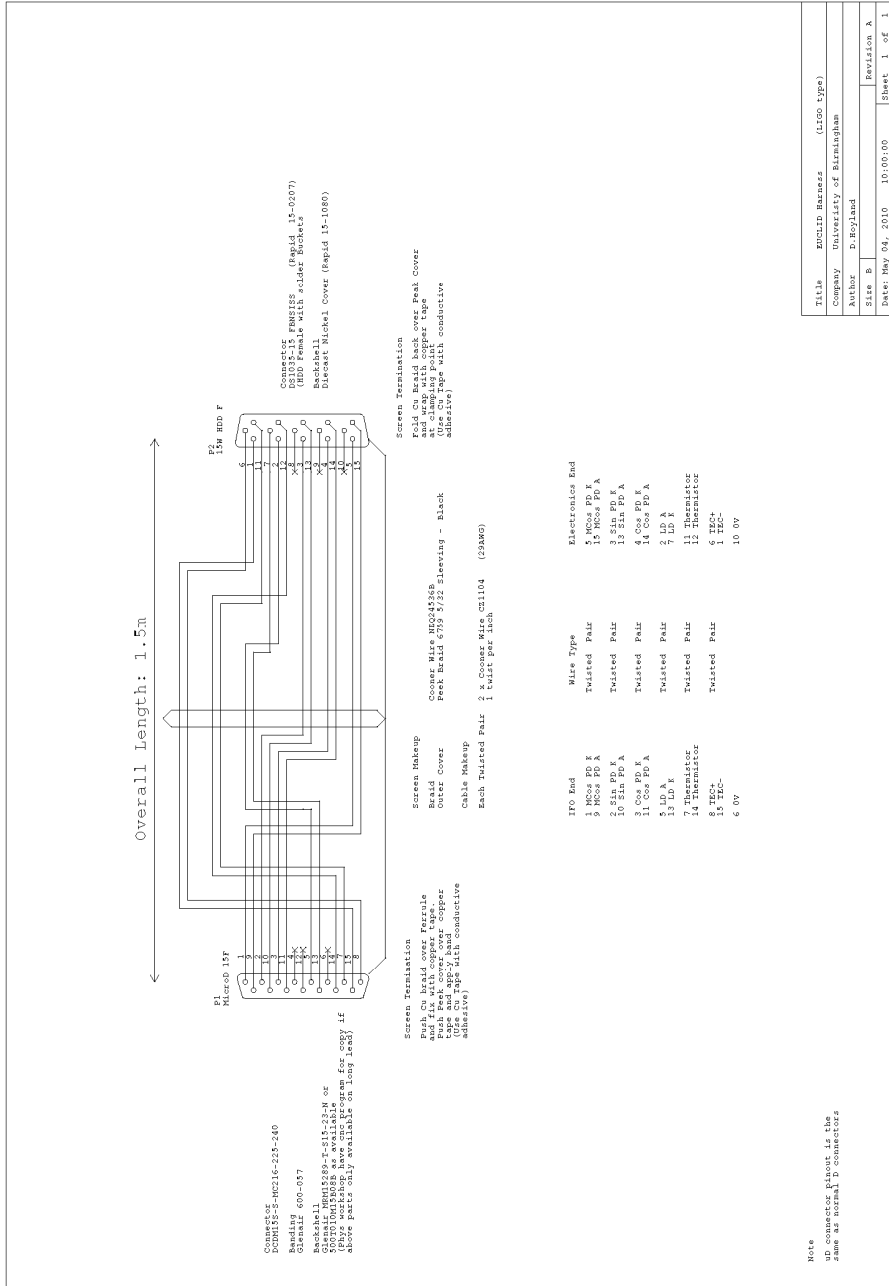
Figure A.1: *EUCLID harness wiring diagram.*

Appendix F - BOSEM 2D CAD Drawings

Figure A.2: *BOSEM top-level assembly (D060218).*

The drawing title block contains the following information:

REV.	DATE	DCN #	DRAWING TREE #
A	4 NOV 05	E060262	E060243
B	1 APR 07	E060262	E060243
C	12 DEC 07	E060262	E060243

ITEM NO	REQ	SPARE	TOT	PART NUMBER	DESCRIPTION
4	1	1	2		PD (BPX65)
3	1	1	2	D060114	PD Retainer
2	1	1	2	D060117	PD Sleeve
1	1	1	2	D060112	PD Carrier

NOTES: (UNLESS OTHERWISE SPECIFIED)

DIMENSIONS ARE IN INCHES

TOLERANCES:
.XX ± 0.01
.XXX ± 0.005
ANGULAR ± 0.5 °

1. DO NOT SCALE FROM DRAWING
2. REMOVE ALL SHARP EDGES R.02 MAX
3. ALL MACHINING FLUIDS SHALL BE WATER SOLUBLE AND FREE OF SULFUR, CHLORINE AND SILICONE SUCH AS CINCINNATI MILACRON'S CIMTECH 410 [STAINLESS STEEL]
4. ASSEMBLE ACCORDING TO THOSE PROTOTYPE OSEM ASSEMBLY SPECIFICATION.

MATERIAL

FINISH

	NAME	DATE
DRAWN	S.Brookes	26 JUN 06
CHECKED	S.Aston	12 OCT 06
APPROVED	A. Vecchio	30 OCT 06

CALIFORNIA INSTITUTE OF TECHNOLOGY
MASSACHUSETTS INSTITUTE OF TECHNOLOGY
IGR, GLASGOW UNIVERSITY GEO 600 GROUP
UNIVERSITY OF BIRMINGHAM

LIGO   ADVANCED LIGO

SYSTEM SUS

SUB-SYSTEM

NEXT ASSY D060218 BOSEM Assembly

PART NAME PD Assembly

SIZE A   DWG. NO. D060217   REV. C

SCALE 1:2   PROJECTION: SHEET 1 OF 1

SECTION A-A
SCALE 2 : 1

Figure A.3: *BOSEM photodiode carrier assembly (D060217).*
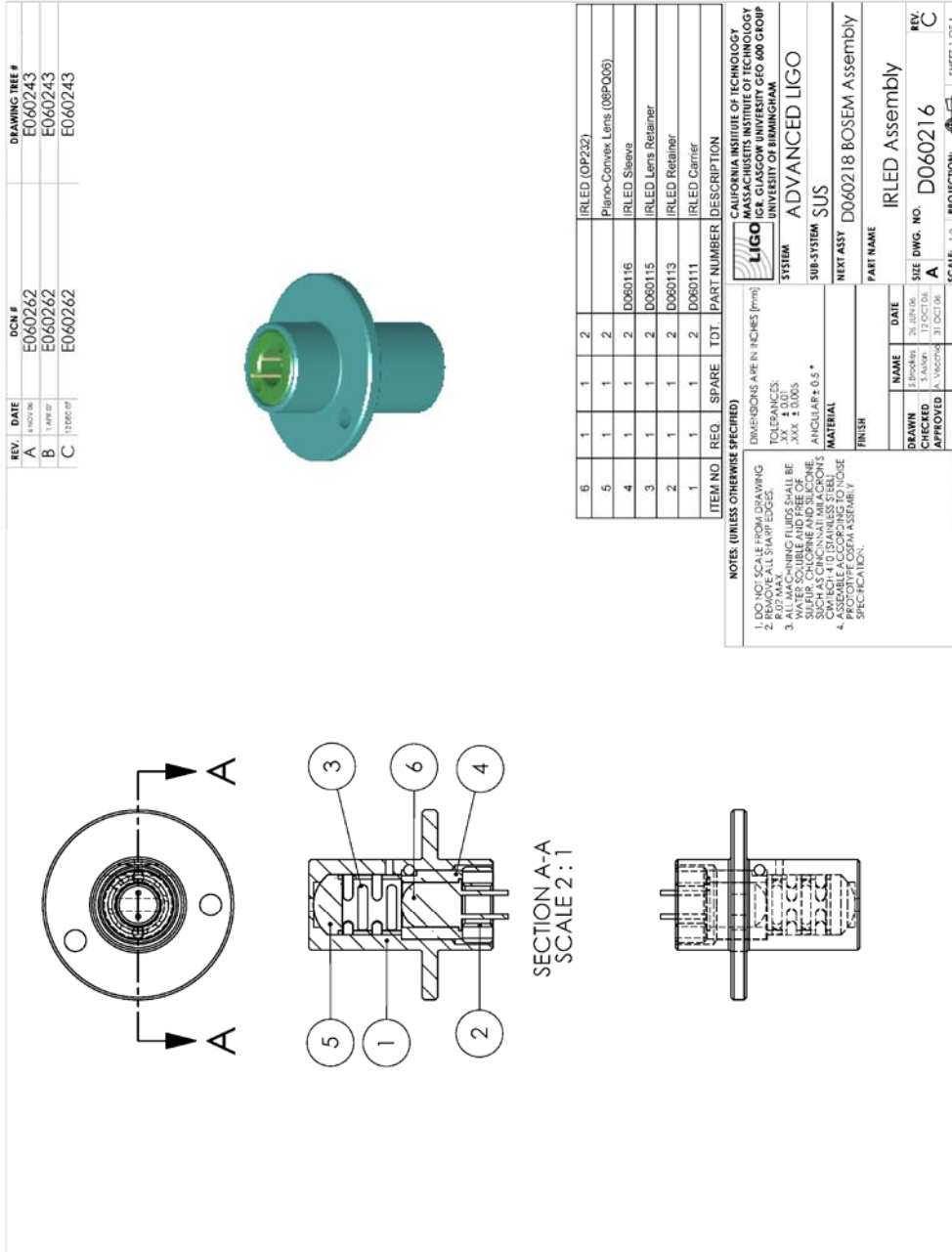
Figure A.4: *BOSEM IRLED carrier assembly (D060216).*
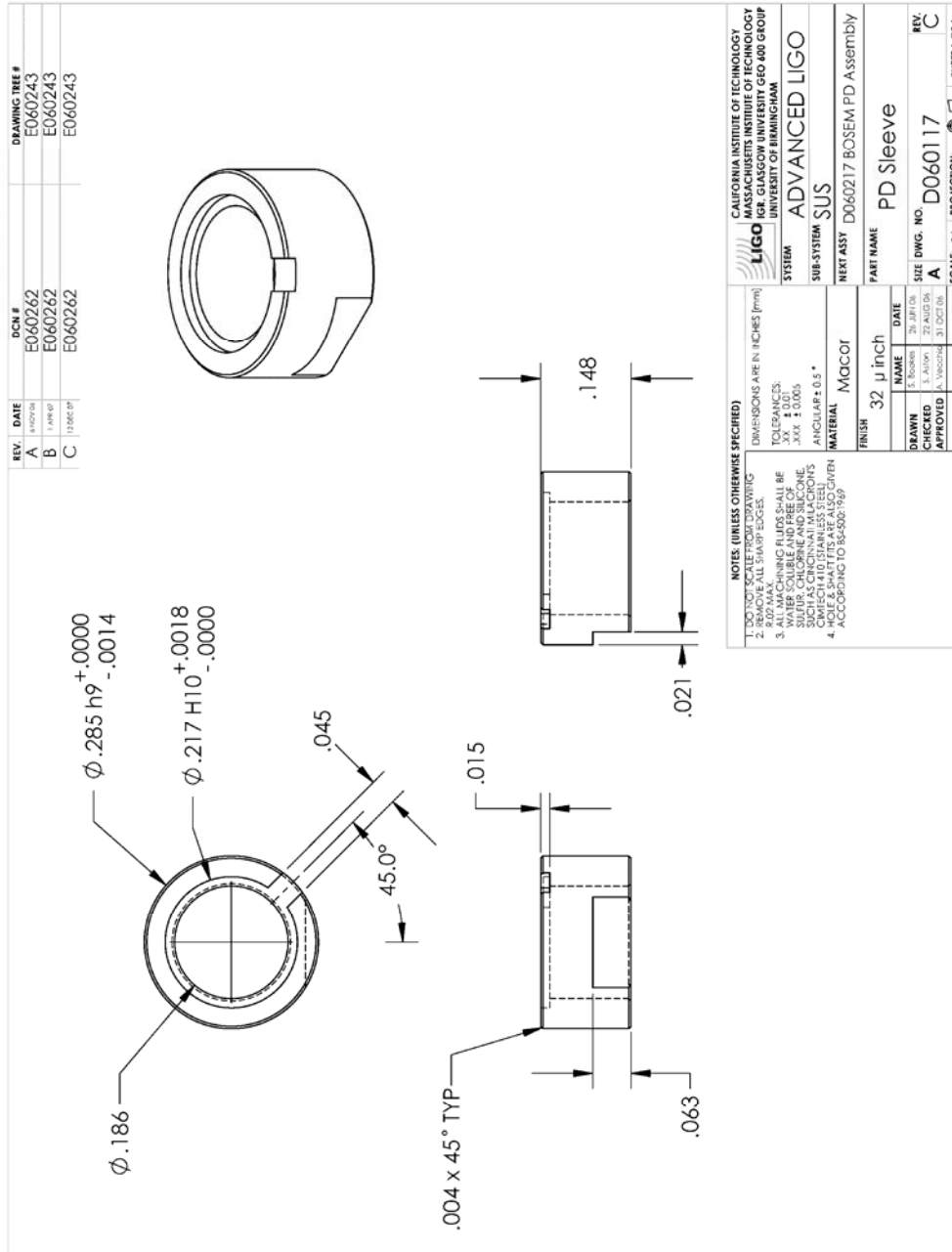
Figure A.5: *BOSEM photodiode sleeve (D060117).*
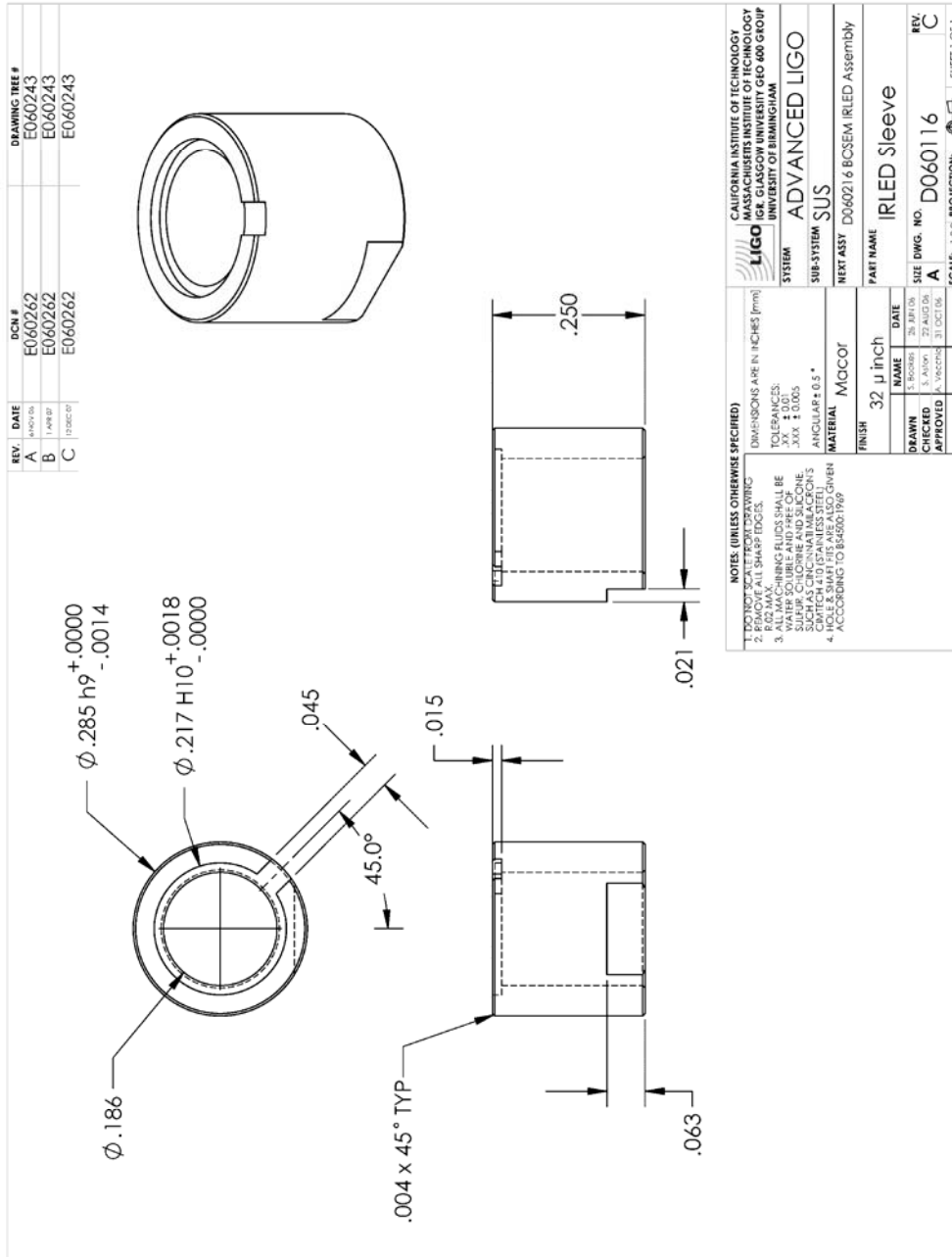
Figure A.6: *BOSEM IRLED sleeve (D060116).*
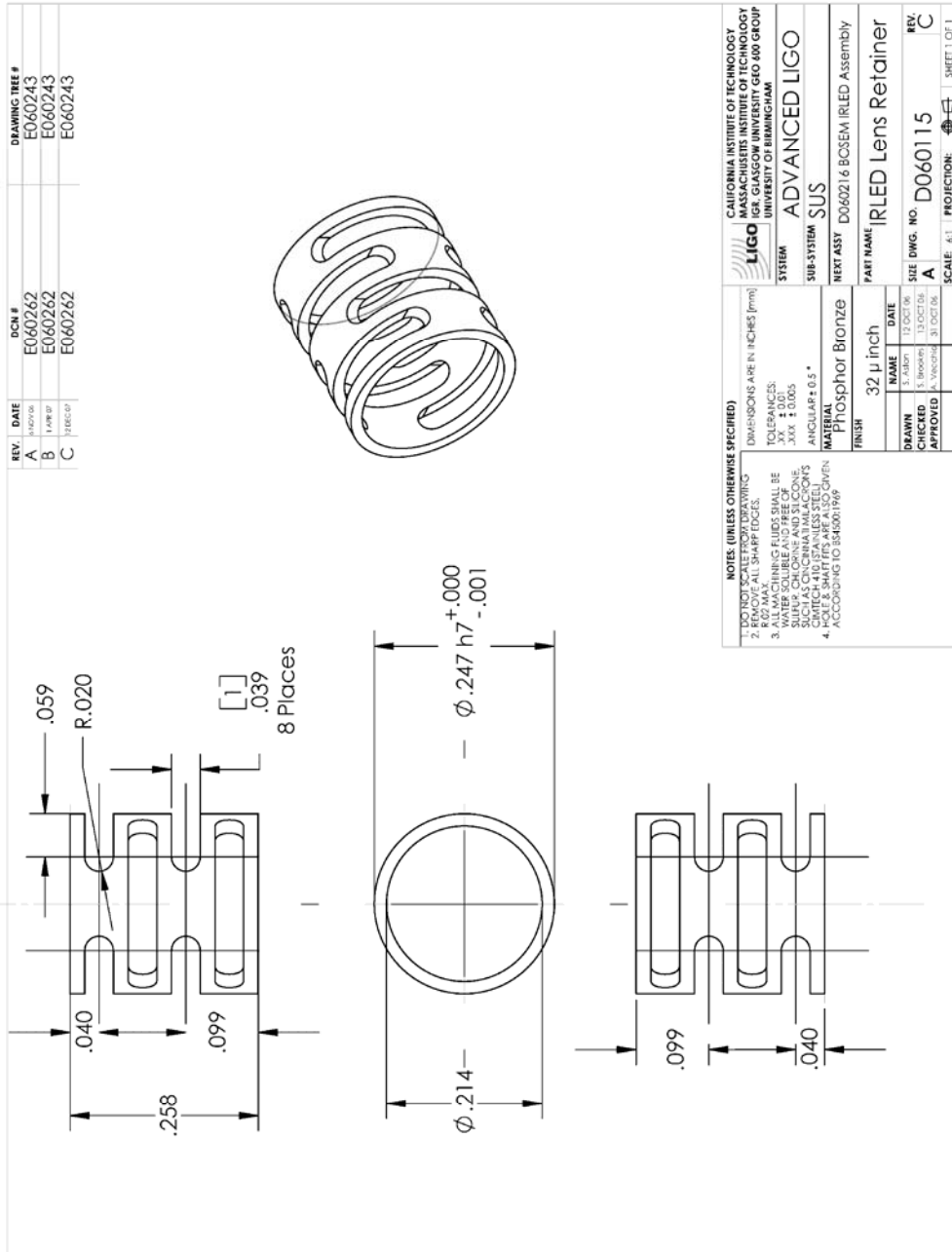
Figure A.7: *BOSEM IRLED lens retainer (D060115).*
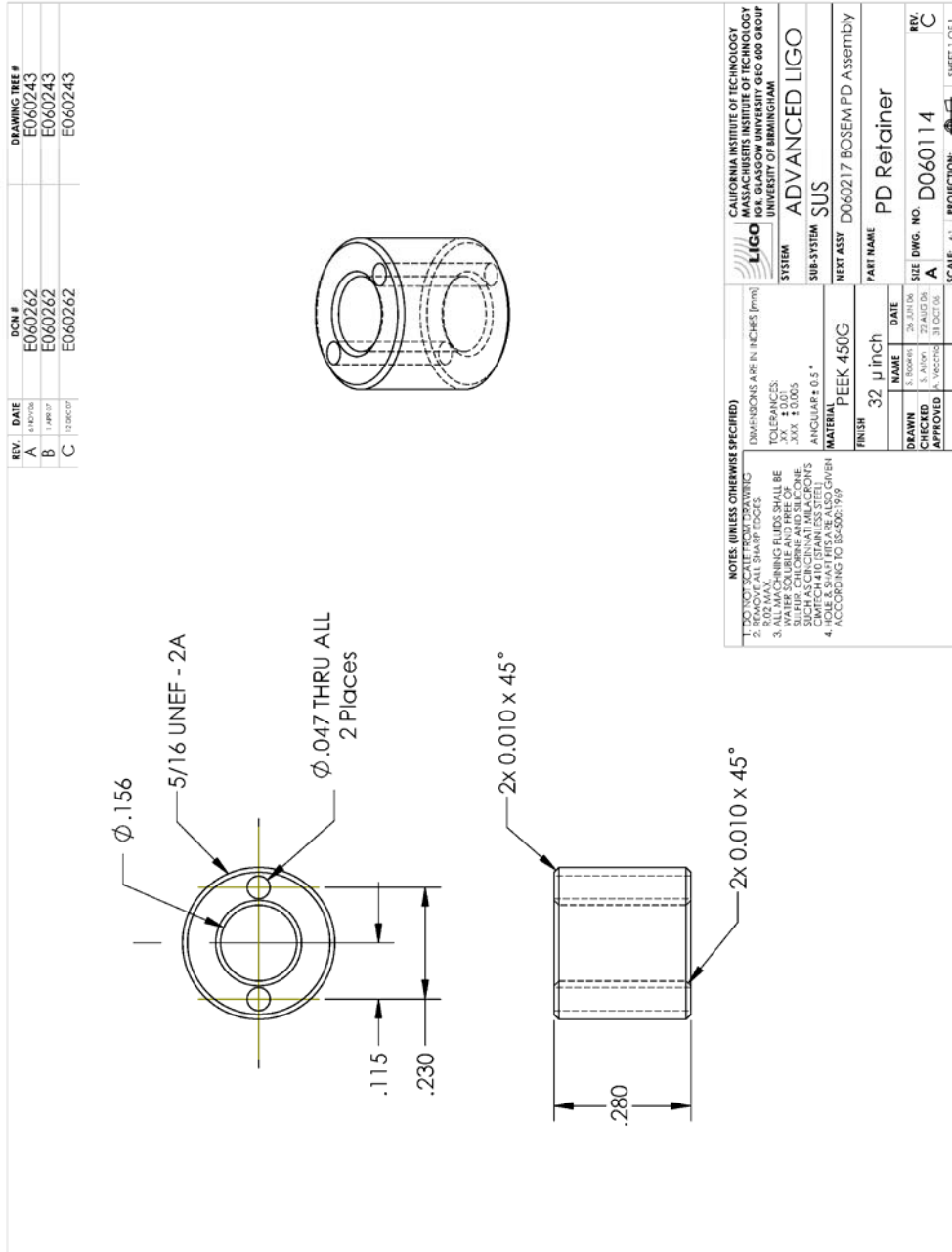
Figure A.8: *BOSEM photodiode retainer (D060114).*
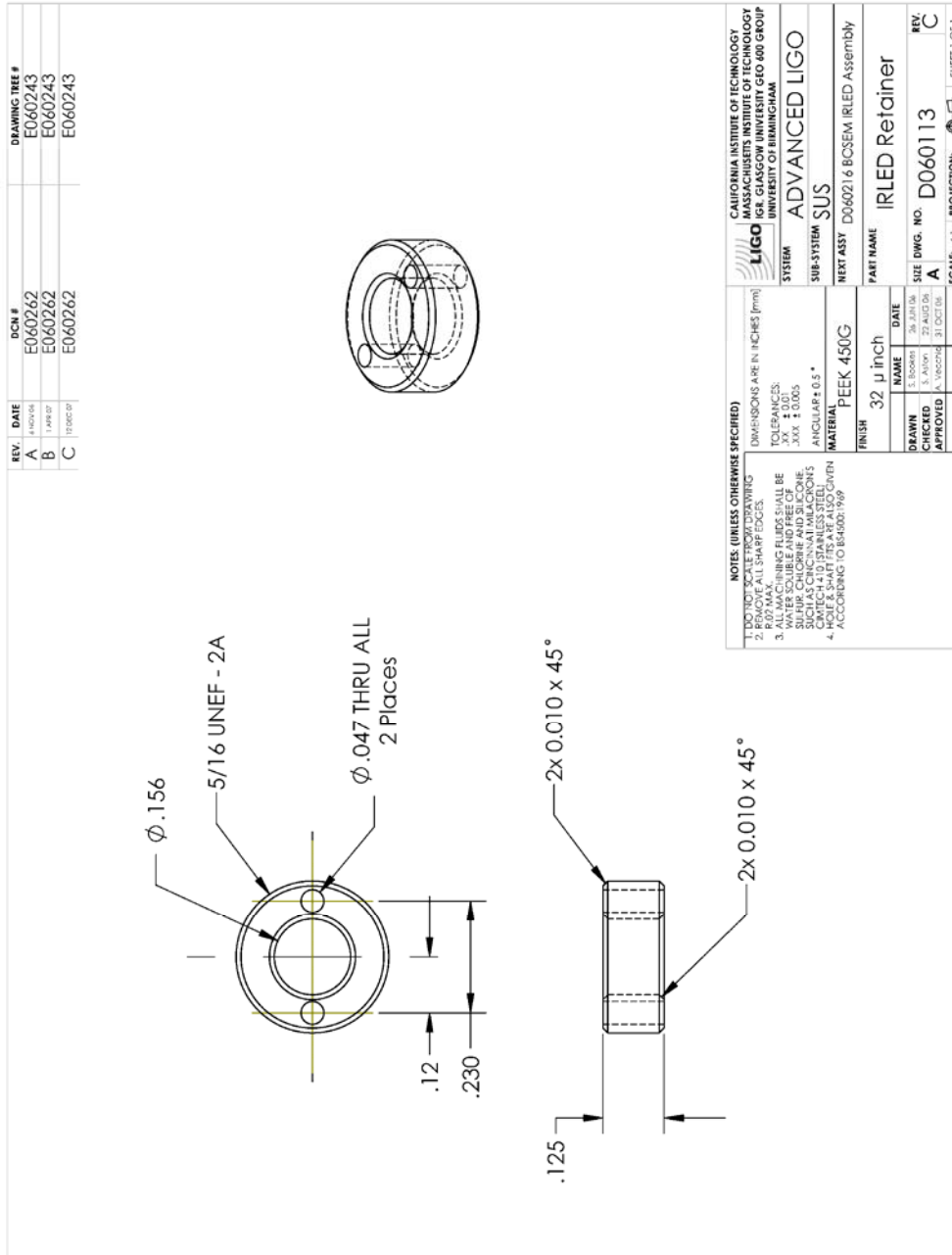
Figure A.9: *BOSEM IRLED retainer (D060113).*
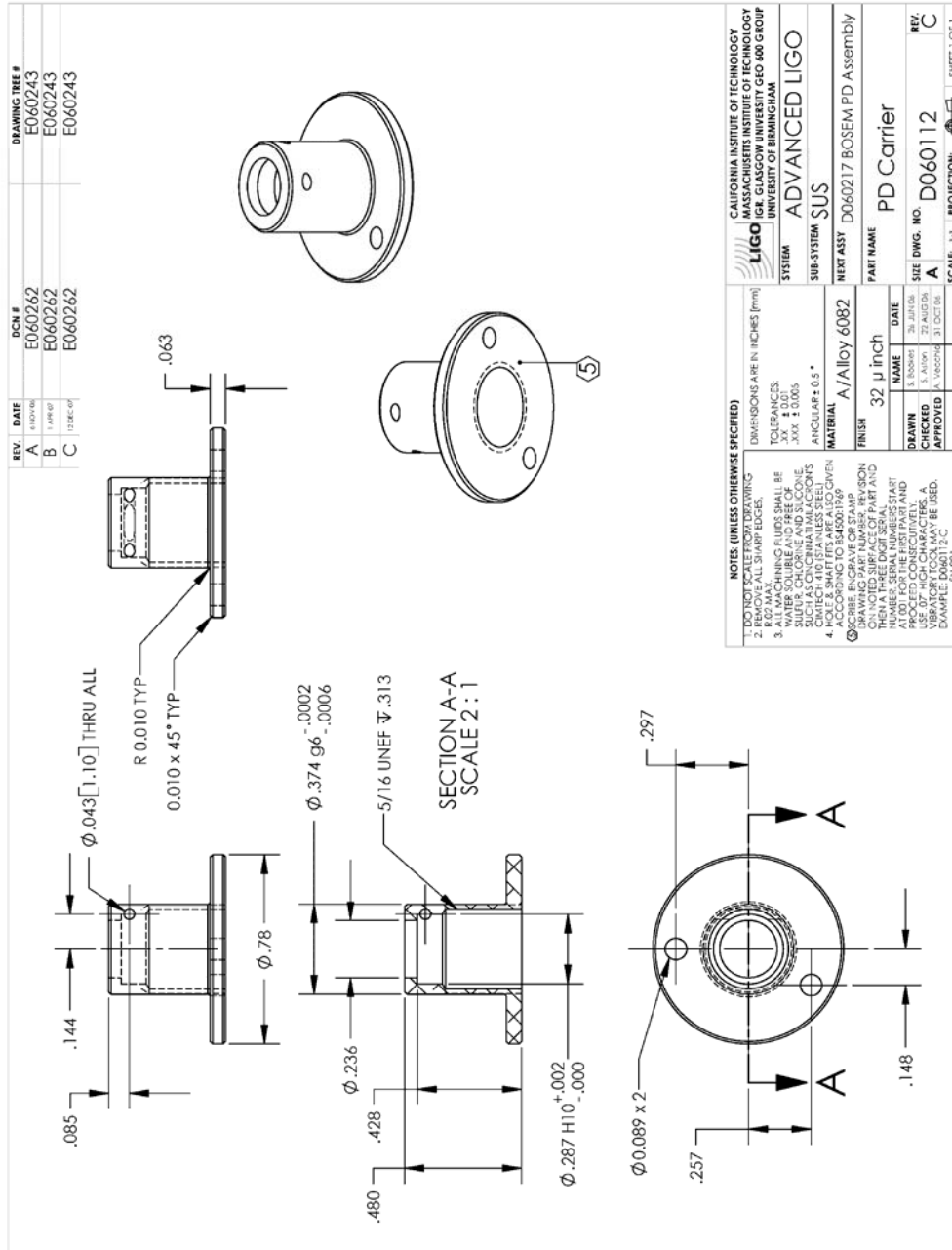
Figure A.10: *BOSEM photodiode carrier (D060112).*

169
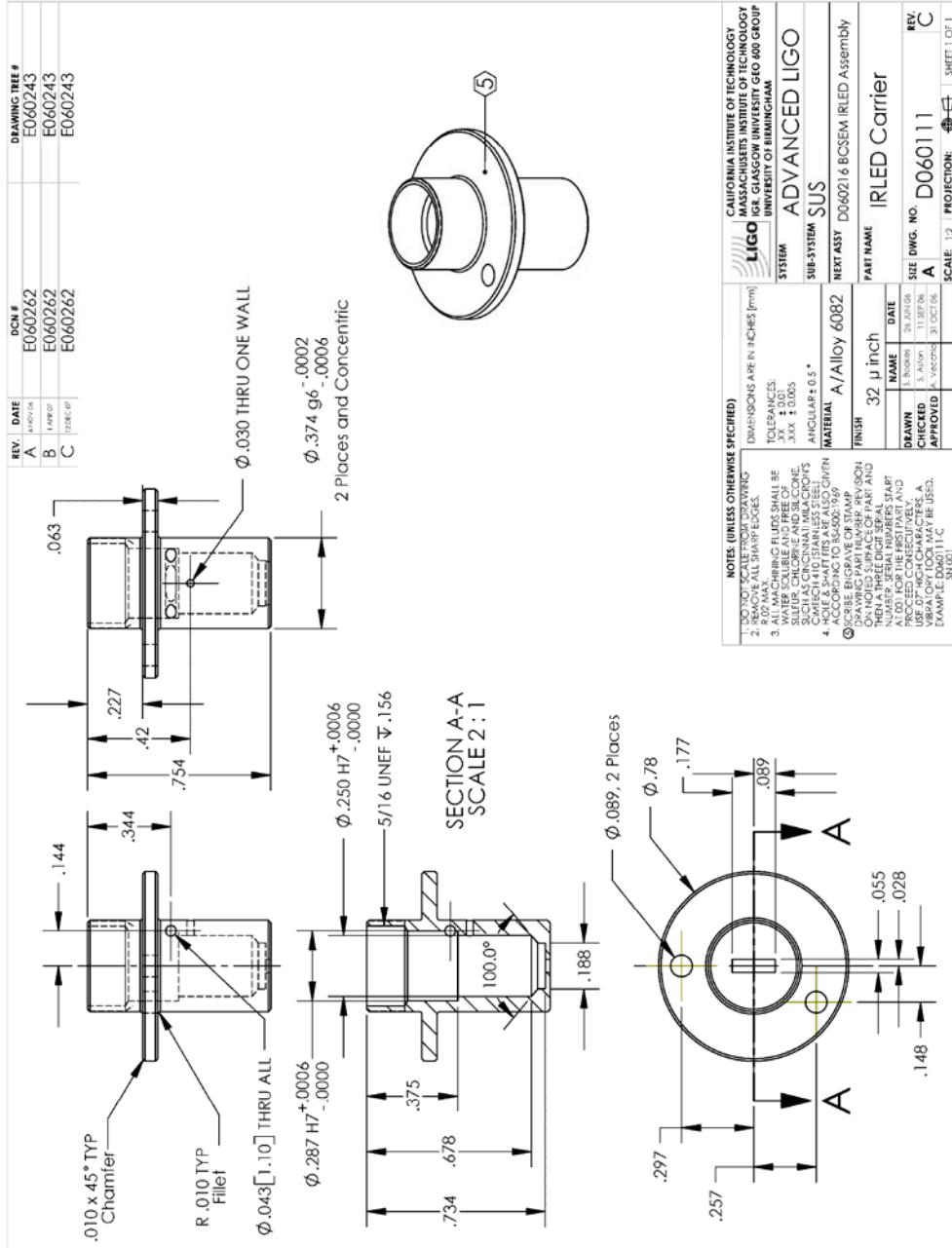
Figure A.11: *BOSEM IRLED carrier (D060111).*
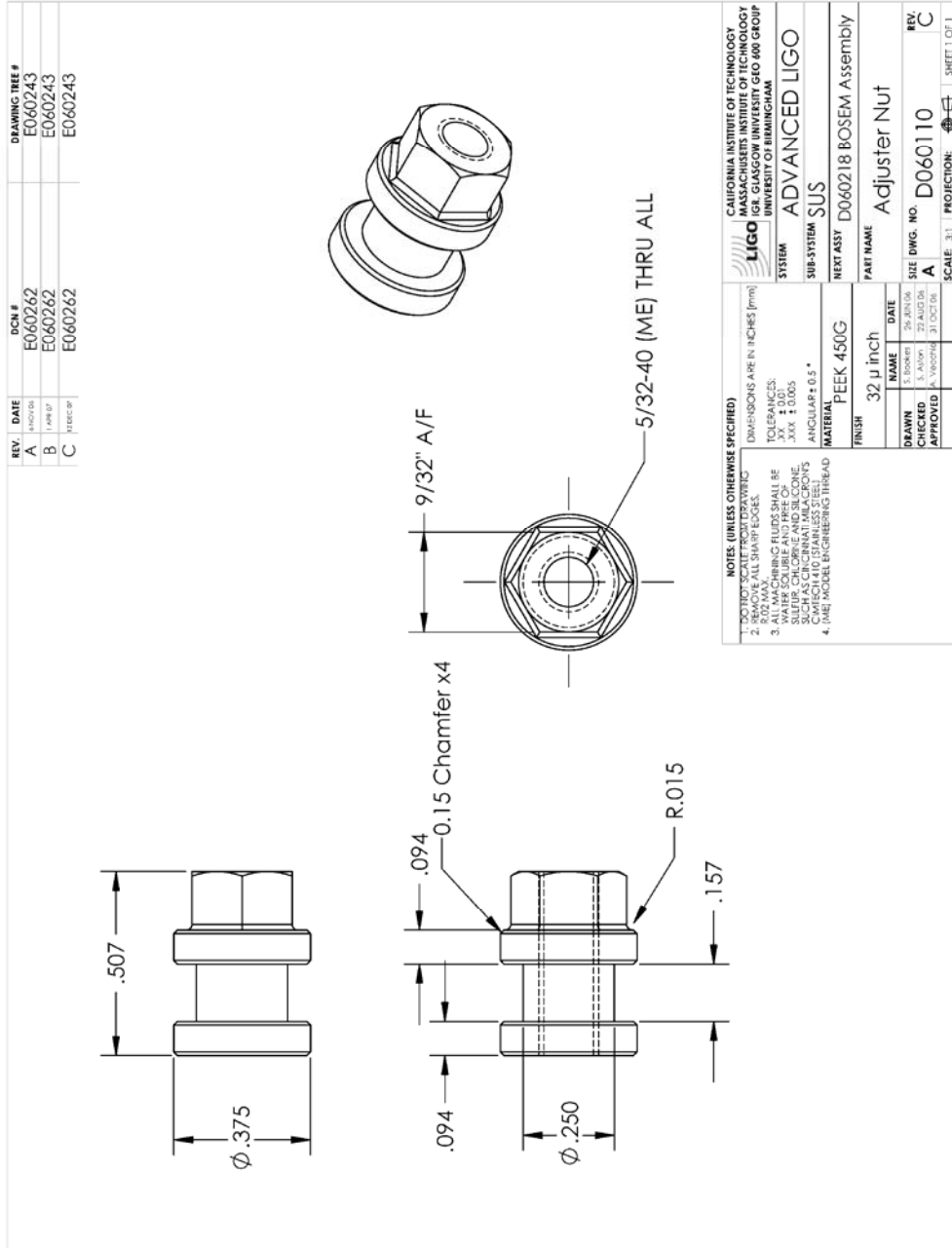
Figure A.12: *BOSEM adjuster nut (D060110).*

Figure A.13: *BOSEM adjuster shaft (D060109).*
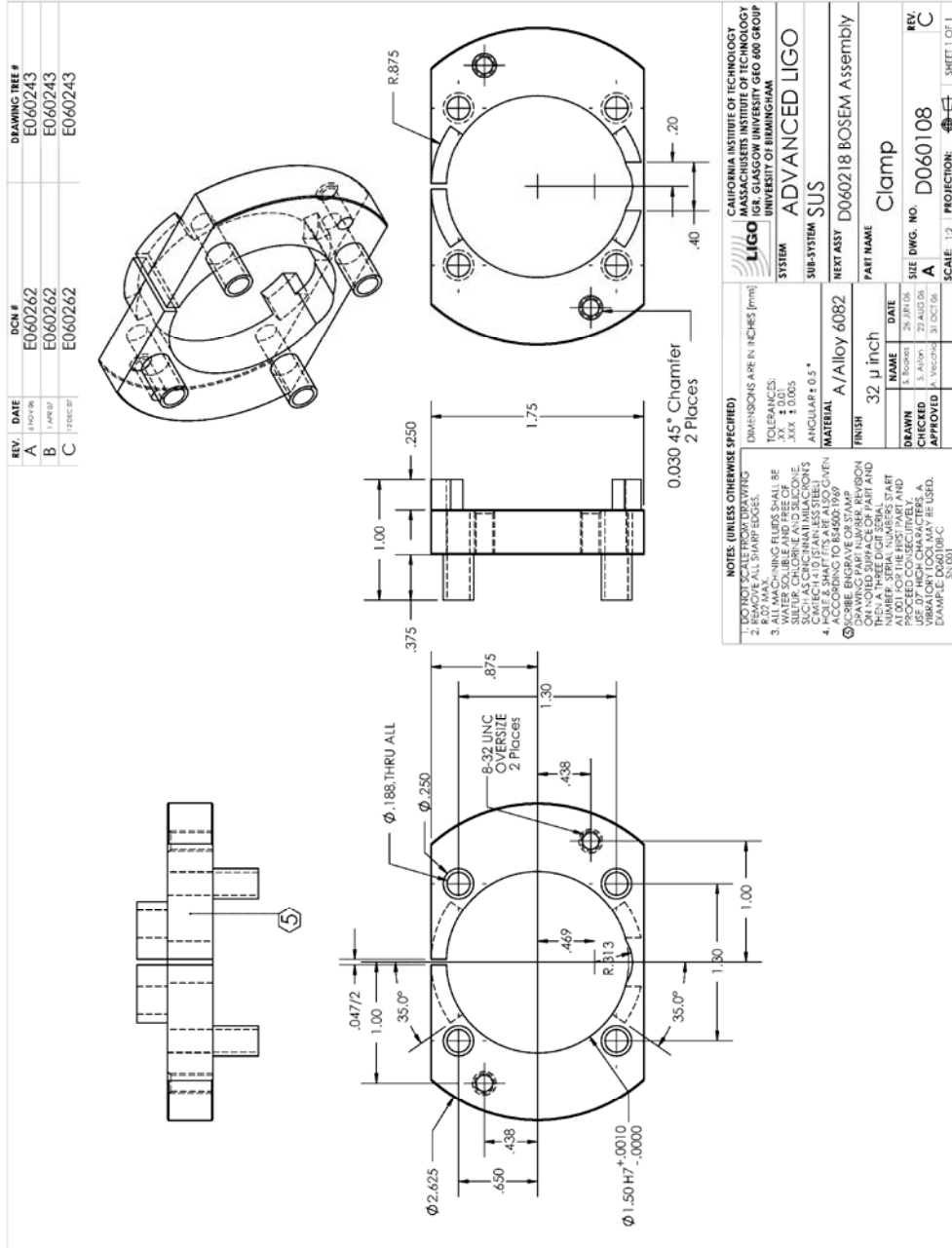
Figure A.14: *BOSEM coil-former clamp (D060108).*
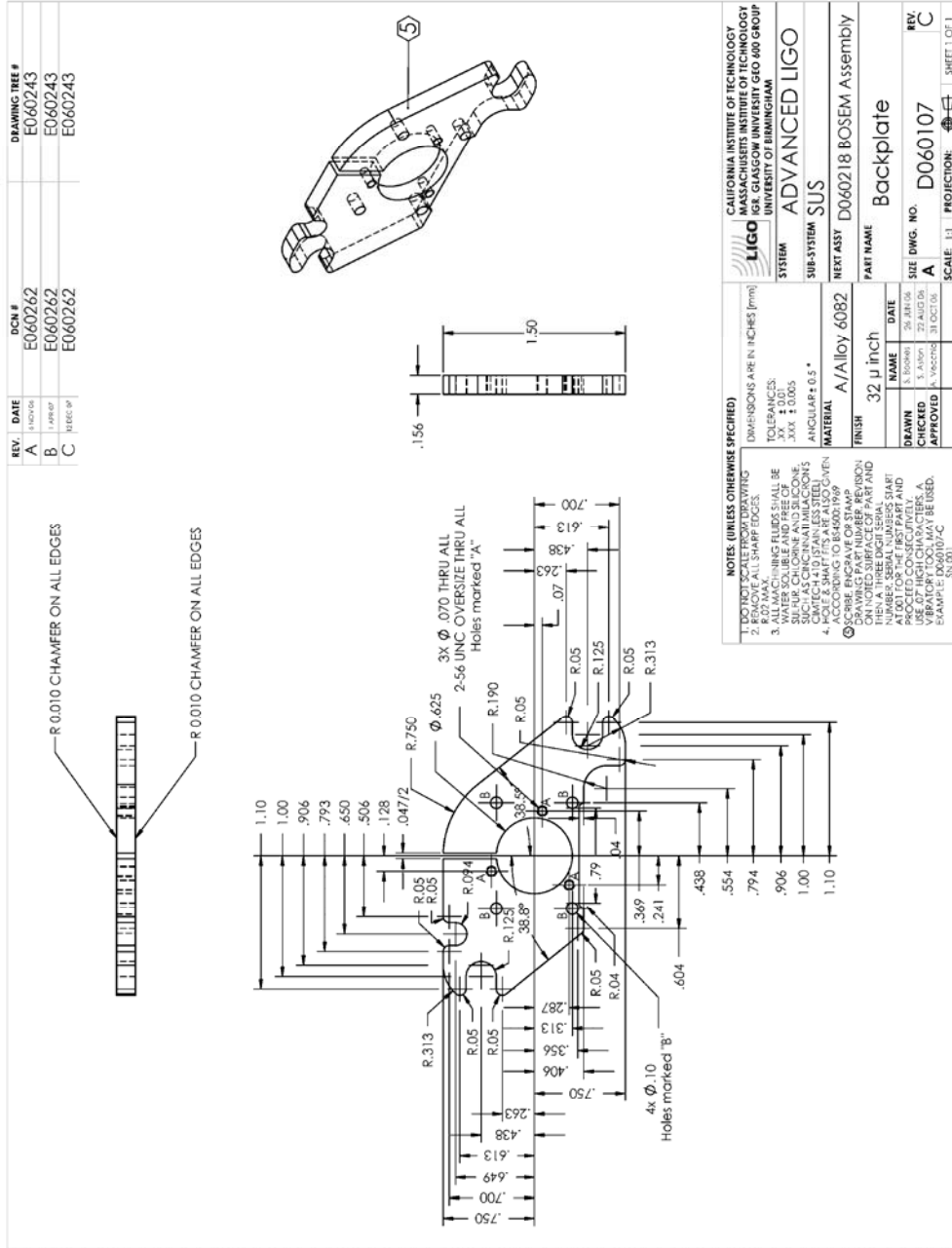
Figure A.15: *BOSEM back-plate (D060107).*
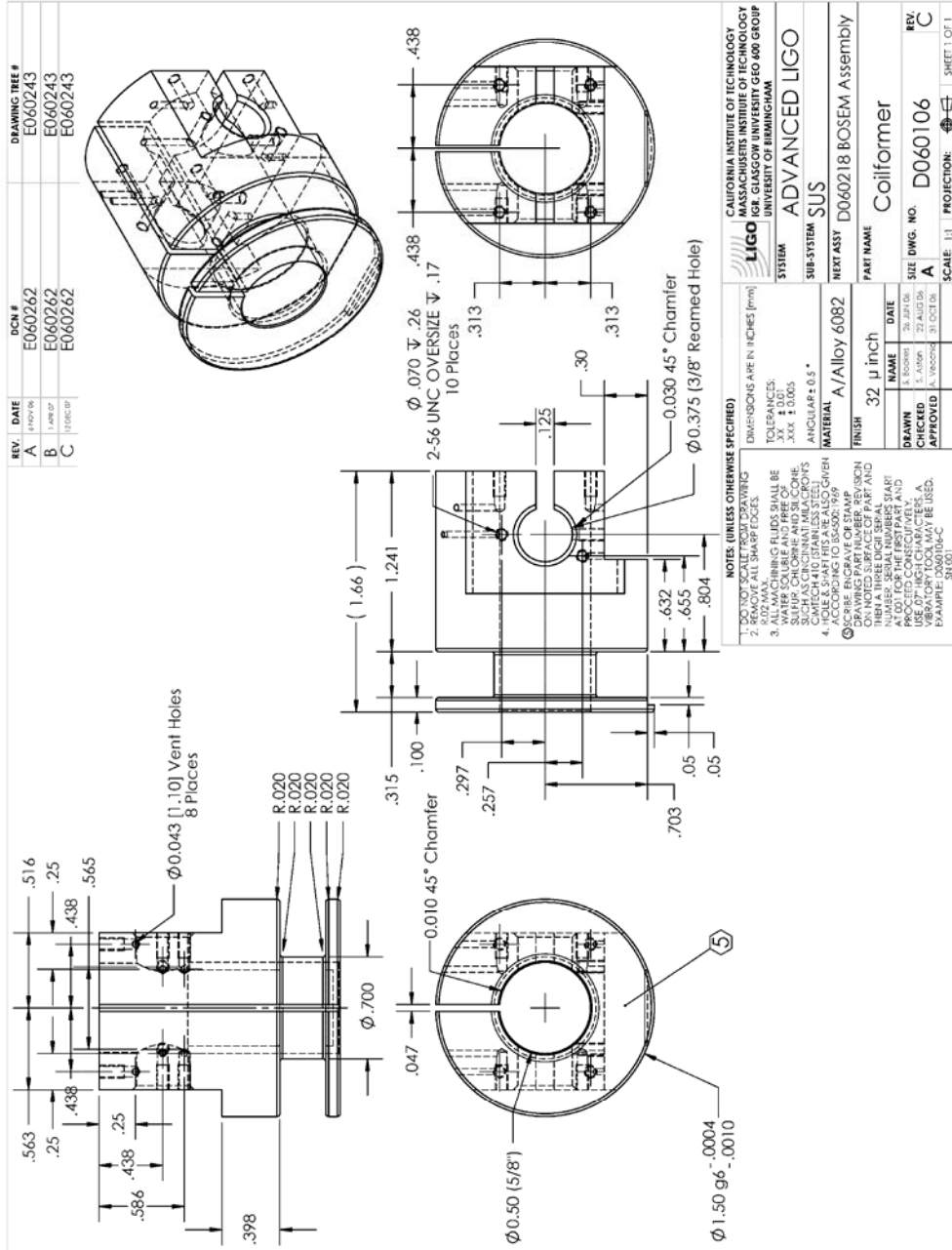
Figure A.16: *BOSEM coil-former (D060106).*
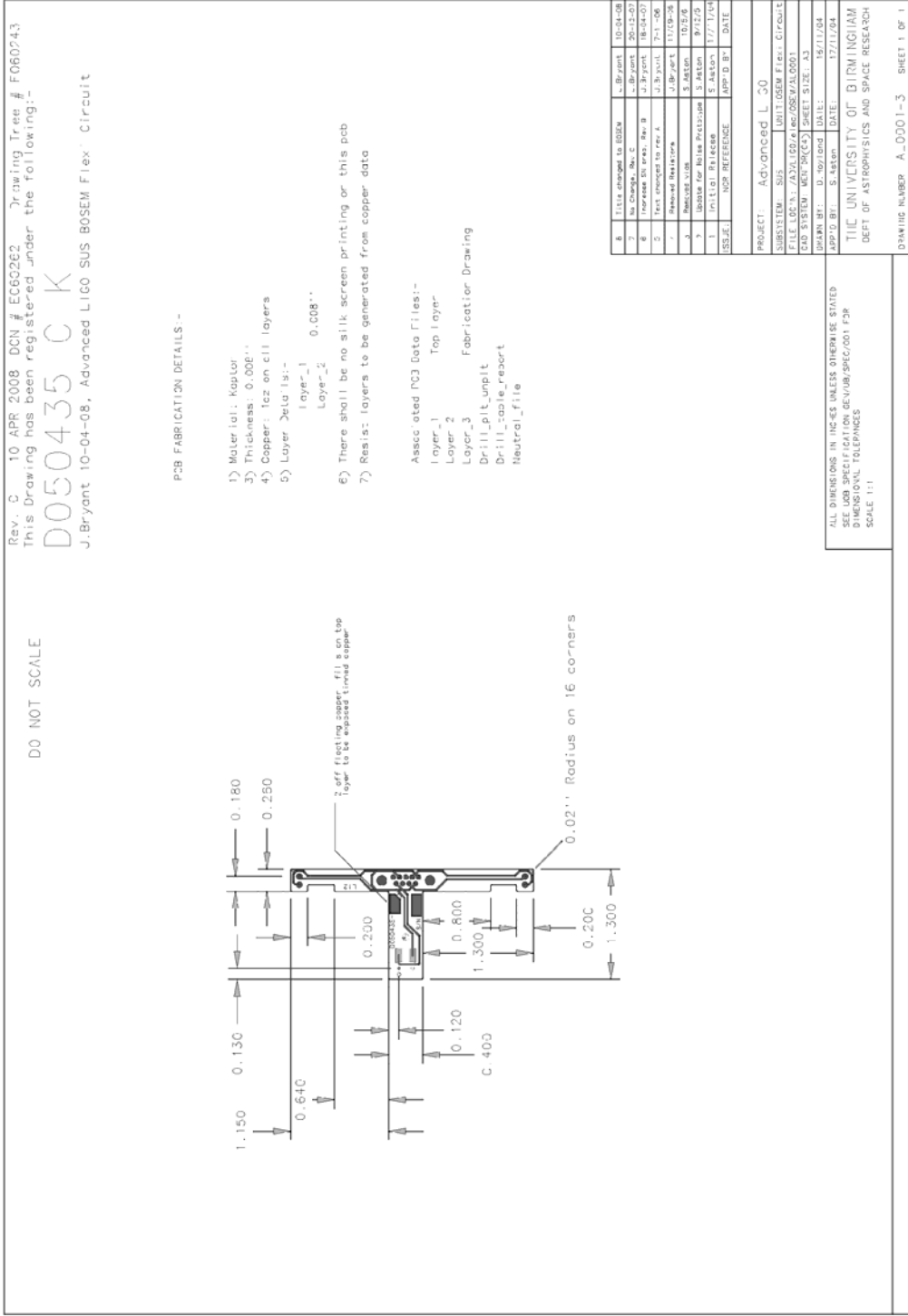
Figure A.17: *BOSEM flexible circuit (D050435).*

Appendix G - EUCLID 2D CAD Drawings
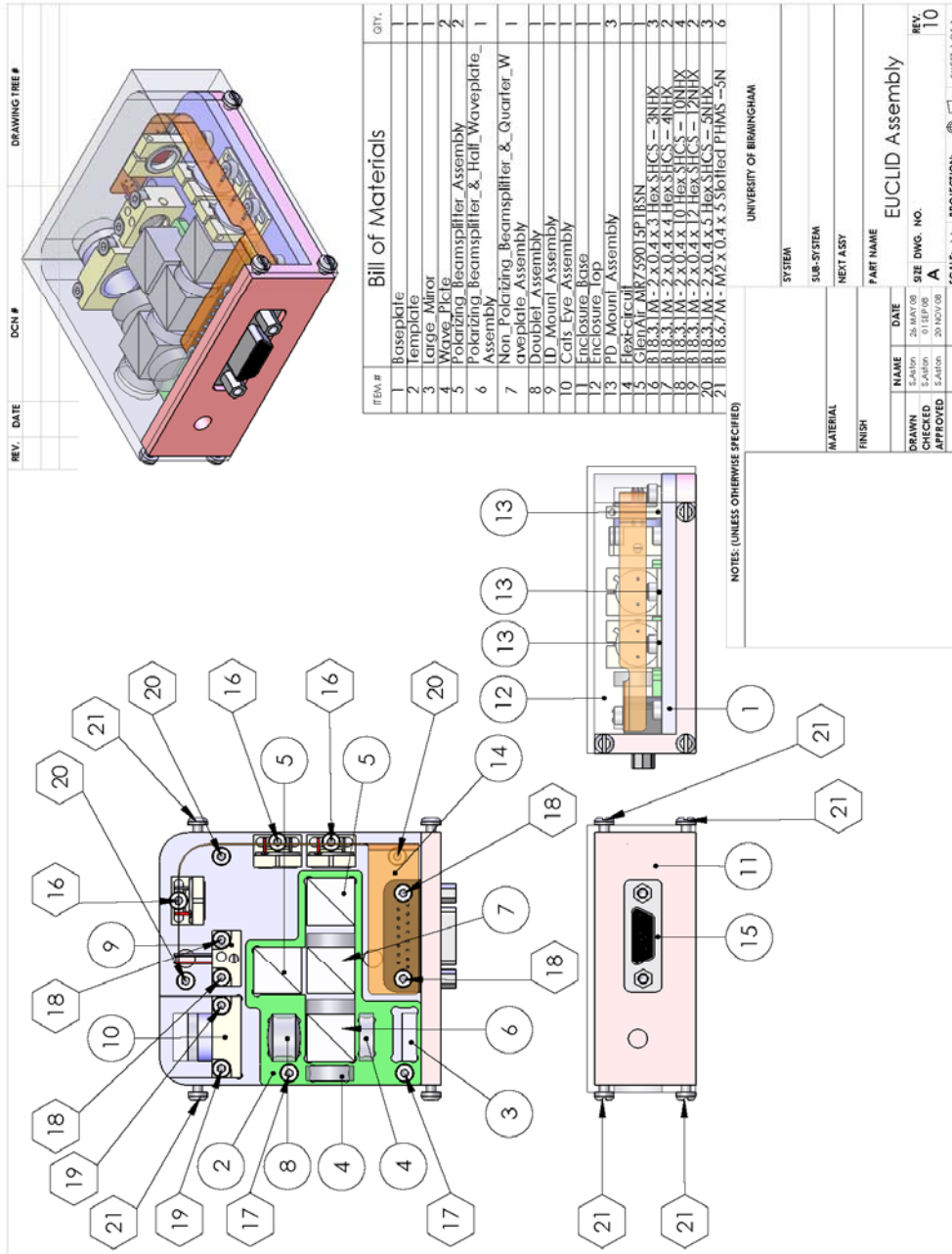
Figure A.18: *EUCLID top-level assembly.*
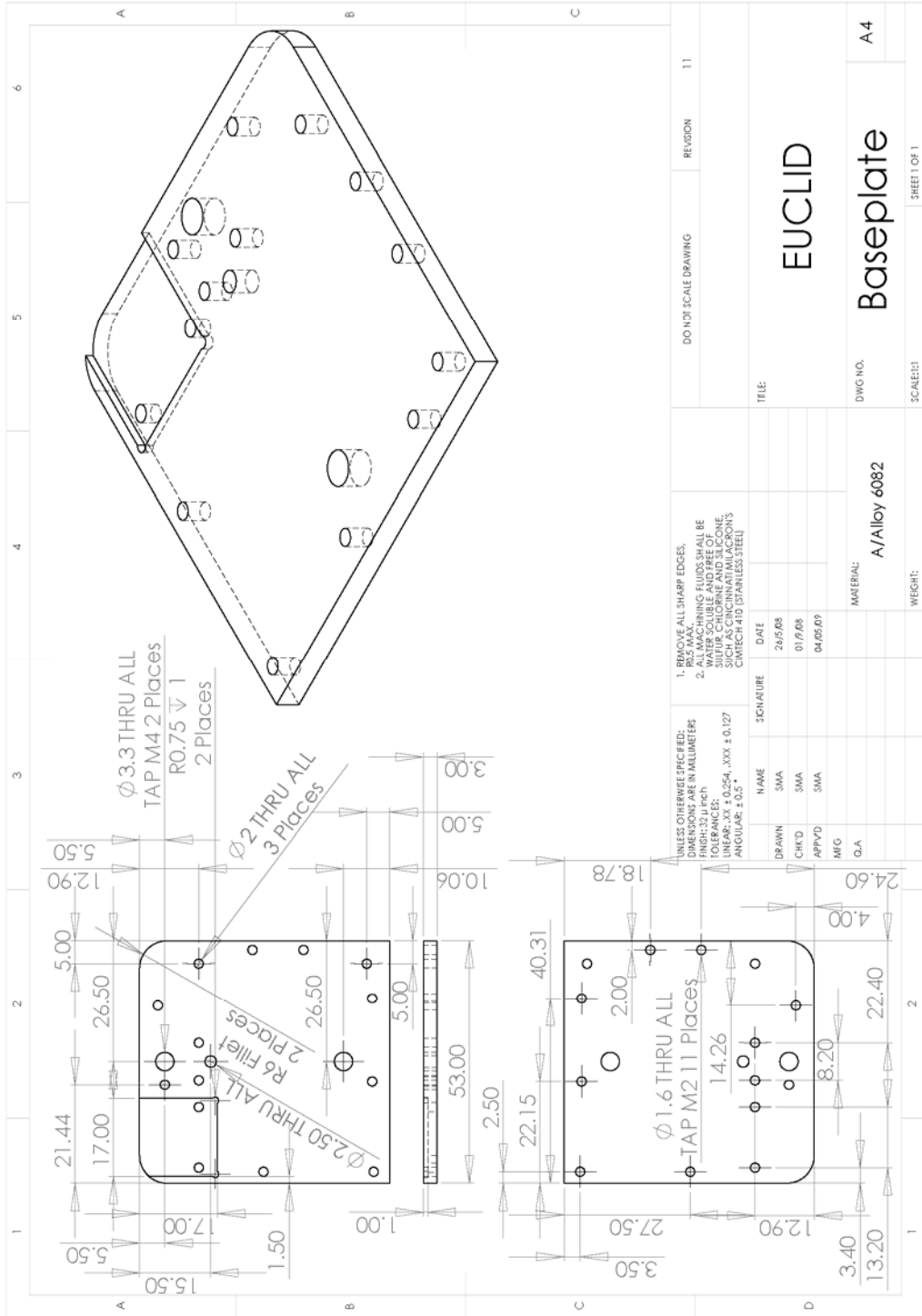
Figure A.19: *EUCLID base-plate.*
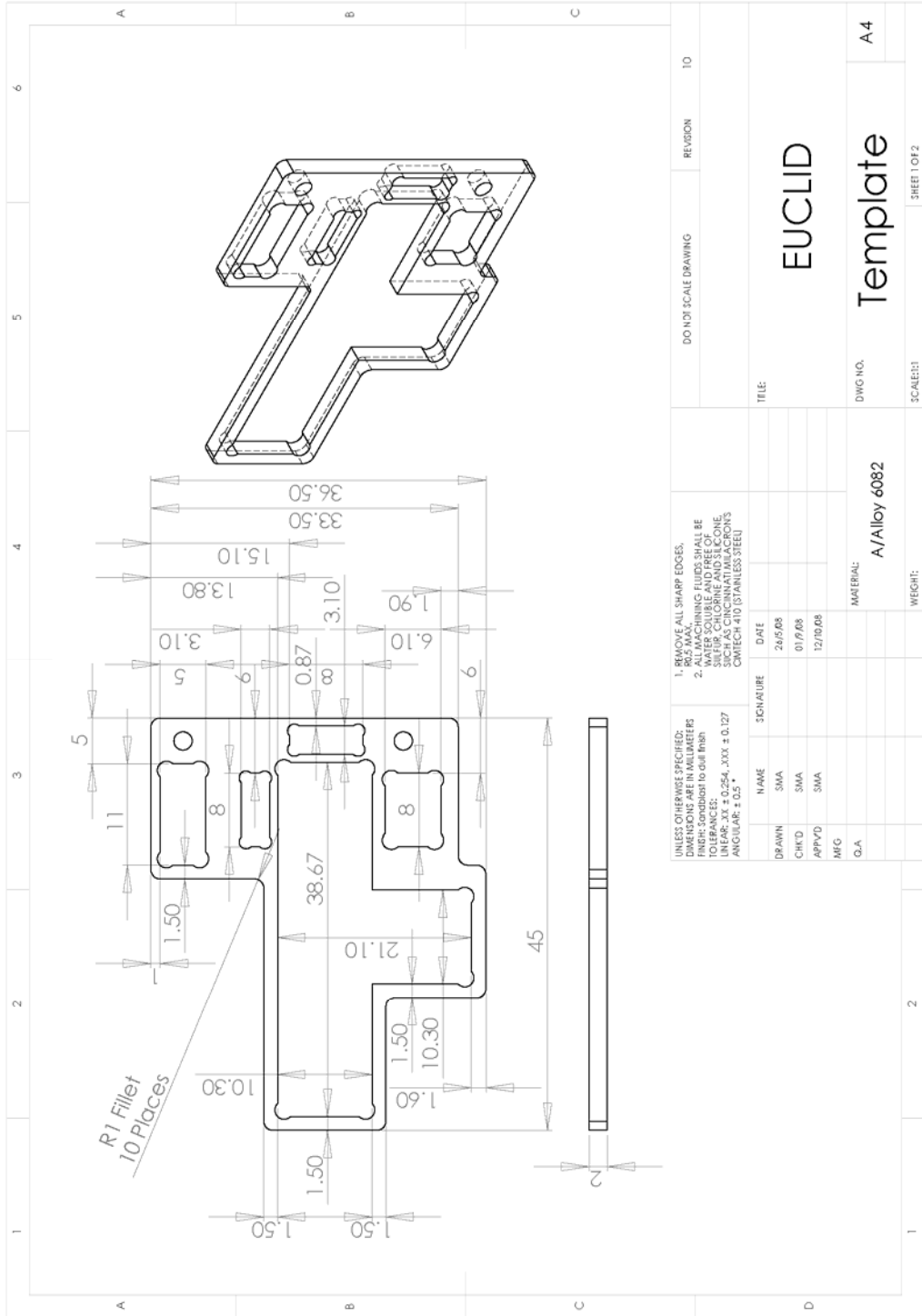
Figure A.20: *EUCLID template (sheet 1).*

179
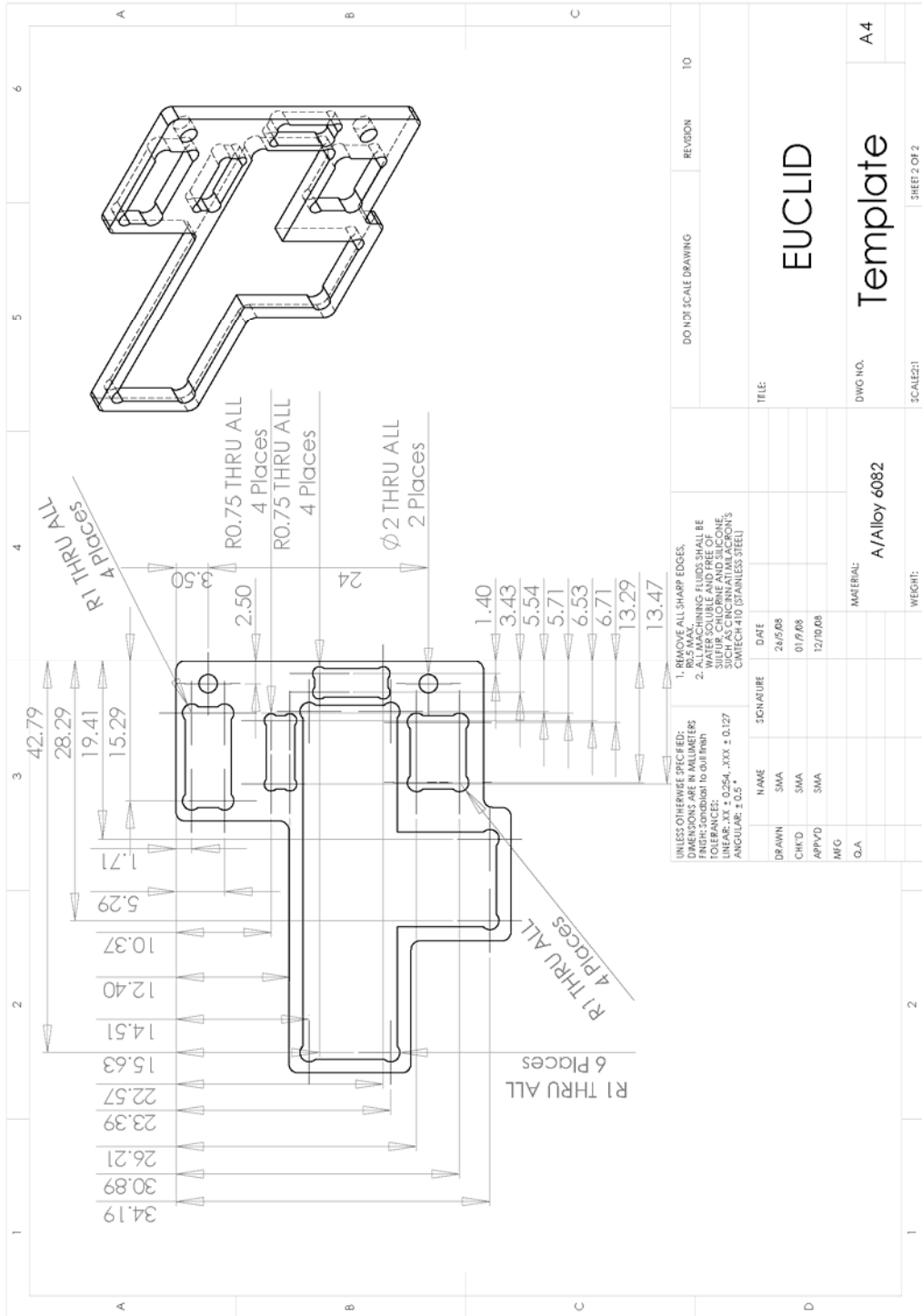
Figure A.21: *EUCLID template (sheet 2).*
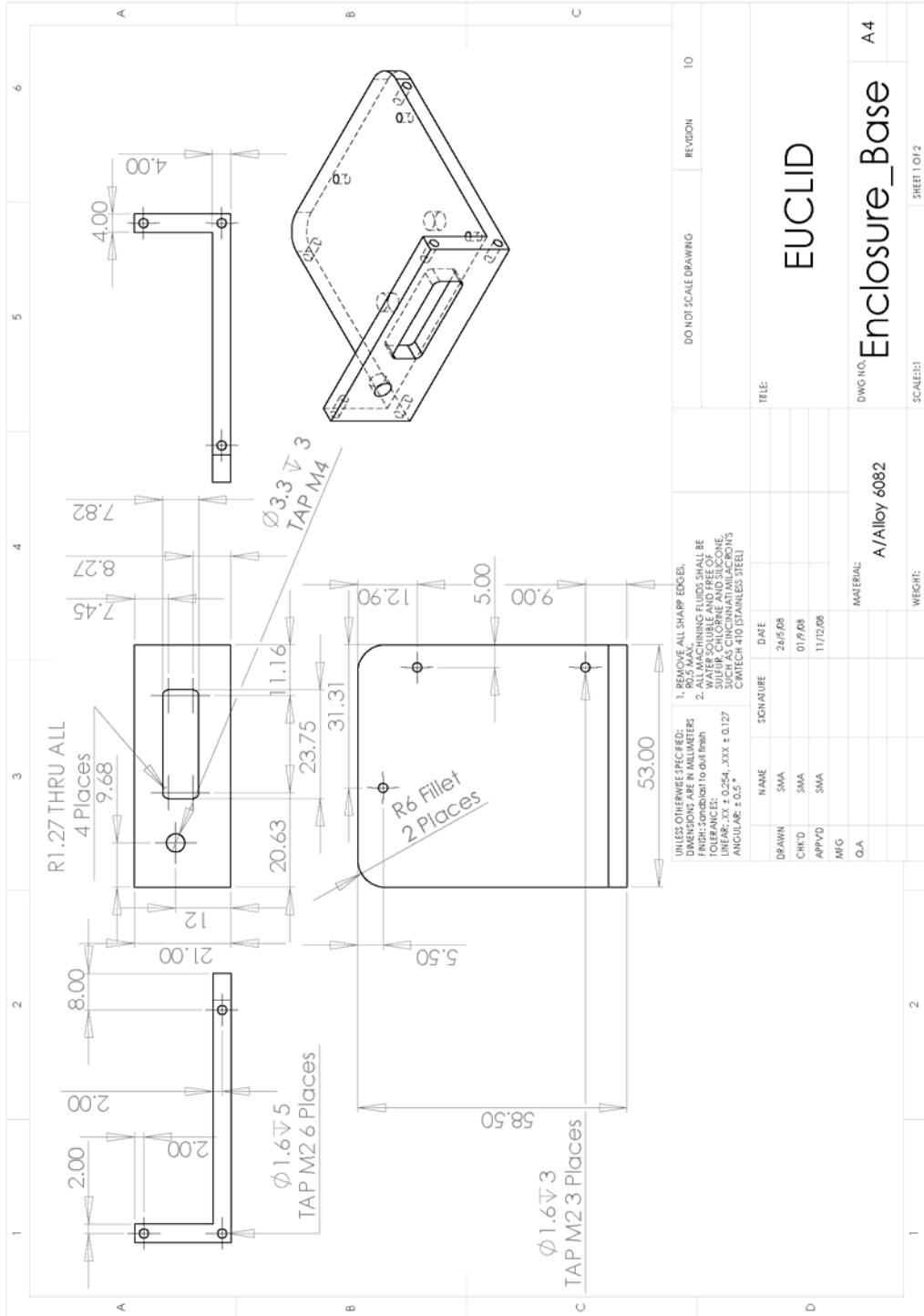
Figure A.22: *EUCLID enclosure base (sheet 1).*

181
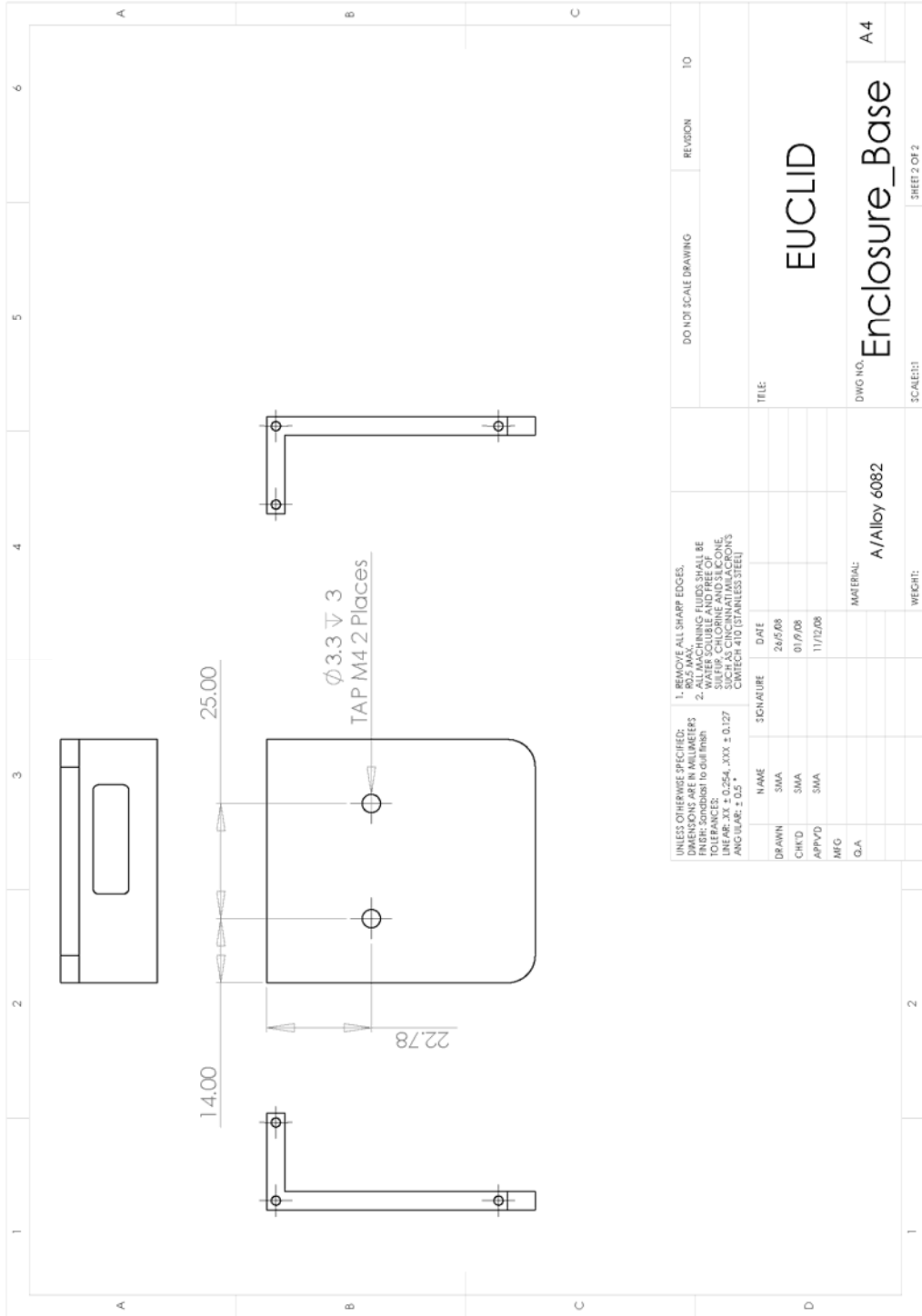
Figure A.23: *EUCLID enclosure base (sheet 2).*
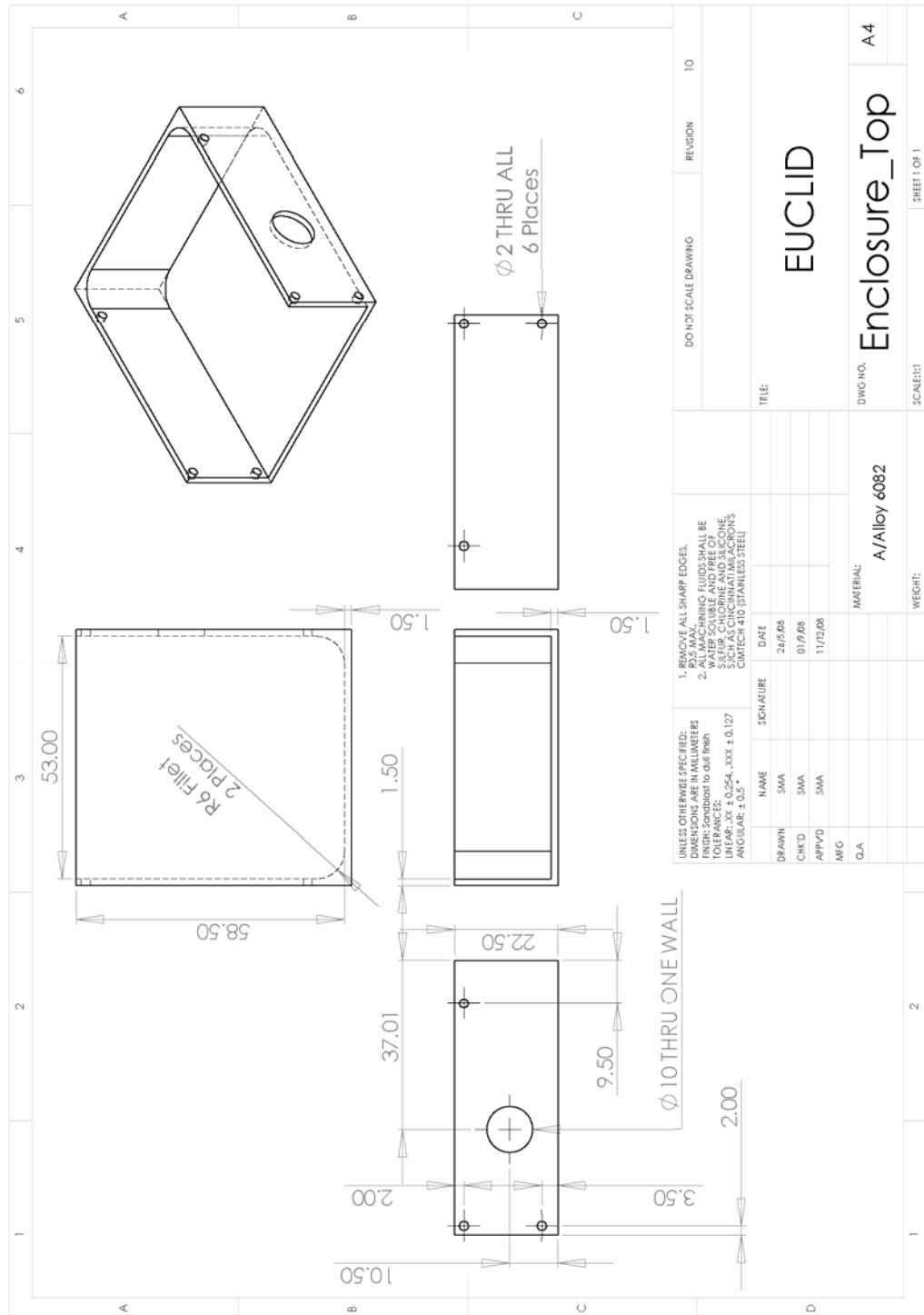
Figure A.24: *EUCLID enclosure top.*
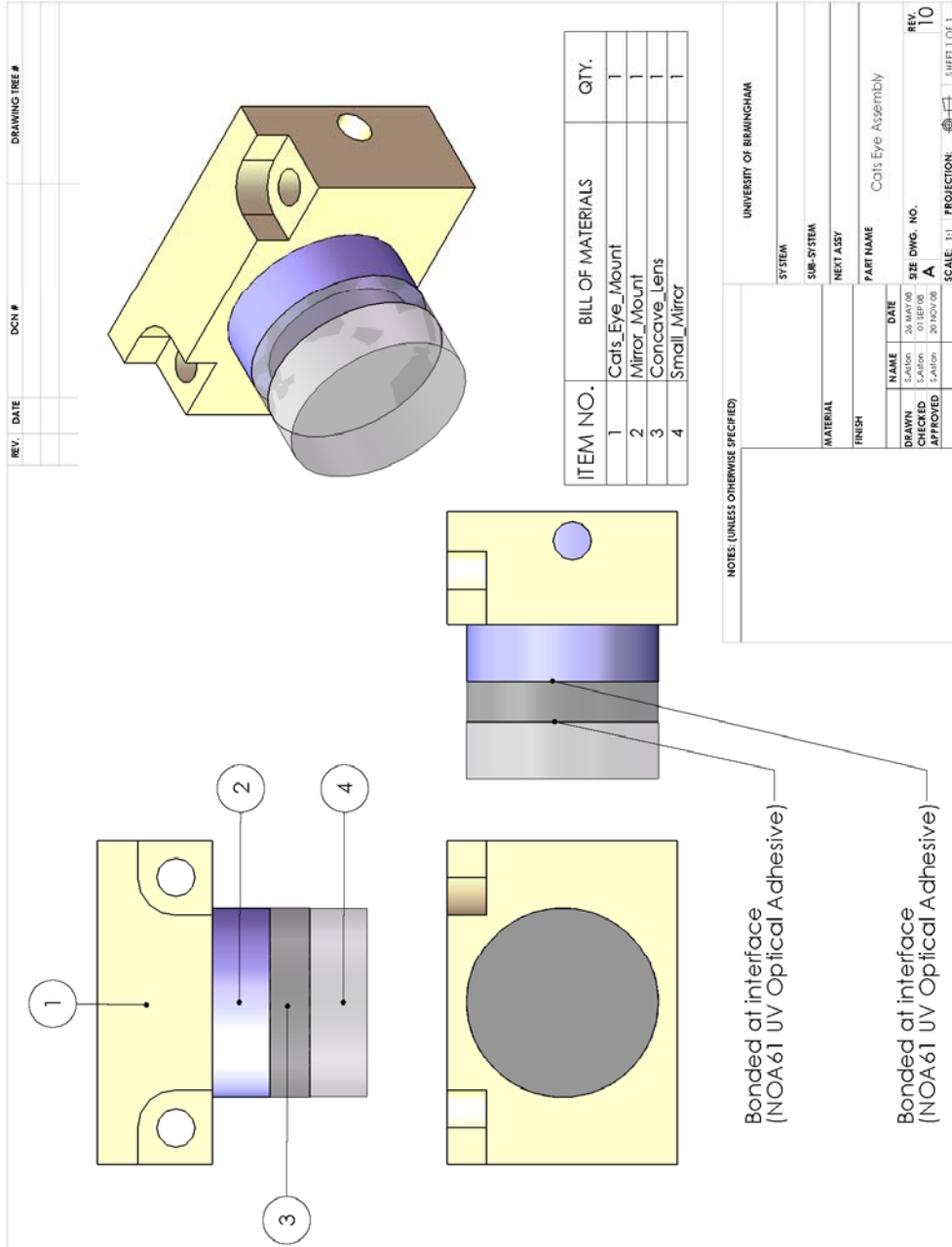
Figure A.25: *EUCLID cat's eye assembly.*
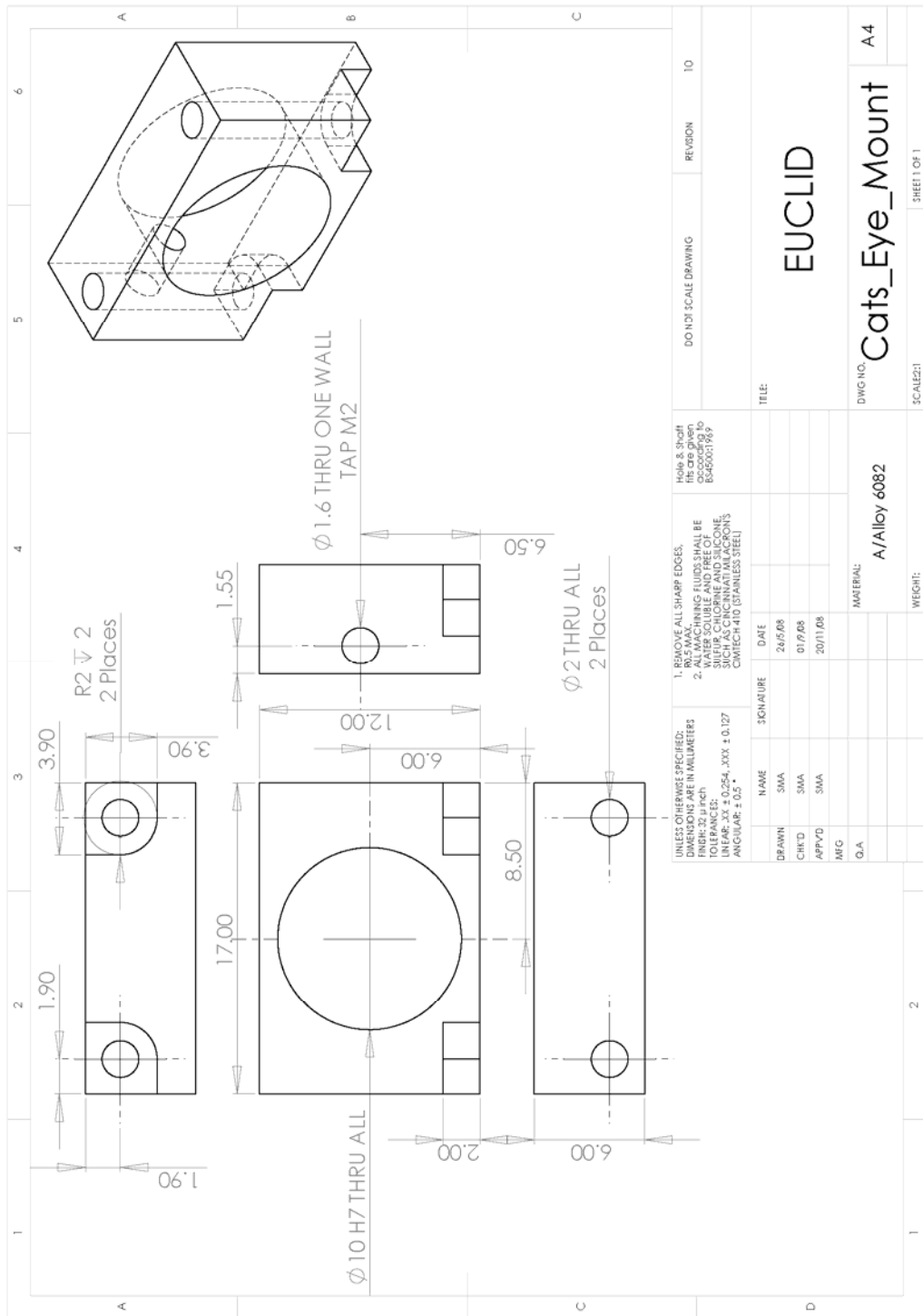
Figure A.26: *EUCLID cat's eye mount.*

185

UNLESS OTHERWISE SPECIFIED:
DIMENSIONS ARE IN MILLIMETERS
FINISH: 32 μ inch
TOLERANCES:
LINEAR: .XX ± 0.254, .XXX ± 0.127
ANGULAR: ± 0.5°

1. REMOVE ALL SHARP EDGES,
   R0.5 MAX.
2. ALL MACHINING FLUIDS SHALL BE
   WATER SOLUBLE AND FREE OF
   SULFUR, CHLORINE AND SILICONE,
   SUCH AS CINCINNATI MILACRON'S
   CIMTECH 410 (STAINLESS STEEL)

Hole & Shaft
fits are given
according to
BS4500:1969

DO NOT SCALE DRAWING   REVISION   10

TITLE:

EUCLID

Mirror_Mount

DWG NO.   A4

SCALE:2:1   SHEET 1 OF 1

	NAME	SIGNATURE	DATE
DRAWN	SMA		26/5/08
CHK'D	SMA		01/9/08
APPV'D	SMA		20/11/08
MFG			
Q.A			

MATERIAL:
A/Alloy 6082

WEIGHT:

∅ 10 g6

∅ 8 THRU ALL

9.00

Figure A.28: *EUCLID laser diode mount assembly.*
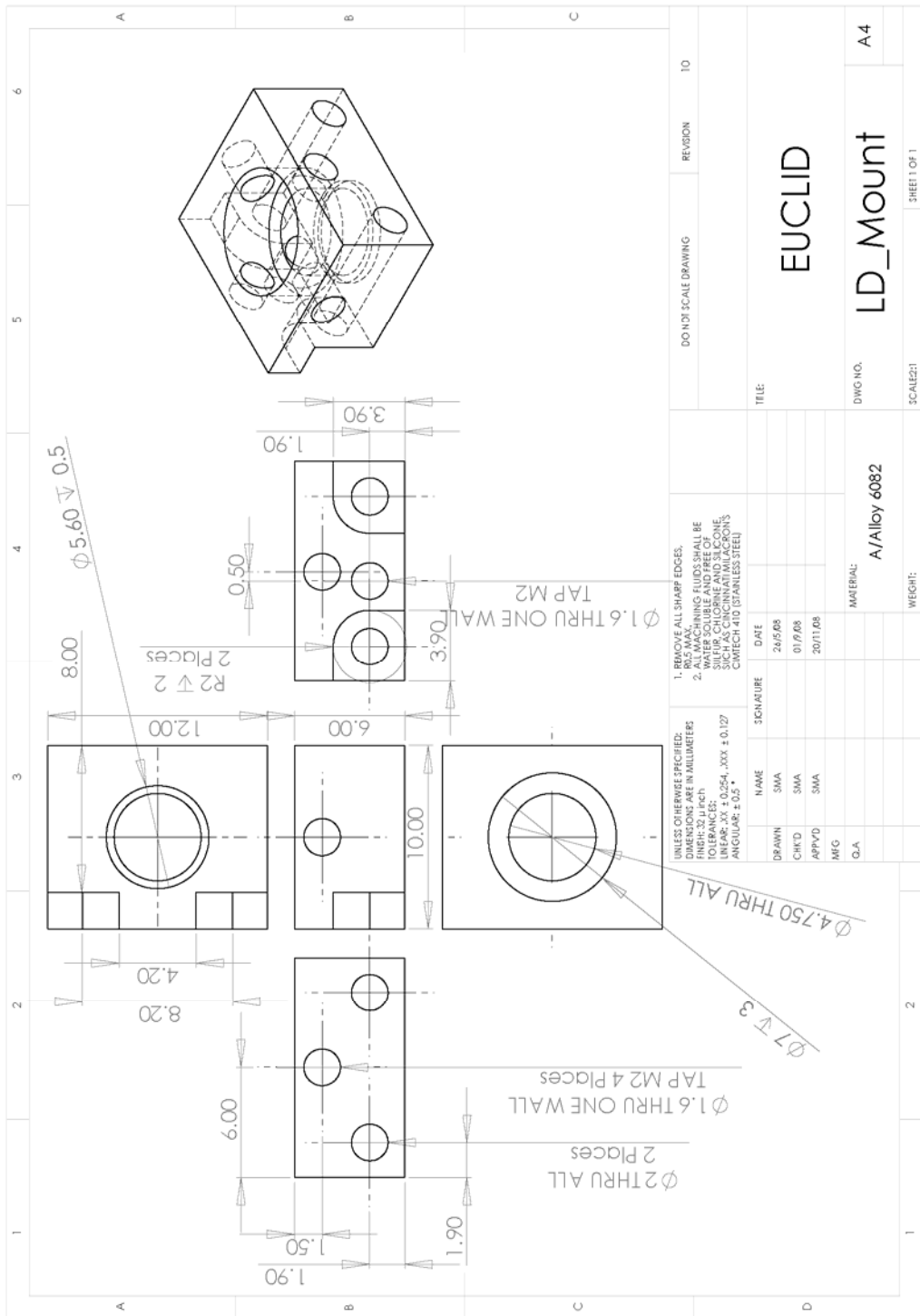
Figure A.29: *EUCLID laser diode mount.*

ITEM NO.	BILL OF MATERIALS	QTY.
1	PD_Mount	1
2	Centronic_OSD15-5T	1

UNIVERSITY OF BIRMINGHAM

SYSTEM
SUB-SYSTEM
NEXT ASSY
PART NAME — PD Mount Assembly

NOTES: (UNLESS OTHERWISE SPECIFIED)

MATERIAL
FINISH

	NAME	DATE
DRAWN	S.Aston	26 MAY 08
CHECKED	S.Aston	01 SEP 08
APPROVED	S.Aston	20 NOV 08

SIZE A | DWG. NO. | REV. 10
SCALE: 1:1 | PROJECTION: | SHEET 1 OF 1

REV. | DATE | DCN # | DRAWING TREE #
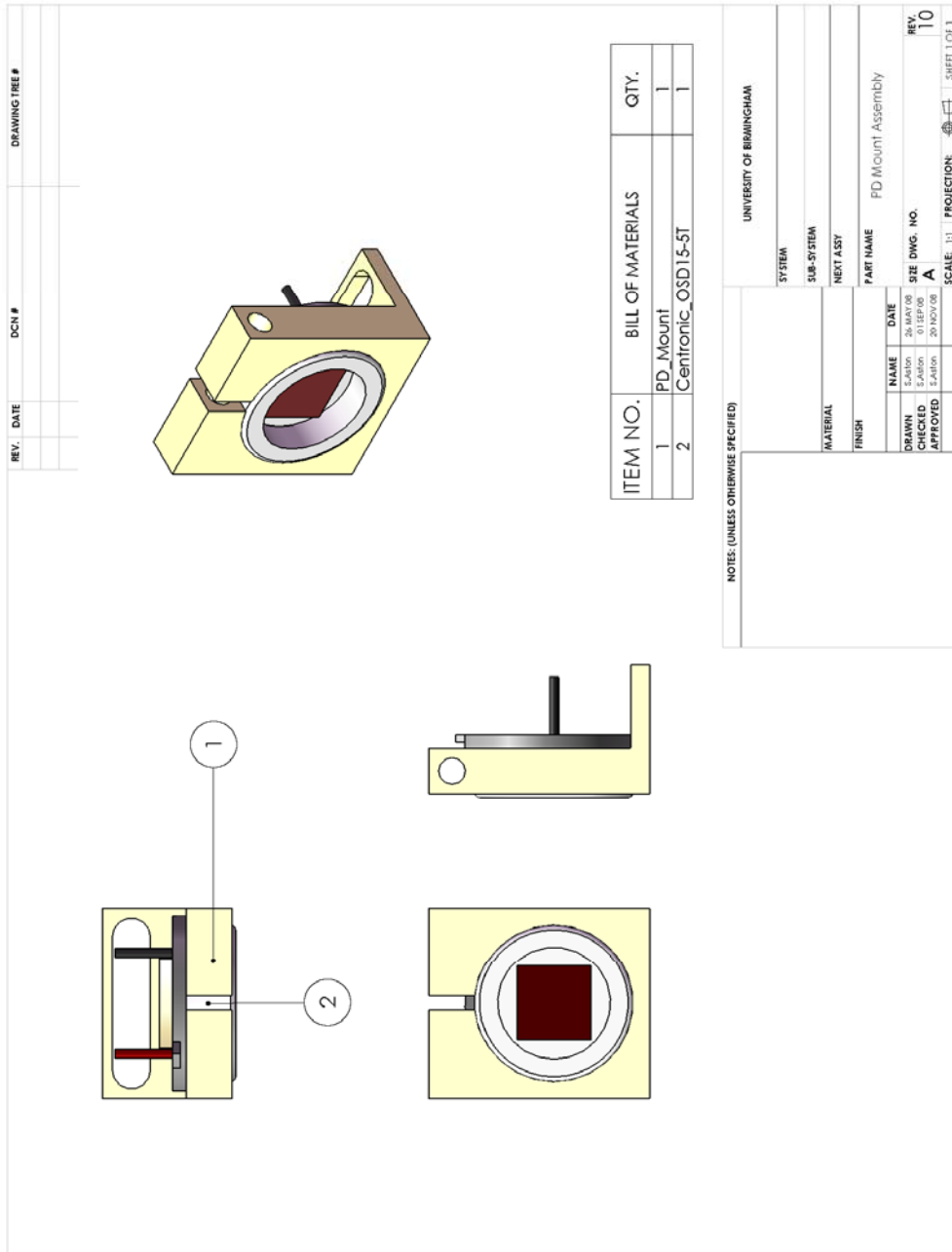
Figure A.30: *EUCLID photodiode mount assembly.*

189
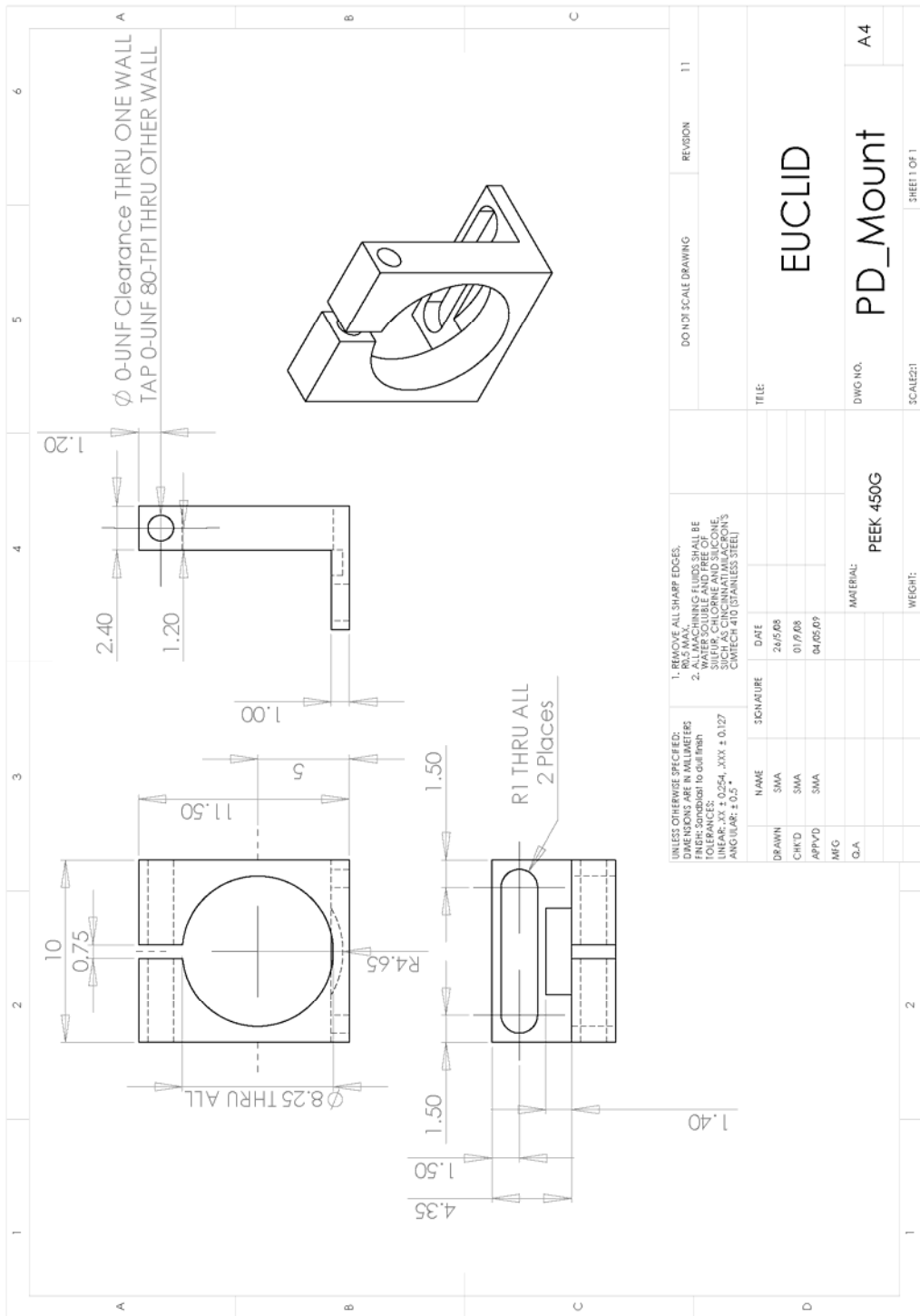
Figure A.31: *EUCLID photodiode mount.*

190
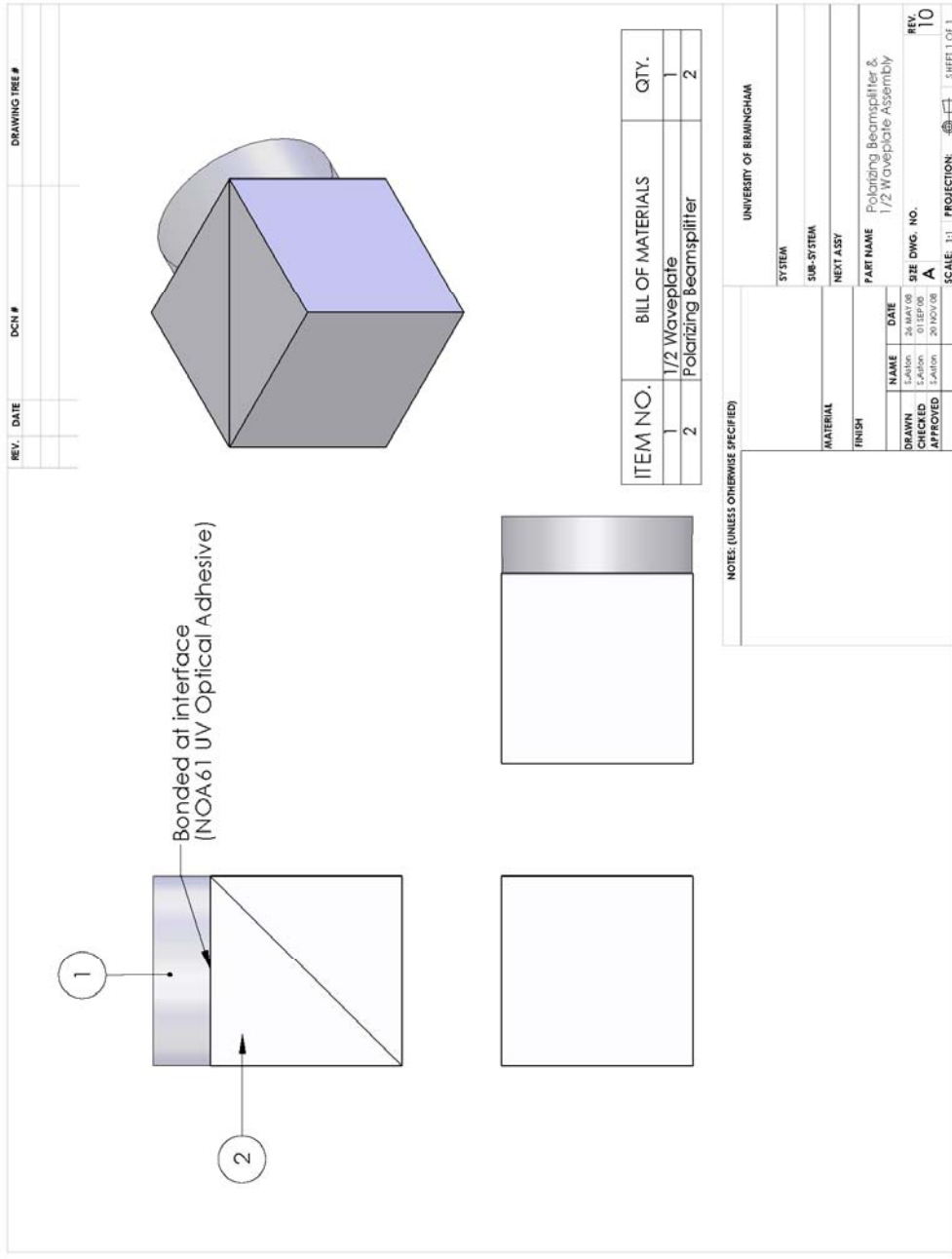
Figure A.32: *EUCLID polarising beam-splitter and half-wave plate assembly.*
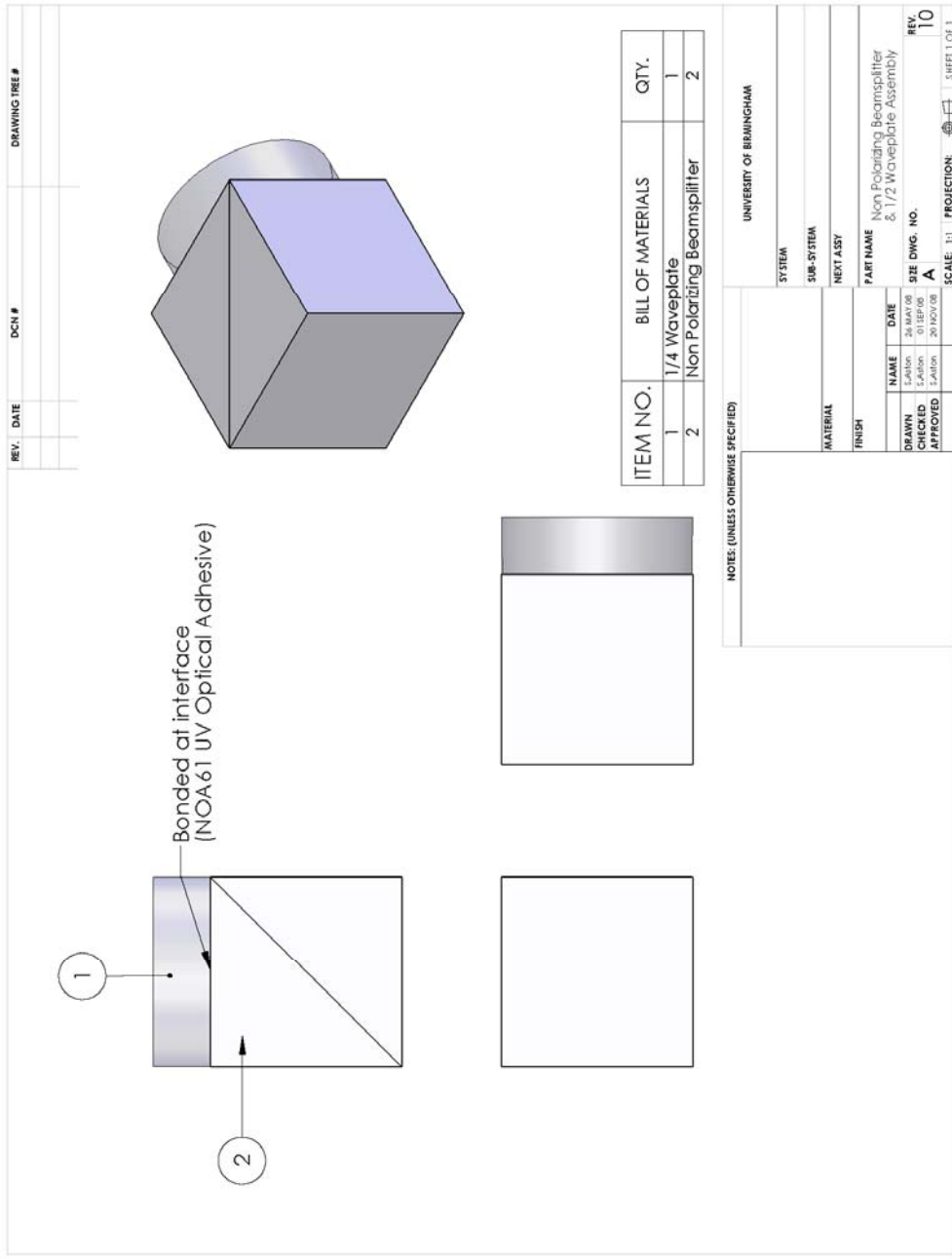
Figure A.33: *EUCLID non-polarising beam-splitter and quarter-wave plate assembly.*

The drawing contains the following text elements:

- DRAWING TREE #
- DCN #
- REV. DATE
- Bonded at interface (NOA61 UV Optical Adhesive)
- 1
- 2

Bill of Materials:

ITEM NO.	BILL OF MATERIALS	QTY.
1	1/4 Waveplate	1
2	Non Polarizing Beamsplitter	2

Title block:

- NOTES: (UNLESS OTHERWISE SPECIFIED)
- UNIVERSITY OF BIRMINGHAM
- SYSTEM
- SUB-SYSTEM
- NEXT ASSY
- PART NAME: Non Polarizing Beamsplitter & 1/2 Waveplate Assembly
- MATERIAL
- FINISH

	NAME	DATE
DRAWN	S.Aston	26 MAY 08
CHECKED	S.Aston	01 SEP 08
APPROVED	S.Aston	20 NOV 08

- SIZE: A
- DWG. NO.
- REV. 10
- SCALE: 1:1
- PROJECTION:
- SHEET 1 OF 1

Figure A.34: *EUCLID flexible circuit.*

193

Appendix H - EUCLID Assembly and Alignment Guide

Figure E.1: *EUCLID alignment support drawing.*

EUCLID assembly and alignment guide (adapted from version 2.3).

To facilitate the alignment of EUCLID optical components, items listed in Table A.6, should not initially be installed. Also, items #6 and #7 should be un-bonded (separate) sub-assemblies at this stage.

Item #	Description
3	Large mirror (reference arm)
4a	¼ wave plate (reference arm)
4b	¼ wave plate (measurement arm)
6	Polarising beam-splitter and ½ wave plate assembly
7	Non-polarising beam-splitter and ½ wave plate assembly
8	Doublet assembly (cat's eye)

Table A.6: *EUCLID optical component list.*

All remaining EUCLID parts should be fully assembled, with the exception of the enclosure top, which enables easy access for the alignment process.

Task (1) - Collimate VCSEL.

Ensure that the protruding tab on the VCSEL package is filed down to be flush with the rest of the package. Then install the VCSEL into the laser diode mount assembly (Item #9). The VCSEL should be rotated to ensure the location denoted by the 'tab' is at a 12 o'clock position. This maintains the correct orientation of the polarisation of the VCSEL. It should be noted that the 6 o'clock position also provides the correct optical polarisation. However the VCSEL orientation in this case would be incompatible with the pin-outs on the flexible circuit.

Install photodiodes, PD1, PD2 and PD3 into their respective mounts (3 x Item #13). Attach flexible circuit (Item #14) to photodiodes / VCSEL and solder in place.

Add UV adhesive at the interface between the laser diode mount and the aspheric lens. Then with the aspheric lens in place, translate the VCSEL along the optical axis until the beam appears collimated on a surface ≈ 5 m away. Secure the VCSEL with a set-screw. Adjust aspheric lens with the four adjustment screws, until the beam path is on axis. Expose adhesive to UV to bond the aspheric lens into its mount.

Add UV adhesive to the underside of the polarising beam-splitter (Item #5a). Place the polarising beam-splitter onto the base-plate (Item #1). Locate one face of the polarising beam-splitter flush against the inside wall of the template (Item #2). Expose adhesive to UV to bond the polarising beam-splitter to the base-plate.

Task (2) - Set ½ wave plate orientation.

Add UV adhesive to the underside of the non-polarising beam-splitter (Item #7). Place the non-polarising beam-splitter onto the base-plate (Item #1). Locate one face of the non-polarising beam-splitter flush against the inside wall of the template (Item #2). Expose adhesive to UV to bond the non-polarising beam-splitter to the base-plate.

Add UV adhesive to the underside of the polarising beam-splitter (Item #6). Place the polarising beam-splitter onto the base-plate (Item #1). Locate one face of the polarising beam-splitter flush against the inside wall of the template (Item #2). Expose adhesive to UV to bond the polarising beam-splitter to the base-plate.

Add UV adhesive at the interface between polarising beam-splitter and ½ wave plate. Rotate ½ wave plate around optical axis until transmitted and reflected intensities are equal. Monitor output intensities with externally mounted photodiodes. n.b. suitable fixtures and photodiodes are required, to enable a photodiode to be located in the limited space available in the reference arm. Expose adhesive to UV to bond the ½ wave plate to the polarising beam-splitter.

Task (3) - Fix reference mirror.

Add UV adhesive at the interface between base of reference mirror (Item #3) and base-plate (Item #1). The reference mirror should be located flush against the inside wall of the template (Item #2), ensuring the largest possible separation between it and the polarising beam-splitter (Item #6). Expose adhesive to UV to bond the reference mirror to the base-plate.

Task (4) - Align target mirror.

Add an externally mounted target mirror approximately at the sweet-spot, which is ≈ 21 mm away from the enclosure. Ensure it is aligned by observing beam overlap at PD1.

Task (5) - Set ¼ wave plate orientation (Reference arm).

Add an externally mounted photodiode to replace the cat's eye components (Items #8 and #10). Place 'free-standing', the ¼ wave-plates (Items #4a and #4b). Cover measurement arm mirror and adjust ¼ wave plate (Item #4a) to maximise intensity on the photodiode replacing the cat's eye. Use UV curing optical adhesive to bond ¼ wave plate to the template (Item #2).

Task (6) - Set ¼ wave plate orientation (Measurement arm).

Leave the cat's eye photodiode in place. Un-cover measurement arm and cover reference arm. Adjust ¼ wave plate (Item #4b) to maximise intensity on the photodiode replacing the cat's eye. Use UV curing optical adhesive to bond ¼ wave plate to the template (Item #2). Un-cover reference arm.

Task (7) - Align cat's eye.

Remove photodiode from cat's eye and replace with an externally mounted mirror. Align mirror by ensuring return beams come back on themselves. Observe these same beams at PD1, noting their diameter. Remove the outboard cat's eye mirror. Place doublet (Item #8) and use UV curing optical adhesive to bond to the template (Item #2).

Install cat's eye assembly (Item #10) and translate assembly so to ensure that the beams are of the same diameter as previously noted at PD1.

Task (8) - Set ¼ wave plate orientation.

Add UV adhesive to the underside of the polarising beam-splitter (Item #5b). Place the polarising beam-splitter onto the base-plate (Item #1). Locate one face of the polarising beam-splitter flush against the inside wall of the template (Item #2). Expose adhesive to UV to bond the polarising beam-splitter to the base-plate.

Add UV adhesive at the interface between polarising beam-splitter and ¼ wave plate. Rotate ¼ wave plate around optical axis until the two Lissajous figures are optimised. The optimisation process is yet to be determined Expose optical adhesive to UV to bond the ¼ wave plate to the polarising beam-splitter.

Appendix I - EUCLID Software and Noise Models

The first is the Visual Basic code written to interface with the EUCLID electronics module. This is known as the USB data acquisition software and is capable of commanding EUCLID into the desired mode of operation. Once commanded to run mode it then receives data packets via the USB port. Data integrity is verified using packet counts and checksums. Valid data is then stored in a binary data file for post-processing by a MATLAB script (see next listing).

```
' Main.frm
'
' EUCLID: USB Data Acquisition Software
'
' Author: SMA
' Date: 19/01/2009
' Project: EUCLID
' Language: Visual Basic 6.0
'
' Version History:
'
' Version |   Date   | Name | Details
' --------+----------+------+-------------------------------------------
'  0.1    | 19/01/09 | SMA  | Adapted LPF TRP Control Software 09/02/05
'         |          |      | Renamed project and related file (forms etc)
'         |          |      | Revised GUI for EUCLID phase telemetry
'  0.2    | 22/01/09 | SMA  | Fixed windows object and made drag-able
'         |          |      | Fixed UoB icon
'  0.3    | 23/01/09 |      | Updated GUI (locked some text boxes)
'         |          |      | Added MSComm control
'  0.4    | 05/03/09 | SMA  | Added COMmanD packet
'  0.5    | 08/03/09 | SMA  | Removed redundant code
'         |          |      | Added VeCToR packet
'         |          |      | Added Start/Stop functions
'  0.6    | 09/02/09 | SMA  | Tidy-Up
'  0.7    | 21/06/10 | SMA  | Revised author list
'         |          |      | Revised to be done list
'  0.8    | 24/06/10 | SMA  | Revised GUI Options
'         |          |      | Checked for open comm port
'         |          | SMA  | Revised command packet format (multi-trans)
'  0.9    | 29/06/10 | SMA  | Revised GUI object (added buttons)
'         |          |      | Revised command packet format (single-trans)
'         |          |      | Added measurement ASCII file storage
'         |          |      | Reverted to binary (from ASCII file storage)
'         |          |      | Fixed Com port already closed issue
'         |          |      | Fixed Fletcher checksum sum1 & sum2 order
'         |          |      | Implemented data validation checks
'         |          |      | Refined GUI layout for validation & status
'         |          |      | Tidy-up GUI labels and default config
'         |          |      | Added LED status indicators to GUI
'  1.0    | 05/07/10 | SMA  | Tidy-Up annotations and checked spelling
'         |          |      | Initial release version
'         |          |      | Fixed buffer overrun s/w issue
'  1.1    | 06/07/10 | SMA  | Relocated default data directory
'  1.2    | 16/07/10 | SMA  | Stores complete VCTR packet in file
'  1.3    | 20/07/10 | SMA  | Add wait delay after start command
```

```
' 1.4    | 15/09/10 | SMA  | Changed default com port to 3
' 1.5    | 16/09/10 | SMA  | Fixed packet count bug (integer to long)
' 1.6    | 17/09/10 | SMA  | Added run duration (s) option to GUI
' --------+----------+------+---------------------------------------------
'
' Bug List:-
'
' Cant reset distance while running (or any other command)
' Optimise port open/close
'
' To Be Done List:-
'
' Check for a change in state before updating status flags
' Start auto reset distance and flags?
' Run from Commandline
' Doc-link Works
' Grey out invalid GUI options
' Add calibration options

Option Explicit

'Declare Prototypes
Private Declare Sub Sleep Lib "kernel32.dll" (ByVal dwMilliseconds As Long)

Private Sub Start_Click()

' ************************************
' *** Start Phase Data Transmission ***
' ************************************

Dim i As Integer
Dim j As Integer
Dim k As Integer

Dim Header1 As Byte
Dim Header2 As Byte
Dim Header3 As Byte
Dim Header4 As Byte

Dim PCountMSB As Byte
Dim PCountLSB As Byte
Dim PCount As Long
Dim Count As Long
Dim Status As Boolean

Dim CheckSum1 As Byte
Dim CheckSum2 As Byte
Dim Sum1 As Integer
Dim Sum2 As Integer

Dim DevRefMSB As Byte
Dim DevRefLSB As Byte
Dim DevRef As Integer

Dim Data As Byte
Dim StatFlag As Byte
Dim Measurement(1 To 1585, 1 To 5) As Byte

Dim fext As String
Dim fpath As String
Dim fname As String
Dim FileName As String

Dim MSCPacket As String
Dim DATAPacket As String

Dim MSCbuf(0 To 4) As Byte
Dim DATAbuf(1 To 7936) As Byte

Call LEDreset

' Turn ON timer
```

```
Timer1.Enabled = True

' Text13.Text = Time

' Extract directory path from GUI
fpath = Text1.Text
' Create filename and header from current date & time
fname = Format(Now, "ddmmyyhhmmss")
' Create filename extension
fext = ".bin"
' Generate full filemame (including path)
FileName = fpath + fname + fext

' Check if file already open
'If FileExists("FileName") Then
'    Debug.Print "Exists"
'End If

' Open file
' Open FileName For Output As 1
Open FileName For Binary As #1
' Print file header
Put #1, , fname$ & Chr$(10) ' header + line feed
'Print #1, fname

' Check if Com Port Already Open
If MSComm1.PortOpen = False Then
    ' Initialize virtual communications port #1
    MSComm1.CommPort = Text2.Text
    ' Set com output buffer size (bytes)
    MSComm1.OutBufferSize = 10 ' 5
    ' Set com input buffer size (bytes)
    MSComm1.InBufferSize = 8192 ' 7936
    ' Set number of bytes to read at a time
    MSComm1.InputLen = 7936
    ' Open the com port
    MSComm1.PortOpen = True
End If

' COMmanD Packet Header Values
Header1 = Asc("C")
Header2 = Asc("O")
Header3 = Asc("M")
Header4 = Asc("D")

' COMmanD Packet Data Values
Data = 1

' Generate Command Packet Header & Data
MSCPacket = Format(Header1, "000") & Format(Header2, "000") & Format(Header3,
"000") & Format(Header4, "000") & Format(Data, "000")

' Break-down packet and store in byte array
For i = 1 To Len(MSCPacket) / 3
    MSCbuf(i - 1) = CByte(Mid(MSCPacket, ((i * 3) - 2), 3))
Next i

' Write the data to the device buffer
MSComm1.Output = MSCbuf

' Set Initial Status
Status = False

Do

    ' Wait until the buffer contains one packet of data (7936 bytes)
    While MSComm1.InBufferCount >= 7936

        ' Read in complete data packet as a string
        DATAPacket = MSComm1.Input

        ' Packet Header (VCTR)
```

200

```vb
        If Mid(DATAPacket, 1, 1) <> "V" Then Debug.Print "Header Sync Error (V)"
        If Mid(DATAPacket, 2, 1) <> "C" Then Debug.Print "Header Sync Error (C)"
        If Mid(DATAPacket, 3, 1) <> "T" Then Debug.Print "Header Sync Error (T)"
        If Mid(DATAPacket, 4, 1) <> "R" Then Debug.Print "Header Sync Error (R)"
        Put #1, , Mid$(DATAPacket, 1, 4)
        ' Debug.Print Mid(DATAPacket, 1, 4)

        ' Device Reference
        DevRefMSB = CByte(Asc(Mid(DATAPacket, 5, 1)))
        DevRefLSB = CByte(Asc(Mid(DATAPacket, 6, 1)))
        Put #1, , DevRefMSB
        Put #1, , DevRefLSB
        DevRef = (DevRefLSB * 2 ^ 0) + (PCountMSB * 2 ^ 8)
        ' Debug.Print DevRef
        ' Debug.Print CByte(Asc(Mid(DATAPacket, 5, 1))); CByte(Asc(Mid(DATAPacket,
6, 1)))

        ' Packet Count
        PCountMSB = CByte(Asc(Mid(DATAPacket, 7, 1)))
        PCountLSB = CByte(Asc(Mid(DATAPacket, 8, 1)))
        Put #1, , PCountMSB
        Put #1, , PCountLSB
        PCount = (PCountLSB * 2 ^ 0) + (PCountMSB * 2 ^ 8)
        ' Debug.Print PCount
        ' Debug.Print CByte(Asc(Mid(DATAPacket, 7, 1))); CByte(Asc(Mid(DATAPacket,
8, 1)))

        ' Store Measurement Data (Binary)
        i = 8

        For j = 1 To 1585
            For k = 1 To 5
                i = i + 1
                Measurement(j, k) = CByte(Asc(Mid(DATAPacket, i, 1)))
                Put #1, , Measurement(j, k)
                DoEvents
            Next k
        Next j

        ' Status Flags
        StatFlag = CByte(Asc(Mid(DATAPacket, 7934, 1)))
        Put #1, , StatFlag
        ' Debug.Print StatFlag

        ' Read Packet Checksum
        CheckSum2 = CByte(Asc(Mid(DATAPacket, 7935, 1)))
        CheckSum1 = CByte(Asc(Mid(DATAPacket, 7936, 1)))
        Put #1, , CheckSum2
        Put #1, , CheckSum1
        ' Debug.Print CByte(Asc(Mid(DATAPacket, 7936, 1)));
CByte(Asc(Mid(DATAPacket, 7935, 1)))

        ' Sequential Packet Check (and check for 1st iteration)
        If Status = False Then
            Count = PCount
            Status = True
        End If

        ' Compare Checksums and Update Status LED
        If Count <> PCount Then Main.Text3.BackColor = &HFF&
        ' Debug.Print Count; PCount

        ' Increment Packet Count for next time
        Count = Count + 1
        If Count = 65536 Then Count = 0 ' 2 bytes i.e. 2^16

        ' Calculate Fletcher Checksum
        Sum1 = 0
        Sum2 = 0

        For j = 1 To 1585
            For k = 1 To 5
```

```
                Sum1 = (Sum1 + Int(Measurement(j, k))) Mod 255
                Sum2 = (Sum2 + Sum1) Mod 255
            Next k
        Next j
        ' Debug.Print Sum1; Sum2

        ' Compare Checksums and Update Status LED
        If CByte(Sum1) <> CheckSum1 Then Main.Text4.BackColor = &HFF&
        If CByte(Sum2) <> CheckSum2 Then Main.Text4.BackColor = &HFF&

        ' Report Error Flags
        If (CByte(Asc(Mid(DATAPacket, 7934, 1))) And CByte(128)) >= 1 Then
Main.Text5.BackColor = &HFF&
        If (CByte(Asc(Mid(DATAPacket, 7934, 1))) And CByte(64)) >= 1 Then
Main.Text6.BackColor = &HFF&
        If (CByte(Asc(Mid(DATAPacket, 7934, 1))) And CByte(32)) >= 1 Then
Main.Text7.BackColor = &HFF&
        If (CByte(Asc(Mid(DATAPacket, 7934, 1))) And CByte(16)) >= 1 Then
Main.Text8.BackColor = &HFF&

        ' Report Status
        If (CByte(Asc(Mid(DATAPacket, 7934, 1))) And CByte(8)) >= 1 Then
Main.Text9.Text = "1"
        If (CByte(Asc(Mid(DATAPacket, 7934, 1))) And CByte(4)) >= 1 Then
Main.Text10.Text = "1"
        If (CByte(Asc(Mid(DATAPacket, 7934, 1))) And CByte(2)) >= 1 Then
Main.Text11.Text = "1"
        If (CByte(Asc(Mid(DATAPacket, 7934, 1))) And CByte(1)) >= 1 Then
Main.Text12.Text = "1"

    Wend

    DoEvents

    Call Sleep(160) ' Added 160ms Delay

Loop Until MSComm1.InBufferCount = 0

' Close File
Close #1

' Check if Com Port Already Closed
If MSComm1.PortOpen = True Then
    ' Close the com port
    MSComm1.PortOpen = False
End If

End Sub

Private Sub Stop_Click()

' **************
' *** Standby ***
' **************

Dim i As Integer
Dim j As Integer

Dim Header1 As Byte
Dim Header2 As Byte
Dim Header3 As Byte
Dim Header4 As Byte

Dim Data As Byte

Dim MSCPacket As String

Dim MSCbuf(0 To 4) As Byte

' Turn OFF timer
Timer1.Enabled = False
```

202

```vb
' Check if Com Port Already Open
If MSComm1.PortOpen = False Then
    ' Initialize virtual communications port #1
    MSComm1.CommPort = Text2.Text
    ' Set com output buffer size (bytes)
    MSComm1.OutBufferSize = 10 ' 5
    ' Set com input buffer size (bytes)
    MSComm1.InBufferSize = 8192 ' 7936
    ' Set number of bytes to read at a time
    MSComm1.InputLen = 7936
    ' Open the com port
    MSComm1.PortOpen = True
End If

' COMmanD Packet Header Values
Header1 = Asc("C")
Header2 = Asc("O")
Header3 = Asc("M")
Header4 = Asc("D")

' COMmanD Packet Data Values
Data = 0

' Generate Command Packet Header & Data
MSCPacket = Format(Header1, "000") & Format(Header2, "000") & Format(Header3,
"000") & Format(Header4, "000") & Format(Data, "000")

' Break-down packet and store in byte array
For i = 1 To Len(MSCPacket) / 3
    MSCbuf(i - 1) = CByte(Mid(MSCPacket, ((i * 3) - 2), 3))
Next i

' Write the data to the device buffer
MSComm1.Output = MSCbuf
Sleep (500)

' Check if Com Port Already Closed
If MSComm1.PortOpen = True Then
    ' Close the com port
    MSComm1.PortOpen = False
End If

End Sub

Private Sub Status_Click()

' **************************
' *** Reset Status Flags ***
' **************************

Dim i As Integer
Dim j As Integer

Dim Header1 As Byte
Dim Header2 As Byte
Dim Header3 As Byte
Dim Header4 As Byte

Dim Data As Byte

Dim MSCPacket As String

Dim MSCbuf(0 To 4) As Byte

' Check if Com Port Already Open
If MSComm1.PortOpen = False Then
    ' Initialize virtual communications port #1
    MSComm1.CommPort = Text2.Text
    ' Set com output buffer size (bytes)
    MSComm1.OutBufferSize = 10 ' 5
    ' Set com input buffer size (bytes)
    MSComm1.InBufferSize = 8192 ' 7936
```

```vb
    ' Set number of bytes to read at a time
    MSComm1.InputLen = 7936
    ' Open the com port
    MSComm1.PortOpen = True
End If

' COMmanD Packet Header Values
Header1 = Asc("C")
Header2 = Asc("O")
Header3 = Asc("M")
Header4 = Asc("D")

' COMmanD Packet Data Values
Data = 2

' Generate Command Packet Header & Data
MSCPacket = Format(Header1, "000") & Format(Header2, "000") & Format(Header3,
"000") & Format(Header4, "000") & Format(Data, "000")

' Break-down packet and store in byte array
For i = 1 To Len(MSCPacket) / 3
    MSCbuf(i - 1) = CByte(Mid(MSCPacket, ((i * 3) - 2), 3))
Next i

' Write the data to the device buffer
MSComm1.Output = MSCbuf
Sleep (500)

' Check if Com Port Already Closed
If MSComm1.PortOpen = True Then
    ' Close the com port
    MSComm1.PortOpen = False
End If

End Sub

Private Sub Distance_Click()

' ***************************
' *** Reset Distance Count ***
' ***************************

Dim i As Integer
Dim j As Integer

Dim Header1 As Byte
Dim Header2 As Byte
Dim Header3 As Byte
Dim Header4 As Byte

Dim Data As Byte

Dim MSCPacket As String

Dim MSCbuf(0 To 4) As Byte

' Check if Com Port Already Open
If MSComm1.PortOpen = False Then
    ' Initialize virtual communications port #1
    MSComm1.CommPort = Text2.Text
    ' Set com output buffer size (bytes)
    MSComm1.OutBufferSize = 10 ' 5
    ' Set com input buffer size (bytes)
    MSComm1.InBufferSize = 8192 ' 7936
    ' Set number of bytes to read at a time
    MSComm1.InputLen = 7936
    ' Open the com port
    MSComm1.PortOpen = True
End If

' COMmanD Packet Header Values
Header1 = Asc("C")
```

```vb
Header2 = Asc("O")
Header3 = Asc("M")
Header4 = Asc("D")

' COMmanD Packet Data Values
Data = 4

' Generate Command Packet Header & Data
MSCPacket = Format(Header1, "000") & Format(Header2, "000") & Format(Header3,
"000") & Format(Header4, "000") & Format(Data, "000")

' Break-down packet and store in byte array
For i = 1 To Len(MSCPacket) / 3
    MSCbuf(i - 1) = CByte(Mid(MSCPacket, ((i * 3) - 2), 3))
Next i

' Write the data to the device buffer
MSComm1.Output = MSCbuf
Sleep (500)

' Check if Com Port Already Closed
If MSComm1.PortOpen = True Then
    ' Close the com port
    MSComm1.PortOpen = False
End If

End Sub


Public Sub LEDreset()

' ****************
' *** LED Reset ***
' ****************

'All LEDs Reset to Bright Green
Main.Text3.BackColor = &HFF00&
Main.Text4.BackColor = &HFF00&
Main.Text5.BackColor = &HFF00&
Main.Text6.BackColor = &HFF00&
Main.Text7.BackColor = &HFF00&
Main.Text8.BackColor = &HFF00&

End Sub


Private Sub Exit_Click()

' **********************
' *** Exit Application ***
' **********************

' Wait for output buffer to clear
'While MSComm1.OutBufferCount <> 0
'    Sleep (100)
'    ' DoEvents
'Wend
End

End Sub


Private Sub Timer1_Timer()

' Decrement time by 1 second
Text13.Text = Val(Text13.Text) - 1

' Check if countdown completed
If Val(Text13.Text) = 0 Then
    Sleep (1000)
    Call Stop_Click
    Call Stop_Click
End If

End Sub
```

The second code listed is the MATLAB script used to interrogate the binary data files produced and post-process the data. A time history of the of the interferometer measurements is produced in addition to a displacement noise plot.

```
% EUCLID_daq.m
%
% EUCLID: USB Data Acquisition Software
%
% Author: SMA
% Date: 05/07/2010
% Project: EUCLID
% Language: MATLAB 7.9.0.529 (R2009b) 12th August 2009
%
% Version History:
%
%  Version |   Date    | Name | Details
%  --------+-----------+------+--------------------------------------------
%   1.0    | 05/07/10  | SMA  | Initial demonstration release
%   1.1    | 16/07/10  | SMA  | Handles full telemetry packets
%          |           |      | Added telemetry filelist selection
%          |           |      | Added packet validation checks
%          |           |      | Added reporting of status flags
%   1.2    | 18/07/10  | SMA  | Added time series to plot
%          |           |      | Revised plot legends and title
%   1.3    | 19/07/10  | SMA  | Fixed status byte interrogation (bitand)
%          |           |      | Fixed measurement data array indexing
%          |           |      | Pre-allocate measurement data arrays
%          |           | SMA  | Remove redundant arrays
%          |           |      | Added pwelch PSD calculation & plot
%   1.4    | 20/07/10  | SMA  | Optimised / removed redundant arrays
%          |           |      | Added tic / toc timer (s) reporting
%   1.5    | 27/07/10  | DMH  | Fixed issue with negative number scaling
%   1.6    | 28/07/10  | SMA  | Made analysis script compatible with V6
%   1.7    | 08/08/10  | SMA  | Added decimation of raw telemetry data
%   1.8    | 19/08/10  | SMA  | Added filesize info (bytes -> seconds)
%          |           |      | Added option to process fixed duration (s)
%          |           |      | Fixed runlength to be integer # of packets
%          |           |      | Fixed pre-allocation of arrays
%          |           |      | Removed decimation
%   1.9    | 20/08/10  | SMA  | Set parameters at beginning of script
%          |           |      | Tidied-up annotations and spell checked
%   2.0    | 22/08/10  | SMA  | Reinstate s/w decimation option
%          |           |      | Tidy-up variable names
%          |           |      | Enabled downsample for large datasets
%   2.1    | 23/08/10  | SMA  | Re-format and scale sensitivity plot
%   2.2    | 02/09/10  | SMA  | Fix Wavelength (from 633nm to 667nm)
%          |           | SMA  | Pre-allocate Measurement Array
%          |           | SMA  | Added EUCLID #1 Calibration Plot Title
%   2.3    | 10/09/10  | SMA  | Average rather than downsample raw data
%   2.4    | 14/09/10  | SMA  | Optimised sample averaging function
%   2.5    | 16/09/10  | SMA  | Fixed final packet averaging bug
%          |           |      | Fixed DDistance pre-allocation issue
%   2.6    | 23/09/10  | SMA  | Added detrend to data prior to p.welch psd
%   2.7    | 12/10/10  | SMA  | Revised parameters for 1 MHz sampling
%   --------+-----------+------+--------------------------------------------
%
% To Do List:
% Need to read 1st packet from each file to get HSR & HDR data?
% (rather than hard-code it)
%
% Bug List:
% Ideally should use Decimate instead of Downsample
% (but within memory constraints)
%

clear all
clc
```

```matlab
% Set VCSEL Wavelength (m)
lamda = 633e-9;

% Set h/w Sample Rate (Hz)
HSR = 1e6;

% Set h/w Decimation Factor
HDF = 50;

% Set h/w Decimated Rate (Hz)
HDR = HSR/HDF;

% Set s/w Decimated Rate (Hz)
SDR = 20e3;

% Set Measurements per Packet
MP = 1585;

% Set Packet Length (bytes)
PL = 7936;

% Set Packet Duration (s)
PD = MP/HDR;

% Report Name and Version Information
fprintf('\n-----------------------------------------------------------')
fprintf('\n EUCLID - Telemetry Processing Script - Version 2.7 - SMA ')
fprintf('\n-----------------------------------------------------------\n\n')

% Navigate to data sub-directory
cd('..\Data\');

% Retrieve data file list from current directory
Filelist = dir('*.bin');

% Number of file entries in file list
n = size(Filelist);

% Echo file index to command line
for i=1:n(1)
    fprintf(' %g. %s - %g seconds \n',i,Filelist(i).name,((Filelist(i).bytes-
13)/PL)*PD)
end

% Input file index required and run length
Filenumber = str2double(input('\n Enter Telemetry File Number to Process >> ',
's'));
Runlength = str2double(input('\n Enter Run Length (s) to Process >> ', 's'));

% Fix runlength to be integer number of packets
Runlength = ceil(Runlength/PD) * PD;

fprintf('\n --- Processing --- \n')
tic % Start Timer

% Pre-allocate Large Arrays
Measurement = zeros(5,MP); % Pre-allocate the Measurement Array
Distance = zeros(1,(Runlength/PD)*MP); % Pre-allocate the Distance Array
DDistance = zeros(1,ceil(((Runlength/PD)*MP)/(HDR/SDR))); % Pre-allocate the
DDistance Array

% Generate Filename from file index
Filename = Filelist(Filenumber).name;

% Read ASCII file header and set EOF
fid = fopen(Filename);
[FileHeader,count] = fscanf(fid,'%12s',1); % Read header (12-bytes x1)
fseek(fid, 0, 'eof'); % Set pointer to EOF
fend = ftell(fid); % Get EOF value
fclose(fid);

% Validation Check (Filename vs. File Header)
```

```matlab
Name = strtok(Filename,'.');
if strcmp(Name, FileHeader) == 0; fprintf('\n *** File Header Validation Error ***
\n'); end

% Read Telemetry Packets (Binary)
fid = fopen(Filename, 'rb', 'ieee-le');
fread(fid, 13, 'uint8', 'ieee-le'); % Ignore file header & line feed
fcurrent = ftell(fid); % Set current pointer position

% Initial Telemetry Packet Count
PC = 0;

while fcurrent ~= fend % Check for EOF exit condition

    fcurrent = ftell(fid); % Set current pointer position
    fseek(fid, 0, 'eof'); % Set pointer to EOF
    fend = ftell(fid); % Set EOF value
    fseek(fid, fcurrent, 'bof'); % Reset current pointer

    pdata = fread(fid, PL, 'uint8', 'ieee-le'); % Read Packet

    if isempty(pdata); break, end

    % Extract & Validate Packet Header (4-bytes)
    if pdata(1) ~= 'V' || pdata(2) ~= 'C' || pdata(3) ~= 'T' || pdata(4) ~= 'R'
        fprintf('\n *** Packet Header Validation Error *** \n')
    end

    % Extract & Report Device Reference (2-bytes)
    DevRef = (pdata(6) * 2^0) + (pdata(5) * 2^8);
    if PC == 0; fprintf('\n Device Reference = %G \n',DevRef); end

    % Extract & Validate Packet Count (2-bytes)
    PktCnt = (pdata(8) * 2^0) + (pdata(7) * 2^8);

    % Sequential Packet Check and check for 1st iteration
    if PC == 0; Count = PktCnt; end

    % Compare & Report Packet Count Error
    if Count ~= PktCnt; fprintf('\n *** Packet Count Validation Error *** \n');
end

    % Increment Packet Count for next time (or reset)
    Count = Count + 1;
    if Count == 65536; Count = 0; end

    % Extract Measurement Data (5-bytes)
    k = 8; % byte off-set (-1)
    for i = 1:MP
        for j = 1:5
            k = k + 1 ;
            Measurement(j,i) = pdata(k);
        end
    end

    for i = 1:MP

    % Create the basic integer
    Distance(i+(PC*MP)) = ((Measurement(1,i) * (2^32)) + (Measurement(2,i) *
(2^24)) + (Measurement(3,i) * (2^16)) + (Measurement(4,i) * (2^8)) +
(Measurement(5,i)));

    % Check for MS-Bit of MS-Byte for sign (1 => Negative)and convert to negative
if sign bit is set
    if Measurement(1,i) >= 128; Distance(i+(PC*MP)) = ((2^40 -
Distance(i+(PC*MP))) * -1); end

    % Scale the resulting signed integer
    Distance(i+(PC*MP))= Distance(i+(PC*MP)) * ((lamda/8)/(2^23));

    end
```

```matlab
    % Extract & Report Status Flags (1-byte)
    if PC == 0
     Status = pdata(7934);
     if bitand(Status,2^7) == 2^7; fprintf('\n *** Laser Temperature Error ***
\n'); end
     if bitand(Status,2^6) == 2^6; fprintf('\n *** Laser Current Error *** \n');
end
     if bitand(Status,2^5) == 2^5; fprintf('\n *** Fringe Error *** \n'); end
     if bitand(Status,2^4) == 2^4; fprintf('\n *** Overrun Error *** \n'); end
     if bitand(Status,2^3) == 2^3; fprintf('\n h/w Sample Mode = Continuous \n')
         if (bitand(Status,2^2) == 2^2) && (bitand(Status,2^1) == 2^1)
            TSR = 250e3; % Telemetry Sample Rate
            fprintf('\n h/w Sample Rate = 250 kHz \n')
         end
         if (bitand(Status,2^2) == 2^2) && (bitand(Status,2^1) == 0)
            TSR = 500e3; % Telemetry Sample Rate
            fprintf('\n h/w Sample Rate = 500 kHz \n')
         end
         if (bitand(Status,2^2) == 0) && (bitand(Status,2^1) == 2^1)
            TSR = 800e3; % Telemetry Sample Rate
            fprintf('\n h/w Sample Rate = 800 kHz \n')
         end
         if (bitand(Status,2^2) == 0) && (bitand(Status,2^1) == 0)
            TSR = 1e6; % Telemetry Sample Rate
            fprintf('\n h/w Sample Rate = 1 MHz \n')
         end
     else
         fprintf('\n h/w Sample Mode = Double Sampling \n')
         if (bitand(Status,2^2) == 2^2) && (bitand(Status,2^1) == 2^1)
            TSR = 10e3; % Telemetry Sample Rate
            fprintf('\n h/w Sample Rate = 10 kHz Switching 500 kHz \n')
         end
         if (bitand(Status,2^2) == 2^2) && (bitand(Status,2^1) == 0)
            TSR = 10e3; % Telemetry Sample Rate
            fprintf('\n h/w Sample Rate = 10 kHz Switching 1 MHz \n')
         end
         if (bitand(Status,2^2) == 0) && (bitand(Status,2^1) == 2^1)
            TSR = 5e3; % Telemetry Sample Rate
            fprintf('\n h/w Sample Rate = 5 kHz Switching 500 kHz \n')
         end
         if (bitand(Status,2^2) == 0) && (bitand(Status,2^1) == 0)
            TSR = 5e3; % Telemetry Sample Rate
            fprintf('\n h/w Sample Rate = 5 kHz Switching 1 MHz \n')
         end
     end
     if bitand(Status,2^0) == 2^0
         TDR = TSR/HDF; % Telemetry Decimated Rate
         fprintf('\n h/w Decimation Rate = %G Hz \n',TDR)
     end
    end

    % Calculate Fletcher Check-sum (2-bytes)
    Sum1 = 0;
    Sum2 = 0;

    for i = 1:MP
        for j = 1:5
            Sum1 = mod((Sum1 + Measurement(j, i)),255);
            Sum2 = mod((Sum2 + Sum1),255);
        end
    end

    % Validate Check-sums and Report Error
    if Sum2 ~= pdata(7935) || Sum1 ~= pdata(PL); fprintf('\n *** Packet Check-sum
Validation Error *** \n'); end

    % Increment Telemetry Packet Count
    PC = PC + 1;

    % Check Exit Condition
    if PC >= (Runlength/PD), break, end
```

```matlab
end % While Loop

% Close Telemetry File
fclose(fid);

% Return to EUCLID_Daq sub-directory
cd('..\EUCLID_daq\');

% Compare Sample Rates (Default Setting and Packet)
if HSR ~= TSR; fprintf('\n *** Sample Rate Inconsistency *** \n'); end

% Compare Decimated Rates (Default Setting and Packet)
if HDR ~= TDR; fprintf('\n *** Decimated Rate Inconsistency *** \n'); end

% s/w Decimation, Downsample or Average Complete Dataset
% DDistance = decimate(Distance,HDR/SDR);
% DDistance = downsample(Distance,HDR/SDR);

for i = 1:ceil((numel(Distance))/(HDR/SDR))
    if i > (numel(Distance)/(HDR/SDR))
        DDistance(i) = mean(Distance((((i-1)*(HDR/SDR))+1):(numel(Distance))));
    else
        DDistance(i) = mean(Distance((((i-1)*(HDR/SDR))+1):(i*(HDR/SDR))));
    end
end

fprintf('\n s/w Decimation or Downsample Rate = %G Hz \n',SDR)

% Clear Large Arrays
clear Measurement
clear Distance

% Total Time (s)
TT = (1/HDR)*(PC*MP);

% Time Series, downsampled & starting from 0 (s)
TS = 0:(1/HDR)*(HDR/SDR):(TT-((1/HDR)));

% Number of Samples
NS = numel(TS);

% Detrend Data-set
dDDistance = detrend(DDistance);

% Calculation of PSD (via P.Welch Method) and Scaling
[PDistance, w] = pwelch(dDDistance,hann(NS),[],NS,SDR,'onesided');
SDistance = sqrt(PDistance);

% Report Number of Packets Processed
fprintf('\n Total Number of Packets Processed = %G \n',PC)
fprintf('\n Total Run Duration = %G seconds \n',TT)
fprintf('\n --- Plotting --- \n')

% Plot Displacement Time Series
figure(1)
plot(TS,DDistance,'LineWidth',2)
xlabel('Time (s)','fontsize',14)
ylabel('Displacement (m)','fontsize',14)
% title (['EUCLID #1 (HeNe) - Free Air Displacement Time Series - (' Filename
')'],'FontWeight','Bold','FontSize',16)
title (['EUCLID #4 - Displacement Time Series - (' Filename
')'],'FontWeight','Bold','FontSize',16)
% title (['EUCLID #1 - Displacement Calibration - (' Filename
')'],'FontWeight','Bold','FontSize',16)

% Plot Displacement Sensitivity
figure(2)
loglog(w, SDistance,'LineWidth',2)
grid on
set(gca,'XMinorGrid','off','YMinorGrid','off','linewidth',1)
axis([1e-5,1e+4,1e-16,1e-6])
xlabel('Frequency (Hz)','fontsize',14)
```

```
ylabel('Displacement (m/rt(Hz))','fontsize',14)
% title (['EUCLID #1 (HeNe) - Free Air Displacement Sensitivity - (' Filename
')'],'FontWeight','Bold','FontSize',16)
title (['EUCLID #1 - Displacement Sensitivity - (' Filename
')'],'FontWeight','Bold','FontSize',16)
% title (['EUCLID - Electronics Noise - (' Filename
')'],'FontWeight','Bold','FontSize',16)
% title (['EUCLID #1 - Calibration - (' Filename
')'],'FontWeight','Bold','FontSize',16)

fprintf('\n --- Complete --- \n\n')
toc % Stop Timer and Report
```

The final code listed is the MATLAB scripts used to combine the EUCLID electronics and displacement noise plots. Models of noise limits are calculated and overlaid onto the displacement noise plots.

```
% -------------------------------------
% EUCLID Noise Budget & Sensitivity Plots
% -------------------------------------
% S. M. Aston - January 2011 - Version 1.2

clear all
clc

% ------------
% Noise Budget
% ------------

% Boltzmann Constant (J/K)
k = 1.38E-23;

% Charge on an Electron (C)
e = 1.60E-19;

% Trans-amp Feedback Resister (Ohms)
R = 68e3;

% Temperature (K)
T = 300;

% Minimum Decade 10^Fmin (Hz)
Fmin = -4;

% Maximum Decade 10^Fmax (Hz)
Fmax = 3;

% Number of Points Between Decades
n = 100;

% Generate a Logarithmically Spaced Frequency Vector
F = logspace(Fmin,Fmax,n);

% VCSEL Wavelength (m)
lamda = 667e-9;

% Photodiode Responsivity (A/W) @ ~667nm
a = 0.42;

% h/w Sample Rate (Hz)
HSR = 250e3;

% ADC Input Voltage Range (V)
Vin = 4;

% ADC Utilization
ADCu = 0.5;
```

```matlab
% ADC Number of Bits
ADCN = 18;

% Photodiode Current (A)
Ip = ((Vin*ADCu)/8)/R; % ADC Driver gain of 8 Vin? or /2?

% Power Incident on Photodiode (W)
Pp = Ip/a;

% ADC Estimated Noise lsb (rms) inc quantization
ADCn = 15;

% ADC Noise voltage (V/rt-Hz)
ADCv = ADCn * (Vin/2^ADCN) * 1/sqrt(HSR/2);

% ADC Noise equivalent to output displacement (m/rtHz)
ADCx = (ADCv/(Vin*ADCu)) * (lamda/(8*pi));

% Johnson Noise current (A/rtHz)
JNi = sqrt((4*k*T)/R);

% Johnson Noise voltage (V/rtHz)
JNv = JNi * R * 8; % ADC driver Gain 8

% Johnson Noise Equivalent output displacement (m/rtHz)
JNx = (JNv/(Vin*ADCu)) * (lamda/(8*pi));

% Shot-Noise current (A/rt-Hz)
SNi = sqrt(2 * e * Ip);

% Shot-Noise Equivalent output displacement (m/rt-Hz)
SNx = (SNi*R*8) * (lamda/(8*pi));

% Generate n data points for frequency vector
JNy(1:n) = JNx;
SNy(1:n) = SNx;
ADCy(1:n) = ADCx;

% Open *.fig file and display 1
openfig('250 kHz Electronics Noise.fig')
set(gca,'XMinorGrid','off','YMinorGrid','off','linewidth',1)
% Extract x-y data from *.fig file
x1=get(findobj('type','line'),'XData');
y1=get(findobj('type','line'),'YData');
close(1)

% Open *.fig file and display 2
openfig('1 MHz Electronics Noise.fig')
set(gca,'XMinorGrid','off','YMinorGrid','off','linewidth',1)
% Extract x-y data from *.fig file
x2=get(findobj('type','line'),'XData');
y2=get(findobj('type','line'),'YData');
close(1)

% Open *.fig file and display 3
openfig('250 kHz Displacement Noise.fig')
set(gca,'XMinorGrid','off','YMinorGrid','off','linewidth',1)
% Extract x-y data from *.fig file
x3=get(findobj('type','line'),'XData');
y3=get(findobj('type','line'),'YData');
close(1)

% Open *.fig file and display 4
openfig('1 MHz Displacement Noise.fig')
set(gca,'XMinorGrid','off','YMinorGrid','off','linewidth',1)
% Extract x-y data from *.fig file
x4=get(findobj('type','line'),'XData');
y4=get(findobj('type','line'),'YData');
close(1)

% Open *.fig file and display 5
openfig('HeNe Diplacement Noise.fig')
```

```
set(gca,'XMinorGrid','off','YMinorGrid','off','linewidth',1)
% Extract x-y data from *.fig file
x5=get(findobj('type','line'),'XData');
y5=get(findobj('type','line'),'YData');
close(1)

% Plot Noise Characterisation
figure(1)
loglog(x1, y1,'-g',x2, y2,'-y',x3, y3,'-b',x4, y4,'-c',F,ADCy,'--c',F,JNy,'--
m',F,SNy,'--r',x5, y5,'-r','LineWidth',2)
grid on
set(gca,'XMinorGrid','off','YMinorGrid','off','linewidth',1)
axis([1e-5,1e+4,1e-16,1e-6])
legend('Front-End Electronics Noise (Fs = 250 kHz)','Front-End Electronics Noise
(Fs = 1 MHz)','EUCLID #4 Displacement Sensitivity (Fs = 250 kHz)','EUCLID #4
Displacement Sensitivity (Fs = 1 MHz)','ADC Noise','Johnson Noise','Shot-
Noise','EUCLID #1 Displacement Sensitivity with He-Ne (Fs = 1 MHz)')
xlabel('Frequency (Hz)','fontsize',14)
ylabel('Displacement (m/rt(Hz))','fontsize',14)
title ('EUCLID - Noise Characterisation','FontWeight','Bold','FontSize',16)
```